

UNIVERSIDADE DE LISBOA
INSTITUTO SUPERIOR TÉCNICO

Construction in Structural Glass

**Flexural Behaviour of Laminated Glass Members and
Development of Glass-GFRP Composite Beams**

Luís Guilherme da Cunha Seixas Valarinho

Supervisor: Doctor João Pedro Ramôa Ribeiro Correia

Co-Supervisor: Doctor Fernando António Baptista Branco

**Thesis approved in public session to obtain the PhD degree in
Civil Engineering**

Jury final classification: Pass with Distinction and Honour

Jury

Chairperson: Chairman of the IST Scientific Board

Members of the Committee:

Doctor João Pedro Ramôa Ribeiro Correia

Doctor Jorge Manuel Vinagre Alfaiate

Doctor Pieter Christiaan Louter

Doctor Sandra Filomena da Silva Jordão Alves

Doctor Albano Luís Rebelo da Silva das Neves e Sousa

2016

UNIVERSIDADE DE LISBOA
INSTITUTO SUPERIOR TÉCNICO

Construction in Structural Glass

**Flexural Behaviour of Laminated Glass Members and
Development of Glass-GFRP Composite Beams**

Luís Guilherme da Cunha Seixas Valarinho

Supervisor: Doctor João Pedro Ramôa Ribeiro Correia

Co-Supervisor: Doctor Fernando António Baptista Branco

**Thesis approved in public session to obtain the PhD degree in
Civil Engineering**

Jury final classification: Pass with Distinction and Honour

Jury

Chairperson: Chairman of the IST Scientific Board

Members of the Committee:

**Doctor João Pedro Ramôa Ribeiro Correia, Associate Professor (with
habilitation), Instituto Superior Técnico, Universidade de Lisboa**

**Doctor Jorge Manuel Vinagre Alfaiate, Assistant Professor (with habilitation),
Instituto Superior Técnico, Universidade de Lisboa**

**Doctor Pieter Christiaan Louter, Assistant Professor, Faculty of Architecture and
the Built Environment, TUDelft – Delft University of Technology, The Netherlands**

**Doctor Sandra Filomena da Silva Jordão Alves, Assistant Professor, Faculdade
de Ciências e Tecnologia, Universidade Coimbra**

**Doctor Albano Luís Rebelo da Silva das Neves e Sousa, Assistant Professor,
Instituto Superior Técnico, Universidade de Lisboa**

Funding institution

Fundação para a Ciência e Tecnologia

2016

ABSTRACT

In the last decades the use of glass with structural functions has attracted a growing interest from construction agents, who have been challenging architects and engineers to strive for new methods and solutions to apply glass as a structural material. That demand was followed by the introduction of several innovations, such as large-size laminated (tempered) glass members and high-performance interlayers for structural applications. In the same way, the research community has also been developing extensive studies to improve the understanding about the structural behaviour of glass members. However, despite the existence of a large number of studies on laboratory environment using small to intermediate-scale specimens, there is a lack of research about the structural behaviour of full-scale structures, including the new multi-layer large-size glass elements. Moreover, as a structural material, glass still exhibits some disadvantages when compared to traditional materials, the most relevant being its brittleness. In that context, several researchers have been trying to overcome the fragile behaviour of glass by combining it with other structural materials, in order to achieve safer failure mechanisms with post-cracking strength and ductility.

This thesis comprises investigations on the structural glass field covering the domains of (i) laminated glass structural members and (ii) structural composite glass systems. In the former domain, two main topics were addressed: (i.1) the lateral-torsional buckling (LTB) behaviour of long-span multi-layer laminated glass beams, and (i.2) the creep behaviour of full-scale laminated glass panels. The studies on the structural composite glass systems comprised two main topics: (ii.1) the characterization of the post-cracking robustness of long-span glass-stainless steel composite beams, and (ii.2) the development of a new composite structural system combining glass panels with pultruded glass fibre reinforced polymer (GFRP) laminates.

The research about the LTB behaviour of long-span laminated glass beams included analytical studies focussed on (i) the assessment of the accuracy of existing expressions for the determination of the effective flexural and torsional stiffness of 3-layer laminated glass beams, (ii) the determination of the LTB resistance and post-buckling behaviour of a 3-layer long-span laminated glass beam, and (iii) the assessment of the influence of the interlayer's viscoelastic behaviour on the LTB behaviour. The analytical studies were complemented with a flexural test of a simply supported and unbraced 8.20 m long PVB 3-layer laminated glass fin used in the facade of the *Champalimaud Centre for the Unknown* (Lisbon). Finally, three-dimensional numerical models were also developed in order to validate both the analytical and experimental studies. The results obtained highlight the high susceptibility of the LTB behaviour to the viscoelastic properties of PVB, which presents significant time and temperature dependency.

The assessment of the creep behaviour of full-scale laminated glass panels comprised flexural creep tests of relatively long-term duration (350 h) on full-scale 3-layer PVB and 4-layer SG-laminated glass panels. The experimental data retrieved was fit using Findley's approach and power laws predictive

models were proposed for both the panels (structural) and the interlayers (material). Such power laws were able to reproduce with high accuracy the creep behaviour of the laminated panels up to 350 h. Significant differences were found between the deflection estimates for loading periods of 50 years using the proposed power laws and the models available in the literature (extrapolated from dynamic mechanical analysis of the interlayers and from short-term small-size creep tests).

In what concerns composite structural systems, this thesis presents further information about the flexural behaviour of glass-stainless steel hybrid systems. To that end, exploratory experimental, analytical and numerical investigations were carried out to assess the influence of the interlayer, the effects of tempering and reinforcement debonding in the post-cracking behaviour of large-scale PVB and SG-laminated hybrid glass beams. The results achieved proved that the small glass fragments combined with the PVB interlayer and stainless steel profiles are able to provide a significant contribution to the global post-cracking flexural stiffness. Furthermore, it was confirmed that large-scale hybrid glass beams with adhesively bonded joints are highly susceptible to premature debonding of the reinforcement.

Regarding the glass-GFRP composite beams, an extensive experimental campaign was carried out to fully characterize their flexural behaviour. The influence of the (i) reinforcement geometry (rectangular and I section), and (ii) type of adhesive (three different adhesives were tested covering a wide range of mechanical properties) was assessed. The experimental campaign comprised, among others, (i) tensile tests on double-lap joints between glass and GFRP pultruded laminates bonded with the three different tested adhesives, and (ii) full-scale flexural tests on multi-span (single and double-span) glass GFRP composite beams (single and double-span bending tests). The obtained results show that it is possible to overcome the brittleness of glass beams by combining them with GFRP pultruded profiles. The post-cracking behaviour achieved is function of the percentage and reinforcement geometry, as well as of the mechanical properties of the adhesive. Furthermore, the structural redundancy of the system (cross-sectional in the case of beams with only one span) can be enhanced by using hyperstatic systems.

Finally, numerical models were developed in order to simulate the non-linear behaviour of the glass-GFRP composite beams. The non-linear behaviour of glass was calibrated assuming the smeared crack approach and the joint behaviour between glass and GFRP was tested either assuming perfect bond between glass and GFRP or using calibrated plane stress or interface elements of each adhesive. The numerical models developed were able to reproduce the non-linear flexural behaviour of the beams using a wide range of fracture energy values for glass and assuming calibrated interface elements.

Keywords: laminated glass members, lateral-torsional buckling, effective and torsional stiffness, creep, polyvinyl butyral, SentryGlas, hybrid/composite/reinforced glass beams, stainless steel, GFRP, structural adhesive, multi-span, post-cracking strength and ductility, tests, analytical study, numerical models.

RESUMO

O interesse em aplicações de vidro estrutural na área da engenharia civil e arquitetura tem vindo a aumentar ao longo das últimas décadas. Esta crescente procura permitiu a introdução de diversas inovações, destacando-se os elementos de vidro laminado (e temperado) de elevadas dimensões e os filmes de elevado desempenho para situações em que o vidro apresente uma importância estrutural relevante. Naturalmente, tal procura despertou igualmente o interesse de diversos investigadores, que têm vindo a contribuir para o aumento do conhecimento sobre o comportamento do vidro estrutural. Contudo, a maioria dos trabalhos de investigação foram desenvolvidos utilizando provetes de escala reduzida, existindo poucos estudos com comprovada aplicabilidade aos recentes elementos de vidro laminado de elevadas dimensões. Para além disso, enquanto material estrutural, o vidro continua a apresentar algumas desvantagens face aos materiais tradicionais, destacando-se o seu comportamento frágil. Neste contexto, combinando o vidro com outros materiais estruturais é possível contornar o seu comportamento frágil e obter modos de rotura mais dúcteis.

Nesta tese são apresentados resultados de vários estudos no domínio do comportamento estrutural tanto (i) de elementos de vidro laminado como de (ii) estruturas mistas com componentes em vidro. No domínio das estruturas de vidro laminado, foram estudados dois tópicos: (i.1) a suscetibilidade de elementos de vidro laminado de elevada dimensão a fenómenos de instabilidade lateral por flexão-torção; e (i.2) o comportamento a longo prazo (fluência) de painéis de vidro laminado à escala real. No domínio das estruturas mistas de vidro, foram estudados dois tipos de combinações: (ii.1) vigas de vidro reforçadas com perfis de aço inoxidável e (ii.2) vigas de vidro reforçadas com perfis pultrudidos de polímero reforçado com fibras de vidro (do inglês, *glass fibre reinforced polymer* – GFRP).

No âmbito do primeiro tópico foi efetuado um estudo analítico focado (i) na avaliação da precisão das expressões analíticas existentes para a determinação da rigidez efetiva de flexão e de torção de elementos de vidro laminado de elevada dimensão, (ii) na determinação da sua carga crítica de instabilidade lateral e das trajetórias de equilíbrio e (iii) na quantificação da influência do comportamento viscoelástico dos filmes poliméricos. O estudo analítico foi complementado com a realização de um ensaio de flexão a uma viga de vidro laminado de três panos, solidarizados através de filmes em polivinil butiral (PVB), com um vão livre de 8.20 m, tendo este elemento sido utilizada como *glass fin* no edifício do *Centro Champalimaud para o Desconhecido em Lisboa*. Finalmente, foram ainda desenvolvidos modelos numéricos tridimensionais com o objetivo de validar os resultados obtidos nos dois estudos anteriores. Os resultados obtidos mostram a elevada suscetibilidade do comportamento à flexão lateral torção dos elementos de vidro laminado às propriedades viscoelásticas do PVB, que dependem consideravelmente do tempo e da temperatura.

No que diz respeito ao estudo da fluência, este envolveu a realização de ensaios de flexão com uma duração de 350 h, em painéis de vidro laminado, tanto com filmes de PVB como com filmes de SentryGlas (SG), à escala real. Os resultados experimentais obtidos foram utilizados para calibrar leis

de previsão, baseadas na teoria das leis de potência desenvolvida por Findley, do comportamento (estrutural) a longo prazo dos respectivos painéis e das propriedades viscoelásticas dos filmes (material). Os resultados obtidos indicam que as leis de potência propostas são capazes de reproduzir com precisão o comportamento de ambos os painéis testados até às 350 h. Porém, as previsões para 50 anos obtidas com as leis de potência propostas apresentam diferenças consideráveis face à utilização dos modelos de degradação existentes na literatura (obtidos através de ensaios de análise mecânica dinâmica ou através de ensaios de curta duração em espécimes de escala reduzida).

O estudo sobre vigas mistas de vidro e aço-inoxidável visou a caracterização experimental da sua rigidez pós-fendilhação. Duas vigas de vidro laminado de elevada dimensão, constituídas por painéis de vidro temperado solidarizados através de PVB e através de SG, foram reforçadas com perfis de aço inoxidável e testadas à flexão. Os resultados obtidos mostram que o vidro temperado solidarizado através de PVB e combinado com perfis de reforço em aço inoxidável, contribuiu significativamente para o comportamento global à flexão mesmo após a sua rotura. O estudo indicou, igualmente, que elementos mistos de vidro de elevada dimensão construídos usando ligações coladas apresentam elevada suscetibilidade a delaminação prematura.

Para as vigas mistas vidro-GFRP, foi executada uma extensa campanha experimental com o objetivo de caracterizar experimentalmente o seu comportamento à flexão, tendo em conta a influência (i) da dimensão e geometria do reforço e (ii) do tipo de adesivo. A campanha experimental incluiu, entre outros, (i) ensaios de tração em ligações coladas por sobreposição dupla entre placas de vidro e GFRP e (ii) ensaios de flexão em vigas mistas vidro-GFRP, simplesmente e continuamente apoiadas em vão duplo. Os resultados obtidos indicam ser possível contornar o comportamento frágil de vigas de vidro, reforçando-as com perfis pultrudidos de GFRP, sendo possível tirar partido da redundância estrutural da sua secção transversal, como também da sua capacidade de redistribuição de esforços internos quando se encontram continuamente apoiadas. Verifica-se que o desempenho pós-fendilhação do vidro depende da geometria (percentagem de reforço), mas também das propriedades mecânicas dos adesivos.

Finalmente, os resultados da campanha experimental foram utilizados para calibrar modelos numéricos capazes de reproduzir o comportamento não linear das vigas mistas vidro-GFRP, considerando a fendilhação do vidro e o comportamento da ligação colada. Os modelos numéricos desenvolvidos foram capazes de simular com precisão o comportamento à flexão de vigas mistas vidro-GFRP utilizando um leque alargado de energias de fratura do vidro e elementos de interface devidamente calibrados.

Palavras chave: vidro laminado, flexão-torção, rigidez de flexão e torção efetiva, fluência, polivinil butiral, SentryGlas, vigas mistas, aço inoxidável, GFRP, adesivos estruturais, simplesmente e continuamente apoiado, resistência e ductilidade pós-rotura, ensaios experimentais, estudo analítico, modelos numéricos.

ACKNOWLEDGEMENTS

The work presented in this thesis was developed over the last 4 years. Such a long journey was full of memorable moments but also of difficult periods, which were only possible to overcome with the help and collaboration of many people. It is uncountable the number of people with whom I have crossed paths with, to whom I am deeply grateful for all the moments of inspiration, support and companionship. In the following paragraphs I would like to express my profound gratitude to the people who made my research work possible. More importantly, I would like to dedicate this thesis to them, and to point out that this study is also theirs; without them, this would not have been possible.

First and foremost, I would like to thank Prof. João Ramôa Correia, technical and scientific supervisor of this thesis. I would not be able to find the right words to describe how thankful I am for all his words of motivation, enthusiasm, wisdom, dedication, and understanding during all these years. I appreciate all the availability and patience, as well as friendship, qualities I have never seen fading. Without him this work would not be the same, and all the quality that may be present here I would like to dedicate it to him. Furthermore, my profile as a researcher, engineer or professional was positively affected by all the knowledge and understanding I could get from him. More than a supervisor, more than a teacher, Prof. João Ramôa Correia was a truly master.

I would like to thank also the valuable help of Prof. Fernando Branco, technical and scientific co-supervisor of this thesis. In many ways, his advice has been a great support and meant significant developments in this project. His extensive carrier and experience were an important input to this thesis, in terms of both project design and research.

I am also grateful to Prof. José Sena-Cruz who kindly embraced this project and ended up being a very important support for the numerical achievements of this thesis. I particularly appreciate the value of his knowledge, patience, dedication, humor and the time spent during the last 4 years.

I would like to acknowledge as well the opportunity granted by Prof. Jean Paul Lebet and Prof. Christian Louter to work with them and of welcoming me at the ICOM of EPFL-Lausanne, one of the most advanced research laboratories on structural glass.

I am also eternally grateful to the positive learning environment provided by the countless Professors, Engineers and Researchers of the Civil Engineering Department of Instituto Superior Técnico (IST), of the School of Engineering of University of Minho (UM) and of the National Laboratory of Civil Engineering (LNEC), with whom I had the opportunity to contact and discuss with. Special thanks to Prof. Alexandre Gonçalves and Prof. Ana Paula Falcão (IST/CERIS) for their technical support with the topographic measurements; to Prof. Jorge Alfaiate for the insights provided on fracture mechanics (IST/CERIS); to Dr. Pedro Neto for the scientific collaboration on fracture mechanics (IST/CERIS); to

Prof. Nuno Silvestre (IST/IDMEC) and Francisco Virtuoso (IST/CERIS) for the collaboration and support on structural stability; and to Dr. Susana Cabral-Fonseca (LNEC) for her valuable advice on adhesives.

I would like to acknowledge ICIST/CERIS and FCT for funding the research, namely through my PhD scholarship SFRH/BD/80234/2011, which allowed me to go through the years with the financial and economical comfort that such effort requires. I would also like to express my gratitude to the industrial partners that made the experimental campaign of this thesis possible by generously providing the materials, namely: Company MARTIFER and Prof. Sérgio Cruz for supplying the laminated glass beams; and companies SIKA (Eng. David Santos), Guardian (Mr. Juan Ramon Egio) and ALTO Perfis (Eng. Mário Rui Alvim de Castro) for supplying the adhesives, the glass panes and the GFRP pultruded profiles used in the experiments of composite glass beams.

I would like to thank to my colleagues and fellow researchers at IST and EPFL, namely Mário Sá, Marco Morgado, Mário Arruda, José Sampaio, José Gonilha, Ana Maria Gonçalves, Cristina López, Mário Garrido, João Sousa, João Firmo, Bruno Matos, David Martins, Tiago Morgado, Francisco Nunes and André Castelo (IST), Kyriaki Datsiou, Manuel Santarsiero and Jagoda Cupac (EPFL) for their friendship, encouragement, valuable suggestions and for being always available to help me during the experimental campaign. I would also like to thank Eng. Giovanni Chiumiento and Eng. Miguel Machado e Costa for their collaboration in different parts of this thesis.

I am also extremely grateful to Mrs. Maria Helena Salvado and Mrs. Alexandra Baixo for their patience, friendship and support on dealing with all the administrative aspects of this work. The extensive experimental work carried out would have never been possible without the indispensable assistance of the technicians Mr. Fernando Alves, Mr. Fernando Costa, Mr. Pedro Costa, Mr. Lionel Silva and Mr. João Lopes, to whom I would like to express my genuine appreciation.

During the last 4 years I have been blessed with some of the best friends' experience that man could wish for. Without them I would never had the inspiration, courage and endurance to make through such a long goal. I am profoundly thankful for their patient and comprehension in moments of absence and for having always provided me with a warm-healing smile. Special thanks to Sofia Kalakou, who distinctly, genuinely and spontaneously have provided me with wisdom, comfort, friendship and heart-warming moments.

Finally, my deepest gratitude goes to my family, namely my mother, sister and father, who have always been supportive of my work, my life and decisions, and for having me provided with the most important feeling that man could aim for: love.

TABLE OF CONTENTS

Abstract	i
Resumo	iii
Acknowledgements	v
Table of contents	vii
List of figures	xiii
List of tables	xix
Notation	xxi
Part I: Introduction and state of the art	1
Chapter 1: Introduction	3
1.1 Context and motivation	3
1.1.1 <i>Previous research at Instituto Superior Técnico</i>	4
1.2 Objectives and methodology.....	6
1.3 Main scientific contributions and publications	8
1.4 Document outline.....	11
1.5 References	13
Chapter 2: State of the art	15
Abstract	15
2.1 Glass	17
2.1.1 <i>Production process</i>	17
2.1.2 <i>Chemical properties</i>	18
2.1.3 <i>Physical and mechanical properties</i>	19
2.1.4 <i>Glass types and assemblages</i>	20
2.1.4.1 <i>Tempered glass</i>	20
2.1.4.2 <i>Laminated glass</i>	22
2.1.4.3 <i>Interlayer materials</i>	22
2.2 Structural applications of glass panels and beams	25
2.2.1 <i>Glass roofs and floors</i>	25
2.2.2 <i>Glass beams</i>	26
2.2.3 <i>All-glazed structures</i>	28
2.3 Hybrid glass elements.....	29
2.3.1 <i>Hybrid glass structures concept</i>	29
2.3.2 <i>Glass-stainless steel hybrid beams</i>	32

2.3.3	<i>Glass-timber hybrid glass beams</i>	35
2.3.4	<i>Glass-reinforced concrete hybrid beams</i>	37
2.3.5	<i>Glass-steel hybrid beam</i>	38
2.3.6	<i>Glass-CFRP hybrid beams</i>	38
2.3.7	<i>Glass-SRP hybrid beams</i>	39
2.3.8	<i>Glass-GFRP hybrid beams</i>	40
2.4	Other fields of research and development.....	41
2.4.1	<i>Glass and interlayers mechanical properties and durability</i>	41
2.4.2	<i>Adhesively bonded connections</i>	43
2.4.3	<i>Thin chemical tempered glass</i>	44
2.4.4	<i>Curved glass</i>	45
2.5	References	47
Part II: Study of the structural behaviour of laminated glass beams and panels		53
Chapter 3: Lateral-Torsional Buckling Behaviour of Long-Span Laminated Glass Beams: Analytical, Experimental and Numerical Study		55
	Abstract	55
3.1	Introduction.....	57
3.2	Geometrical and mechanical properties of the analysed beam.....	59
3.2.1	<i>Beam geometry</i>	59
3.2.2	<i>Mechanical properties</i>	59
3.3	Analytical study	61
3.3.1	<i>Flexural and torsional stiffness</i>	61
3.3.2	<i>Elastic LTB critical load</i>	63
3.3.3	<i>Load vs. displacement path</i>	64
3.3.4	<i>Southwell equation</i>	65
3.4	Experimental study.....	66
3.4.1	<i>Test setup</i>	66
3.4.2	<i>Measurement of geometrical imperfections</i>	68
3.4.3	<i>Test procedure</i>	68
3.4.4	<i>Test results</i>	69
3.4.4.1	<i>Initial imperfections</i>	69
3.4.4.2	<i>Load-displacement response</i>	70
3.4.4.3	<i>Elastic buckling load</i>	72
3.5	Numerical study.....	73
3.5.1	<i>Description of the numerical models</i>	73
3.5.2	<i>Results and discussion</i>	74
3.6	Concluding remarks.....	77

3.7	References	79
Chapter 4: Flexural creep behaviour of full-scale laminated glass panels		81
	Abstract	81
4.1	Introduction	83
4.2	Review of creep models	84
4.2.1	<i>Creep models for polymer interlayers</i>	84
4.2.2	<i>Findley's power law</i>	86
4.3	Experimental campaign	87
4.3.1	<i>Specimens geometry</i>	87
4.3.2	<i>Test setup</i>	88
4.3.3	<i>Test procedure</i>	89
4.3.4	<i>Experimental mid-span deflection</i>	90
4.4	Analytical study	90
4.4.1	<i>Methodology</i>	91
4.4.1.1	<i>Modelling approach</i>	91
4.4.1.2	<i>Effective flexural stiffness</i>	93
4.4.2	<i>Findley's power law fitting</i>	93
4.4.3	<i>Long-term deflection predictions</i>	96
4.4.3.1	<i>PVB panel</i>	96
4.4.3.2	<i>SG Panel</i>	97
4.4.4	<i>Estimates of PVB and SG viscoelastic shear modulus</i>	98
4.4.5	<i>Assessment of the long-term shear coupling</i>	100
4.5	Conclusions	102
4.6	References	104
Part III 3: Study of the structural behaviour of composite glass beams		107
Chapter 5: Structural behaviour of large-scale laminated glass-stainless steel hybrid beams		109
	Abstract	109
5.1	Introduction	111
5.2	Experimental Programme	113
5.2.1	<i>Structural design</i>	113
5.2.2	<i>Materials</i>	114
5.2.3	<i>Manufacturing of the beams</i>	115
5.2.4	<i>Test setup and procedure</i>	115
5.3	Experimental Results	118
5.3.1	<i>Load-deflection behaviour and strength</i>	118
5.3.2	<i>Failure behaviour</i>	120
5.3.2.1	<i>Beam S1</i>	120

5.3.2.2	<i>Beam S2</i>	121
5.3.3	<i>Composite action and position of the neutral axis</i>	122
5.4	Analytical and numerical study	124
5.4.1	<i>Preliminary remarks</i>	124
5.4.2	<i>Analytical estimate of the flexural performance of the hybrid glass beams</i>	125
5.4.3	<i>Beam S1</i>	127
5.4.3.1	<i>Comparison of analytical and experimental values of flexural stiffness</i>	127
5.4.3.2	<i>Determination of the equivalent elastic modulus of the cracked glass plies</i>	127
5.4.4	<i>Beam S2</i>	130
5.4.4.1	<i>Comparison of analytical and experimental values of flexural stiffness</i>	130
5.4.4.2	<i>Numerical study of the interfacial stresses at the bonded joints</i>	131
5.5	Concluding remarks.....	134
5.5	References.....	136
Chapter 6: Experimental study on the flexural behaviour of multi-span glass–GFRP composite beams		139
	Abstract	139
6.1	Introduction.....	141
6.2	Structural concept and materials	142
6.2.1	<i>Structural concept</i>	142
6.2.2	<i>Materials</i>	143
6.2.3	<i>Manufacturing of the beams</i>	146
6.3	Experimental programme.....	148
6.4	Tests on double-lap joints	149
6.4.1	<i>Specimen geometry and test setup</i>	149
6.4.2	<i>Results and discussion</i>	150
6.4.2.1	<i>Load vs. relative displacement response</i>	150
6.4.2.2	<i>Failure modes</i>	151
6.4.2.3	<i>Axial strains</i>	152
6.5	Flexural tests: test setup and procedure.....	153
6.5.1	<i>Test setup and procedure</i>	153
6.6	Flexural tests: Results and discussion.....	155
6.6.1	<i>Simply supported R-section beams</i>	155
6.6.1.1	<i>Load-deflection behaviour and strength</i>	155
6.6.1.2	<i>Composite action</i>	157
6.6.2	<i>Simply supported I-section beams</i>	158
6.6.2.1	<i>Load-deflection behaviour and strength</i>	158
6.6.2.2	<i>Composite action</i>	160
6.6.3	<i>Continuous beams</i>	161
6.6.3.1	<i>Load-deflection behaviour and strength</i>	161

6.6.3.2	<i>Composite action</i>	163
6.6.3.3	<i>Reactions, internal forces and moment redistribution</i>	164
6.6.4	<i>Summary of results</i>	166
6.6.4.1	<i>Simply supported series</i>	166
6.6.4.2	<i>Continuously supported series</i>	168
6.7	Concluding remarks.....	170
6.8	References.....	172
Chapter 7: Numerical simulation of the flexural behaviour of glass-GFRP composite beams using smeared crack models		175
Abstract		175
7.1	Introduction.....	177
7.2	Literature review	178
7.3	Description of the numerical models	180
7.3.1	<i>Initial considerations</i>	180
7.3.2	<i>Geometry, boundary conditions and type of elements</i>	181
7.3.2.1	<i>Double-lap joints</i>	181
7.3.2.2	<i>Composite beams</i>	181
7.3.3	<i>Constitutive models of materials and interfaces</i>	182
7.3.3.1	<i>Glass</i>	182
7.3.3.2	<i>GFRP</i>	185
7.3.3.3	<i>Adhesives and interfaces</i>	186
7.3.4	<i>Type of analysis</i>	187
7.4	Double-lap joints: Results and discussion.....	187
7.5	Composite beams: Results and discussion	188
7.5.1	<i>Effect of glass material options</i>	188
7.5.1.1	<i>Fracture energy</i>	188
7.5.1.2	<i>Tensile strength</i>	190
7.5.1.3	<i>Tension-softening diagram</i>	191
7.5.1.4	<i>Shear retention factor</i>	192
7.5.2	<i>Effect of adhesive's properties</i>	193
7.6	Concluding remarks.....	196
7.7	References.....	198
Part IV: Conclusions and future developments		201
Chapter 8: Conclusions and future developments		203
8.1	Conclusions.....	203
8.1.1	<i>General conclusions</i>	203
8.1.2	<i>Structural behaviour of laminated glass members</i>	203

8.1.2.1	<i>Flexural behaviour of large-scale multi-layer laminated glass beams.....</i>	203
8.1.2.2	<i>Creep behaviour of full-scale laminated glass panels.....</i>	204
8.1.3	<i>Structural behaviour of large-scale laminated glass-stainless steel hybrid beams.....</i>	205
8.1.4	<i>Structural behaviour of glass-GFRP composite glass beams.....</i>	206
8.1.4.1	<i>Experimental study.....</i>	206
8.1.4.2	<i>Numerical study.....</i>	207
8.2	<i>Future developments</i>	208
8.2.1	<i>Flexural behaviour of laminated glass structural members</i>	208
8.2.2	<i>Structural behaviour of hybrid glass systems.....</i>	209
8.3	<i>References</i>	212

LIST OF FIGURES

Fig. 2.1 - Float glass production process	17
Fig. 2.2 – Processing of large-size glass elements at SEDAK	18
Fig. 2.3 - Comparison of the stress profile obtained by thermal and chemical tempering	20
Fig. 2.4 - Fracture pattern of (left to right) annealed float glass, heat strengthened glass and fully tempered glass	21
Fig. 2.5 - Post-fracture capacity of laminated glass members as a function of the (left to right) type of glass and type of interlayer (<i>SentryGlas</i> and PVB)	23
Fig. 2.6 - Qualitative comparison of the bending stiffness of PVB and SG with equal thickness	24
Fig. 2.7 - Shear modulus master curves for the reference temperature of 20 °C of PVB <i>Butacite</i> (Kuraray), PVB <i>Saflex</i> (Solutia) and ionoplast <i>SentryGlas</i> (Kuraray).	24
Fig. 2.8 – Free-form glass structures as part of a roof	25
Fig. 2.9 - Glass roof with (a) linear and (b) pointed supports	26
Fig. 2.10 - Glass facade with glass fins along its height at the (a) <i>Champalimaud Centre for the Unknown</i> and (b) and (c) at several Apple stores	26
Fig. 2.11 – Examples of glass beam applications	27
Fig. 2.12 – Examples of glass beams with (a) and (b) segmented-bolted configuration, and (c) and (d) spliced laminated configuration	28
Fig. 2.13 – Examples of all-glass (a) staircase, (b) walkway and (c) and (d) building envelope	29
Fig. 2.14 - All-glazed building envelope at the 5 th Avenue Apple Store in (a) 2006 (Glass cube v1.0) and (b) 2011 (Glass cube v2.0)	29
Fig. 2.15 – Structural behaviour of laminated glass members: (a) post-fracture performance of <i>laminated safety glass</i> and reinforced glass, and (b) illustrative flexural behaviour of SG-laminated glass beams under displacement control bending tests	30
Fig. 2.16 – Hybrid glass members: (a) cross-section of several concepts of structural hybrid glass beams (not to scale) and (b) timber-glass composite beam applied on the construction of a hotel	31
Fig. 2.17 – General behaviour of hybrid glass beams.	32
Fig. 2.18 – Glass-stainless steel reinforced glass beams developed at Delft University of Technology: (a) different cross-sections studied and (b) segmentation scheme used for long-span beams.....	33
Fig. 2.19 – Glass-stainless steel reinforced glass beams at Delft University of Technology: (a) reinforcement configurations tested, and (b) corresponding effects on the flexural response of glass-stainless steel reinforced beams	33
Fig. 2.20 - Illustrative behaviour of the structural effects of (a) glass type and (b) reinforcement percentage	34

Fig. 2.21 - Flexural results on glass-stainless hybrid steel beams with 3 different types of anchorages at the beams end . 35

Fig. 2.22 – Glass-timber hybrid beams: flexural tests on (a) beams and (b) panels carried out by Cruz and Pequeno 36

Fig. 2.23 – Glass-timber composite beams: configurations of the shear tests on adhesively bonded joints 36

Fig. 2.24 – Glass-reinforced concrete hybrid beams: (a) flexural tests performed by Freytag and (b) analytical model considered 37

Fig. 2.25 – Glass-steel composite beams: connections types studied within the project *Innoglast*..... 38

Fig. 2.26 – Glass-CFRP hybrid beams developed by (a) Palumbo and (b) developed by Louter 39

Fig. 2.27 - Reinforced glass beams with embedded (top) CFRP and (bottom) GFRP rods 39

Fig. 2.28 – Glass-SRP hybrid beams: (a) prototype illustration and (b) flexural experiments..... 39

Fig. 2.29 - Glass-GFRP composite glass beams tested by (a) Speranzini and (b) Valarinho..... 40

Fig. 2.30 – Damaged in glass surface (a) scratch induced, (b) sand abraded and (c) surface naturally aged/exposed to outdoor conditions. 42

Fig. 2.31 - Adhesively bonded (a) glass-to-glass and embedded (b) linear and (c) pointed connections 43

Fig. 2.32 - Numerical analysis of the stress distribution of linear embedded connection 44

Fig. 2.33 – Ring test used for the determination of the tensile strength of a thin glass sample..... 45

Fig. 2.34 – Cold bent laminated glass panels applied in the Strasbourg train station 45

Fig. 2.35 – Ongoing research on cold-bent glass: (a) 2-D numerical model developed to study the snap-through instability and (b) optical distortion 46

Fig. 3.1 – *Champalimaud Centre for the Unknown* building facade and its glass fins (courtesy of José Campos)..... 58

Fig. 3.2 – Lateral-torsional buckling instability model for a 3-layer laminated glass beam (left) and respective cross-section (right)..... 62

Fig. 3.3 – LTB critical load (P_{cr}) as a function of (a) interlayer’s (PVB) shear modulus G_{int} (grey curve), loading time (black and dashed curves) and (b) glass panes thickness (considering the same total thickness, $t_{total} = 48.04$ mm); black and white symbols correspond to service temperatures of 20 °C and 23 °C respectively. 64

Fig. 3.4 – Load vs. displacement paths of the laminated glass beam: influence of (a) G_{int} (i.e. loading time) and of (b) thickness of glass panes (and interlayer) and G_{int} (i.e. loading time). 66

Fig. 3.5 – LTB test setup: (a) overall view, (b) and (c) supports, and (d) and (e) load application system..... 67

Fig. 3.6 – Reflective tape targets: (left) location and (right) detail at the vicinity of the mid-span section. 68

Fig. 3.7 – Measuring equipment, (left) illustration and (right) experimental application (view in perspective)... 69

Fig. 3.8 – Experimental and sinusoidal approximation of the initial deformed shape. 70

Fig. 3.9 – Experimental load equilibrium path in terms of (a) twist rotation, vertical and lateral displacements; (b) experimental, analytical and numerical load equilibrium path (for different glass panes thicknesses)..... 71

Fig. 3.10 – Deformed shape at the end of the test.	71
Fig. 3.11 – Southwell plot.	72
Fig. 3.12 – 3D numerical model: (a) overview, (b) support and (c) point load details.	73
Fig. 3.13 – Experimental and numerical (for different glass panes thicknesses) vertical deflection.	75
Fig. 3.14 – Numerical buckling shape, (a) displacements (in m, according to colour scale) (b) and principal stresses (in Pa, according to colour scale).	75
Fig. 3.15 – Evolution of the numerical principal (tensile) stresses evolution during LTB deflection.	76
Fig. 4.1 – Shear modulus master curves for the reference temperature of 20 °C of PVB1999 (<i>Butacite</i>), PVB2007 (<i>Saflex</i>), SG2005 (DMA tests) and SG2012 (tests on glass laminates).	85
Fig. 4.2 - Creep test setup: illustration of the two stages of the tests.	88
Fig. 4.3 – Flexural creep test of the SG panel.	89
Fig. 4.4 – Initial mid-span deflections and their derivative values measured in the flexural creep test of the (a) PVB and (b) SG laminated glass panels.	90
Fig. 4.5 – Mid-span deflection during the creep tests and power law fittings to the experimental data for the PVB and SG laminated glass panels.	91
Fig. 4.6 - General laminated glass panel (top) out-of-plane deflection, and (bottom) cross-section geometry of 3 and 4-layer glass panels.	94
Fig. 4.7 – Viscoelastic mid-span deflection (bi- \log_{10} scale) during the creep tests and fitting of a power law to the experimental data for the PVB and SG panels.	95
Fig. 4.8 – Comparison between the (a) PVB and (b) SG experimental creep deflection evolution with the corresponding power law fittings and estimates obtained using the PVB and SG material models reported in the literature	95
Fig. 4.9 – Mid-span deflection evolution for a creep period of (a) 50 years and (b) 20,000 h (linear and uni- \log_{10} scale), according to the power law regression (black curve), and to models PVB1999 (dashed curves) and PVB2007 (grey curves).	96
Fig. 4.10 - Mid-span deflection evolution predictions for a creep period of (a) 50 years and (b) 100,000 h (linear and uni- \log_{10} scale), according to the power law regression (black curve), and to models SG2005 (dashed curves) and SG2012 (grey curves).	97
Fig. 4.11 – Comparison of absolute (a) and normalized (b) $G_{PVB}(t)$ curves of power law regression (black) and models PVB1999 (ref. temperature 19.1 °C, dashed curves), and PVB2007 (ref. temperature 20 °C, grey curves).	99
Fig. 4.12 – Comparison of absolute (a) and normalized (b) $G_{SG}(t)$ curves of power law regression (black) and models SG2005 (dashed curves), and SG2012, (grey curves), ref. temperature 17.4 °C.	100
Fig. 4.13 – Shear coupling of the (a) PVB and (b) SG panels.	101

Fig. 5.1 - Cross-section of the glass-stainless steel hybrid beams.....	113
Fig. 5.2 – Longitudinal view of (a) PVB and (b) SG-laminated glass-stainless steel hybrid beams tested (note that the outer glass plies in the former beam are cracked).	114
Fig. 5.3 – Manufacturing process of laminated glass-stainless steel hybrid beams: (a) positioning of the laminated glass element, (b) positioning of the PVC spacers, (c) application of the structural adhesive, (d) positioning of the reinforcement profile and (e) finishing of the joint (picture (b) refers to beam S2, all the others to beam S1).	116
Fig. 5.4 – Glass-stainless steel hybrid beams test setup: (a) mid-span metal frames; (b) load application point; (c) supports; (d) load (top) and deflection (bottom) measurement devices.	116
Fig. 5.5 – Illustration of the flexural test setup and its features.	117
Fig. 5.6 – Test setup of the glass-stainless steel hybrid glass beams (a) S1 and (b) S2.	117
Fig. 5.7 – Load vs. mid-span deflection curves of (a) beam S1 and (b) beam S2.	119
Fig. 5.8 – Flexural stiffness evolution of (top) beam S1 and (bottom) beam S2.	119
Fig. 5.9 – Failure behaviour of beam S1.	121
Fig. 5.10 – Failure behaviour of beam S2.	122
Fig. 5.11 – Axial strains vs. section height in beam S1 for different load levels (in kN) measured at (a) the inner glass ply and (b) the outer glass plies.....	123
Fig. 5.12 - Axial strains vs. section height for different load levels (in kN) for the beam S2.	124
Fig. 5.13 – Schematic representation of the strain distribution in the hybrid glass beams.....	129
Fig. 5.14 – Experimental height of the neutral axis and analytical evolution of the compressive ($E_{equiv,c}$) and tensile ($E_{equiv,t}$) elastic modulus of cracked glass plies of beam S1.	130
Fig. 5.15 – Composite action degree (ξ) of beam S2 in function of the total applied load.	131
Fig. 5.16 – Equilibrium of forces at the interfaces of an infinitesimal glass-stainless steel hybrid beam.	132
Fig. 5.17- Mesh representation of the numerical model of the hybrid glass beam S2.	133
Fig. 5.18 – Longitudinal distribution of shear (τ_{xy}) and normal stresses (σ_{yy}) at the adhesively bonded interface adhesive-stainless steel of beam S2, for a total load of 600 kN: (a) development at the overhang and in the shear span and (b) development at the vicinity of the support.	133
Fig. 6.1 - Cross-section of the glass-GFRP composite beams and strain-gauges position.....	143
Fig. 6.2 - Adhesives tensile tests: (a) dumbbell specimens' geometry (left to right) of <i>SFlex</i> , <i>SForce</i> (Young's modulus), <i>SForce</i> (tensile strength) and <i>SDur</i> and (b) experimental setup.....	145
Fig. 6.3 – Apparent stress vs. axial strain curves of a representative set of specimens (specimens used for the determination of the Young's modulus) from (a) <i>SFlex</i> (b) <i>SForce</i> and (c) <i>SDur</i> adhesives.	145

Fig. 6.4 – Manufacturing process of the R-section composite glass beams: (a) glass beam and GFRP reinforcing profile (with epoxy (*SDur*) adhesive); (b) application of polyurethane (*SFlex*) adhesive in the GFRP reinforcement; (c) beam curing using light weights. 146

Fig. 6.5 – Manufacturing process of the I-section composite glass beams – positioning of the GFRP angle profiles: (a) positioning of the PVC spacers on glass; (b) application of the (epoxy) adhesive; (c) curing of the adhesive applied in the angle profiles using light weights; (d) repositioning of the composite beam for the positioning of the two other GFRP angle profiles..... 147

Fig. 6.6 – Manufacturing process of the I-section composite glass beams – positioning of the GFRP flanges: (a) curing process of the adhesive applied at the bottom GFRP flange; (b) repositioning of the beam for the positioning of the top GFRP flange; (c) curing process of the adhesive applied at the top GFRP flange..... 148

Fig. 6.7 - Geometry of the double-lap joints and location of the strain-gauges along the GFRP bonded interface. 149

Fig. 6.8 - Load vs. relative displacement curves of specimens from (a) *SFlex*, (b) *SForce* and (c) *SDur* series. 151

Fig. 6.9 - Failure modes of double-lap joints made of (a) *SFlex*, (b) *SForce* and (c) *SDur* adhesives..... 152

Fig. 6.10 - Measured axial strains for (a) *SFlex*, (b) *SForce*, and (c) *SDur*..... 153

Fig. 6.11 - Experimental setup of the flexural tests on (a) R-section and (b) I-section simply supported beams. 153

Fig. 6.12 -Experimental setup of the flexural tests on continuously supported beams (*CS-SDur*). 154

Fig. 6.13 - Load vs. mid-span deflection curves of (a) *SS-R-SFlex*, (b) *SS-R-SForce* and (c) *SS-R-SDur* series. 155

Fig. 6.14 – Illustration of the experimental crack pattern of (a) *SS-R-SFlex* and (b) *SS-R-SDur* series. 156

Fig. 6.15 - Axial strains vs. section height for different load levels (in kN) for the (a) *SS-R-SFlex*, (b) *SS-R-SForce* and (c) *SS-R-SDur* series..... 157

Fig. 6.16 - Load vs. mid-span deflection curves of *SS-I-* (a) *SFlex*, (b) *SForce* and (c) *SDur* series..... 158

Fig. 6.17 - Crack pattern of (a) *SS-I-SFlex* and (b) *SS-I-SDur* beams..... 160

Fig. 6.18 - Axial strains vs. section height for different load levels (in kN) for *SS-I-* (a) *SFlex*, (b) *SForce* and (c) *SDur* series. 160

Fig. 6.19 - Load vs. mid-span deflection curves of the (a) *CS-I-SFlex*, (b) *CS-I-SForce* and (c) *CS-I-SDur* series. 161

Fig. 6.20 - Crack pattern of beam *CS-I-SFlex-1* (before unloading). 163

Fig. 6.21 – Crack pattern of beam (a) *CS-I-SForce-1* and (b) *CS-I-SDur-1* (after failure). 163

Fig. 6.22 - Axial strains vs. section height for different total loads (in kN) for beams (a) *CS-I-SFlex-1* (M+), (b) *CS-I-SForce-1* (M-) and (c) *CS-I-SDur-1* (M+) (prior to glass cracking)..... 164

Fig. 6.23 - Beam *CS-I-SDur-3* (a) experimental and theoretical load vs. distribution of reactions, (b) load vs. variation of reactions and (c) load vs. variation of bending moments..... 164

Fig. 6.24 - Redistribution of bending moments during the tests of beams (a) *CS-I-SFlex-3*, (b) *CS-I-SForce-1* and (c) *CS-I-SDur-2*..... 165

Fig. 6.25 – Example specimen of each series of the simply supported glass-GFRP composite beams.	167
Fig. 7.1 - Mesh and boundary conditions of the double-lap joints numerical models.....	181
Fig. 7.2 - Mesh, boundary conditions and joint properties of the beams numerical models.	182
Fig. 7.3 – Tension-softening diagrams simulated for glass non-linear material.....	185
Fig. 7.4 – Double-lap joints: experimental and numerical comparison of the load vs. relative displacement for specimens (a) <i>DL-SFlex</i> and (b) <i>DL-SDur</i>	187
Fig. 7.5 – Double-lap joints: experimental (dots) and numerical (lines) axial strains (a) at 5.0 kN for <i>DL-SFlex-2</i> and (b) at 20 kN for <i>DL-SDur-4</i>	188
Fig. 7.6 - Effect of G_f on the load vs. mid-span deflection curves of <i>R-SDur</i> beams.	189
Fig. 7.7 - Effect of G_f on the composite beam’s crack pattern. Crack legend: fully-open (purple).....	189
Fig. 7.8 - Numerical results of model “ $G_{f,min} - Aelement - 50 - Linear - 2$ ” in terms of (a) stress distribution, (b) crack pattern and (c) deformed shape. Crack legend: closed (green), and fully-open (purple).	190
Fig. 7.9 – Effect of $f_{g,t}$ on the load vs. mid-span deflection curves, considering (a) approach 1, and (b) approach 2... 190	190
Fig. 7.10 - Effect of $f_{g,t}$ on the crack pattern for (left to right) $f_{g,t} = 45$ MPa, 50 MPa and 55 MPa (approach 1). Crack legend: fully-open (purple).	191
Fig. 7.11 - Effect of the tension-softening diagram shape on the load vs. mid-span deflection curves.....	192
Fig. 7.12 - Effect of the tension-softening diagram shape on the crack pattern. Crack legend: opening (blue), closed (green), reopening (red) and fully-open (purple).	192
Fig. 7.13 - Effect of (a) constant and (b) variable β on the load vs. mid-span deflection.	193
Fig. 7.14 – Effect of β on the composite beam crack pattern ($\delta = 13.75$ mm). Crack legend: closed (green), and fully-open (purple).	194
Fig. 7.15 – Experimental and numerical flexural behaviour of (a) <i>R-SFlex</i> and (b) <i>R-SDur</i> beams assuming: (i) no adhesive layer (PB), (ii) plane stress elements (PSE), or (iii) interface elements (IE) to represent the adhesive layer. 194	194
Fig. 7.16 - Crack pattern of <i>R-SFlex</i> beams when (left) PSE or (right) IE models were adopted to represent the adhesive layer. Crack legend: closed (green), and fully-open (purple).....	195
Fig. 7.17 - Crack pattern of <i>R-SDur</i> beams with (left) PSE and (right) IE models representing the adhesive layer. Crack legend: closed (green), and fully-open (purple).....	196

LIST OF TABLES

Table 2.1 – Chemical composition (% of mass) of soda lime silica glass (SLSG) and borosilicate glass (BSG)	18
Table 2.2 – Physical and mechanical properties of soda lime silica glass (SLSG).	19
Table 2.3 – Glass type according to the level of tempering residual stresses	21
Table 2.4 - Main material and mechanical properties of the most popular interlayers	23
Table 3.1 – Mechanical properties of the interlayer (considered to be PVB) as a function of the load duration and ambient temperature (20 °C and 23 °C).....	60
Table 3.2 – Analytical, numerical and experimental buckling loads of the beam tested for two different levels of interaction (different G_{int}) and for three different glass thicknesses (within standard tolerances of ± 0.5 mm)....	76
Table 4.1 - Geometrical properties of panels: nominal and measured (in brackets).	87
Table 4.2 – Expressions of I_{gl} , I_s and A for cross-sections with 3 and 4 glass plies.....	94
Table 5.1 - Average physical and mechanical properties of the materials used on hybrid beams.	114
Table 5.2 – Test setup of the flexural tests on glass-stainless steel hybrid glass beams.	115
Table 5.3 – Results of tests of glass-stainless steel hybrid beams.....	120
Table 5.4 – Analytical estimates of the flexural performance of beams S1 and S2, with and without reinforcement and considering the cracking of the outer glass plies (beam S1).....	126
Table 5.5 – Comparison between experimental and analytical flexural stiffness values of beam S1.	127
Table 5.6 – Comparison between experimental and analytical flexural stiffness values of beam S2.	131
Table 6.1 - Mechanical properties in tension of the materials used in the glass-GFRP composite beams.....	145
Table 6.2 - Summary of the flexural tests on glass-GFRP composite beams.....	149
Table 6.3 - Summary of results (average plus coefficient of variation) from double-lap joint tests (K , P_{max} , d_{max} and failure mode).....	151
Table 6.4 – Average displacement speed of the bending tests on composite beams.....	154
Table 6.5 - Summary of the results (average plus coefficient of variation) of the 4-point bending tests on <i>SS-R</i> glass-GFRP composite beams.....	156
Table 6.6 - Summary of the results (average plus coefficient of variation) from flexural tests on <i>SS-I</i> series....	159
Table 6.7 - Summary of average results from flexural tests on <i>CS-I</i> series.	161
Table 6.8 - Analysis of maximum bending moments, ductility index and moment redistribution for the continuously supported beams.	165
Table 6.9 - Comparison between simply supported (<i>SS-I</i>) and continuously supported (<i>CS-I</i>) series.....	169

List of tables

Table 7.1 - Numerical options tested for the definition of the glass non-linear behaviour.	180
Table 7.2 - Summary of the <i>FE</i> models developed for the composite beams adhesively bonded joints.....	181
Table 7.3 - Properties of the interface elements considered for the two adhesives.	186

NOTATION

Roman lower case

a_i	Distance between the centre-lines of adjacent glass layers
b	Panel's section width; maximum unidimensional slope
b_{real}	Panel's section real width
d	Distance between the centre-lines of the outer glass plies; distance between the centre-lines of the bottom and top reinforcement profile bars
d_g	Distance between the shear centre and the load application point
d_i	Distance between the centre-lines of the material i section and the neutral axis of the beam cross-section
d_{max}	Maximum relative displacement
$f_{g,t}$	Glass tensile strength
$f_{i,t}$	Tensile strength of the material i
h	Section height; crack band width
h_{real}	Beam's section real height;
m_d	Vertical deflection/displacement stress-temperature-dependent coefficient
m_e	Axial strain stress-temperature-dependent coefficient
m_g	Shear strain stress-temperature-dependent coefficient
n_d	Vertical deflection/displacement stress-independent material constant
n_e	Axial strain stress-independent material constant
n_g	Shear strain stress-independent material constant
p	Exponent of the potential function
s	Slip
s_m	Slip at the peak point
t_0	Initial time
t	Time
t_a	Thickness of the adhesive layer
t_i	Thickness of the inesimal glass ply/pane/beam
t_{int}	Thickness of the interlayer sheet
t_{re}	Thickness of the reinforcement profile
t_{total}	Beam's total nominal thickness
$t_{total,real}$	Beam's total measured thickness
u	Lateral displacement at mid-span
u_o	Maximum amplitude of the initial bow
u_{max}	Maximum amplitude of the initial bow estimated by a sinusoidal approximation

$u(x)$	Lateral displacement on a coordinate x along the beam's span
x	Longitudinal coordinate along beam's span; neutral axis height

Roman capital

A	Effective flexural stiffness auxiliary parameter; beam cross-sectional area
A_i	Cross-sectional area of the material i
A_{re}	Cross-sectional area of the reinforcement profiles
$A_{element}$	Area of the finite element
$C_1; C_2$	Auxiliary parameter for the lateral-torsional behaviour of a beam subjected to in-plane loads
dM_i	Differential increment of the cross-sectional internal moment in the material i
E	Glass Young's modulus
E_{equiv}	Equivalent Young's modulus of cracked glass
$E_{equiv,t}$	Equivalent tensile Young's modulus of cracked glass
$E_{equiv,c}$	Equivalent compressive Young's modulus of cracked glass
E_i	Young's modulus of the material i
E_{int}	Young's modulus of the interlayer
E_{re}	Young's modulus of reinforcement material
EI	Flexural stiffness around the major bending axis
EI_{comp}	Flexural stiffness of a hybrid glass beam around the major bending axis
EI_{comp}^{cr}	Flexural stiffness of a cracked hybrid glass beam around the major bending axis
EI_{comp}^{sec}	Experimental secant flexural stiffness of a hybrid glass beam around the major bending axis
$EI_{comp}^{sec,i}$	Initial experimental secant flexural stiffness of a hybrid glass beam around the major bending axis
$EI_{comp}^{sec,max}$	Maximum experimental secant flexural stiffness of a hybrid glass beam around the major bending axis
$EI_{comp}^{sec,u}$	Ultimate experimental secant flexural stiffness of a hybrid glass beam around the major bending axis
EI_y	Flexural stiffness around the minor bending axis
$EI_{y,eff}$	Effective flexural stiffness around the minor bending axis
EI_{gl}	Flexural stiffness of glass layers w.r.t. their centroid axes (major and minor axes)
EI_s	Flexural stiffness of glass layers w.r.t. section neutral axis (major and minor axes)
F_c	Cross-sectional compressive internal force
F_t	Cross-sectional tensile internal force

G	Glass shear modulus
G_0	Shear modulus for a time $t \approx 0$
G_f	Glass mode-I fracture energy
$G_{f,\min}$	Minimum mode-I fracture energy
G_{int}	Interlayer shear modulus
GJ_{gl}	Torsional stiffness of glass layers w.r.t. their centroid axes
GJ_s	Torsional stiffness of glass layers w.r.t. section neutral axis
GJ_t	Torsional stiffness
$GJ_{t,\text{eff}}$	Effective torsional stiffness
G_{PVB}	Interlayer PVB shear modulus
$G_{\text{PVB}}(t)$	Interlayer PVB shear modulus as a function of time
G_{SG}	Interlayer SG shear modulus
$G_{\text{SG}}(t)$	Interlayer SG shear modulus as a function of time
I_{gl}	Second moment of area of glass layers w.r.t. section centroid axes
I_i	Second moment of area of a material i w.r.t. section centroid axes
I_s	Second moment of area of glass layers w.r.t. section neutral axis
J_{gl}	Torsion constant component associated with the shear contribution of the interlayer
J_s	Torsion constant component associated with the thin-walled contribution of the glass layers
K	Elastic flexural stiffness
K_n	Linear elastic normal stiffness
K_t	Linear elastic tangential stiffness
L	Total length
L_0	Flexural span
L_a	Distance from the support to the load application point
L_1	Overhangs length
M_{cr}	Lateral-torsional buckling critical moment
M_i	Cross-sectional internal moment in the material i
$M_{\text{max,cs}}$	Maximum elastic moment of continuously supported beam
$M_{\text{max,ss}}$	Maximum elastic moment of simply supported beam
M_z	Maximum applied moment
P	Total applied mid-span load in a 3-point bending test; total applied load in a 4-point and in a 5-point bending test
P_{cr}	Lateral-torsional buckling experimental critical load; cracking load of a laminated glass beam
$P_{\text{cr,comp}}$	Cracking load of a hybrid glass beam

$P_{cr,comp}^{cr}$	Cracking load of a cracked hybrid glass beam
$P_{cr,Sth}$	Lateral-torsional buckling experimental critical load determined using Southwell method
P_{max}	Total maximum load experimentally observed
R	Correlation coefficient
T	Temperature
V_i	Cross-sectional internal transverse load in the material i

Greek symbols

α	Effective flexural stiffness auxiliary parameter; parameter that defines the shape of the pre-peak curve
α'	Parameter that defines the shape of the post-peak curve
β	Effective flexural stiffness auxiliary parameter; shear retention factor
γ	Transverse shear strain
$\gamma(\tau, t)$	Transverse shear strain as a function of τ and t
γ_0	Initial transverse shear strain
$\gamma_0(\tau)$	Initial transverse shear strain as a function of τ
δ	Vertical deflection/displacement
δ_0	Instantaneous vertical deflection/displacement
$\delta_0(\sigma)$	Stress-dependent initial vertical deflection/displacement
$\delta_0(\sigma, t)$	Stress-time-dependent vertical deflection/displacement
δ_c	Creep vertical deflection/displacement
δ_c^{PVB}	Creep vertical deflection/displacement of PVB-laminated glass panel
δ_c^{SG}	Creep vertical deflection/displacement of SG-laminated glass panel
$\delta^{PVB}(t)$	Total vertical deflection/displacement of PVB-laminated glass panel as a function of time
$\delta^{SG}(t)$	Total vertical deflection/displacement of SG-laminated glass panel as a function of time
$\delta(x)$	Vertical deflection/displacement at the longitudinal coordinate x
$\epsilon_0(\sigma)$	Stress-dependent initial elastic strain
ϵ_c	Glass compressive axial strain
$\epsilon_{i,b}$	Tensile elongation of a material i
ϵ_n^{cr}	Crack normal strain
$\epsilon_{n,ult}^{cr}$	Ultimate crack normal strain
$\epsilon_{re,c}$	Reinforcement compressive axial strain
$\epsilon_{re,t}$	Reinforcement tensile axial strain
ϵ_t	Glass tensile axial strain

$\varepsilon(\sigma, t)$	Stress-time-dependent total axial strain
θ	Effective flexural stiffness auxiliary parameter
θ_0	Maximum amplitude of the initial rotational imperfection
λ_f	Effective flexural stiffness auxiliary parameter
λ_t	Effective torsional stiffness auxiliary parameter
ν	Glass Poisson's ratio
ν_i	Poisson's ratio of a material i
ν_{int}	Interlayer Poisson's ratio
ν_{SDur}	Sikadur 31-cf adhesive Poisson's ratio
ν_{SFlex}	Sikaflex 265 adhesive Poisson's ratio
ν_{SForce}	Sikaforce 7710-L100 adhesive Poisson's ratio
ξ_f	Effective flexural stiffness auxiliary parameter
ξ_t	Effective torsional stiffness auxiliary parameter
σ	Tensile stress
σ_n^{cr}	Crack normal stress
σ_{yy}	Interface normal stresses
τ	Shear stress
τ_m	Shear stress at the peak point
$\tau(s)$	Shear stress as a function of s
τ_{xy}	Interface shear stresses
ϕ	Effective flexural stiffness auxiliary parameter
φ	Effective flexural stiffness auxiliary parameter
ψ	Effective flexural stiffness auxiliary parameter

Acronyms

2D	Two-dimensional
3D	Three-dimensional
ANG	Annealed float glass
ASTM	American Society for Testing and Materials
BSG	Borosilicate glass
CFRP	Carbon fibre reinforced polymer
CEN	European Committee for Standardization
CS	Continuously supported beams series
CS-I	Continuously supported I-section beams series
CS-I-SDur	Continuously supported I-section beams series bonded with Sikadur 31-cf adhesive

CS-I-SFlex	Continuously supported I-section beams series bonded with Sikaflex 265 adhesive
CS-I-SForce	Continuously supported I-section beams series bonded with Sikforce 7710-L100 adhesive
CTG	Chemically tempered glass
DCA	Discrete crack approach
DL	Double-lap joints series
DL-SDur	Double-lap joints series using Sikadur 31-cf adhesive
DL-SFlex	Double-lap joints series using Sikaflex 265 adhesive
DL-SForce	Double-lap joints series using Sikaforce 7710-L100 adhesive
DMA	Dynamic mechanical analysis
EC	European Code
EN	European Standard
EVA	Ethylene-vinyl acetate
FCT	Fundação para a Ciência e a Tecnologia (Portuguese National Foundation for Science and Thecnology)
FE	Finite element
FTG	Fully tempered glass
GFRP	Glass fibre reinforced polymer
HSG	Heat strengthened glass
IE	Interface elements
ISI	Institute for Scientific Information
ISO	International Organization for Standardization
KEA	<i>Killing-element</i> approach
LD	Left span
LERM	Laboratório de Estruturas e Resistência de Materiais (Structures and Strength of Materials Laboratory)
LTB	Lateral-torsional buckling
LVDT	Linear variable displacement transducer
PB	Perfect bond
PSE	Plane stress elements
PVB	Polyvinyl butyral interlayer
PVC	Polyvinyl chloride
RD	Right span
SCA	Smeared crack approach
SDur	Sikadur 31-cf adhesive
SFlex	Sikaflex 265 adhesive

SForce	Sikaforce 7710-LL100 adhesive
SG	SentryGlas interlayer
SGP	SentryGlas Plus interlayer
SLSG	Soda lime silica glass
SS	Simply supported beams series
SS-I	Simply supported I-section beams series
SS-I-SDur	Simply supported I-section beams series bonded with Sikadur 31-cf adhesive
SS-I-SFlex	Simply supported I-section beams series bonded with Sikaflex 265 adhesive
SS-I-SForce	Simply supported I-section beams series bonded with Sikaforce 7710-L100 adhesive
SS-R	Simply supported rectangular section beams series
SS-R-SDur	Simply supported rectangular section beams series bonded with Sikadur 31-cf adhesive
SS-R-SFlex	Simply supported rectangular section beams series bonded with Sikaflex 265 adhesive
SS-R-SForce	Simply supported rectangular section beams series bonded with Sikaforce 7710-L100 adhesive
SRP	Steel reinforced polymer
TPU	Thermoplastic polyurethane
TTSP	Time-temperature superposition principle
WLF	Williams-Landel-Ferry

PART I
INTRODUCTION AND STATE OF
THE ART

CHAPTER

1

INTRODUCTION

1.1 CONTEXT AND MOTIVATION

Glass is one of the most versatile materials ever discovered. It can easily assume different shapes and it can be applied in a wide range of fields, such as communications, automotive and construction. Up to the second half of the twentieth century, glass was used in construction mainly as a covering material [1.1], first as a filling component for windows and subsequently for covering large areas of building envelopes. Until then, besides the purpose of separating the interior of the building from the outside and, at the same time, allowing for visible light to enter the building (with some thermal insulation), glass had only slight structural functions; indeed, glass elements were only required to sustain their own self-weight, as well as possible wind or snow actions. Architects were mainly requested to take advantage of the special physical properties of glass, namely its transparency and its numerous aesthetical possibilities.

During the last decades there was a significant increase of structures in which glass is used with more relevant structural functions, i.e. as a load bearing material. The increase of structural applications of glass started when it was found that glass was strong enough to be used as a load bearing element. Such increase was possible due to the rising of an architectural trend that has elected glass as a symbol of modern architecture together with the developments of the glass industry, which has been able to fulfil architects' requirements for transparency, enhancing production processes and introducing new glass products.

Among the several technological innovations introduced in the glass industry, the tempering of glass and the production of laminated glass elements are some of the most important ones. On the one hand, the tempering of glass allows glass structures to be designed assuming a characteristic bending strength of about 120 MPa, in opposition to the 45 MPa of annealed glass [1.2]. On the other hand, the introduction of laminated glass elements allows assuming that glass elements can have relatively safe failure mechanisms, thus increasing the safety of the buildings' users. The combination of both products has allowed architects and engineers to apply glass members in a wide spectrum of structural applications. Presently, numerous examples of structural applications of glass can be found, such as roofs, floors, beams or even columns. More recently, in order to fulfil the demand for larger and longer glass structures, the glass industry has developed new manufacturing plants and processing technologies aiming at the production of multi-layer tempered laminated glass elements of about 15 m long, extending the previous standard size of $6.00 \times 3.21 \text{ m}^2$ [1.3, 1.4]. Finally, due to the increase of the structural requirements and structural relevance of glass elements, the glass industry was also able to generalize

the use of stiffer interlayers (e.g. ionomer SentryGlas) in laminated assemblages, as they allow for substantial gains in terms of pre and post-cracking behaviour [1.5, 1.6], being also less prone to the effects of environmental agents, such as moisture and UV radiation [1.5, 1.7].

With the above-mentioned technological and industrial developments and the increasing structural application of glass, new concerns/requirements were raised and new research needs were identified. This attracted the interest of the international research community, which has been publishing different studies regarding several topics concerned with the structural behaviour of glass elements. Such endeavour also resulted in the development or improvement of existing guidelines and standards (e.g. [1.2, 1.8–1.10]). However, despite the large number of studies conducted on laboratory environment and on small to intermediate-scale specimens, there is a lack of research about the structural behaviour of full-scale structural elements, namely on the *in situ* performance of the new long-span multi-layer laminated glass elements.

In spite of the achievements and improvements regarding the robustness and safety of glass structures with the application of laminated glass members with stiff interlayers, common laminated glass elements still present low post-cracking residual capacity [1.11]: in most of the situations, once all glass layers are broken, laminated glass members can barely withstand their own self-weight [1.12]¹. In recent years, as an alternative or complement to laminated structures, several studies have been carried out on hybrid structural systems that combine glass with other structural materials, such as wood, steel, stainless steel, and fibre reinforced polymer (FRP) components, made of either carbon (CFRP) or glass (GFRP) [1.13, 1.14]. The principle of these hybrid/composite/reinforced systems is similar to reinforced concrete, i.e. glass, a material that presents low tensile strength and fragile failure, is combined/reinforced with other materials in order to enhance the stiffness and cracking strength of the hybrid/composite/reinforced elements, but mostly, to guarantee safer and more ductile failure mechanisms.

1.1.1 Previous research at Instituto Superior Técnico

The MSc dissertation of the author [1.15] (concluded in 2010 at Instituto Superior Técnico (IST) of the University of Lisbon) about the structural behaviour of composite systems made of glass and GFRP profiles provided important background knowledge for the research developed in the subsequent years and presented in this PhD thesis. The main objectives of the author's MSc dissertation were two-fold: (i) to present a state of the art review of glass for structural applications in the civil engineering field, and (ii) to assess the feasibility of a composite system made of glass and GFRP components that could be used to overcome the main drawbacks of glass members, namely their brittleness, while keeping their transparency.

¹ In spite of the considerable improvements regarding the serviceability behaviour (prior to glass cracking) of laminated glass structures using high performance interlayers, their post-cracking performance is irrelevant for structural applications.

The review of the literature conducted then (and updated in the present thesis in chapter 2) shows that applications making use of glass as load bearing material have been increasing during the last decades, mainly due to improvements in the manufacturing process (higher and automated factories and improved quality control), the introduction of new glass products (laminated and tempered glass), the development of new connection methods (bolted and bonded supports) and, mostly, due to an architectural trend that has been requiring an increasing use of glass in common buildings. As a result, glass is being used in new applications that require in-depth understanding about the mechanical behaviour of glass products, namely of laminated ones. Within this scope, the research of glass structures over the last decades has focused on the experimental, analytical and numerical investigation of common structural problems of laminated glass elements when used in civil engineering applications, such as their structural stability or long-term behaviour.

The literature review also showed that several researchers are developing hybrid structural systems combining glass with other structural materials in order to overcome the fragile behaviour of glass. Hybrid glass structures can be designed combining glass with materials that present higher tensile strength and ductile behaviour, thus providing (pseudo) ductile failure mechanisms or safer failure modes.

Based on this review, an exploratory experimental campaign was carried out in order to fully characterize the pre and post-cracking flexural behaviour of a composite structural system that combines annealed glass panes and GFRP pultruded profiles, used as reinforcing material. The effects of the reinforcement geometry were addressed by testing beams with two different cross-sections: rectangular and I-shape geometry. The effects of the mechanical properties of the structural adhesives used to bond the GFRP profiles to glass were evaluated in both geometries using two different adhesives: a gap-filling polyurethane silicone and a structural epoxy resin. One specimen of each type of beam was produced and subjected to 4-point bending tests. The experimental tests proved the advantages and technical viability of glass-GFRP composite beams. In particular, it was shown that it is possible to obtain relatively safe and ductile failure mechanisms in transparent glass beams, provided that they are bonded to GFRP reinforcing elements. All beams were able to keep their integrity after the appearance of the first crack, exhibiting residual strength that was function of the mechanical properties of the adhesive and geometry of the cross-section. In terms of post-cracking residual strength and ultimate load capacity, composite beams with epoxy adhesive presented much better performance than their counterparts bonded with polyurethane adhesive. Such better performance was provided essentially by the much higher stiffness of the former adhesive, which provided a high level of coupling between both materials. On the other hand, the post-cracking ductility of the beams bonded with polyurethane silicone was significantly higher compared to the beams bonded with epoxy resin. The higher ductility of the former beams stemmed, essentially, from the high deformation capacity and low stiffness of the polyurethane adhesive, which caused significant slipping at the glass-GFRP interface. It should be mentioned, however, that the achievement of higher ductility levels had a counterpart, namely the lower values of

initial stiffness, post-cracking strength and ultimate load capacity. The flexural behaviour of beams with the two geometries studied was qualitatively similar; however, the rectangular composite beams presented significantly lower pre and post-cracking performances due to the much lower area of GFRP reinforcement.

In spite of this relevant scientific contribution, this preliminary experimental study lacked on statistical significance due to the very low number of specimens tested. In addition, limited understanding was obtained about the effects of the mechanical properties of the adhesive (used to bond glass to GFRP) on the post-cracking performance of the beams. Finally, in this study the non-linear behaviour of glass and the behaviour of the adhesively bonded glass-GFRP joints were not numerically simulated.

1.2 OBJECTIVES AND METHODOLOGY

The main objectives of this PhD thesis are two-fold: (i) to improve the understanding about the flexural behaviour of large-scale multi-layer laminated glass elements, and (ii) to develop a composite structural beam system able to provide transparent glass beams with safer failure modes. Regarding the first objective, the study of the flexural behaviour of multi-layer large-scale laminated glass members, two different topics are studied:

1. Lateral-torsional buckling (LTB) behaviour of long-span multi-layer laminated glass beams;
2. Flexural creep behaviour of polyvinyl butyral (PVB) and SentryGlas (SG) full-scale multi-layer laminated glass panels.

The first topic is assessed through analytical, experimental and numerical investigations. The applicability and accuracy of existing analytical and numerical tools to simulate the LTB behaviour of long-span 3-layer laminated glass beams is first investigated. The analytical studies include (i) the assessment of expressions for the determination of the effective flexural and torsional stiffness of 3-layer laminated glass beams (developed within the scope of this thesis in collaboration with Eng. Miguel Machado e Costa – described ahead in this section); (ii) the determination of the buckling resistance and post-buckling behaviour of long-span laminated glass beams, and (iii) the assessment of the effects of the production geometric tolerances of glass panes and of the viscoelastic properties of the interlayers on the LTB behaviour of the laminated glass beams. The results obtained from the analytical studies are compared with results of a flexural test of a simply supported and unbraced 8.20 m long 3-layer PVB-laminated glass fin, used in the facade of the *Champalimaud Centre for the Unknown* (Lisbon). Finally, three-dimensional (3D) numerical models are developed in order to simulate the experiments and validate the analytical results, in terms of critical load and equilibrium path, and also to evaluate the stress distributions in the beam, namely at the post-buckling stage.

The assessment of the long-term behaviour of laminated glass panels is accomplished by performing an experimental study comprising relatively long-term (350 h) flexural creep tests on full-scale 3-layer PVB

and 4-layer SG-laminated glass panels. The experimental data retrieved is fit using Findley's approach and power laws predictive models are proposed. An analytical study is carried out by comparing short-term and long-term (over a 50 years loading period) estimates using the proposed power laws and the models available in literature, based either on dynamic mechanical analysis (DMA) on interlayer coupons or short-term creep tests on small-scale laminates.

The second main objective set for this thesis, the study and development of hybrid structural glass beams, is achieved by carrying out the following three tasks:

1. Characterization of the post-cracking residual robustness of long-span laminated glass-stainless steel hybrid beams;
2. Characterization of the structural response of multi-span glass-GFRP composite beams;
3. Numerical modelling of the flexural behaviour of glass-GFRP composite beams.

Regarding the first task, an exploratory campaign is carried out aiming at the characterization of the post-cracking residual robustness of long-span laminated glass-stainless steel hybrid beams, made with fully tempered glass. Two long-span laminated glass beams (a 3-layer PVB and 4-layer SG) are reinforced at the bottom and top edges with stainless steel profiles (designed to withstand 80% of the cracking load) and subjected to flexural tests up to failure. The outer glass plies of the PVB hybrid beam are cracked prior testing and the post-cracking performance is compared with analytical predictions. The SG hybrid beam is tested uncracked and its failure mode is analytically and numerically investigated.

As mentioned, the feasibility of glass-GFRP composite beams was assessed in a preliminary work, developed by the author within his MSc dissertation [1.15, 1.16] (*cf.* section 1.1.1). In this thesis, the previous work is further extended to provide in-depth knowledge about the structural behaviour of full-scale glass-GFRP composite beams. In particular, full-scale flexural tests are performed in order to improve the understanding about the effects of (i) the geometry of the GFRP reinforcement elements, and (ii) the adhesive's mechanical properties. In order to achieve such goals, an extensive experimental campaign is conducted comprising: (i) mechanical characterization tests of the GFRP pultruded profiles and of the three different adhesives used to manufacture the composite beams; (ii) tensile tests on glass-GFRP double-lap joints bonded with the three mentioned adhesives; and (iii) flexural tests on single and double-span glass-GFRP composite beams. The first two types of tests provide basic data about the mechanical properties of the materials and joints, respectively, which are needed as input in the numerical models to be developed later (task 3). In the flexural tests, the serviceability (stiffness, cracking loads) and ultimate behaviour (cracking pattern, failure loads, failure modes, force redistribution, ductility) of the beams are analysed and compared, and conclusions are drawn regarding the potential advantages achieved by the structural redundancy of the system.

The last task, numerical modelling of the flexural behaviour of glass-GFRP composite beams, comprises an extensive numerical study aiming at the simulation of the post-cracking behaviour of the composite structural system proposed here. The objectives of this numerical study are: (i) to fully characterize the non-linear behaviour of glass using the smeared crack approach; and (ii) to assess the viability and applicability of different modelling options to simulate adhesively bonded glass-GFRP joints.

1.3 MAIN SCIENTIFIC CONTRIBUTIONS AND PUBLICATIONS

The present thesis presents results of investigations about the application of structural glass in civil construction, providing scientific contributions mainly on the following two domains: (i) structural behaviour of laminated glass structures, and (ii) structural behaviour of composite systems made of glass and stainless steel or GFRP pultruded profiles. These contributions, which are further detailed in the following paragraphs, are considered to have added in-depth knowledge on the design of laminated glass beams of any scale and promoted the use of new glass hybrid systems. More specifically, such contributions can be divided in five different topics:

1. Lateral torsional buckling (LTB) behaviour of laminated glass beams;
2. Flexural creep behaviour of laminated glass panels;
3. Flexural behaviour of glass-stainless steel hybrid beams;
4. Flexural behaviour of glass-GFRP composite beams;
5. Numerical simulation of composite glass beams bonded with different adhesives.

Regarding the first topic, this thesis provides relevant analytical, experimental and numerical data concerning the LTB behaviour of long-span laminated glass beams, which are very scarce in the literature. In particular, the results obtained proved the applicability of existing analytical and numerical tools (the former having been developed within the scope of this work) to accurately determine (i) the effective flexural and torsional stiffness of 3-layer laminated glass beams (in this regard, the literature presented several inconsistent expressions), as well as (ii) the LTB critical load, and (iii) the post-buckling behaviour of laminated glass beams. Furthermore, the analytical study provided a useful contribution for the design of long-span multi-layer laminated glass beams prone to LTB phenomena, by quantifying the dependency of the LTB resistance of laminated glass beams on both the material properties of the interlayer (time and temperature dependent) and the glass production (geometric) tolerances. This particular research work resulted in the following publications:

1. Valarinho L, Correia JR, Machado-e-Costa M, Branco FA, Silvestre N. Lateral-torsional buckling behaviour of long-span laminated glass beams: Analytical, experimental and numerical study. *Materials and Design* 2016; 102: 264–275.

2. Machado-e-Costa M, Valarinho L, Correia JR, Silvestre N. Modelling of the structural behavior of multilayer laminated glass beams: Flexural and torsional stiffness and lateral-torsional buckling. *Engineering Structures* 2016; 128: 265-282².

The study on the flexural creep behaviour of laminated glass panels retrieved relevant experimental data about the long-term response of full-scale multi-layer laminated glass panels at the scale of civil engineering applications (long-span laminated specimens) and for a relatively long duration; this type of information was not yet available in the literature on structural glass. In fact, the existing models available to predict the long-term behaviour of laminated glass elements were based either on data provided by short-term experimental tests of small-scale laminates or DMA tests of interlayer coupons - both methodologies have not yet been validated at the full-scale. The above-mentioned work resulted in the following publication:

3. Valarinho L, Correia JR, Garrido M, Sa M, Branco FA. Creep behaviour of laminated glass panels. *Journal of Structural Engineering*, submitted for publication.

The work developed about glass-stainless steel hybrid beams provided relevant experimental data concerning the post-cracking behaviour of this type of hybrid systems. In particular, the residual load carrying mechanism reported in the literature for hybrid beams using annealed glass was now observed and quantified for laminated glass beams using PVB and fully tempered glass. Furthermore, it is shown that the production of long-span hybrid glass beams using fully tempered glass requires further studies, namely concerning the application and structural design of adhesively bonded joints.

In this thesis, new experimental results concerning the flexural behaviour of full-scale glass-GFRP composite beams are reported, complementing the preliminary studies performed by the author in his MSc dissertation. The experimental data obtained now confirmed the advantages and technical viability of the composite solution, being supported by statistically relevant data. In addition, new insights regarding the behaviour of adhesively bonded joints between glass and GFRP covering a significant range of adhesives' mechanical properties are provided. Finally, the concept of composite glass systems was, for the first time, extended to continuously supported beams, thus showing new methods to take structural advantage of the cross-sectional redundancy provided by the glass-GFRP composite system. The aforementioned studies resulted in the following publications:

4. Correia JR, Valarinho L, Branco FA. Post-cracking strength and ductility of glass-GFRP composite beams. *Composite Structures* 2011; 93: 2299–2309.

² This publication was prepared in collaboration with Miguel Machado-e-Costa, who developed his MSc dissertation anchored in the present PhD thesis: Machado-e-Costa M. *Modelling of the Structural Behavior of Laminated Glass Beams. Study of the Lateral-Torsional Buckling Phenomenon*. MSc dissertation in Civil Engineering, Lisbon University, Portugal, 2015.

5. Valarinho L, Correia JR, Branco FA. Experimental study on the flexural behaviour of multi-span transparent glass–GFRP composite beams. *Construction and Building Materials* 2013; 49: 1041–1053.

Finally, the numerical study developed to simulate the flexural behaviour of glass-GFRP composite beams proved the applicability of existing (non-commercial) FE tools to accurately simulate the non-linear behaviour of such beams assuming the classical principles of the smeared crack approach to simulate the effects of glass fracture. In particular, it was shown that the non-linear behaviour of glass can be modelled assuming fracture energy values higher than the ones experimentally determined for soda lime silica annealed glass, which contributes avoiding convergence problems stemming from numerical instabilities in the models. Moreover, the bond behaviour between glass and GFRP was for the first time modelled using experimentally calibrated interface elements, proving the versatility of such elements to numerical simulate a wide range of mechanical properties of glass-GFRP joints. The above-mentioned work resulted in the following publication:

6. Valarinho L, Sena-Cruz J, Correia JR, Branco F. Numerical simulation of the flexural behaviour of glass-GFRP composite glass beams using smeared crack models. *Composites Part B: Engineering*, accepted for publication.

In the frame of the present PhD thesis, in collaboration with researchers from the *Mechanics, Modelling and Structural Analysis* group of CERIS (namely with Prof. Jorge Alfaiate and Doctor Pedro Neto), the author participated in a numerical study where a different modelling strategy was used to simulate the non-linear flexural behaviour of glass-GFRP composite beams, the discrete strong discontinuity approach. From this work, the following publication was prepared:

7. Neto P, Alfaiate J, Valarinho L, Correia JR, Branco FA, Vinagre J. Glass beams reinforced with GFRP laminates: Experimental tests and numerical modelling using a discrete strong discontinuity approach. *Engineering Structures* 2015; 99: 253–263.

In addition to the above-mentioned published (four) and submitted (three) ISI journal papers, the research developed in this thesis was also disseminated in the following four international conference papers and one national conference paper:

8. Valarinho L, Correia JR, Branco F, Sena-Cruz J. Experimental investigations on continuous glass-GFRP beams. Preliminary non-linear numerical modelling. In: Bos, Louter, Nijse, Veer (Eds.). *Challenging Glass 3 - Conf. Archit. Struct. Appl. Glas.*, Delft: Amsterdam: IOS Press; 2012, p. 745–58.
9. Valarinho L, Correia JR, Branco FA, Sena-Cruz J. Experimental and numerical study on GFRP-glass adhesively bonded joints. In: Louter, Bos, Belis, Lebet (Eds.). *Challenging Glass 4. COST Action TU0905 Final Conference*, Taylor & Francis Group, London; 2014, p. 393–400.

10. Valarinho L, Sena-Cruz J, Correia JR, Branco FA. Numerical simulation of transparent glass-GFRP composite beams using smeared crack models. *6th International Conference on FRP Composites in Civil Engineering (CICE 2012)*, Roma: 2012, p. 537–611.
11. Neto P, Alfaiate J, Valarinho L, Correia JR, Branco FA, Vinagre J. Characterization of the bond behaviour between glass and GFRP. In: J.G.M. Van Mier, G. Ruiz, C. Andrade, R.C. Yu and X.X. Zhang (Eds). *VIII International Conference Fracture Mechanics of Concrete and Concrete Structures (FramCoS-8)*, Toledo: 2013.
12. Valarinho L, Correia JR, Branco FA, Chiumiento G. Instabilidade lateral por flexão-torção de vigas em vidro estrutural. Estudo experimental e analítico. *Jornadas Portuguesas de Engenharia de Estruturas 2014*, Lisboa: 2014, p. 1–16 (in Portuguese).

1.4 DOCUMENT OUTLINE

The present thesis is organized in eight chapters, which are grouped into four parts:

- Part I – Introduction and state of the art review (chapters 1 and 2);
- Part II – Study of the structural behaviour of laminated glass beams and panels (chapters 3 and 4);
- Part III – Study of the structural behaviour of hybrid glass beams (chapters 5, 6 and 7);
- Part IV – Conclusions and future developments (chapter 8).

The first and present chapter introduces the thesis theme in the general context of civil engineering, describing the main objectives, the methodology and the main scientific contributions of the research developed.

Chapter 2 presents the state of the art review of the structural applications of glass in civil engineering. It starts describing the production method, the main physical and mechanical properties of the different types of glass and of the different glass products commonly used. Few examples of glass structures are selected and described providing a general overview of the most common applications involving the structural use of glass in construction. Finally, a brief description of the glass connection technology and of the most recent research concerns is presented.

In chapter 3, the experimental study carried out for the characterization of the LTB behaviour of a 3-layer laminated glass beam used in the construction of the facade of the *Champalimaud Centre for the Unknown* building is presented, together with the results of a comprehensive analytical study that aimed at the determination of the accuracy of the most recent analytical and numerical tools when applied to long-span laminated glass beams. Special attention is given to the effects of the glass production tolerances and of the viscoelastic behaviour of PVB. Finally, the numerical results concerned with the determination of the post-buckling stresses of the laminated glass beam are also described.

Chapter 4 presents the study about the creep behaviour of full-scale laminated glass panels. The results of long-term flexural creep tests on PVB and SG-laminated glass panels are first presented, together

with their analytical modelling using Findley's power law. Next, deformability predictions over 50 years of load using the power law proposed for each interlayer are compared with those obtained considering different material models of the interlayers available in the literature.

Chapter 5 of this thesis presents the experimental, analytical and numerical studies carried out on glass-stainless steel hybrid beams. The experiments included flexural tests of long-span laminated glass beams made with fully tempered glass and assembled with either PVB or SG and reinforced with stainless steel profiles. As mentioned, in these experiments the outer glass plies of the PVB-laminated hybrid glass beam were cracked prior to testing in order to quantify the residual post-cracking performance provided by the PVB-glass system. The final part of the chapter presents the analytical and numerical assessment of the SG-laminated hybrid glass beam (tested unbroken), namely of the structural behaviour of its adhesively bonded joint.

Chapter 6 presents the experimental campaign carried out for the flexural characterization of full-scale glass-GFRP composite beams. First, the structural concept and the properties of the materials are presented. Next, the shear behaviour of adhesively bonded glass-GFRP joints using three different adhesives is described based on results of tensile tests on double-lap joints. Finally, the pre and post-cracking performance of single-span and multi-span beams tested in bending is presented, including the effects of the reinforcement geometry and of the structural adhesives used to bond the GFRP to glass.

Chapter 7 presents the numerical study about the flexural behaviour of composite glass-GFRP beams. The experimental results of rectangular glass-GFRP composite beams bonded with the epoxy adhesive (reported in the preceding chapter 6) are used to fully characterize the non-linear numerical behaviour of glass using the smeared crack approach. Next, the experimental data retrieved from the tensile tests on double lap joints are used (i) to calibrate numerical models of the glass-GFRP joints, and (ii) to evaluate the applicability of different modelling options available to simulate the behaviour of glass-GFRP composite beams bonded with different adhesives.

Chapter 8 presents the main conclusions that can be drawn from this thesis and presents recommendations for future developments.

1.5 REFERENCES

- [1.1] Ritchie I. Aesthetics in glass structures. *Struct Eng Int J Int Assoc Bridg Struct Eng* 2004;14:73–5.
- [1.2] Report EUR 26439 EN Guidance for European Structural Design of Glass Components. Institute for the Protection and Security of the Citizen, Joint Research Centre, Luxembourg: 2014.
- [1.3] Haldimann M, Luible A, Overend M. *Structural Use of Glass*. Zurich: IABSE-AIPC-IVBH; 2008.
- [1.4] O’Callaghan J, Bostick C. The Apple Glass Cube: Version 2.0. In: Bos, Louter, Nijse, Veer, editors. *Challenging Glas. 3*, Delft: Amsterdam: IOS Press; 2012, p. 57–65.
- [1.5] Bennison SJ, Smith CA, Duser A van, Jagota A. Structural Performance of Laminated Glass with a “Stiff” Interlayer. *Glas. Build. ASTM STP 1434*. V. Block, West Conshohocken, PA: ASTM International; 2002.
- [1.6] Callewaert D. *Stiffness of Glass / Ionomer Laminates in Structural Applications*. PhD thesis, Ghent University, Belgium, 2012.
- [1.7] Bennison SJ, Qin MH, Davies PS. High-performance laminated glass for structurally efficient glazing. *Innov. Light. Struct. Sustain. Facades*, Hong Kong: 2008, p. 1–12.
- [1.8] The Institution of Structural Engineers. *Structural Use of Glass in Buildings (Second edition)*. London: The Institution of Structural Engineers (ISE); 2014.
- [1.9] CNR-DT 210/2013 Istruzioni per la Progettazione, l’Esecuzione ed il Controllo di Costruzioni con Elementi Strutturali di Vetro. Consiglio Nazionale Delle Ricerche, Roma: 2013.
- [1.10] DIN 18008-1: Glass in Building - Design and construction rules - Part 1: Terms and general bases. DIN Deutsches Institut Für Normung e.V., Berlin: n.d.
- [1.11] Belis J, Depauw J, Callewaert D, Delincé D, Van Impe R. Failure mechanisms and residual capacity of annealed glass/SGP laminated beams at room temperature. *Eng Fail Anal* 2009;16:1866–75.
- [1.12] Bos FP. *Safety Concepts in Structural Glass Engineering Towards an Integrated Approach*. PhD thesis, Delft University of Technology, Netherlands, 2009.
- [1.13] Martens K, Caspeele R, Belis J. Development of composite glass beams – A review. *Eng Struct* 2015;101:1–15.
- [1.14] Martens K, Caspeele R, Belis J. Development of reinforced & post-tensioned glass beams - review. *J Struct Eng* 2015:1–23.
- [1.15] Valarinho L. *Construção em vidro estrutural: comportamento estrutural de vigas mistas vidro-GFRP*. MSc dissertation (in Portuguese), Technical University of Lisbon, Portugal, 2010.
- [1.16] Correia JR, Valarinho L, Branco FA. Post-cracking strength and ductility of glass-GFRP composite beams. *Compos Struct* 2011;93:2299–309.

ABSTRACT

Glass is one of the most interesting and attractive materials in construction. It stands out due to its transparency and many aesthetical possibilities, but it is also one of the few materials that is 100% recyclable. Modern architectural trends are requiring increasing application of glass in their structures, not just as infill material, but also as a load-bearing material. For the latter application, glass also presents interesting properties, such as high resistance to compressive loads and relatively high Young's modulus and tensile strength. During the last decades several constructions were built in which glass was applied as a load-bearing material on different elements, such as panels, roofs, beams, columns and walls. Lately, the production of large-size glass elements and the application of interlayers with superior mechanical performance has enabled the execution of all-glazed structures, which use minor non-glass components. Regardless of the recent developments of the glass industry, common laminated glass elements still present brittle failure behaviour and have reduced post-fracture residual strength and ductility, not complying with the traditional design philosophies and most recent structural standards, thus requiring special safety measures. In order to overcome the aforementioned drawbacks, several researchers have been combining glass with other structural materials, such as steel, concrete, timber and fibre reinforced polymers in order to enhance the post-fracture behaviour and obtain safer failure modes. Extensive experimental, analytical and numerical investigations have been presented and promising results were achieved. The high demand for structural glass applications attracted the attention of researchers on other fields that include, among other topics, the fracture mechanics of glass, interlayer materials and their mechanical properties, adhesively bonded connections, thin chemically tempered and curved glass. This chapter presents a brief state of the art review of structural glass. First, in section 2.1 the production process and the chemical, physical and mechanical properties of glass are described, as well as the main types of glass and assemblages. Next, in section 2.2 a brief overview of structural applications of glass panels and beams is presented. Subsequently, in section 2.3 a review of hybrid structural concepts is presented, where glass elements are combined with other structural materials. Finally, in section 2.4 an overview of other fields of research and development about structural glass is presented.

2.1 GLASS

2.1.1 Production process

The majority (90%) of flat glass used in construction is produced with the float production method [2.1], introduced in industry in the year of 1959 by the company Pilkington Brothers [2.2]. In comparison with the previous production methods (e.g. the Fourcault process), the float production method is less expensive and provides smooth, parallel, uniform and high quality glass panes. Fig. 2.1 illustrates the main stages of a modern float production process, being possible to distinguish the following key-stages:

1. Mixing: the raw materials are weighed, mixed and introduced in the furnace;
2. Smelting: the raw materials become molten at temperatures reaching 1550 °C;
3. Purification: the molten glass is homogenised, clean of air (bubbles) and cooled to 1200 °C;
4. Forming: the molten glass flows onto the float area where it floats on the top of a bath of molten tin and starts to cool slowly (the glass panes thickness is controlled in this stage by applying different stream speeds or by controlling the float area);
5. Cooling: glass is rolled onto the annealing *lehr* where it is slowly cooled (from 600 °C to 60 °C) in order to prevent thermal shocks and growth of residual stresses;
6. Quality control: glass panes are automatically inspected to detect major flaws;
7. Cutting and storage: glass panes are cut into a standard size of 6.00 m × 3.20 m and stored until they are further processed.

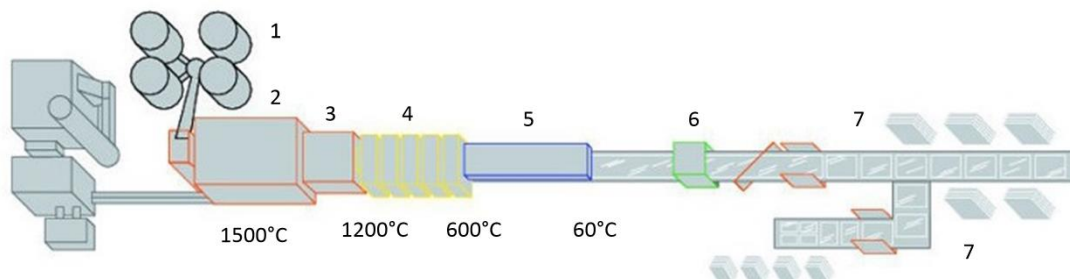


Fig. 2.1 - Float glass production process [2.3].

Modern float glass production plants work 24/7, require very low maintenance periods and produce glass panes with thicknesses ranging from 2 to 25¹ mm within their standard size. The maximum size of glass panes is mainly restricted by the plant's facilities, glass processing equipment (autoclave lamination process), and constraints during transport and application. Over the last years, the technical development of glass construction as well as the growing interest in glass products has technically and economically enabled the mass-production of large-size glass elements, being now possible to produce any kind of glass product up to a length of 15 m [2.4, 2.5] (Fig. 2.2).

¹ Thin glasses (0.03 to 2.00 mm) are mainly produced with the fusion overflow method [2.10].



Fig. 2.2 – Processing of large-size glass elements at SEDAK [2.5].

2.1.2 Chemical properties

Glass is a non-crystalline, homogenous and inorganic solid material, which results from the fast cooling of a mass in fusion. The crystallization (geometrically regular network of crystals) of the material is avoided due to the fast cooling and the solid state is kept in between the crystalline and amorphous (geometrically irregular network of crystals) structures. The most common glass used in construction is soda lime silica glass (SLSG), followed by the borosilicate glass (BSG) [2.1]. The latter is mainly required for special applications, such as fire protection glazing and heat resistant glazing, due to its high resistance to thermal shocks (it has a low coefficient of thermal expansion). The chemical composition of both types of glass according to current European product standards [2.6, 2.7] are presented in Table 2.1.

Table 2.1 – Chemical composition (% of mass) of soda lime silica glass (SLSG) and borosilicate glass (BSG) [2.6, 2.7].

Chemical compound	Chemical Formula	Soda lime silica glass (SLSG)	Borosilicate glass (BSG)
Silica dioxide (Sand)	SiO ₂	69-74%	70-87%
Calcium oxide (Lime)	CaO	5-14%	-
Sodium oxide (Soda)	Na ₂ O	10-16%	0-8%
Boron oxide (Boria)	B ₂ O ₃	-	7-15%
Potassium oxide (Potash)	K ₂ O	-	0-8%
Magnesium oxide (Magnesia)	MgO	0-6%	-
Aluminium oxide (Alumina)	Al ₂ O ₃	0-3%	0-8%
Others		0-5%	0-8%

Recently, some studies have been presented [2.8, 2.9] regarding the architectural application of alkali-alumino-silicate glass, whose chemical composition contains up to 25% of aluminium oxide [2.10]. This type of glass is highly advantageous² if chemically tempered (*cf.* section 2.1.4.1)

² Chemical tempering is more effective if applied in aluminium ions rather than in sodium ones.

2.1.3 Physical and mechanical properties

The transparency is the most important property of glass, which is proved by its high value of visible transmittance. In fact, SLSG presents high values of transmittance up to the mid-wavelength of infrared ($\lambda > 5000$ nm) but very low transmittance for higher wavelengths, which is no more than heat. Consequently, glass allows visible light to be transmitted through it, but retains all the heat that is generated in such wavelength. In practice, glass not only allows to achieve high levels of luminosity inside buildings, but it also provides extra heating to it. Such effect is usually referred to as *Greenhouse* effect.

The main physical and mechanical properties of glass are summarized in Table 2.2. Comparing with the traditional materials used in construction, the specific weight of glass is similar to that of reinforced concrete (but glass presents higher Young's modulus) and is considerably lower than that of steel.

Table 2.2 – Physical and mechanical properties of soda lime silica glass (SLSG).

Properties	SLSG
Density ¹ [kg/m ³]	2 500
Young's modulus ¹ [GPa]	70
Shear modulus ¹ [GPa]	28
Poisson's ratio ¹ [-]	0.23
Softening point ¹ [°C]	720
Coefficient of thermal expansion ¹ [K ⁻¹]	9×10^{-6}
Specific thermal capacity ¹ [Jkg ⁻¹ K ⁻¹]	720
Mohs hardness ¹ [-]	6.5
Tensile strength ² [MPa]	20 to 110
Compressive strength ¹	800

¹ According to [2.11]; ² According to [2.12]

At room temperature, glass presents linear elastic behaviour and does not allow for either stress redistributions or plastic deformations, which results on a brittle failure. The theoretical glass tensile strength, i.e. based on molecular forces, is very high and may reach 32 GPa [2.1]. However, such strength is of no practical relevance for engineering applications: as for other brittle materials, the actual tensile strength of glass will depend on the existing microscopic flaws on its surface (Griffith flaws), which are responsible for a much lower value. It is beyond the scope of this study to detail the fracture mechanics of glass. Nevertheless, it is relevant to highlight that according to the recent *Guidance for European Structural Design of Glass Components* [2.13], the bending strength of glass ranges from 30 to 80 MPa. It depends on a variety of factors, such as the size of the existing microscopic flaws, the surface side of the glass panel where the flaw is located, the size and length of the specimen edge, the applied load history and load distribution, as well as on the surrounding humidity conditions. As for the molecular strength, the compressive strength of glass (800 MPa [2.11]) is of no practical relevance since glass elements will exhibit stability problems or will fail under tension (due to Poisson's effect) long before their compressive strength is attained.

2.1.4 Glass types and assemblages

Annealed float glass (ANG) presents low and unpredictable tensile strength, which generally makes it unsafe for structural glass applications. Therefore, ANG is often further processed to produce glass products that meet current structural requirements. Glass members commonly applied in structures are either toughened, laminated or a combination thereof.

2.1.4.1 Tempered glass

The tempering of glass (also referred to as toughening) is the most important process applied on glass members, that are used in structural applications. It consists of the introduction of a favourable residual compressive stress on the glass edges to increase its strength compared with annealed float glass. The toughening of glass introduces compression on the outer surfaces and tensile stresses in the inner core. The latter region does not present any flaws, thus it is not affected by the introduced stresses and can still offer good resistance to tensile stresses. On the other hand, the undesirable and existing flaws in the outer surfaces can only grow when the applied load produces tensile stresses higher than the applied compressive residual ones. As long as the applied tensile stresses are smaller than the residual compressive ones, there is no effective tensile stress and consequently no crack growth [2.1]. Tempered glass can be obtained using thermal or chemical treatments, whose products are also referred to as heat/thermal and chemical treated glass.

The thermally treated glass is obtained by reintroducing the ANG glass into a furnace and heating it up to temperatures between 625 – 675 °C. After removal from the furnace, the glass surfaces are rapidly cooled by jets of cold air, whereas the inner core is cooled down more slowly. This process creates an approximately parabolic stress distribution (Fig. 2.3), with compressive stresses in the outer surfaces and tensile stresses in the inner core. The depth of the compressive zone is approximately 20% of the section height [2.1]. In addition, once the thermal tempering process is applied, glass elements cannot be further cut, drilled or gridded, due to the risk of causing involuntary stress release.

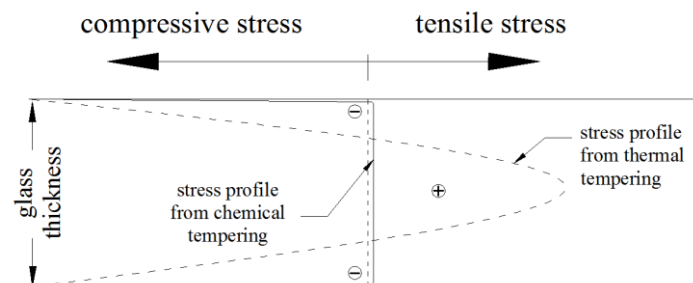


Fig. 2.3 - Comparison of the stress profile obtained by thermal and chemical tempering [2.1].

The level of introduced residual stresses is controlled by the cooling speed rate. Two types of heat-treated glass are commonly described in the literature (Table 2.3): (i) heat strengthened glass (HSG),

and (ii) fully tempered glass (FTG). In the former, the typical residual compressive stresses vary between 40 MPa and 80 MPa, while in the latter they vary between 80 MPa and 170 MPa [2.1]^{3,4}.

Table 2.3 – Glass type according to the level of tempering residual stresses [2.1].

Type of glass	Level of residual surface compression
Annealed float glass (ANG)	None (0 MPa)
Heat strengthened glass (HSG)	Medium (40 – 80 MPa)
Fully tempered glass (FTG)	High (80 – 170 MPa)

The glass fracture pattern is function of the energy stored in the glass element, which, on its turn is function of the level of residual stresses and accumulated tensile loads. Annealed float glass normally breaks into relatively large fragments. The increase of residual stresses or applied loads results in a progressive reduction of the fragments size (Fig. 2.4). Therefore, HSG usually breaks into medium-to-small-size glass fragments, and FTG breaks into small-size diced glass fragments⁵. The fracture pattern affects both the post-failure safety and post-failure performance: on the one hand, the small-size blunt fragments may be considered less harmful (depending always on the final structural application), but on the other hand, they provide poor post-failure performance due to the lack of integrity of the tiny fragments.

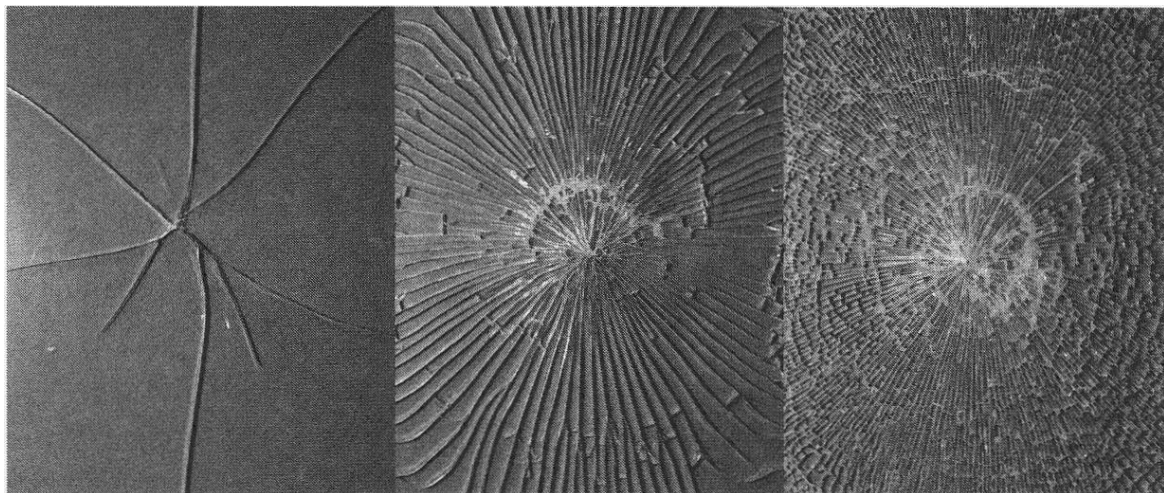


Fig. 2.4 - Fracture pattern of (left to right) annealed float glass, heat strengthened glass and fully tempered glass [2.1].

Chemical tempered glass (CTG) is an alternative to heat-treated glass obtained without the use of thermal processes. In the chemical tempering process glass is immersed in a bath of potassium salts at approximately 400 °C, that causes the exchange of sodium ions in the glass surface by larger potassium ions. The residual compressive stresses, which can go up to 800 MPa [2.14], are introduced in a very thin layer at the surface

³ The product requirements of each glass type can be found in the corresponding standards available in each region [2.6, 2.107–2.113].

⁴ The range of the residual compressive stresses may slightly change according to the reference.

⁵ ANG can have a fracture pattern similar to that of heat strengthened glass if it breaks under high tensile loads.

(Fig. 2.3) that can go from 20 to 50 μm [2.8]. Besides the much higher strength, cutting and drilling remains possible after chemical tempering. For now, the application of chemically tempered glass in architecture is rather scarce, mostly due to its cost and limited dimensions; the most effective chemical tempering process has been applied mostly to thin glass [2.10] which, for now, is produced with very limited size dimensions (detailed ahead in section 2.4.2). However, some authors have presented promising results regarding the structural application of chemically tempered glass in the building industry [2.8, 2.9].

2.1.4.2 Laminated glass

In spite of the increase of tensile strength of single toughened glass panels, such elements still exhibit a brittle behaviour, i.e. they do not present plastic deformations prior to failure or residual strength after. Toughened glass elements fail suddenly and without any warning signs, thereby they still represent a risk for safety if applied as a load-bearing material.

Laminated glass consists of two or more glass layers bonded together by means of polymeric interlayers in the form of sheets. Unlike tempering, the structural safety of laminated glass assemblies is achieved by providing structural redundancy and not by increasing the material failure resistance. Under the breakage of one glass layer, the interlayer sheets will hold the glass fragments together and transfer the loads to the remaining uncracked glass layers, thus proving post-fracture structural safety. By laminating glass into composite elements (laminated glass panels), the load-bearing behaviour, post-fracture integrity and robustness can be substantially improved.

Laminated glass is obtained by subjecting the assemblage to a controlled environment in autoclave, in terms of pressure (14 bar) and temperature (140 °C), which triggers the bond mechanism between glass and the interlayer sheets. Laminated glass assemblages can comprise any type of glass (ANG, HSG, FTG or CTG) with any thickness, and several different interlayer types are available. Polyvinyl butyral (PVB), ethylene vinyl acetate (EVA) and ionoplast polymers (e.g. SentryGlas) are amongst the most popular and suitable for structural glass applications.

The post-fracture performance and residual load bearing capacity of laminated glass elements is function of the (i) type of glass, and (ii) mechanical properties of the interlayer. Regarding the type of glass, the remaining post-failure capacity decreases with the increase of glass fragmentation (or decrease of fragments size - Fig. 2.5-a). Therefore, a considerable remaining post-fracture capacity is achieved if ANG or HSG layers are used, and a poor one if FTG layers are applied. Regarding the interlayer mechanical properties, the post-failure (residual) capacity increases with the interlayer's stiffness (Fig. 2.5-b).

2.1.4.3 Interlayer materials

Different interlayer products are available in the market, covering a wide range of functions and properties. Up to now, PVB is the most common interlayer found in the building industry. However, the

use of stiffer interlayers (structural PVBs, ionoplast or thermoplastic polyurethane (TPU)) has been growing during the last years due to the increase of structural glass applications where higher bearing capacity and relevance is required. Interlayer sheets are produced in rolls with different widths and thicknesses (e.g. PVB is usually provided in roles with widths up to 3.2 m and thicknesses in multiples of 0.38 mm). Table 2.4 presents the main material properties of the three most common interlayers found in building applications.

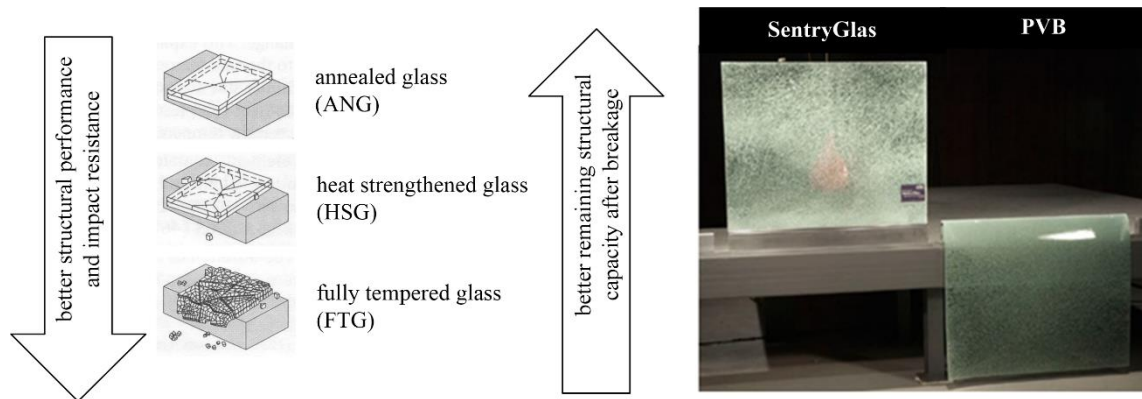


Fig. 2.5 - Post-fracture capacity of laminated glass members as a function of the (left to right) type of glass [2.1] and type of interlayer (*SentryGlas* and PVB) [2.15].

Table 2.4 - Main material and mechanical properties of the most popular interlayers [2.19, 2.21] ⁶.

Property	PVB	PVB	Ionoplast	EVA	TPU
	standard	structural			
Density [kg/m ³]	1070	1080	950	930	-
Tensile strength [MPa]	25 to 27	33	34.5	9 to 31	20.5
Tensile elongation [%]	200 to 250	190	≥ 500	≥ 415	≥ 400
Coefficient of thermal expansion [10 ⁻⁶ /K]	468	155	100 - 150	98	-
Glass transition temperature [°C]	28 to 32	40 to 45	50 to 55	-43 to -15	-60 to -31

The choice of the most suitable interlayer depends on the corresponding glass member's requirements. PVB is the interlayer most commonly found in architectural applications being also the cheapest one. Nevertheless, it is highly susceptible to ageing and it loses part of its transparency with time (yellowing). Furthermore, it presents low mechanical properties, even at room temperature, and it is highly susceptible to time and temperature actions, which makes it unsuitable for relevant structural glass applications [2.1, 2.13, 2.16]. In those cases, structural PVBs and ionomers are the most suitable solutions since they offer superior mechanical properties (Fig. 2.6) and are less prone to the effects of environmental agents, such as temperature, humidity and ultraviolet radiation [2.17]. In particular, ionoplast interlayers, such as SentryGlas (SG), allow for substantial gains in terms of pre and post-failure behaviour, since they present much higher mechanical properties [2.17–2.20].

⁶ The authors highlighted that the main properties may slightly change according to the producer.

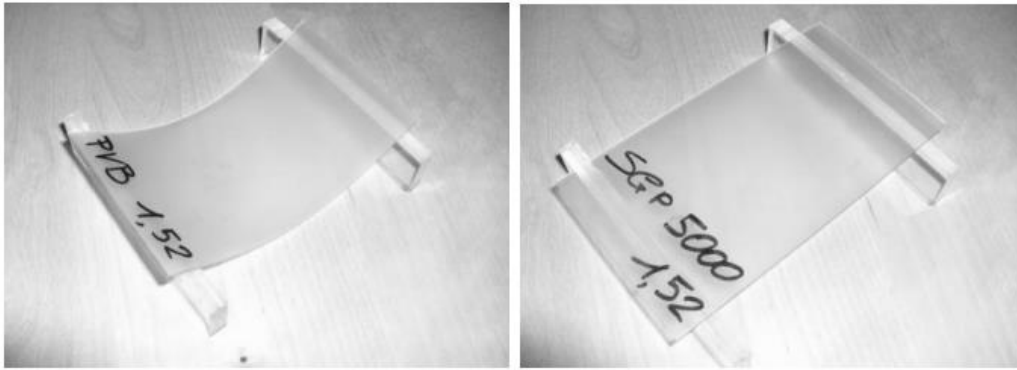


Fig. 2.6 - Qualitative comparison of the bending stiffness of PVB and SG with equal thickness [2.6].

Both PVB and ionoplast interlayers present viscoelastic mechanical behaviour in the common temperature range for building temperatures ($-20\text{ }^{\circ}\text{C}$ to $80\text{ }^{\circ}\text{C}$ [2.22]). The mechanical properties of interlayers are usually presented in the form of reduction master curves of the corresponding property at a reference temperature, obtained from either dynamic mechanical analysis (DMA) tests on interlayer coupons or torsional and flexural creep/relaxation tests on small-scale laminates (further information in this respect is provided in chapter 4). Fig. 2.7 illustrates the shear modulus master curves of PVB *Butacite* produced by Kuraray⁷ [2.23], PVB *Saflex* produced by Solutia [2.24] and ionoplast *SentryGlas*⁸ produced by Kuraray [2.25] (all curves were obtained from DMA tests).

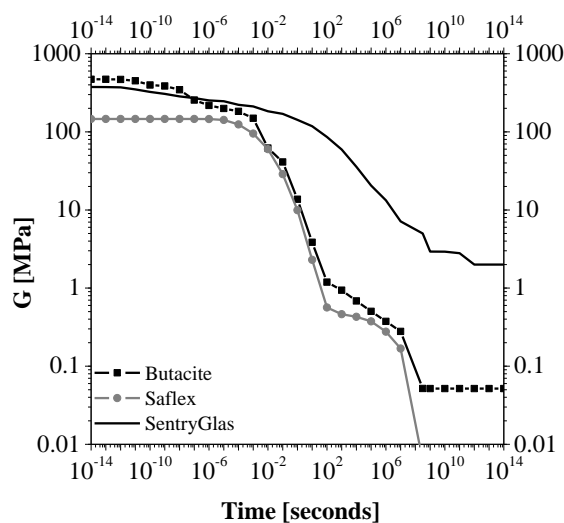


Fig. 2.7 - Shear modulus master curves for the reference temperature of $20\text{ }^{\circ}\text{C}$ of PVB *Butacite* (Kuraray [2.23]), PVB *Saflex* (Solutia [2.26]) and ionoplast *SentryGlas* (Kuraray [2.25]).

The interlayers EVA and TPU are much more expensive than standard PVB, and the gains obtained from their use not always far outweigh their cost disadvantages. Nevertheless, EVA presents improved performance to sound insulation, as well as high transparency and excellent durability to heat, humidity

⁷ Butacite used to be supplied by DuPont until June 2014.

⁸ The ionoplast product supplied by Kuraray (it used to be supplied by DuPont until June 2014) named as SentryGlas[®] has evolved since its first years of production from SentryGlas[®], through SentryGlas[®] Plus, SentryGlas[®] Plus 2000, SentryGlas[®] Plus 5000 back to SentryGlas.

and ultraviolet radiation. TPU also presents enhanced structural behaviour at high temperatures and superior transparency properties and ageing durability [2.27].

2.2 STRUCTURAL APPLICATIONS OF GLASS PANELS AND BEAMS

Glass has played a central role on modern architecture since the 19th century, due to its many aesthetical possibilities together with its main feature: transparency. Over the last decades, following the architectural trend of pursuing more creative and transparent building envelopes and structures, besides the common application of glass in enclosing elements, glass has started to be applied as load-bearing material and used in load-bearing elements, such as panels, beams, columns and walls. In the following paragraphs, examples of structural applications of glass panels and glass beams are presented. Due to the scope of this thesis, it was considered more relevant to present examples of glass panels mainly subjected to out-of-plane loads and of glass beams mainly subjected to bending loads.

2.2.1 Glass roofs and floors

Together with glazed facades glass roofs are one of the most popular applications of glass in construction. With the developments of light steel structures during the second half of the 19th century, architects and engineers have faster looked for the implementation of glass as infill material of light steel domes [2.28], guaranteeing at the same time the maximum transparency and light inside buildings. Such domes were made of single-small glass elements (the dimensions were restricted to the available production methods and the advantages of laminated glass elements were yet to be found). The small-size of the numerous glass elements was advantageous, since it provided redundancy to the structure. Over the years, the construction of glass domes and roofs has followed the architectural trend of free form structures, which allows for multi-directional bearing systems where glass panes can be used plan or bent, and are mainly subjected to shell and membrane stresses (Fig. 2.8).



Fig. 2.8 – Free-form glass structures as part of a roof [2.29].

Currently, glass has also been increasingly applied on traditional flat roofs/floors (Fig. 2.9-a), replacing the conventional infill materials (e.g. wood or roof tiles). In both applications, free forms or flat roofs,

the structural role of glass is still very limited, since the glass panels have only to withstand their own self weight and carry loads from wind, snow or impact (the latter can always occur during maintenance actions). The glass panel structural role increases with the use of large-size glass panels and with the replacement of linear supports by pointed ones (Fig. 2.9-b).

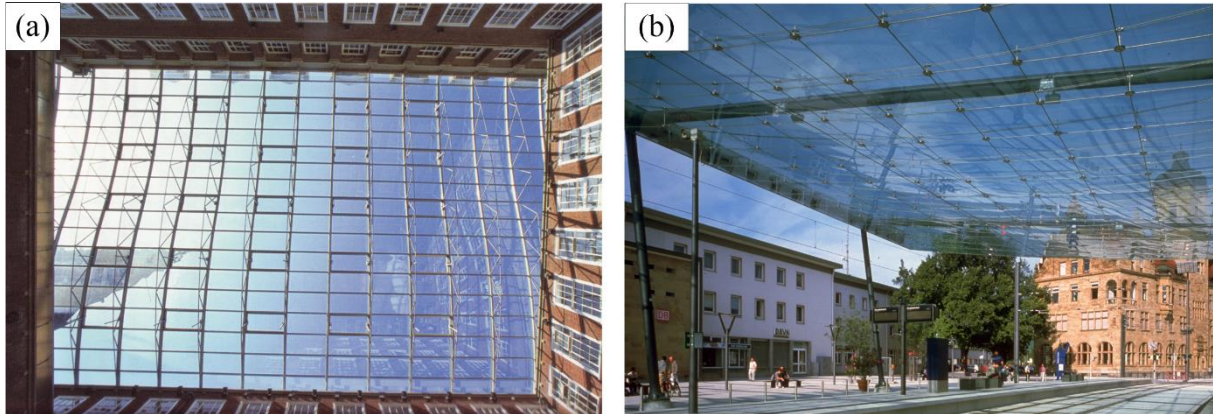


Fig. 2.9 - Glass roof with (a) linear [2.2] and (b) pointed supports [2.28].

2.2.2 Glass beams

Beam elements, together with columns, take the most relevant structural role on a building supporting frame, since it is through them that the gravity loads are transferred to the building's foundations. It would be to expect that architects' efforts to maximize buildings transparency would sooner or later rely on these elements. One of the most popular applications of glass as a beam element are the so called glass fins, vertical glass beams applied along the glass facades, which replace traditional metal frames or cables, carrying horizontal wind loads out of the facade's glass panes (Fig. 2.10). These elements are usually characterized by high length/height and height/thickness ratios making them highly susceptible to the lateral torsional buckling phenomenon (analysed in chapter 3). In all-glazed structures (described ahead in section 2.2.3) glass fins also carry vertical loads to the foundations and behave as columns.

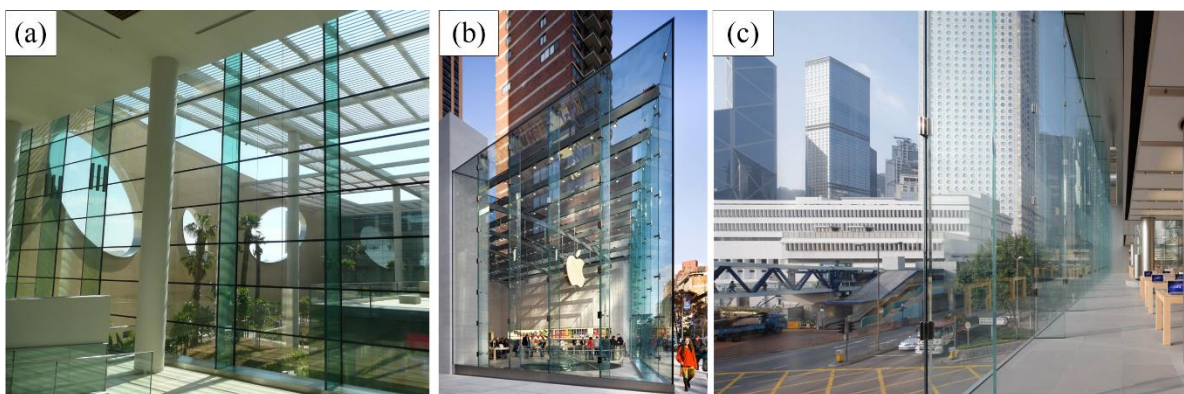


Fig. 2.10 - Glass facade with glass fins along its height at the (a) *Champalimaud Centre for the Unknown* and (b) and (c) at several Apple stores [2.30].

In spite of the psychological barrier (and existing technical concerns) caused by the brittle behaviour of glass, during recent years several projects have been developed where glass beams were applied to support loads from roofs/ceilings (Fig. 2.11-a and b), floors (Fig. 2.11-c) and stairs (Fig. 2.11-d).

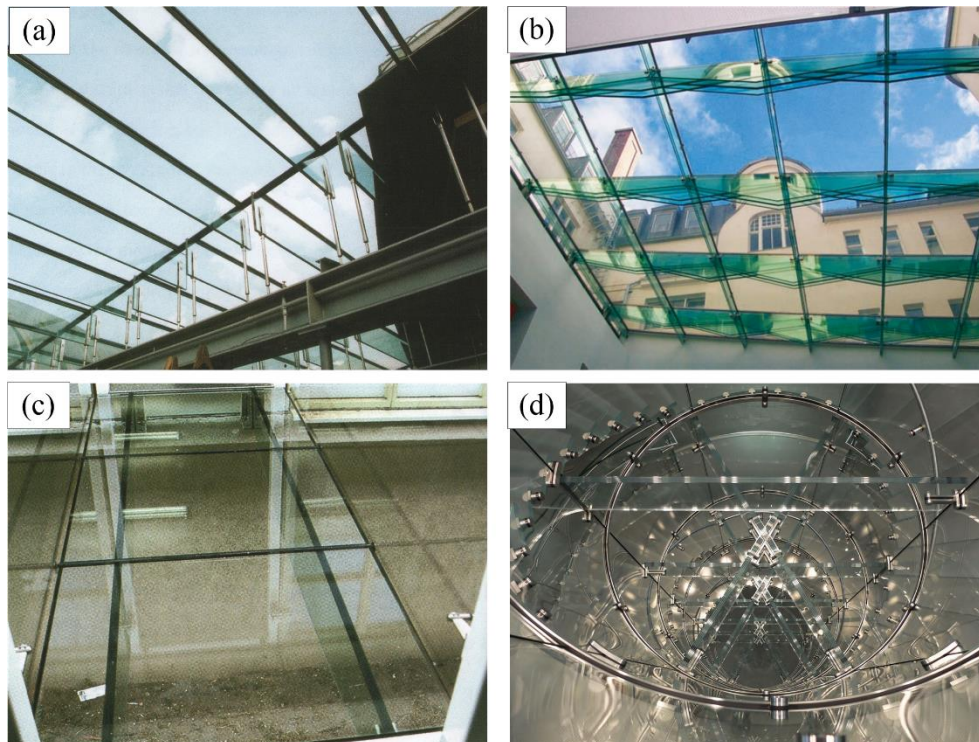


Fig. 2.11 – Examples of glass beam applications [2.1, 2.30, 2.31].

According to Louter [2.32], glass beams/fins can be divided as a function of their span configuration into:

- Continuous glass beams: beams that are made of one single (laminated) glass element that covers the full span length;
- Segmented or spliced glass beams: beams composed of multiple glass elements that are joined using metallic joints or adhesive connections.

Until the first years of this century, the length of continuous glass beams (Fig. 2.11-a) was restricted to the standard size production limit (lower than 6 m). Segmented and spliced glass beams were originally developed in order to cover greater span lengths. Two or more glass segments are joined together using, for example, bolted connections (Fig. 2.12-a and b) or simply by overlapping glass segments and joining them through lamination (Fig. 2.12-c and d). Regardless of the span configuration, most of the glass beams comprise three layers of glass (laminated), which, at least, the outer glass layers were heat strengthened. Fully tempered glass was applied whenever bolted connections were used due to the punctual stress concentrations caused by such joining method [2.31].

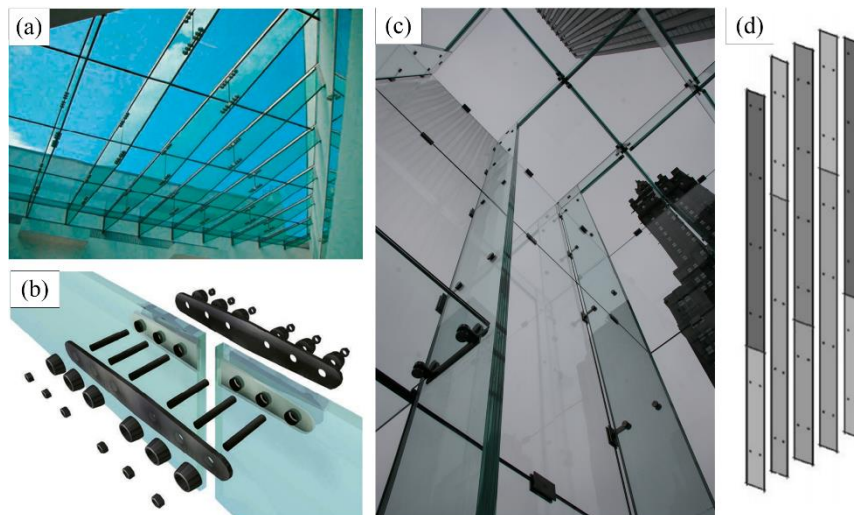


Fig. 2.12 – Examples of glass beams with (a) and (b) segmented-bolted configuration [2.31], and (c) and (d) spliced laminated configuration [2.31, 2.33, 2.34].

2.2.3 All-glazed structures

The ultimate achievement on glass architecture is the construction of all-glazed structures, i.e. glass structures that maximize the use of glass and reduce to the minimum the use of steel or other materials⁹. During the last years several projects have been developed aiming at the construction of glass structures that make use of glass in all load carrying components. Such structures are usually all-glazed staircases (Fig. 2.13-a), pedestrian bridges (Fig. 2.13-b) or full building envelopes (Fig. 2.13-c and d). In these structures the main load-bearing components (panels, beams/fins, columns and shear walls) can be found. The complexity of the load-carrying mechanism varies from project to project, as well as the elements size/length, number and structural behaviour.

The most recent developments at the production level (large-size elements, stiffer interlayers and adhesively bonded joints) and at the design level (namely with the dissemination of advanced numerical analysis) has allowed for a visible optimization of these structures, which have been continuously brought to a new extent, reducing more and more the presence of steel or non-glass secondary elements.

One of the most popular examples of those achievements was the refurbishment of the 5th Avenue Apple store glass entrance envelope. The first *glass cube* (Fig. 2.14-a), finished in 2006, was made of 106 glass elements, from vertical and horizontal glass panels to roof beams and facade fins, whose maximum size was restricted to the standard production size at the time (6 m) [2.36, 2.33]. Its updated version comprised only 35 glass elements, with a maximum size of 10 m [2.4] (Fig. 2.14-b). The application of stiffer interlayers allowed not only for the increase of the elements size, but also for the execution of embedded connections which also allowed for a substantial reduction of the metallic elements' visual impact.

⁹ The remaining non-glass elements are usually found at the support and connection elements.

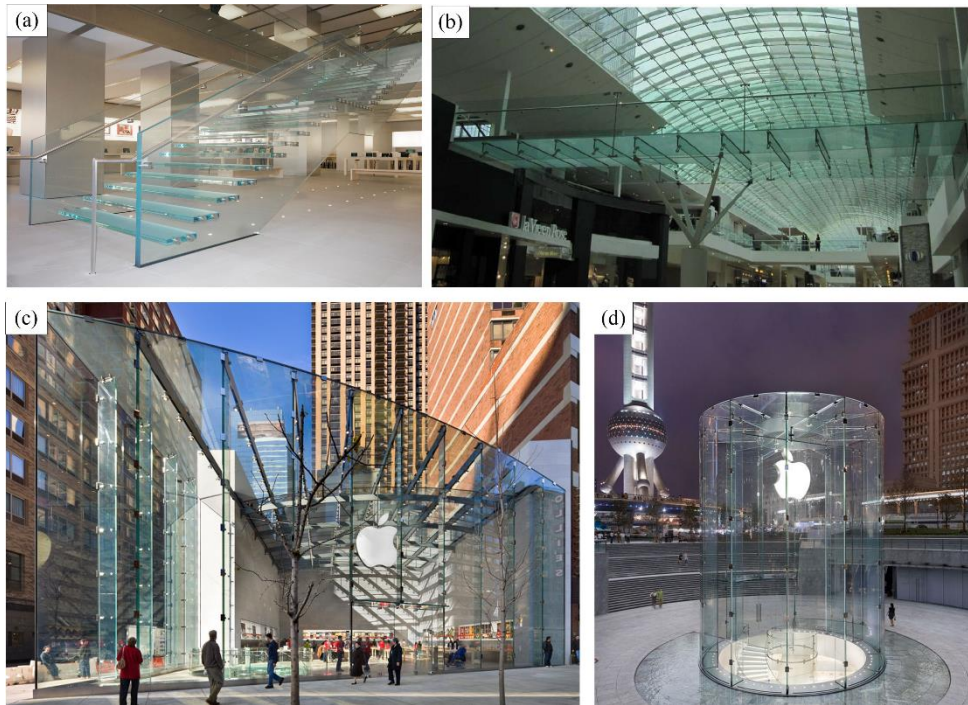


Fig. 2.13 – Examples of all-glass (a) staircase, (b) walkway and (c) and (d) building envelope [2.30, 2.35].

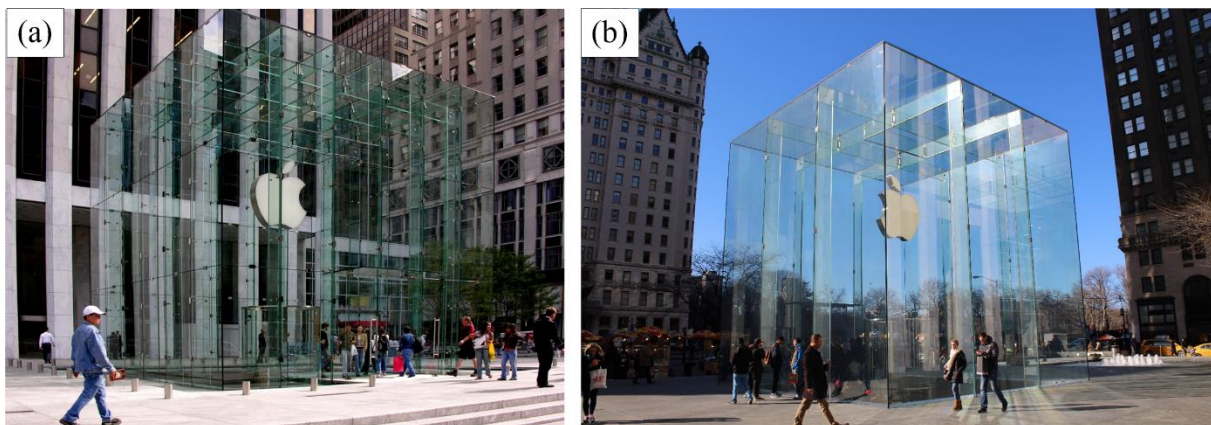


Fig. 2.14 - All-glazed building envelope at the 5th Avenue Apple Store in (a) 2006 (Glass cube v1.0) and (b) 2011 (Glass cube v2.0) [2.4, 2.33].

2.3 HYBRID GLASS ELEMENTS

2.3.1 Hybrid glass structures concept

In section 2.2 the main applications of glass as a load bearing material were presented, and the recent growing demand for larger and structurally relevant glass structures was highlighted. Producers have been answering to such call by providing larger glass elements and laminated glass elements with stiffer interlayers, more suitable for structural glass applications. Another interesting recent development was the introduction of adhesively bonded connections to a wider broad of forms and types (discussed ahead in section 2.4.2). Although relatively expensive, such solutions were able to answer most of the requirements set for glass in the range of structural applications.

In spite of the several innovations introduced, the (brittle) mechanical behaviour of glass still represents a major safety drawback for structural glass applications. In opposition to the mechanical behaviour of traditional materials used in construction, such as steel and reinforced concrete, glass presents a significantly unpredictable brittle behaviour, regardless of its type, form or assemblage. Once the glass element (fully) breaks, glass is unable to redistribute stresses (plasticity), thus it does not present any post-fracture (residual) strength. In order to overcome the aforementioned intrinsic limitations of glass and increase the safety of glass elements, the glass industry has made use of over-designing techniques, such as sacrificial glass panes and unnecessarily high glass thicknesses. Besides negative economic impacts, over-dimensioned laminated glass members neither overcome the fragile behaviour of glass, nor provide structural glass members with sufficient residual strength. In most of the situations, once all glass layers are broken, laminated glass members can barely withstand their own self-weight (Fig. 2.15), even on laminated assemblages with stiff interlayers¹⁰ [2.18, 2.20] (Fig. 2.15).

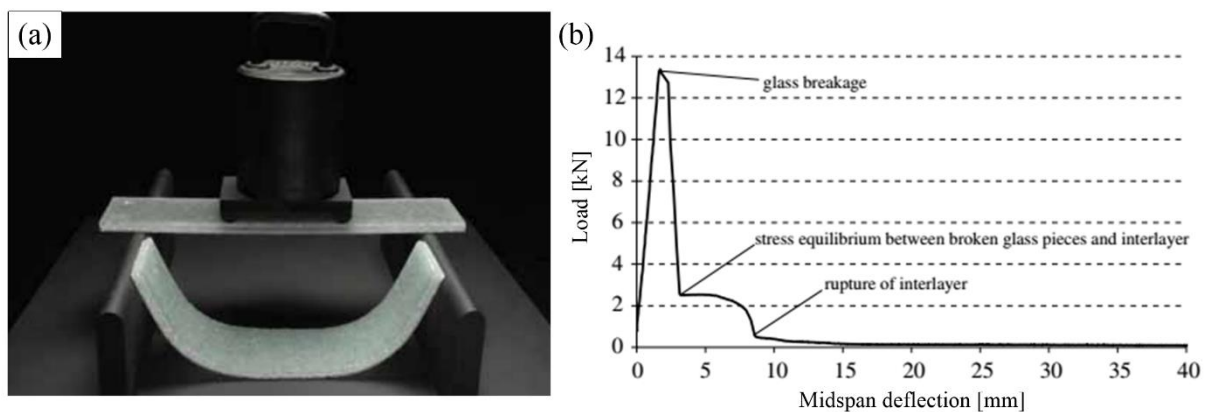


Fig. 2.15 – Structural behaviour of laminated glass members: (a) post-fracture performance of *laminated safety glass* and reinforced glass [2.37], and (b) illustrative flexural behaviour of SG-laminated glass beams under displacement control bending tests [2.18].

In order to overcome the aforementioned intrinsic limitations of (laminated) glass elements, a different approach has been pursued by several authors, which consists of joining glass panes to other structural materials in order to enhance the linear behaviour (prior to cracking) of glass elements, but mostly to obtain ductile (safe) failure modes. Several different structural materials have been tested (Fig. 2.16-a), namely stainless steel [2.32, 2.38–2.44], timber [2.45–2.50], reinforced concrete [2.51], steel [2.52, 2.53], carbon fibre reinforced polymers (CFRP) [2.54, 2.55], steel reinforced polymer (SRP) [2.56], and glass fibre reinforced polymers (GFRP) [2.57–2.62]. Many of these structures have been applied within the scope of real bearing structures, most of them as reinforced beams (Fig. 2.16-b).

The main objective of combining glass with other structural materials is to overcome the brittle behaviour of elements made exclusively of glass, even if they consist of laminated assemblages. The

¹⁰ Laminated glass structures, regardless of the number of glass plies or type of interlayer, present low residual strength, which requires specific safety measures [2.20].

structural concept of hybrid glass beams is equivalent to that of beams made of reinforced concrete: the main material, glass, which presents a fragile behaviour, is combined with other material that presents significantly higher tensile strength and in some cases (not in all concepts) ductile (plastic deformations) failure. Once glass cracks, the tensile stresses are transferred to the reinforcement, which, together with the compressive zone on glass, provides significant post-fracture residual strength and ductility due to the development of an internal load-carrying mechanism. This way, the initial brittle failure behaviour of the glass element is avoided and replaced by a progressive and safer failure mechanism. The glass element will exhibit signs and warnings indicating that total failure is imminent and, at the same time, it will withstand sufficient load allowing measures to be taken towards the safety of the occupants or even the integrity of the structure.

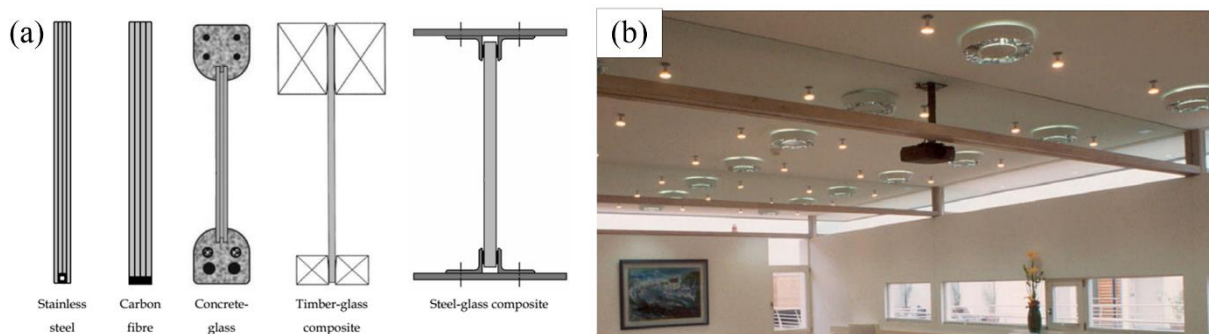


Fig. 2.16 – Hybrid glass members: (a) cross-section of several concepts of structural hybrid glass beams (not to scale) [2.63] and (b) timber-glass composite beam applied on the construction of a hotel [2.48].

The general flexural behaviour of hybrid glass beams can be divided into two stages (Fig. 2.17):

1. Linear elastic behaviour up to the moment of the appearance of the first crack;
2. Non-linear stage characterized by a progressive loss of stiffness due to the increase of cracks on the glass element(s).

The post-fracture response (second stage) can be either ductile or pseudo-ductile (Fig. 2.17) if, respectively, the reinforcement material has the capability of developing plastic deformations (e.g. steel alloys) or not (e.g. FRP). In either way, the post-fracture capacity of hybrid glass systems relies on the existence of cross-sectional redundancy, which is responsible for the existence of the abovementioned internal tie mechanism.

In the following sections a brief description of selected studies on the structural behaviour of hybrid glass elements developed in the last years is given. A broad and detailed description of these selected studies and several other investigations can be found in the literature reviews of Louter [2.63] and Martens *et al.* [2.64, 2.65]. In those studies, hybrid glass beams were divided in two groups according to the amount of reinforcing/strengthening material applied: beams whose cross-section presents reinforcement areas higher than 25% of the total cross-section area are referred to as *composite glass beams*, while all the others are referred to as *reinforced/post-tensioned glass beams*. In this study such

classification was not followed, and the terms *hybrid*, *composite* and *reinforced* are indistinctively applied, regardless of the material, reinforcement area or any other parameter.

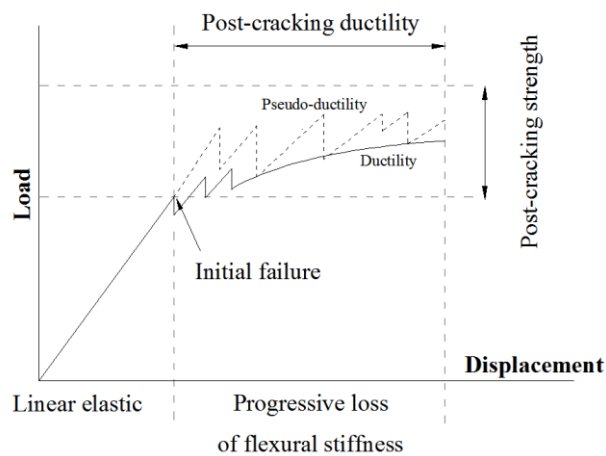


Fig. 2.17 – General behaviour of hybrid glass beams.

2.3.2 Glass-stainless steel hybrid beams

One of the largest studies made on the field of hybrid glass beams was developed by researchers from Delft University and the École Polytechnique Fédérale de Lausanne and comprise the combination of glass with stainless steel profiles. Comprehensive experimental campaigns have been carried out [2.32, 2.38–2.44] to study the influence on the structural response of the glass-stainless steel reinforced beams of different parameters, such as the cross-section geometry, the reinforcement geometry and percentage, the beam size, the glass type, the type of adhesive, the bond system, the environmental agents (humidity, temperature) and the load duration.

The feasibility of the system has been proved for different cross-section configurations (U and T-shape, box shape or rectangular full section - Fig. 2.18-a) and on beams up to 7200 mm long [2.40, 2.63]. The longest beams were produced and tested before the generalization (and the corresponding cost reduction) of large-size laminated glass beams. Therefore, spans beyond the dimensional limit of 6000 mm were built by overlapping several glass layers, both in length and in thickness (Fig. 2.18-b). Likewise, the most complex geometries were obtained through the bonding of successive glass panes (laminated or not) by means of common use interlayers or transparent structural adhesives. In any case, all beams were built without using any metal-to-glass joints. Box and T-cross-sections have the advantage of being less prone to the lateral-torsional buckling phenomenon, which was found to occur in an advanced cracking stage on slender full-section beams [2.25].

The effect of the reinforcement geometry (bonded perimeter) was assessed in the study of Louter *et al.* [2.41]. A similar reinforcement percentage was applied in three different configurations, whose main difference was the number of bonded faces (cross-sectional adhesively bonded perimeter - Fig. 2.19-a). The efficiency of the reinforcement configuration was assessed by the extension of the post-fracture

ductility. All specimens were able to keep their integrity after the appearance of the first crack even though with different post-fracture performances. On the one hand, specimens with one face bonded (1F) presented a premature failure due to the detachment of the reinforcement profile. On the other hand, specimens with two (2F) and three (3F) faces bonded were able to mobilize higher post-fracture ductility due to the increase of number of bonded faces. Specimens 3F were the ones which consistently provided the highest levels of post-fracture ductility and presented an explosive failure without any visible detachment of the reinforcement [2.42]. Despite the considerable enhanced performance of specimens 3F, their cross-section complexity requires more labour and quality control during the production process due to the inherent production defects and tolerances, which are easier to control when the cross-section presents higher simplicity. In spite of the interesting results regarding the importance of the bonded area, no analytical or numerical studies were carried out in order to further develop the knowledge about the bond behaviour between glass and stainless steel.

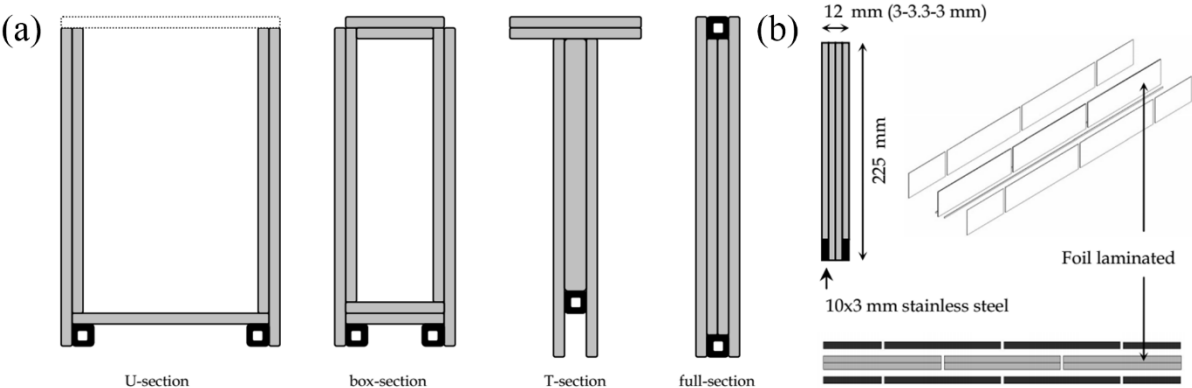


Fig. 2.18 – Glass-stainless steel reinforced glass beams developed at Delft University of Technology: (a) different cross-sections studied and (b) segmentation scheme used for long-span beams [2.63].

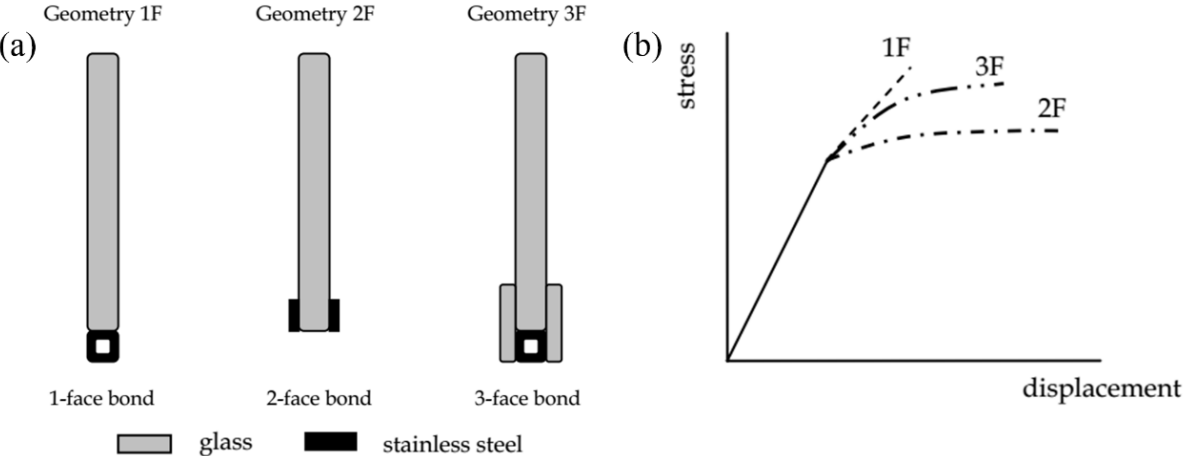


Fig. 2.19 – Glass-stainless steel reinforced glass beams at Delft University of Technology: (a) reinforcement configurations tested, and (b) corresponding effects on the flexural response of glass-stainless steel reinforced beams [2.41].

The effects of reinforcement percentage, glass type and beam size were assessed in the works of Louter [2.32] and Louter *et al.* [2.43]. The results obtained proved that these parameters have different effects on the structural response of the beams. On the one hand, it was observed that the post-fracture residual strength increases with the increase of reinforcement percentage (Fig. 2.20-a) while, on the other hand, the increase of the glass tempering, despite increasing the load value that causes the initial glass failure, decreases significantly the post-fracture robustness (both post-fracture strength and ductility) of the reinforced beam: the crack pattern with higher fragmentation of tempered glass (with respect to annealed float glass) does not provide sufficient integrity in the cracked stage (Fig. 2.20-b). Finally, from the tests on large-size specimens it was concluded that size has minor effects on the structural behaviour of reinforced glass beams and, for the tested concept, no instability phenomena were observed.

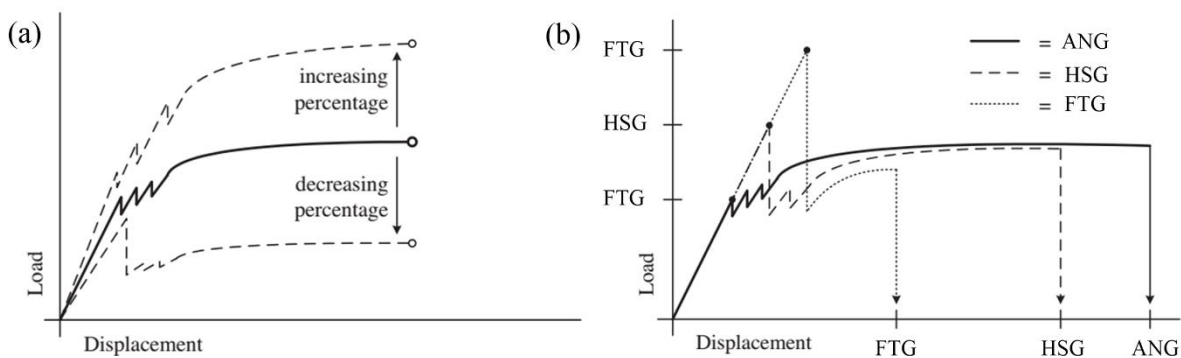


Fig. 2.20 - Illustrative behaviour of the structural effects of (a) glass type and (b) reinforcement percentage [2.43].

In most previous studies, the analysis of the structural behaviour of hybrid glass beams assumes that the connection between the two materials is assured at all stages of the flexural response. Therefore, the mechanical properties of the adhesively bonded joints are of the utmost importance for the efficiency of the system. Several different studies have been performed in order to assess the effects of different adhesives on the overall flexural response of the beams. Among the adhesives tested, structural adhesives of polymeric nature stand out, such as acrylic or epoxy [2.41], as well as the interlayers used on the production of laminated glass members. Each adhesive presents its own advantages and disadvantages and these need to be duly considered in the selection process. A final concept was achieved using the interlayer SentryGlas. Its superior material properties guarantee an efficient stress transfer between both materials and the glass industry is already familiarized with it.

Besides the type of the adhesive, also the effects of anchoring the stainless steel reinforcement at the beams ends was investigated [2.42]. This constructive detail (Fig. 2.21) aimed at maintaining the residual capacity even in conditions when the adhesive joint no longer provides enough stress transfer or after a premature detachment of the reinforcement due to unpredictable actions, such as fire. In those situations, the anchorage was able to provide extra redundancy to the structural concept, since it was possible to mobilize tensile stresses on the reinforcement making use of the so called *tie-effect* [2.66].

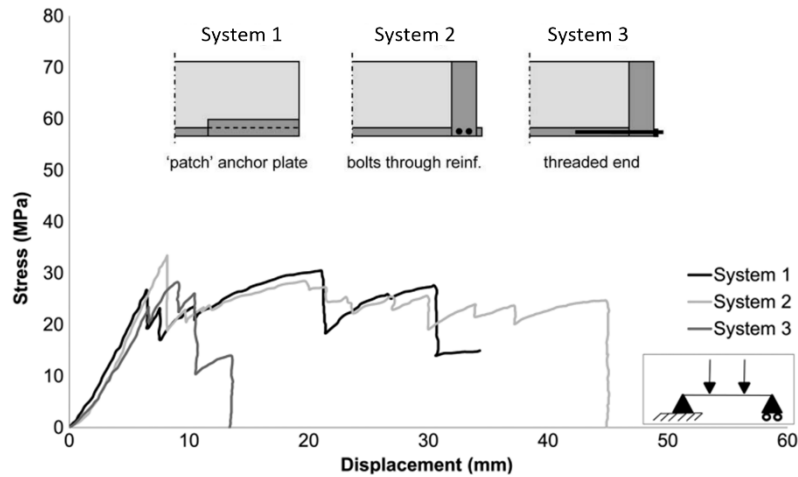


Fig. 2.21 - Flexural results on glass-stainless hybrid steel beams with 3 different types of anchorages at the beams end [2.64].

Finally, within this project, small experimental campaigns have been carried out to assess the effects of environmental agents and load duration on the structural response of glass-stainless steel reinforced beams [2.32, 2.44]. The attention was focused on the influence of those parameters on the structural behaviour of the adhesively bonded joints, which have to withstand the stress transfer under different environmental conditions and for a significant load period. In addition, it is known that material properties of polymeric adhesives are time and temperature dependent. The results obtained showed that temperatures up to 60 °C have minor effects on the structural response of the glass-stainless steel reinforced beams (with respect to similar beams tested at room temperature). However, at high temperatures beams failure occurred due to the debonding of the stainless steel profile. The long-term experiments allowed to conclude that the robustness of the beam is not affected within the load-period of 72 h after the initial failure of glass.

In summary, the comprehensive experimental campaigns carried out proved the feasibility of this hybrid structural system with alternative configurations, and the final concept presents promising results. Nevertheless, for now, few examples can be found of its applicability on real structures [2.67].

2.3.3 Glass-timber hybrid glass beams

Several researchers have been studying the structural behaviour of hybrid systems combining glass with timber rafters [2.45–2.49]. Wood is chosen mainly due to its architectural advantages (current trends in architecture have elected wood as a symbol of environmentally friendly and sustainable construction), but also due to its physical and mechanical properties, including its thermal properties and tensile behaviour [2.49].

In the studies of Hamm [2.45] and Kreher [2.46] extensive experimental campaigns were performed on I-section beams made with a transparent glass web (single pane) embedded in between timber profiles (Fig. 2.16). The feasibility of the system was proved for different glass thicknesses, reinforcement sizes

and types of glass (ANG, HSG and FTG). The investigated concept showed improved post-fracture performance on beams with length up to 2000 mm and was finally applied in the construction of 6000 mm long beams in the Palafitte Hotel in Switzerland [2.48] (Fig. 2.16-b). The authors highlighted that such concept is aesthetically advantageous (transparent beams combined with a noble material) and is also able to comply the demanding requirements of the most recent standards, namely those regarding the structural performance under fire.

The hybrid concept of glass reinforced with timber rafters was also investigated in the experimental studies of Cruz and Pequeno [2.49, 2.50]. In the former study, the feasibility of the glass-wood hybrid system was further extended to laminated glass beams (Fig. 2.22-a), while in the latter the authors applied the concept to glass panels which were linearly supported on timber beams using adhesive bonding (Fig. 2.22-b). Glass-timber beams were tested on a wider range of cross-section sizes and shapes (I-section and rectangular), beam lengths (from 650 mm to 3200 mm) and adhesives (silicone, polymer and polyurethane). In both studies, the authors proved the ability of the concept to provide transparent glass structures with post-fracture resistance and safe failure mechanisms. In addition, the authors also carried out an extensive experimental campaign to study the effects of temperature and moisture on the shear behaviour provided by the glass-timber adhesively bonded joint [2.68] (Fig. 2.23).

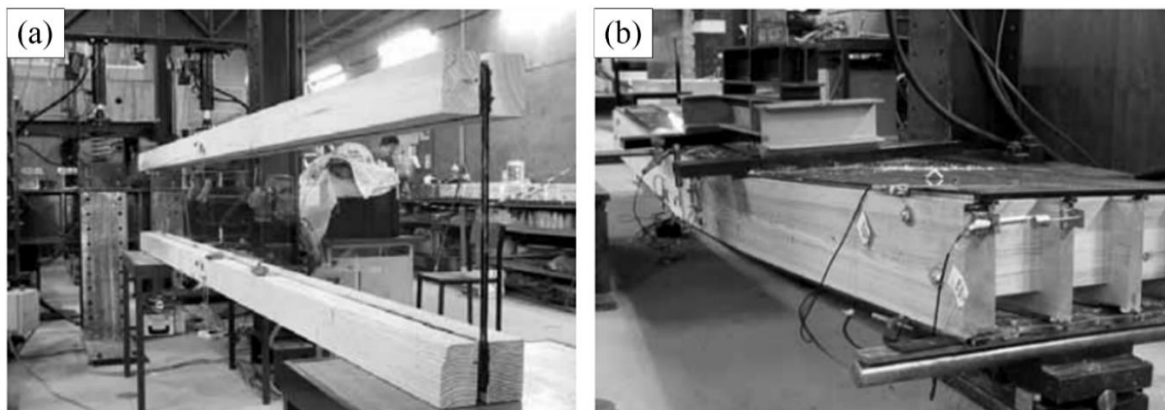


Fig. 2.22 – Glass-timber hybrid beams: flexural tests on (a) beams and (b) panels carried out by Cruz and Pequeno [2.49, 2.50].

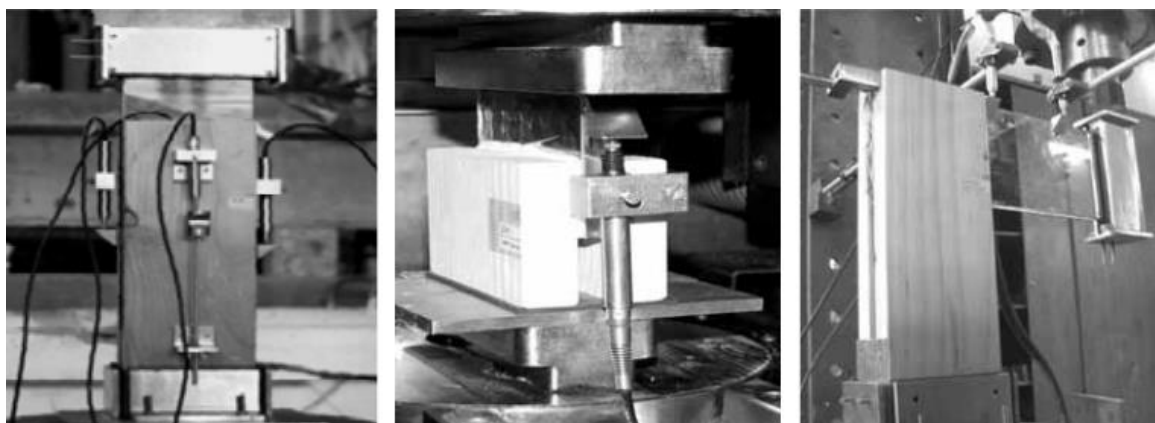


Fig. 2.23 – Glass-timber composite beams: configurations of the shear tests on adhesively bonded joints [2.68].

More recently, the post-cracking performance of I-section adhesively bonded timber-glass hybrid beams was investigated by Kozłowski [2.47]. The author performed flexural tests on small and full-scale hybrid glass beams (from 1800 to 4800 mm of length), made with different types of glass (annealed and heat strengthened) and bonded with different adhesives, which covered a wide range of elastic modulus (from 1-3 MPa to 1500 MPa). The results of the experimental campaign were compared with the results from 3D numerical models, developed using ABAQUS Explicit and brittle cracking material model. The study confirmed the feasibility of the hybrid glass system on providing safe failure mechanisms using a wide range of adhesives. However, specimens using heat strengthened glass failed to present post-fracture residual strength. The numerical study proved the applicability of the corresponding numerical tool on simulating the flexural behaviour of the hybrid glass system and also that the load-deflection response is unaffected by the finite element's geometry, size and glass fracture energy (tested on range from 3 to 8 N/m).

2.3.4 Glass-reinforced concrete hybrid beams

The concept of combining glass with reinforced concrete was investigated by Freytag [2.51], who performed experimental tests on I-section hybrid beams with a total length of 8100 mm. The web consisted of 3-layer laminated panels made of fully tempered glass layers, while the flanges were made of reinforced or pre-stressed concrete poured into the glass. The total length of the beam was covered using the segmentation principle. The glass surface in contact with the concrete was pre-treated and especially roughened in order to assure the adhesion between both materials.

In addition to the experimental work, Freytag [2.51] also presented an analytical approach, based on a *struts and ties* model, to design the corresponding hybrid system. The complex post-fracture bearing system was explained based on the hypothesis that the transmission of shear stresses occurs in three ways: (i) adhesion, (ii) interlocking, and (iii) friction.



Fig. 2.24 – Glass-reinforced concrete hybrid beams: (a) flexural tests performed by Freytag and (b) analytical model considered [2.51].

2.3.5 Glass-steel hybrid beam

The combination of glass with steel was studied by Wellershoff and Sedlacek [2.52] and, within the Innoglast project, by several researchers [2.53]. Most of the studies were similar to the ones already presented in the aforementioned hybrid concepts and comprised: (i) shear tests on adhesively bonded glass-steel joints, to choose a suitable adhesive to bond the steel profiles to glass; (ii) investigations on different connections types, and (iii) flexural and stability tests on prototypes of I-section glass-steel hybrid beams. In these beams steel profiles, acting as flanges, were bonded to a glass beam, comprising a transparent web (Fig. 2.16). The hybrid concept was developed not just to provide enhanced post-fracture behaviour with respect to laminated glass beams, but also to increase the LTB resistance of glass fins [2.53].

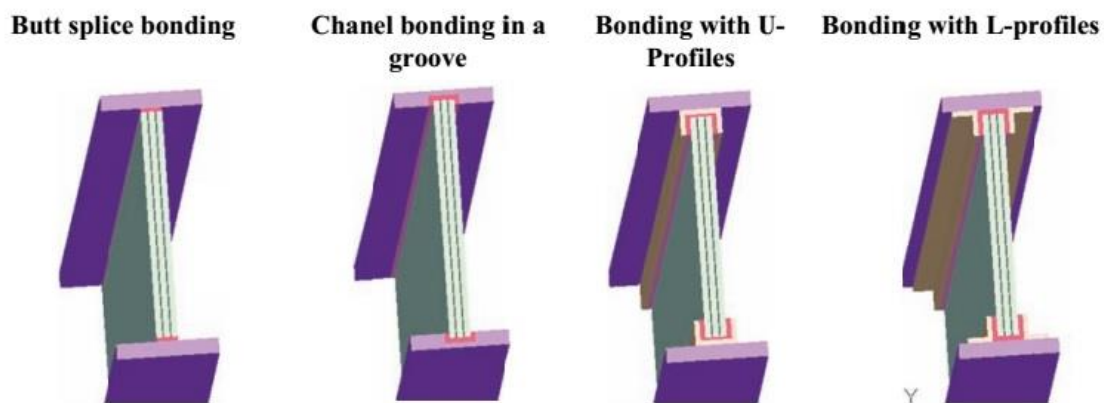


Fig. 2.25 – Glass-steel composite beams: connections types studied within the project *Innoglast* [2.53].

2.3.6 Glass-CFRP hybrid beams

One of the first applications in construction of hybrid glass beams was developed in Italy, in the rehabilitation of a roof of a church from the XIII century [2.54] (Fig. 2.26). Currently, FRP profiles and, in particular, CFRP laminates, are being widely applied in the repair and strengthening of both building and bridge structures. Such materials are adopted as an alternative to traditional construction materials (e.g. steel and reinforced concrete), mostly due to their enhanced material and mechanical properties (low weight, high Young's modulus and tensile strength), ease of application and minimum visual impact in the rehabilitation of existing concrete and masonry structures. Besides the safe failure mechanism achieved due to the cross-sectional redundancy (similarly to the other hybrid systems detailed in the previous sections), the high Young's modulus [2.69] of the CFRP laminates is expected to reduce the tensile stresses in the glass beams on the linear stage, i.e. before glass breakage. To prove the feasibility of the hybrid structural concept, a short experimental campaign on prototype beams of 1100 mm long was conducted.

Later, in the work of Louter [2.55], CFRP flat rods were embedded in 2-layer SG-laminated glass beams in order to increase their post-fracture behaviour. The results were highly promising and high levels of post-fracture strength were achieved, using a concept that presents attractive levels of transparency (Fig. 2.27).

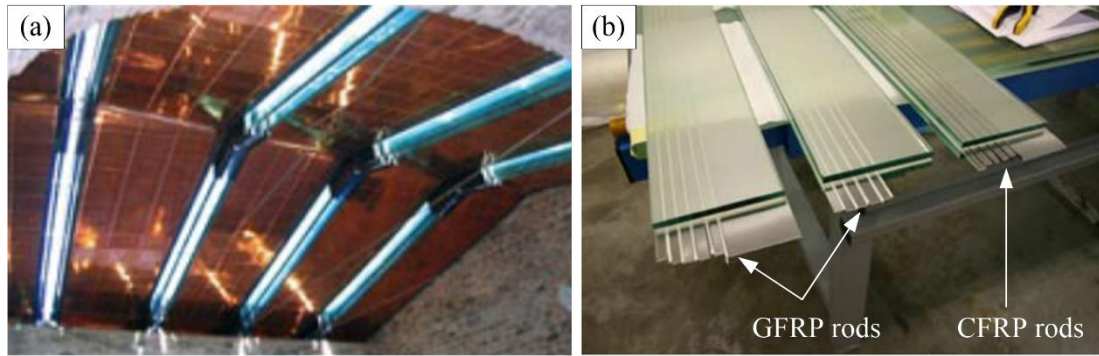


Fig. 2.26 – Glass-CFRP hybrid beams developed by (a) Palumbo [2.54] and (b) developed by Louter [2.55].



Fig. 2.27 - Reinforced glass beams with embedded (top) CFRP and (bottom) GFRP rods [2.55].

2.3.7 Glass-SRP hybrid beams

Few works have been performed on hybrid glass beams made of glass and profiles of steel reinforced polymer (SRP). In fact, due to the high cost of its carbon counterparts, SRP has been recently applied as a substitute of CFRP on strengthening interventions. In the work of Speranzini and Agnetti [2.56], a concept of a glass beam reinforced with SRP profiles made of ultra-high tensile strength steel (UHTSS) and stainless steel fibres was presented. The flexural tests made on 48 specimens proved the ability of the structural system to provide glass beams with post-fracture residual strength, namely on beams reinforced with UHTSS fibres. Due to their high Young's modulus, the steel based fibres are active since the linear stage of the beams flexural response, which also allows to achieve significant improvements in terms of glass breakage loads. Besides the experimental study, an analytical methodology for the design of glass-SRP hybrid beams was also provided.

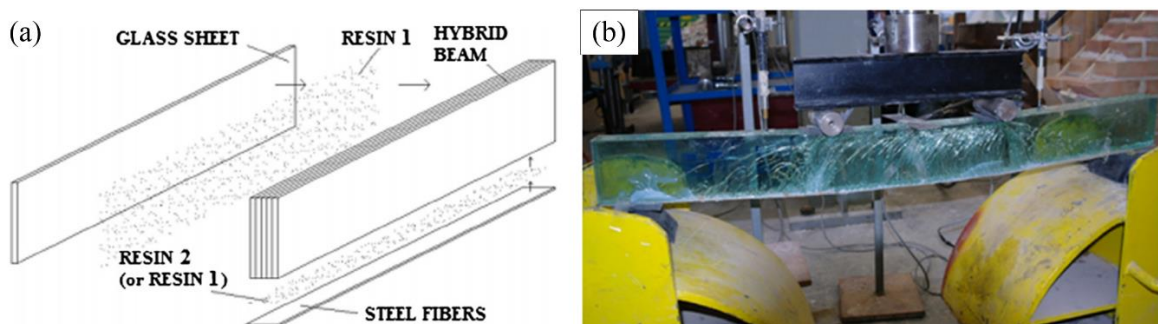


Fig. 2.28 – Glass-SRP hybrid beams: (a) prototype illustration and (b) flexural experiments.

2.3.8 Glass-GFRP hybrid beams

As for CFRP laminates, in the last two decades GFRP profiles were increasingly applied in building [2.70] and bridge [2.71, 2.72] construction. This material stands out from other construction materials due to its high strength/weight and stiffness/weight ratios and its high durability. Compared to glass, GFRP profiles present a similar mechanical behaviour (linear elastic with brittle failure), but exhibit much higher strength (the tensile strength in the longitudinal direction ranges from 200 to 500 MPa [2.73]). Despite its considerably higher strength, GFRP presents a relatively low Young's modulus in comparison with steel, CFRP, or even glass: the Young's modulus in the longitudinal direction ranges from 20 to 40 GPa [2.73], resulting in high deformation capacity. Such feature can be used in structural beams as a sign of imminent failure. Furthermore, GFRP profiles can assume a variety of forms and shapes, as well as different colours and finishing (including semi-transparent), thus opening a wide range of architectural possibilities.

GFRP profiles have been used to reinforce glass beams in two different ways: (i) embedded on the laminated glass assemblage (*cf.* Fig. 2.27 and Fig. 2.29-a), or (ii) adhesively bonded to glass beams (Fig. 2.29-b).

In the works of Louter [2.32] and Louter *et al.* [2.58], GFRP round and flat rods were embedded in 2-layer SG-laminated glass beams in order to increase the post-fracture behaviour of laminated glass beams. The results were very promising, namely on beams reinforced with flat rods, which presented the highest reinforcement-adhesive-glass contact area, crucial for an effective stress transfer. In the studies of Speranzini [2.59–2.61], flexural tests were performed on (i) glass beams reinforced with embedded GFRP sheets and (ii) glass beams coupled with U-shaped GFRP pultruded profiles, the latter tested both with annealed float glass and tempered glass. The results were also very promising and a pseudo-ductile failure mode was reported for all beam types.

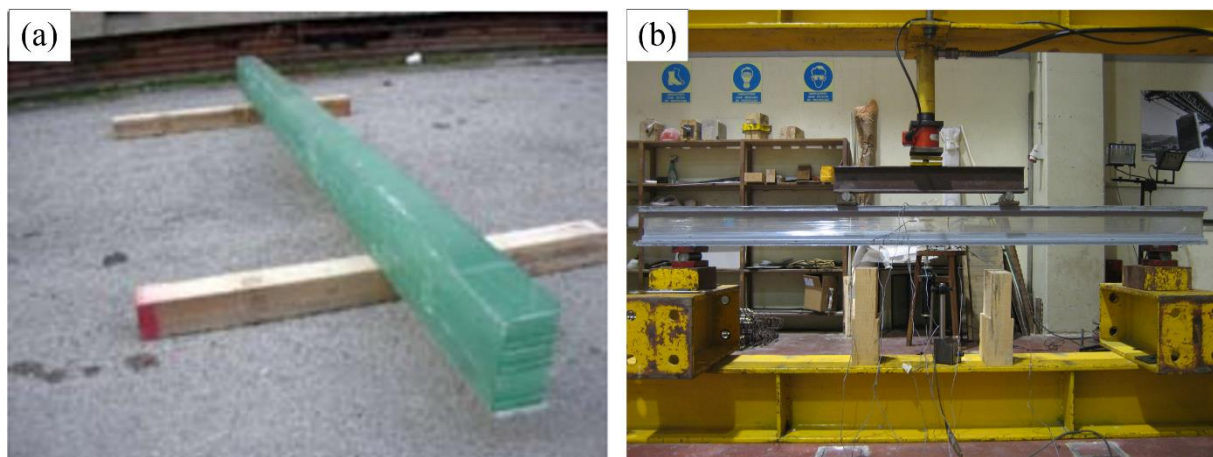


Fig. 2.29 - Glass-GFRP composite glass beams tested by (a) Speranzini [2.60] and (b) Valarinho [2.74].

Finally, the author of this thesis has also performed preliminary flexural tests on glass beams reinforced with GFRP pultruded profiles by means of structural adhesives [2.62] (briefly described in chapter 1, section 1.1.1). Two different cross-sections were tested and the influence of different

adhesives was assessed. The results obtained were also highly promising and partly motivated for the development of this thesis.

2.4 OTHER FIELDS OF RESEARCH AND DEVELOPMENT

The application of glass as a load-bearing material is still recent. As discussed above, the main concerns about its structural application are related with glass brittleness, which requires special design options in order to comply with the requirements and general philosophy of the most recent design standards [2.20]. The inability of glass to redistribute stresses or present plastic deformations requires accurate knowledge about the glass strength and about the local stress distribution and concentrations, this aspect being particularly relevant for the design of connections. Therefore, several authors have been developing comprehensive studies in order to clarify the fracture mechanics of glass, namely how environmental agents as well as natural and human ageing actions affect the glass strength. New fields of application have also been tested for interlayer materials used on laminated glass members, for which scarce information is available regarding its long-term behaviour under multiple ageing agents. The application of structural adhesively bonded connections on (hybrid) glass members is also increasing. However, there is a lack of information about their behaviour, range of applicability and, foremost, they are yet to be covered by the most recent guidelines and codes. The recent widespread use of thin chemically tempered glass in electronics has also attracted the attention of architects and of the building industry, which have high expectations on the potential applications of this type of glass. Finally, with the increasing demand for structural glass applications, new possibilities of application have been developed for curved glass, but requiring also further studies and developments. In summary, in the last decade several different topics concerned with the structural glass research field have arisen. In the next sections, the research recently performed on those selected topics is briefly described.

2.4.1 Glass and interlayers mechanical properties and durability

Due to the architectural trend of using glass with structural functions there was the need of determining with high accuracy the actual value of glass strength, one of the most important engineering parameters of any material. During the last years several studies have addressed this problem and assessed the effects of different parameters on the strength of glass elements, aiming at establishing a sufficiently accurate/reliable value for glass strength.

One of the factors whose effect on glass strength still remains unclear is ageing. Several authors have investigated the effects of artificial ageing (damage) on glass panels. In these studies, artificial damage was induced on the glass surface, usually through mechanical abrasion. Different erosive methods have been tested on the glass surface, such as sand trickling [2.75, 2.76], sandblasting [2.77] and scratch indenters [2.78, 2.79, 2.80], in order to simulate service life damage situations. The first method simulates the impact of flying objects, while the last one simulates the exposed risk of flaws during glass

service life. As expected, the results of artificial ageing have shown a significant reduction of glass strength. However, the glass strength models established in those studies are yet to be validated, mostly due to the lack of data on naturally aged glass, which is needed to correlate and eventually validate the results obtained from artificial ageing methods [2.79].

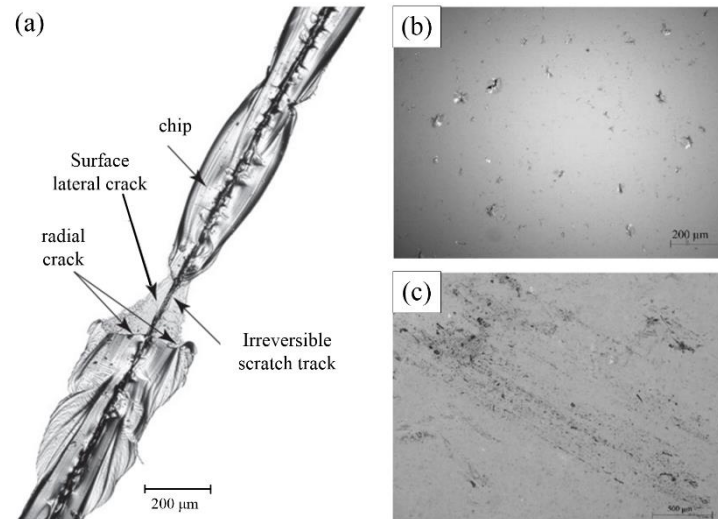


Fig. 2.30 – Damaged in glass surface (a) scratch induced [2.78], (b) sand abraded [2.79] and (c) surface naturally aged/exposed to outdoor conditions.

Another open discussion is concerned with the effects of the different existing edge finishing treatments on the edge strength of glass elements. For now, despite the extensive literature available (e.g. [2.81, 2.82]), a comprehensive model that accurately predicts the edge strength of any type of edge finishing is yet to be established.

In addition to the studies about the influence of different factors on glass strength, there is still an open discussion about the applicability of the Weibull distribution to model annealed float glass fracture data [2.12, 2.83]. New technology is also being developed aiming at the determination of the glass strength using non-destructive methods, such as non-linear ultrasonic techniques [2.84]. Such techniques could be used to detect defected glass elements and avoid their premature failure not only at the production level, but also during maintenance operations on glass structures.

New structural roles have been assigned to laminated glass elements. Such applications require extensive research to characterize comprehensively and accurately the mechanical behaviour of both glass and interlayers materials, which work together as a composite element. For now, the DMA technique seems to have been accepted as a sufficiently accurate method to determine the mechanical properties of interlayers for the range of environmental conditions (temperature) likely to be found in building applications. Ongoing research on the mechanical properties of interlayers revolves around the effects of long-term actions, namely the effects of ageing and of environmental agents; in this domain the existing literature is still scarce [2.79, 2.85–2.87].

2.4.2 Adhesively bonded connections

During recent years, the use of adhesively bonded joints or fixings has increased in structural civil engineering applications in general, and in structural glass applications in particular. The development of high performance structural silicones, adhesives/resins or other viscous polymers with good adherence to glass has been a major contribution to such development. Adhesive connections are advantageous since they allow for (more) uniform stress distribution along the bonded area, provided that the joint's structural properties are designed to guarantee so¹¹. Several successful examples have showed the potential use of glass-to-glass and glass-to-metal (or other material) adhesively bonded joints (Fig. 2.31). However, for now, the information in the literature about the structural behaviour of adhesively bonded connections is scarce.

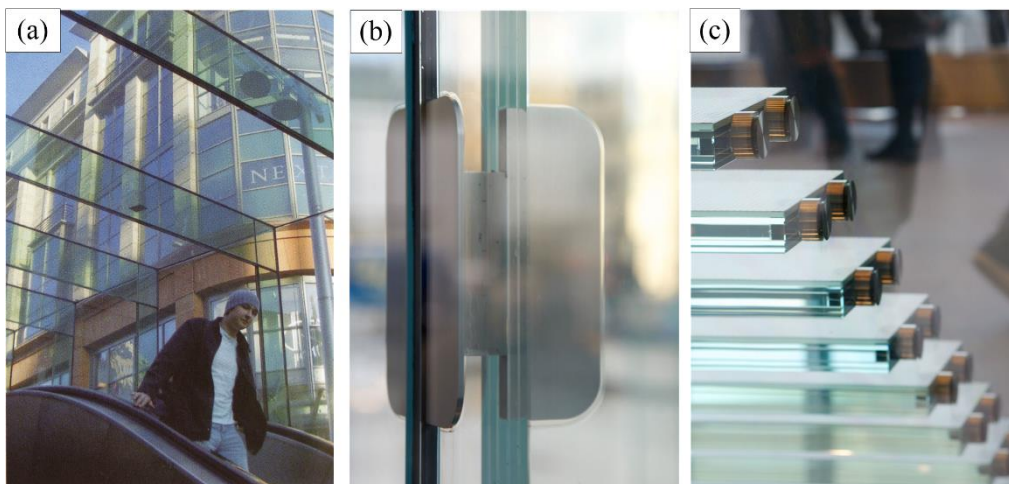


Fig. 2.31 - Adhesively bonded (a) glass-to-glass and embedded (b) linear and (c) pointed connections [2.30, 2.31].

Structural silicones and adhesives/resins have been widely applied in hybrid glass systems (*cf.* section 2.3) due to their versatility and enhanced structural performance. Different experimental studies have been developed aiming at the determination (i) of the viscoelastic behaviour of different types of adhesives and (ii) of their performance under different load, environmental conditions and surface treatments [2.88–2.94]. The major difficulties encountered in those studies stem from the high variety of design options, either in terms of adhesives available in the market or joint geometries. Such variety makes it difficult to define the most adequate adhesive properties for a given structural application. Moreover, widespread codes, standards and guidelines that could be used as reference and tools for design are yet to be published.

Embedded connections (or laminated adhesive connections) are one of the most recent examples of the application of adhesively bonded connections (Fig. 2.31-b and c). Such connections have been introduced together with the widespread use of stiff interlayers, whose superior mechanical properties

¹¹ Indeed, the stress distribution is function of the mechanical properties of the adhesive and adherends and also of the joint geometry.

allow for higher load/stress transfer [2.95]. With respect to common linear and point fixed connections, embedded connections can be cost saving since they are applied during the lamination process and without any hole or drilling on the glass panes. Several researchers have recently presented results of experimental and numerical investigations addressing the effects of different geometrical parameters [2.96], loading time, temperature and environmental agents on the structural behaviour of embedded connections [2.95] (Fig. 2.32). Ongoing research is addressing the stress distributions on linear and point fixed embedded connections under different load types and exploring the present possibilities of advanced numerical simulation tools.

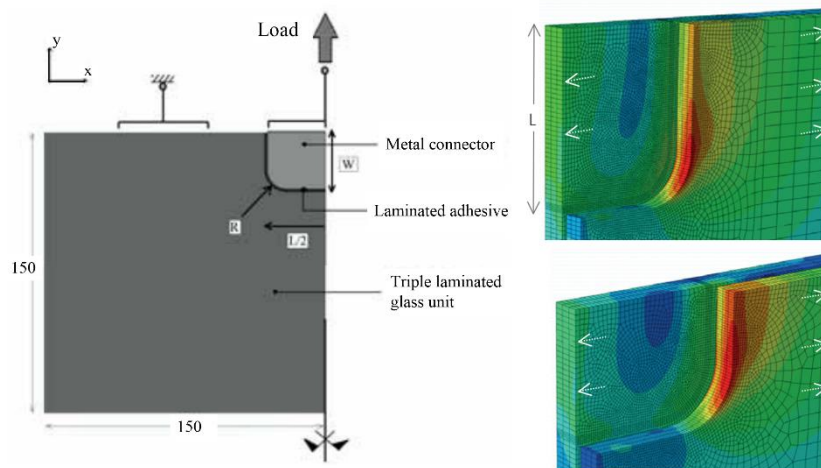


Fig. 2.32 - Numerical analysis of the stress distribution of linear embedded connection [2.96].

2.4.3 Thin chemical tempered glass

One of the most relevant innovations that can be anticipated concerning the structural use of glass in architectural and building applications is the introduction of the new generation of thin chemically tempered glass, which enables tensile strengths higher than 800 MPa [2.14]. For now, thin glasses (thickness below 2 mm [2.97]) were used mainly for displays and touch screens (e.g. GorillaGlas [2.98]), and their application in architecture is reduced to small balustrades and glazed barriers [2.98].

The application of thin glass could bring noticeable savings in terms of weight and raw material, together with indirect savings in transportation and application. However, in addition to the reduced size and geometry (the maximum size of a GorillaGlass sheets announced by Corning is 1390 mm × 1270 mm [2.98]), one must bear in mind that structural systems made with thin and super thin glasses will necessarily present low structural stiffness. This can affect their structural potential, either on systems made exclusively of thin glass or on composite glass systems that combine thin glass with standard float glass. Therefore, the existing solutions of glass shapes and systems must be duly adapted in order to incorporate such material and take full advantage of its potential.

For now, the major challenges for the structural application of thin glasses rely on the assessment of their strength. For instance, the small deformation theory is not applicable; standard test methods need to be adapted ([2.98–2.100]) and the development of connections (due to their reduced thickness, such glasses only allow for adhesively bonded connections [2.101]).

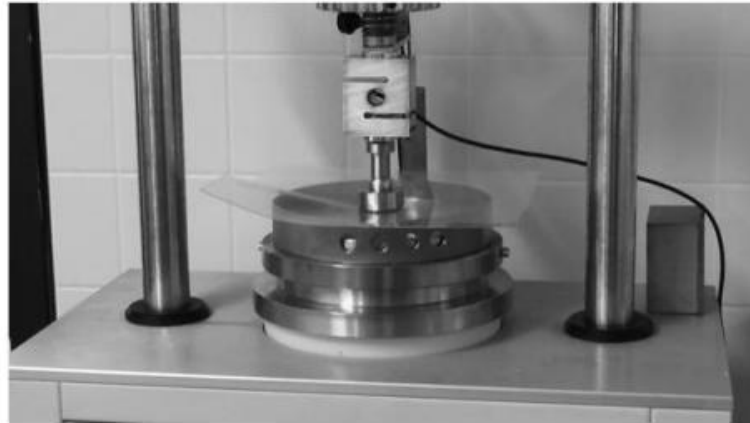


Fig. 2.33 – Ring test used for the determination of the tensile strength of a thin glass sample [2.100].

2.4.4 Curved glass

Modern architectural design is also increasingly requiring the use of curved glass. Several examples can be found on free-form glass skins, whose geometrical complexity can be filled using either small quadrangular or triangular glass panes (method used on the built greenhouses of the 19th century [2.102]), or by adopting complex glass shapes which often revolve around curved/bent glass shapes (Fig. 2.34) [2.103]. Besides enabling complex architectural shapes and being visually appealing, curved glass provides structural advantages with respect to its flat counterparts: when used in structural glazing applications curved glass offers higher stiffness and possesses enhanced load resistance [2.104].



Fig. 2.34 – Cold bent laminated glass panels applied in the Strasbourg train station [2.103].

Curved glass shapes can be achieved either by using hot or cold bending process methods. The former is the conventional method and the oldest technique, while the latter is a relatively recent alternative that not only can be cost-effective (if different curvatures are required), but also provides enhanced optical

qualities in comparison with traditional hot bending processes [2.104]. The challenges in the field of cold-bent glass are associated with the assessment of its bending behaviour and structural stability performance (Fig. 2.35-a) and the evaluation of the optical quality of the curved plates (Fig. 2.35-b) [2.105, 2.106].

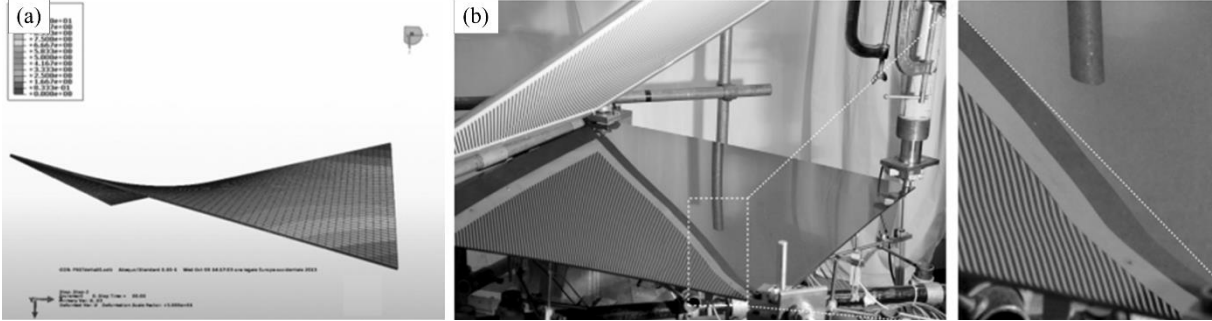


Fig. 2.35 – Ongoing research on cold-bent glass: (a) 2-D numerical model developed to study the snap-through instability [2.105] and (b) optical distortion [2.106].

2.5 REFERENCES

- [2.1] Haldimann M, Luible A, Overend M. Structural Use of Glass. Zurich: IABSE-AIPC-IVBH; 2008.
- [2.2] Nijssse R. Glass in Structures. Basel: Birkhauser; 2003.
- [2.3] Web site of “Euroglass”: <http://www.euroglas.com/>. 2016.
- [2.4] O’Callaghan J, Bostick C. The Apple glass cube: Version 2.0. In: Bos, Louter, Nijssse, Veer, editors. Challenging Glas. 3, Delft: Amesterdam: IOS Press; 2012, p. 57–65.
- [2.5] Web site of “SEDAK”: <https://www.sedak.com/>. 2016.
- [2.6] EN 572-1: 2012 Glass in building - Basic soda lime silicate glass products – Part 1: Definitions and general physical and mechanical properties. European Committee for Standardization (CEN), Brussels: 2012.
- [2.7] EN 1748-1: 2012 Glass in buildings - Special basic products - Borosilicate glasses - Part 1: Definitions and general physical and mechanical properties. European Committee for Standardization (CEN), Brussels: 2004.
- [2.8] Overend M, Butchart C, Lambert H, Prassas M. The mechanical performance of laminated hybrid-glass units. Compos Struct 2014;110:163–73.
- [2.9] Hundevad J. Super lightweight glass structures – a study. Glas. Glob. - Innov. Glas. Technol., Philadelphia: 2014, p. 324–37.
- [2.10] Schott AG - Research and development. Technical Glasses - Physical and technical properties. Mainz: 2014.
- [2.11] Hess R. Material glass. Struct Eng Int J Int Assoc Bridg Struct Eng 2004;14:76–9.
- [2.12] Veer FA. The strength of glass, a nontransparent value. Heron 2007;52:87–104.
- [2.13] Report EUR 26439 EN Guidance for European Structural Design of Glass Components. Institute for the Protection and Security of the Citizen, Joint Research Centre, Luxembourg: 2014.
- [2.14] Solinov VF. Ways to strengthen glass: Toughening, ion-Exchange. Glas Ceram 2015;72:191–3.
- [2.15] Web site “Kurakay”: <http://glasslaminatingsolutions.kuraray.com/>. 2016.
- [2.16] The Institution of Structural Engineers. Structural Use of Glass in Buildings (Second edition). London: The Institution of Structural Engineers (ISE); 2014.
- [2.17] Bennison SJ, Qin MH, Davies PS. High-performance laminated glass for structurally efficient glazing. Innov. Light. Struct. Sustain. Facades, Hong Kong: 2008, p. 1–12.
- [2.18] Belis J, Depauw J, Callewaert D, Delincé D, Van Impe R. Failure mechanisms and residual capacity of annealed glass/SGP laminated beams at room temperature. Eng Fail Anal 2009;16:1866–75.
- [2.19] Callewaert D. Stiffness of Glass / Ionomer Laminates in Structural Applications. PhD thesis, Ghent University, Belgium, 2012.
- [2.20] Bos FP. Safety Concepts in Structural Glass Engineering Towards an Integrated Approach. PhD thesis, Delft University of Technology, Netherlands, 2009.
- [2.21] Savineau GF, Butchart C, Delincé D, Speelman R. Characterization of interlayer properties – TG06 Status Report. In: Belis, Louter, Mocibob, editors. COST Action TU0905 Mid-term Conf. Struct. Glas., Porec: CRC Press Taylor & Francis Group; 2013, p. 339–47.
- [2.22] EN 1990: Eurocode 0 Basis of structural design. European Committee for Standardization (CEN), Brussels: 2002.
- [2.23] Duser A van, Jagota A, Bennison SJ. Analysis of glass/polyvinyl butyral laminates subjected to

- uniform pressure. *J Eng Mech* 1999;125:435–42.
- [2.24] D’Haene P. Flexural stiffness of laminated glass panels under dynamic conditions. *Glas. Process. Days* 2003, Tampere: 2003, p. 399–402.
- [2.25] Belis J. *Kipsterkte van Monolithische en Gelamineerde Glazen Liggers*. PhD thesis, Ghent University, Belgium, 2005.
- [2.26] D’Haene P, Savineau G. Mechanical properties of laminated safety glass - FEM Study. *Glas. Perform. Days* 2007, Tampere: 2007, p. 594–8.
- [2.27] Savineau G, Larcher M, Franz J, Speelman R, Groos T, Hiss S. *Structural Glass COST Training School 2013 - Interlayers*. Darmstadt: 2013.
- [2.28] Schober H, Schneider J. Developments in structural glass and glass structures. *Struct Eng Int* 2004;14:84–7.
- [2.29] Web site “Wagner Biro”: <http://www.wagner-biro.com/en>. 2016.
- [2.30] Web site of “Eckersley O’Callaghan”: <http://www.eocengineers.com/>. 2016.
- [2.31] Wurm J. *Glass structures - Design and construction of self-supporting skins*. Berlin: Birkhauser; 2007.
- [2.32] Louter C. *Fragile yet Ductile - Structural Aspects of Reinforced Glass Beams*. PhD thesis, Delf University of Technology, Netherlands, 2011.
- [2.33] O’Callaghan J. Glass structures from stairs to cubes. In: Bos, Louter, Veer, editors. *Challenging Glas. - Conf. Archit. Struct. Appl. Glas.*, Delft: IOS Press BV; 2008, p. 29–38.
- [2.34] Web site of “Bruce Coleman” at Flickr: <https://www.flickr.com/>. 2016.
- [2.35] Krynski M, Wittenberg D, DeLong D. Eaton’s Center: design of a pedestrian glass sky bridge. *Struct Congr* 2012 2012:438–47.
- [2.36] O’Callaghan J. An all glass cube in New York city. *Glas. Perform. Days* 2007, Tampere: 2007, p. 98–101.
- [2.37] Feirabend S. Reinforced laminated glass. In: Bos, Louter V, editor. *Challenging Glas. - Conf. Archit. Struct. Appl. Glas.*, Delft: IOS Press BV; 2008, p. 469–77.
- [2.38] Veer F, Groos S, Hobbelman GJ, Vredeling M, Janssen MJHC, van den Berg R, et al. Spanning structures in glass. *Proc. Glas. Process. Days* 2003, Tampere: 2003.
- [2.39] Bos FP, Veer F, Hobbelman GJ, Louter PC. Stainless steel reinforced and post-tensioned glass beams. *Proc. 12th Int. Conf. Exp. Mech.*, Bari, Italy: 2004.
- [2.40] Louter C, Belis J, Bos F, Veer F, Hobbelman G. Reinforced glass cantilever beams. *Glas. Process. Days* 2005, Tampere: 2005.
- [2.41] Louter C, Veer F, Hobbelman G. Reinforcing glass, effects of reinforcement geometry and bonding technology. *Glas. Perform. Days* 2007, Tampere: 2007.
- [2.42] Louter PC, Herwijnen F, Schetters L, Romein T, Veer FA. Experimental research on scale 1:8 models of an 18 m reinforced glass beam, part I. *Int. Symp. Appl. Archit. Glas.*, 2006, p. 215–22.
- [2.43] Louter C, Belis J, Veer F, Lebet J-P. Structural response of SG-laminated reinforced glass beams; experimental investigations on the effects of glass type, reinforcement percentage and beam size. *Eng Struct* 2012;36:292–301.
- [2.44] Louter C, Veer F, Belis J. Redundancy of reinforced glass beams; temperature, moisture and time dependent behaviour of the adhesive bond. In: Bos, Louter V, editor. *Challenging Glas. - Conf. Archit. Struct. Appl. Glas.*, Delft: 2008, p. 479–90.
- [2.45] Hamm J. *Tragverhalten von Holz und Holzwerkstoffen im Statischen Verbund Mit Glas*. PhD thesis, École Polytechnique Fédérale de Lausanne, Switzerland, 2000.

- [2.46] Kreher K. Tragverhalten und Bemessung von Holz-Glas-Verbundträgern Unter Berücksichtigung der Eigenspannungen im Glas. PhD Thesis, École Polytechnique Fédérale de Lausanne, Switzerland, 2004.
- [2.47] Kozłowski M. Experimental and Numerical Analysis of Hybrid Timber-Glass Beams. PhD Thesis, Silesian University of Technology, Poland, 2014.
- [2.48] Kreher K, Natterer J, Natterer J. Timber-glass-composite girders for a hotel in Switzerland. *Struct Eng Int J Int Assoc Bridg Struct Eng* 2004;14:149–51.
- [2.49] Cruz P, Pequeno J. Timber-Glass composite beams: Mechanical behaviour & architectural solutions. In: Bos, Louter V, editor. *Challenging Glas. Conf. Archit. Struct. Appl. Glas.*, Delft: IOS Press BV; 2008.
- [2.50] Cruz PJS, Pequeno J. Timber-glass composite structural panels: experimental studies & architectural applications. In: Bos, Louter V, editor. *Challenging Glas. - Conf. Archit. Struct. Appl. Glas.*, Delft: IOS Press BV; 2008, p. 449–58.
- [2.51] Freytag B. Glass-concrete composite technology. *Struct Eng Int J Int Assoc Bridg Struct Eng* 2004;14:111–7.
- [2.52] Wellershoff F, Sedlacek G. Structural use of glass in hybrid elements : steel-glass beams, glass-GFRP plates. *Glas. Process. Days* 2003, Tampere: 2003.
- [2.53] Report EUR 25316 EN Development of innovative steel-glass structures in respect to structural and architectural design (Innoglast). Unit G.5 - Research Fund for Coal and Steel, Research and Innovation, Luxembourg: European Union; 2013.
- [2.54] Palumbo D, Palumbo M, Mazzuchelli M, Schiavon A, Rebeschini A. A new roof for the XIII th Century “Loggia de Vicari” (Arquà Petrarca -PD – Italy) based on structural glass trusses : a case study. *Glas. Process. Days* 2005, Tampere: 2005.
- [2.55] Louter PC. High-strength fibre rods as embedded reinforcement in SentryGlas-laminated glass beams. *Glas. Perform. Days*, Tampere: 2009, p. 285–9.
- [2.56] Speranzini E, Agnetti S. Strengthening of glass beams with steel reinforced polymer (SRP). *Compos Part B Eng* 2014;67:280–9.
- [2.57] Louter C, Bos F, Callewaert D, Veer F. Performance of SentryGlas-laminated metal-reinforced glass beams at 23, -20 and 60 °C . *Glas. Perform. Days*, Tampere: 2009, p. 334–9.
- [2.58] Louter C, Leung C, Kolstein H, Vamberský J. Structural glass beams with embedded glass fibre reinforcement. In: Bos, Louter V, editor. *Challenging Glas. 2 - Conf. Archit. Struct. Appl. Glas.*, Delft: 2010, p. 439–48.
- [2.59] Speranzini E, Neri P. Structural behavior of “reinforced glass”. *Glas. Perform. Days* 2009, Tampere: 2009, p. 355–60.
- [2.60] Speranzini E, Neri P. Structural behaviour of GFRP “reinforced glass beams.” *Glas. Perform. Days* 2011, Tampere: 2011, p. 604–9.
- [2.61] Speranzini E, Agnetti S. Flexural performance of hybrid beams made of glass and pultruded GFRP. *Constr Build Mater* 2015;94:249–62.
- [2.62] Correia JR, Valarinho L, Branco FA. Post-cracking strength and ductility of glass-GFRP composite beams. *Compos Struct* 2011;93:2299–309.
- [2.63] Louter PC. Adhesively bonded reinforced glass beams. *Heron* 2007;52:31–57.
- [2.64] Martens K, Caspeepele R, Belis J. Development of reinforced & post-tensioned glass beams - review. *J Struct Eng* 2015:1–23.
- [2.65] Martens K, Caspeepele R, Belis J. Development of composite glass beams – A review. *Eng Struct* 2015;101:1–15.

- [2.66] Firmo JP, Correia JR, França P. Fire behaviour of reinforced concrete beams strengthened with CFRP laminates: Protection systems with insulation of the anchorage zones. *Compos Part B Eng* 2012;43:1545–56.
- [2.67] Mamone V, Masiello G, Lani L. A 6 metre long glass footbridge for the ancient public slaughterhouse of Pisa. In: Belis, Bos, Louter, editors. *Challenging Glas. 5 - Conf. Archit. Struct. Appl. Glas.*, Ghent: 2016, p. 515–25.
- [2.68] Cruz P, Pequeno J. Structural timber-glass adhesive bonding. In: Bos, Louter V, editor. *Challenging Glas. - Conf. Archit. Struct. Appl. Glas.*, Delft: IOS Press BV; 2008.
- [2.69] Bank LC. *Composites for Construction: Structural Design with FRP Materials*. New York: John Wiley & Sons, Inc; 2006.
- [2.70] Keller T. Recent all-composite and hybrid fibre-reinforced polymer bridges and buildings. *Prog Struct Eng Mater* 2001;3:132–40.
- [2.71] Gonilha JA, Correia JR, Branco FA. Structural behaviour of a GFRP-concrete hybrid footbridge prototype: Experimental tests and numerical and analytical simulations. *Eng Struct* 2014;60:11–22.
- [2.72] Sá MF, Correia JR, Gomes AM, Silvestre N. The GFRP-steel hybrid footbridge of S. Mateus park, Portugal: From conceptual design to in situ assessment. *Struct Eng Int* 2016; (in press).
- [2.73] Correia JR. *GFRP Pultruded Profiles in Civil Engineering: Hybrid Solutions, Bonded Connections and Fire Behaviour*. PhD Thesis, Technical University of Lisbon, Portugal, 2008.
- [2.74] Valarinho L. *Construção em vidro estrutural: comportamento estrutural de vigas mistas vidro-GFRP*. MSc dissertation (in Portuguese), Technical University of Lisbon, Portugal, 2010.
- [2.75] Völker C, Philipp D, Masche M, Kaltenbach T. Development of a test method for the investigation of the abrasive effect of sand particles on components of solar energy systems. 29th Eur. PV Sol. Energy Conf. Exhib., Amsterdam: 2014, p. 22–6.
- [2.76] Roumili F, Benbahouche S, Sangleboeuf J-C. Mechanical strength of soda-lime glass sandblasted by gravitation. *Friction* 2015;3:65–71.
- [2.77] Adjouadi N, Laouar N, Bousbaa C, Bouaouadja N, Fantozzi G. Study of light scattering on a soda lime glass eroded by sandblasting. *J Eur Ceram Soc* 2007;27:3221–9.
- [2.78] Schneider J, Schula S, Weinhold WP. Characterisation of the scratch resistance of annealed and tempered architectural glass. *Thin Solid Films* 2012;520:4190–8.
- [2.79] Datsiou KC, Overend M. Evaluation of artificial ageing methods for glass. In: Belis, Bos, Louter, editors. *Challenging Glas. 5 - Conf. Archit. Struct. Appl. Glas.*, Ghent: 2016, p. 581–612.
- [2.80] Overend M, Louter C. The effectiveness of resin-based repairs on the inert strength recovery of glass. *Constr Build Mater* 2015;85:165–74.
- [2.81] Vandebroek M, Belis J, Louter C, Van Tendeloo G. Experimental validation of edge strength model for glass with polished and cut edge finishing. *Eng Fract Mech* 2012;96:480–9.
- [2.82] Vandebroek M, Louter C, Caspeele R, Ensslen F, Belis J. Size effect model for the edge strength of glass with cut and ground edge finishing. *Eng Struct* 2014;79:96–105.
- [2.83] Kinsella DT, Persson K. On the applicability of the Weibull distribution to model annealed glass strength and future research needs. In: Belis, Bos, Louter, editors. *Challenging Glas. 5 - Conf. Archit. Struct. Appl. Glas.*, Ghent: 2016, p. 593–606.
- [2.84] Zubkov VA, Kondratieva N V. Ultrasonic examination of sheet glass macrostructure. In: Louter, Bos, Belis, Lebet, editors. *Challenging Glas. 4 COST Action TU0905 Final Conf.*, Lausanne: CRC Press Taylor & Francis Group; 2014, p. 755–61.
- [2.85] Andreozzi L, Zulli F, Briccoli Bati S, Fagone M, Ranocchiali G. Weathering of laminated glass - Degradation of interlayer mechanical properties. In: Louter, Bos, Belis, Lebet, editors.

- Challenging Glas. 4 COST action TU0905 Final Conf., Lausanne: CRC Press Taylor & Francis Group; 2014, p. 419–24.
- [2.86] Kothe M, Weller B. Influence of environmental stresses to the ageing behaviour of interlayer. In: Louter, Bos, Belis, Lebet, editors. Challenging Glas. 4 COST Action TU0905 Final Conf., Lausanne: CRC Press Taylor & Francis Group; 2014, p. 439–46.
- [2.87] Serafinavicius T, Lebet J-P, Louter C, Kuranovas A, Lenkimas T. The effects of environmental impacts on durability of laminated glass plates with interlayers (SG, EVA, PVB). In: Louter, Bos, Belis, Lebet, editor. Challenging Glas. 4 COST Action TU0905 Final Conf., Lausanne: CRC Press Taylor & Francis Group; 2014, p. 455–62.
- [2.88] Weller PB, Tasche DS. Adhesive fixing in glass construction. Glas. Process. Days 2005, Tampere: 2005.
- [2.89] Ølgaard AB, Nielsen JH, Olesen JF, Stang H. Properties of an adhesive for structural glass applications. In: Bos, Louter, Veer, editors. Challenging Glas. - Conf. Archit. Struct. Appl. Glas., Delft: 2008, p. 263–72.
- [2.90] Weller B, Nicklisch F, Wunsch J. Dynamic behaviour of adhesives for structural glass applications. Glas. Performance Days 2009, Tampere: 2009.
- [2.91] Belis J, Van Hulle A, Out B, Bos F, Callewaert D, Poulis H. Broad screening of adhesives for glass-metal bonds. Glas. Perform. Days 2011 - Proc. 12th Int. Conf., 2011, p. 286–9.
- [2.92] Kothe C, Weller B. Effects of surface pretreatments on adhesive properties of glass and metals. In: Louter, Bos, Belis, Lebet, editors. Challenging Glas. 4 COST Action TU0905 Final Conf., Lausanne: CRC Press Taylor & Francis Group; 2014, p. 353–9.
- [2.93] Netusil M, Eliasova M. Trends and requirements for adhesives with load bearing role. In: Louter, Bos, Belis, Lebet, editors. Challenging Glas. 4 COST Action TU0905 Final Conf., Lausanne: CRC Press Taylor & Francis Group; 2014, p. 369–74.
- [2.94] Santarsiero M, Louter C, Lebet J-P. The mechanical behavior of SentryGlas and TSSA laminated polymers in cured and uncured state in uniaxial tensile test. In: Louter, Bos, Belis, Lebet, editors. Challenging Glas. 4 COST Action TU0905 Final Conf., Lausanne: CRC Press Taylor & Francis Group; 2014, p. 375–84.
- [2.95] Puller K, Denonville J, Sobek W. An innovative glass connection technique using an ionomer interlayer. Glas. Perform. Days 2011, Tampere: 2011, p. 638–41.
- [2.96] Santarsiero M, Louter C. Embedded and point laminated adhesive connections for glass structures: parametric non-linear numerical investigations. Glas. Perform. Days 2013, Tampere: 2013, p. 265–73.
- [2.97] Spitzhüttl J, Nehring G, Maniatis I. Investigations on determining the bending strength of thin glass. In: Louter, Bos, Belis, Lebet, editors. Challenging Glas. 4 COST Action TU0905 Final Conf., Lausanne: CRC Press Taylor & Francis Group; 2014, p. 521–30.
- [2.98] Web site of “GorillaGlas”: <https://www.corning.com/gorillaglass/worldwide/en.html>. 2016.
- [2.99] Siebert G. Thin glass elements – A challenge for new applications. Glas. Perform. Days 2013, Tampere: 2013, p. 316–9.
- [2.100] Neugebauer J. Determination of bending tensile strength of thin glass. In: Belis, Bos, Louter, editors. Challenging Glas. 5 - Conf. Archit. Struct. Appl. Glas., Ghent: 2016, p. 419–29.
- [2.101] Lenk P. Designing with structural glass. In: Belis, Bos, Louter, editors. Challenging Glas. 5 - Conf. Archit. Struct. Appl. Glas., Ghent: 2016, p. 49–54.
- [2.102] Schlaich J, Schober H. Freeform glass roofs. Struct. Congr. 2005 Metrop. Beyond, New York: ASCE; 2005, p. 1–13.
- [2.103] Baldassini N. Hidden and expressed geometry of glass. In: Bos, Louter, Veer, editors.

- Challenging Glas. - Conf. Archit. Struct. Appl. Glas., Delft: IOS Press BV; 2008, p. 9–18.
- [2.104] Vákár LI, Design HS, Railconsult H. Cold bendable, laminated glass – New possibilities in design. *Struct Eng Int* 2004;2:95–7.
- [2.105] Galuppi L, Massimiani S, Royer-Carfagni G. Large deformations and snap-through instability of cold-bent glass. In: Louter, Bos, Belis, Lebet, editors. *Challenging Glas. 4 COST Action TU0905 Final Conf.*, Lausanne: CRC Press Taylor & Francis Group; 2014, p. 681–9.
- [2.106] Datsiou KC, Overend M. The mechanical response of cold bent monolithic glass plates during the bending process. *Eng Struct* 2016;117:575–90.
- [2.107] EN 572-9: 2004 Glass in building - Basic soda lime silicate glass products – Part 9: Evaluation of conformity / Product standard. European Committee for Standardization (CEN), Brussels: 2004.
- [2.108] EN 1863-1: 2000 Glass in building - Heat strengthened soda lime silicate glass - Part 1: Definition and description. European Committee for Standardization (CEN), Brussels: 2000.
- [2.109] EN 1863-2: 2000 Glass in building - Heat strengthened soda lime silicate glass - Part 2: Evaluation of conformity / Product standard. European Committee for Standardization (CEN), Brussels: 2004.
- [2.110] EN 12150-1: 2000 Glass in building - Thermally toughened glass soda lime silicate safety glass - Part 1: Definition and description. European Committee for Standardization (CEN), Brussels: 2000.
- [2.111] EN 12150-2: 2004 Glass in building - Thermally toughened glass soda lime silicate safety glass - Part 2: Evaluation of conformity / Product standard. European Committee for Standardization (CEN), Brussels: 2004.
- [2.112] ASTM C1036 - 11e1, Standard Specification for flat glass. West Conshohocken, PA: ASTM International; 2011.
- [2.113] ASTM C1048-12e1, Standard specification for heat-strengthened and fully tempered flat glass. West Conshohocken, PA: ASTM International; 2012.

PART II
STUDY OF THE STRUCTURAL
BEHAVIOUR OF LAMINATED
GLASS BEAMS AND PANELS

LATERAL-TORSIONAL BUCKLING BEHAVIOUR OF LONG-SPAN LAMINATED GLASS BEAMS: ANALYTICAL, EXPERIMENTAL AND NUMERICAL STUDY

ABSTRACT

Due to their high span-to-height ratio, glass fins are highly susceptible to the lateral-torsional buckling (LTB) phenomenon. Previous studies already assessed the LTB behaviour of small to intermediate-scale 2-layer glass beams, but this phenomenon is yet to be evaluated in long-span laminated glass beams. This chapter presents results of analytical, experimental and numerical studies on the LTB behaviour of long-span laminated glass beams. The analytical study focused (i) on the assessment of existing expressions for the determination of the effective flexural and torsional stiffness of 3-layer laminated glass beams; (ii) on the determination of the LTB resistance and post-buckling behaviour of long-span laminated glass beams, and (iii) on the influence on the LTB resistance of changes in the thickness of the glass panes and of the viscoelastic properties of the interlayers. The experimental study comprised a flexural test of a simply supported and unbraced 8.20 m long 3-layer PVB-laminated glass fin used in the facade of the *Champalimaud Centre for the Unknown* (Lisbon). Finally, three-dimensional numerical models were developed in order to simulate the experiments and validate the analytical results, in terms of critical load and equilibrium path, as well as to evaluate the stress distributions in the beam at the post-buckling stage. The results obtained show that the analytical formulae and the numerical tools available for design, are able to accurately predict the LTB behaviour of long-span 3-layer laminated glass beams. The results also draw the attention to the importance of adequately considering at the design stage the influence of possible thickness reductions on the glass panes and of temperature and loading time effects on the shear behaviour of PVB interlayers.

3.1 INTRODUCTION

In chapter 2 it was shown that glass fins are one of the most popular examples where glass is used as a structural element with load-bearing functions. One of the main features of glass fins is their high slenderness (ratio between flexural span (L_0) and height (h)), which makes them highly susceptible to the lateral-torsional buckling (LTB) phenomenon. During the last years, several authors have experimentally addressed this issue [3.1–3.4], conducting comprehensive experimental campaigns where the influence of the following parameters was analysed: total length, slenderness, initial imperfections, glass type, interlayer material, glass or interlayer thickness, temperature and load duration. In addition, most of the authors have also developed analytical and numerical studies, having reported accurate predictions of the LTB behaviour of 2-layer laminated glass beams. Although providing relevant results, the above-mentioned experimental campaigns were limited in terms of the span of the laminated glass beams. In fact, the vast majority of the tests were conducted in small to intermediate-scale specimens and, according to the best of the author's knowledge, no experiments were reported for beams longer than 3 m.

Previous investigations have also addressed the analytical methods available for the design of those structural glass members to the LTB phenomenon [3.5–3.9]. In most studies, the design approach developed for steel structures has been successfully adapted to equivalent monolithic laminated glass beams. The basic procedure relies on the principle of transforming the several layers of the glass fin (glass panes and polymeric interlayers) into a structurally equivalent monolithic element [3.1, 3.6, 3.10–3.12]. The works performed so far can be distinguished based on the approach used to determinate the effective bending ($EI_{y,eff}$) and torsional ($GJ_{t,eff}$) stiffnesses of the cross-section. Bedon *et al.* [3.8] and Machado-e-Costa [3.9] recently presented an extensive review of the available formulations, showing that such approaches provide accurate estimates of the LTB behaviour of 2-layer laminated glass beams. The main analytical studies in this field ultimately led to the publication of new design guidelines [3.13, 3.14] and standards [3.15, 3.16] that are a result of the main developments achieved so far. Each guideline or standard presents and adopts a given calculation approach, and the formulae available in the various documents can differ significantly among each other. Therefore, a unified design approach applicable to the most frequent design situations is still missing. Additionally, with the exception of the Italian standard [3.16], there are no expressions available for the design of laminated glass beams with more than three glass panes. Furthermore, due to the lack of experiments on long-span beams or on laminated glass beams with more than two layers, those design equations have not been duly validated at full-scale.

In addition to experimental and analytical studies, several authors have also developed numerical finite element (FE) models in order to simulate the LTB behaviour of laminated glass beams [3.3, 3.6]. Due to the complexity of the problem (i.e. the heterogeneous section or the viscoelastic behaviour of interlayers), numerical modelling is a convenient tool that allows to obtain accurate estimates of the buckling resistance and post-buckling behaviour of laminated glass members. This approach proved to be successful in

several previous studies (e.g. [3.1, 3.3, 3.9, 3.10]); however, as for the experiments, it was only used for small to intermediate-scale laminated glass beams.

This chapter presents further experimental and numerical investigations about the LTB behaviour of laminated glass beams and assesses the accuracy of existing analytical formulae. The beams studied herein are similar to the glass fins used in the facade of the *Champalimaud Centre for the Unknown*, in Lisbon (Fig. 3.1). The main distinctive characteristic of these 3-layer glass fins is their dimensions (8.20 m long \times 0.60 m high \times 0.048 m thick), much larger than those used in the studies mentioned above. The main goal of the work presented here was three-fold: (i) to experimentally investigate the flexural and LTB behaviour of these long-span laminated glass beams, including their linear, buckling and post-buckling responses; (ii) to assess the accuracy of the analytical expressions recently presented by Machado-e-Costa [3.9] (developed in straight collaboration with the author), for the design of 3-layer laminated glass beams; and (iii) to investigate the accuracy and (practical) applicability of conventional numerical FE models when applied to such large beams.



Fig. 3.1 – *Champalimaud Centre for the Unknown* building facade and its glass fins (courtesy of José Campos).

In addition to the present introduction, the remainder of the chapter is organized as follows. Section 3.2 describes the main geometrical properties of the beam studied and the main mechanical properties of the materials involved: the glass panes and the interlayer polymer (polyvinyl butyral, PVB); special attention is given to the temperature and long-term mechanical behaviour of the interlayer. Section 3.3 describes the analytical approach used to evaluate the LTB behaviour of the beam, regarding (i) the effective flexural stiffness, (ii) the effective torsional stiffness, (iii) the critical buckling load, and (iv) the post-buckling behaviour. Section 3.4 presents the experimental study, which comprised the measurement of the initial bow and the flexural test of the long-span laminated glass beam. Section 3.5 describes the numerical study, which aimed at simulating the linear, buckling and post-buckling behaviour of the beam tested. Experimental, analytical and numerical results are compared, in terms of elastic critical load and load-displacement post-buckling path. Finally, section 3.6 summarizes the main conclusions of this chapter.

3.2 GEOMETRICAL AND MECHANICAL PROPERTIES OF THE ANALYSED BEAM

3.2.1 Beam geometry

The laminated glass beam analysed in this chapter has 3 layers of fully tempered glass with polished edges and 2 PVB interlayers films. The nominal geometry of each glass pane is 8200 mm of length, 600 mm of height and 15 mm of thickness. The nominal thickness of the interlayer films is 1.52 mm.

The thickness of the laminated glass beam, as well as that of the individual components, has remarkable influence on both torsional and bending stiffness around the minor axis, thus it also has significant impact on the LTB behaviour. According to EN 572-8 standard [3.17], glass panels with 15 mm of thickness may present differences in thickness up to ± 0.5 mm. In what concerns the PVB interlayer, according to Callewaert *et al.* [3.18], these elements present a very precise thickness prior to the lamination process. However, differences up to 9% were detected after lamination.

Due to the above-mentioned reasons, the height (h) and the total thickness (t_{total}) of the beam were measured in several sections along its length, using a metric ruler with 1 mm of precision for h and a calliper rule with 0.05 mm precision for t_{total} . Some differences were detected between the nominal and the actual dimensions of the beam. In particular, the measured average height was $h_{real} = 601.54$ mm (*vs.* 600 mm) and the mean thickness was $t_{total,real} = 48.26$ mm (*vs.* 48.04 mm). After lamination, with exception of the extremity sections, it is extremely hard to measure the actual thickness of each layer. Nevertheless, the author was able to conclude that the glass panes used in the beam could not present the nominal thickness of 15 mm; indeed, based on local measurements, the geometry of the beam most likely included 14.50 mm thick glass panels and 2.28 mm thick PVB interlayers films. The influence of these geometrical differences (nominal *vs.* actual) on the overall structural response and susceptibility to instability of the beam is analytically and numerically analysed in section 3.3 and section 3.5, respectively.

3.2.2 Mechanical properties

It was not possible to perform mechanical characterization tests on the constituent materials of the laminated glass beam, since it was provided after the lamination process and the manufacturer was not able to supply additional samples of glass or PVB. Therefore, the mechanical properties considered in the analytical and numerical models are average values taken from the literature, namely from the recent *Guidance for European Structural Design of Glass Components* [3.13].

For the glass panes, the following properties were considered (soda lime silica glass): Young's modulus (E) of approximately 70 GPa (which has been reported to present low scatter), Poisson's ratio of 0.23, and (characteristic) bending strength of 120 MPa (fully tempered glass).

PVB is a thermoplastic polymeric material that presents viscoelastic behaviour in the range of service temperatures for building applications (-20 °C to +80 °C). The material is highly susceptible to creep or

relaxation phenomena (the phenomenon of creep is further developed in chapter 4), with mechanical properties being highly dependent on load duration and temperature [3.19]. Therefore, in order to accurately model the mechanical behaviour of a PVB-laminated glass member, it is important to accurately identify (i) the type of applied load(s) and (ii) the environmental conditions the structural element is subjected to during its service life, and (iii) to consider the corresponding mechanical properties of PVB, in terms of load duration and temperature.

The formulation and application of viscoelastic material models (function of time and temperature) is complex and generally of difficult implementation. In most common situations, the structural response of laminated glass members for a specific action and environmental condition can be easily and approximately determined by running quasi-static analysis considering the properties of the interlayer for a relevant time and temperature range [3.8, 3.20]. For the most popular interlayers used in laminated glass (PVB, ethylene-vinyl acetate (EVA) and ionoplast), the material properties (usually the shear modulus) can be found in the literature or technical sheets under the form of reduction curves¹ function of time and for a standard temperature. In the present study, the mechanical properties of PVB at 20 °C and for load durations commonly considered in the design of laminated glass elements were taken from the study of van Duser *et al.* [3.21]. Further discussion about the viscoelastic behaviour of polymeric interlayers is provided in chapter 4. Table 3.1 presents the values of G_{int} and E_{int} (PVB) for a temperature of 20 °C (as originally presented in [3.21]) and 23 °C, which was the average temperature during the experimental test. One can observe that a small temperature increase of only 3 °C causes remarkable reductions in the mechanical properties of PVB (up to 60% less stiffness).

Table 3.1 – Mechanical properties of the interlayer (considered to be PVB) as a function of the load duration and ambient temperature (20 °C and 23 °C) [3.3].

Property	Temp. [°C]	3 s	1 min	20 min	1 h	1 day	1 week	3 months	6 months	10 years
G_{int} [MPa]	20	8.06	1.64	0.93	0.84	0.51	0.41	0.29	0.25	0.05
	23	3.45	0.97	0.78	0.61	0.44	0.33	0.17	0.10	0.05
E_{int} [MPa]	20	24.17	4.92	2.80	2.52	1.52	1.23	0.87	0.75	0.16
	23	10.34	2.92	2.35	1.82	1.33	0.98	0.52	0.31	0.16

Finally, according to Callewaert [3.19], PVB presents tensile strength higher than 20 MPa, Poisson's ratio of 0.49, ultimate axial deformation higher than 250%, and glass-transition temperature of about 20 °C.

¹ The reduction curves are usually obtained from dynamic mechanical analysis (DMA) and applying the Williams-Landel-Ferry (WLF) theory: based on coupon material tests, carried out for a range of temperatures and load frequencies, it is possible to predict the long-term behaviour of the material.

3.3 ANALYTICAL STUDY

The analysis of the elastic LTB critical load and of the post-buckling behaviour of laminated glass elements summarized in this section follows the classic theory of structural stability, widely applied to steel members. The main difference between laminated glass and steel members relies on the formulation used to compute the bending stiffness (EI_y) and the torsional stiffness (GJ_t) of the cross-sections. In the case of laminated glass members, these parameters must be computed taking into account the contribution of the two constituent materials, the glass panes and the polymer interlayer (affecting the level of interaction at the interfaces). The prevalent analytical method is based on replacing the stiffness parameters for a homogeneous (monolithic) section (EI_y and GJ_t) by effective stiffnesses ($EI_{y,eff}$ and $GJ_{t,eff}$, respectively) corresponding to the laminated glass member.

This section describes the analytical study about the LTB behaviour of the full-scale laminated glass beam. It first describes the method for computing the above-mentioned effective stiffnesses. Next, the LTB critical load and the post-buckling path are calculated. The final part of the section summarizes the Southwell method, which is subsequently applied in section 3.4 to estimate the experimental critical load.

3.3.1 Flexural and torsional stiffness

The effective flexural ($EI_{y,eff}$) and torsional ($GJ_{t,eff}$) stiffness can be determined based on several analytical approaches. The ones more frequently used are based on theories originally developed for (i) sandwich structures [3.1, 3.9], and (ii) composite beams with partial interaction [3.6]. Several analytical expressions have been published in the literature, for both flexural [3.2, 3.11, 3.22–3.24] and torsional stiffness [3.1, 3.25]. However, most of the works are limited to 2-layer laminated glass beams and the formulas available for multi-layer beams have been shown to be inaccurate for the entire range of mechanical properties of interlayer materials [3.9, 3.26]. Machado-e-Costa [3.9] recently published an extensive review and assessment of the accuracy of several different analytical approaches available in the literature. The author clarified some inconsistencies in the literature (including in the most recent European guidance, where a parameter seems to be missing) and extended the applicability of sandwich theory to 3, 4 and 5-layer laminated glass beams, taking also into account the influence of overhangs.

Fig. 3.2 illustrates a simply supported 3-layer laminated glass beam, similar to that investigated herein, subjected to a mid-span load (P). According to Machado-e-Costa [3.9], the $EI_{y,eff}$ of the beam can be determined (Eq. (3.1)) from the sum of (i) the flexural stiffness of the glass layers w.r.t. their own centroidal axes (EI_{gl}), and (ii) the flexural stiffness w.r.t. the neutral axis (EI_s) multiplied by a factor ζ_f (varying from 0 to 1) that reflects the level of interaction provided by the interlayer's mechanical properties, and depends on the following parameters: interlayer stiffness, overhangs' length, loading and support conditions and ratio between I_s and I_{gl} . The calculations necessary to evaluate the above-mentioned effects are described in Eqs. (3.2) to (3.10), where E and G are respectively the Young's

modulus and the shear modulus of glass, G_{int} is the interlayer shear modulus, L_0 , L_1 , h , t_i , t_{int} , and d are geometrical parameters (Fig. 3.2), α , β , λ_f and θ are non-dimensional parameters that account for the influence of the interlayer's stiffness, and ϕ is a non-dimensional parameter that depicts the influence of the overhangs' length:

$$EI_{y,eff} = EI_{gl} + \xi_f EI_s \quad (3.1)$$

$$I_{gl} = 2 \cdot ht_1^3/12 + ht_2^3/12 \quad (3.2)$$

$$I_s = ht_1 d^2/2 \quad (3.3)$$

$$A = hd^2/(2t_{int}) \quad (3.4)$$

$$\alpha = \frac{I_{gl}}{I_s} \quad (3.5)$$

$$\beta = \frac{1}{AG_{int}} \frac{EI_s}{L_0^2} \quad (3.6)$$

$$\lambda_f = \sqrt{(1 + \alpha)/\alpha\beta} \quad (3.7)$$

$$\theta = \lambda_f/2 \quad (3.8)$$

$$\phi = \lambda_f L_1/L_0 \quad (3.9)$$

$$\xi_f = \frac{1 + \alpha}{1 + \frac{3}{\alpha\theta^2} \left(1 - \frac{3 \sinh(\theta + \phi) - \sinh(\theta - \phi) - 4 \sinh(\phi)}{2\theta \cosh(\theta + \phi)} \right)} - \alpha, \alpha \in [0,1] \quad (3.10)$$

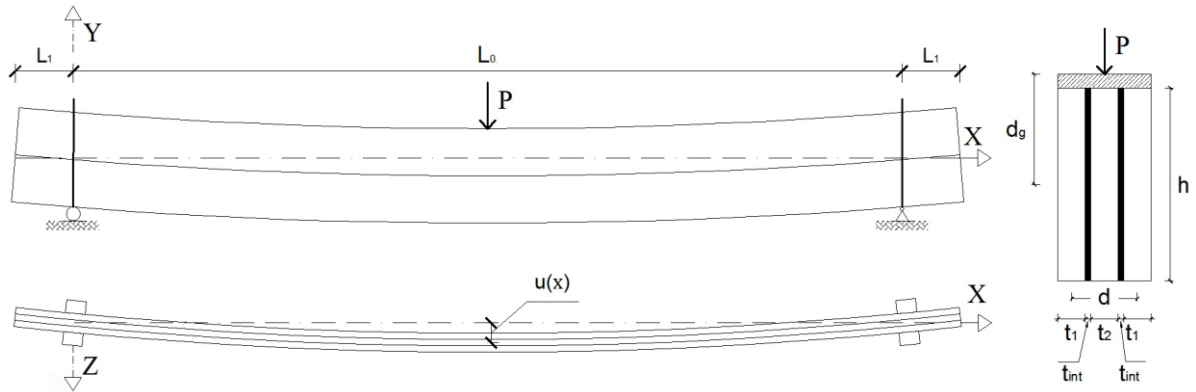


Fig. 3.2 – Lateral-torsional buckling instability model for a 3-layer laminated glass beam (left) and respective cross-section (right) – adapted from [3.1].

For a 3-layer laminated glass beam, Machado-e-Costa [3.9] used a similar procedure, defining the effective torsional stiffness $GJ_{t,eff}$ as the sum of (i) the torsional stiffness of the glass layers w.r.t. their own centroidal axes (GJ_{gl}), and (ii) the torsional stiffness of the interlayer (GJ_s) multiplied by a factor ζ_t (also varying from 0 to 1), function of the interlayer shear stiffness. Eqs. (3.11) to (3.15) describe the procedure used to calculate the $GJ_{t,eff}$, where the meaning of the parameters is that set previously:

$$GJ_{t,eff} = GJ_{gl} + \xi_t GJ_s \quad (3.11)$$

$$J_{gl} = \frac{2ht_1^3}{3} + \frac{ht_2^3}{3} \quad (3.12)$$

$$J_s = 4 I_s \quad (3.13)$$

$$\lambda_t = \sqrt{\frac{G_{int}}{G} \frac{1}{t_1 t_{int}}} \quad (3.14)$$

$$\xi_t = 1 - \frac{2}{\lambda_t h} \tanh \frac{\lambda_t h}{2} \quad (3.15)$$

3.3.2 Elastic LTB critical load

The elastic LTB critical load of laminated glass beams can be obtained analytically using equations available in the technical literature for structural stability [3.27], steel design (e.g. [3.28]) or glass (e.g. [3.2, 3.4, 3.5, 3.8, 3.29]), the latter being already part of some design guidelines [3.13, 3.14] and standards [3.15, 3.16]. As mentioned, the main differences between those approaches rely mostly in the calculation of the flexural and torsional stiffness and also in the coefficients that take into account the load configuration. In the present study, the design approach described in Eurocode 3 (including the last coefficients update available at [3.30]) is considered. Accordingly, the LTB critical load (P_{cr}) of a bi-symmetric laminated glass beam, simply supported (with supports free to rotate and warp but prevented to twist) and subjected to a concentrated load at the top of its mid-span section (Fig. 3.2) can be calculated as follows,

$$P_{cr} = 4 \cdot \frac{M_{cr}}{L_0} = 4 \times 1.348 \times \frac{\pi^2 EI_{y,eff}}{L_0^3} \left\{ \sqrt{\frac{L_0^2 GJ_{t,eff}}{\pi^2 EJ_{y,eff}} + (0.590 \cdot d_g)^2} - 0.590 \cdot d_g \right\} \quad (3.16)$$

where M_{cr} is the critical moment for LTB, L_0 , $EI_{y,eff}$ and $GJ_{t,eff}$ have the meaning already defined and d_g is the distance between the shear centre and the load application point (Fig. 3.2). As explained in the previous subsection, $EI_{y,eff}$ and $GJ_{t,eff}$ represent respectively the effective flexural and torsional stiffness of the laminated glass beam, which take into account the shear modulus of the interlayer and its ability to transfer shear stresses between the glass panes. Despite the stiffnesses $EI_{y,eff}$ and $GJ_{t,eff}$ provide the influence of the interlayer to transfer shear stresses between the glass panes, the critical moment formula (Eq. (3.16)) does not consider the additional degree-of-freedom corresponding to the relative vertical displacement between different glass layers. This was done by Challamel and Girhammar [3.31] for the case of a two-layer beam under uniform moment.

Fig. 3.3-a depicts the elastic LTB critical load of the beam investigated herein as a function of the interlayer's (PVB) shear modulus, G_{int} (bottom horizontal axis) or as function of time (top horizontal axis).

The geometrical properties of the beam are those described in section 3.2.1 ($L_0 = 7.80$ m, $L_I = 200$ mm and $d_g = 389$ mm), corresponding to a slenderness (L/h) of 13.8, and the interlayer properties are those listed in Table 3.1, thus illustrating the influence of the service temperature (20 °C and 23 °C) and the load duration on the buckling resistance. In Fig. 3.3-a, the LTB critical loads for time durations of 3 s, 20 min and 1 h are also highlighted. One can see that the LTB critical load is highly dependent on both parameters (time and temperature). Indeed, the LTB critical load corresponding to a very short-term loading (for instance, 3 s corresponds to a wind gust) is about 47% higher than that corresponding to a one-hour sustained load. In addition, for a temperature increase of only 3 °C (from 20 °C to 23 °C), the LTB critical load can decrease by 23% (for a short-term loading of 3 s).

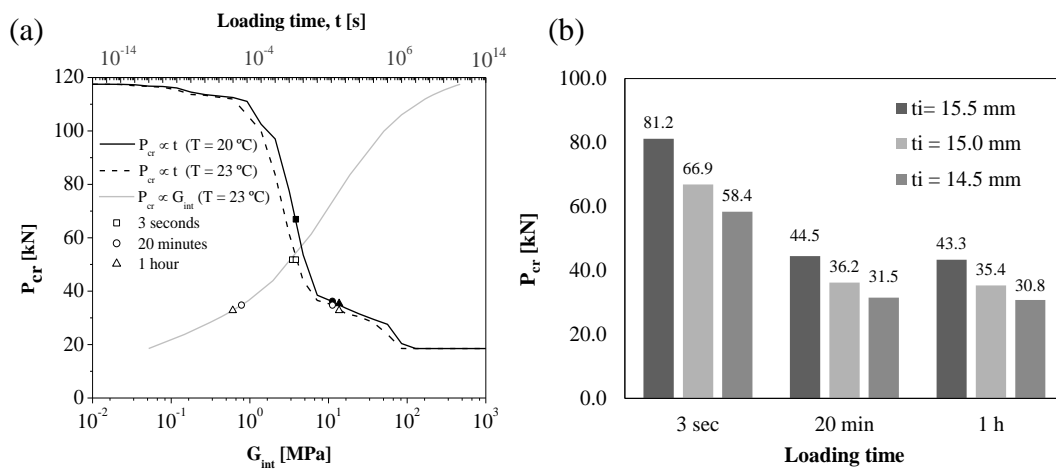


Fig. 3.3 – LTB critical load (P_{cr}) as a function of (a) interlayer's (PVB) shear modulus G_{int} (grey curve), loading time (black and dashed curves) and (b) glass panes thickness (considering the same total thickness, $t_{total} = 48.04$ mm); black and white symbols correspond to service temperatures of 20 °C and 23 °C respectively.

In the present study, the influence of the glass thickness on the LTB critical load was also evaluated. Fig. 3.3-b lists the LTB critical load of the beam investigated herein (computed using Eq. (3.16)) considering small changes in the thickness of the glass panes, namely the standard tolerances defined in EN 572 [3.17] (± 0.5 mm) and keeping constant the total thickness of the beam (i.e. adjusting the interlayer thickness). In this case, one may observe that changing the glass thickness from 15.0 mm to 14.5 mm (3% decrease) can cause a 13% decrease in the resistance against the LTB phenomenon². Considering the lower and upper bounds of the above-mentioned standard tolerances (glass panes thicknesses of 14.5 mm and 15.5 mm), the relative differences in critical loads are as high as 28%.

3.3.3 Load vs. displacement path

Due to geometrical imperfections, the load paths exhibited by real structures are asymptotic to the critical load, giving rise to out-of-plane displacements that can be very significant before the buckling

² As explained in section 3.2.1, for the beam investigated in this chapter, the difference between the nominal and real (measured) thickness of the glass panes was very significant.

strength is attained. Eq. (3.17), provided by the *Guidance for European Structural Design of Glass Components* [3.13]³, allows predicting the horizontal displacements at the barycentric axis of a general section x along the buckling length (L_0) of a beam subjected to a mid-span point load and a maximum moment M_z ,

$$u(x) = \frac{\frac{1}{C_1^2} \frac{M_z^2}{EI_{y,eff}} \cdot u_0 + \frac{1}{C_1} \frac{GJ_{t,eff}}{EI_{y,eff}} \cdot M_z \theta_0}{GJ_{t,eff} \cdot \left(\frac{\pi}{L_0}\right)^2 - \frac{1}{C_1^2} \frac{M_z^2}{EI_{y,eff}} + \frac{2C_2}{C_1} M_z d_g \left(\frac{\pi}{L_0}\right)^2} \cdot \sin\left(\frac{\pi}{L_0} x\right) \quad (3.17)$$

where u_0 and θ_0 are, respectively, the maximum amplitude of the initial bow and the maximum amplitude of the initial rotational imperfection, assuming a sinusoidal shape for both imperfections, with maximum amplitude at mid-span; all the other parameter have the same meaning as for Eqs. (3.1) to (3.15).

As for the buckling resistance, the influence of the following parameters on the load-displacement path was analytically assessed: (i) load duration, (ii) temperature, and (iii) thickness of the glass panes. In this analysis, once more, the total thickness of the beam was kept constant and the following imperfections were considered (based on measurements reported in section 3.4): $u_0 = 1$ mm and $\theta_0 = 0.0012$ rad. The results of this study, illustrated in Fig. 3.4, show that lateral displacements can be highly affected by stiffness changes, especially due to the reduction of the PVB shear modulus (corresponding to long-term loadings and/or high temperatures) and, to a lesser extent, due to reductions in the thickness of the glass panes. However, from a qualitative point of view, the overall trends of the load vs. displacement paths are similar (they are mainly affected by the imperfections value). In conclusion, stiffness reductions involve much higher lateral deflections (for the same load) and lower critical loads (as discussed in the preceding section).

3.3.4 Southwell equation

As mentioned before, real structures comprising initial imperfections do not exhibit primary paths with null lateral displacements; instead, they present nonlinear paths that are asymptotic to both primary and bifurcated (post-buckling) paths and depend on the imperfection amplitude, making it hard to directly extract buckling loads from experimental tests. The Southwell plot [3.32] is a useful tool that allows to infer the buckling load from experimental tests on specimens with small initial shape imperfections. Another advantage of this procedure is the possibility of experimentally estimating the buckling strength without causing the ultimate failure of the member. However, relatively large displacements generally need to be attained.

³ The expression was readjusted in order to be applied using updated EC3 coefficients [3.30], instead of the ones proposed in the European guidance [3.13].

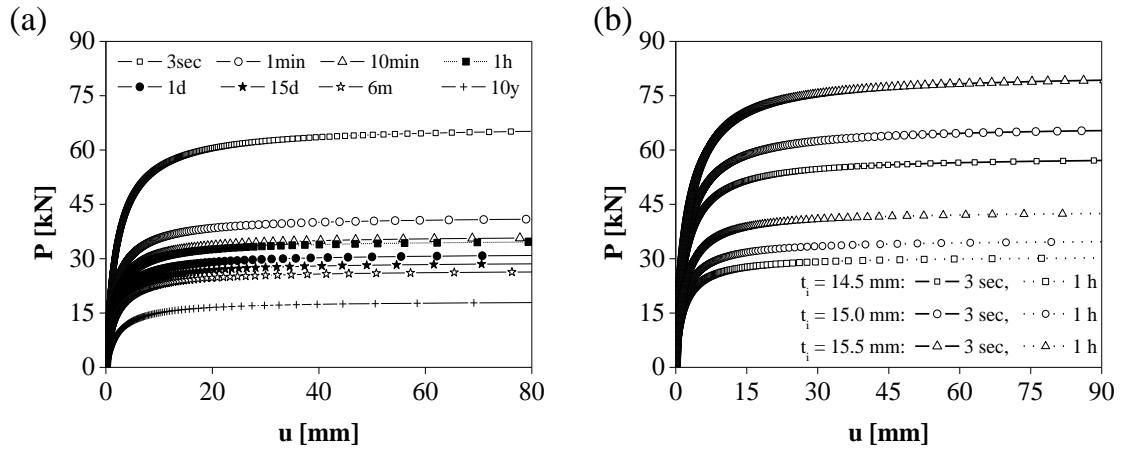


Fig. 3.4 – Load vs. displacement paths of the laminated glass beam: influence of (a) G_{int} (i.e. loading time) and of (b) thickness of glass panes (and interlayer) and G_{int} (i.e. loading time).

The Southwell plot (used ahead in section 3.4.4.3 of the present chapter) represents the best straight line that fits experimental data obtained in successive load-displacements steps. The slope is the buckling load and the lateral displacement at zero load is the amplitude of the initial imperfection. For practical reasons, the Southwell method is applied together with Eq. (3.18), where P_{cr} is the experimental critical load, u and u_0 are respectively the lateral displacement at mid-span and the initial bow or imperfection at the same section, and P is the total applied load:

$$\frac{u}{P} = \frac{1}{P_{cr}} \cdot u + \frac{u_0}{P_{cr}} \quad (3.18)$$

3.4 EXPERIMENTAL STUDY

This section presents the experimental study about the LTB behaviour of the full-scale laminated glass beam described in section 3.2.1 and analytically studied in section 3.3. The experimental procedure first consisted on the measurement of the geometrical imperfections of the beam, and then loading it in a 3-point bending configuration. The test results, namely the LTB critical load and the respective equilibrium path of the beam, are presented and compared with the previously presented analytical results.

3.4.1 Test setup

The test consisted of loading the 8.20 m long simply supported 3-layer laminated glass beam (geometry and mechanical properties detailed in section 3.2) in a 3-point bending configuration, with a free span of 7.80 m. Fig. 3.5-a depicts an overall view of the lateral-torsional buckling test setup.

In order to ensure a reliable comparison with the analytical results, the supports were designed in order to meet the theoretical assumptions as close as possible. Therefore, the supports comprised closed fork steel bearings, fixed and transversely restrained by steel frames (Fig. 3.5-b). The bearings enabled the rotations

around the major and minor bending axes and restrained rotations around the longitudinal (torsion) axis (Fig. 3.5-b and c). One of the supports also restrained the horizontal displacements along the longitudinal axis. In order to minimize the friction w.r.t. all free rotations and displacements, the following procedure was followed: (i) all the bearings were lubricated with grease before testing, (ii) polytetrafluoroethylene (*Teflon*) films were placed between the steel frames and the glass beam, and (iii) the pressure of the steel frames over the bearings was also controlled allowing all the bearings to rotate freely.

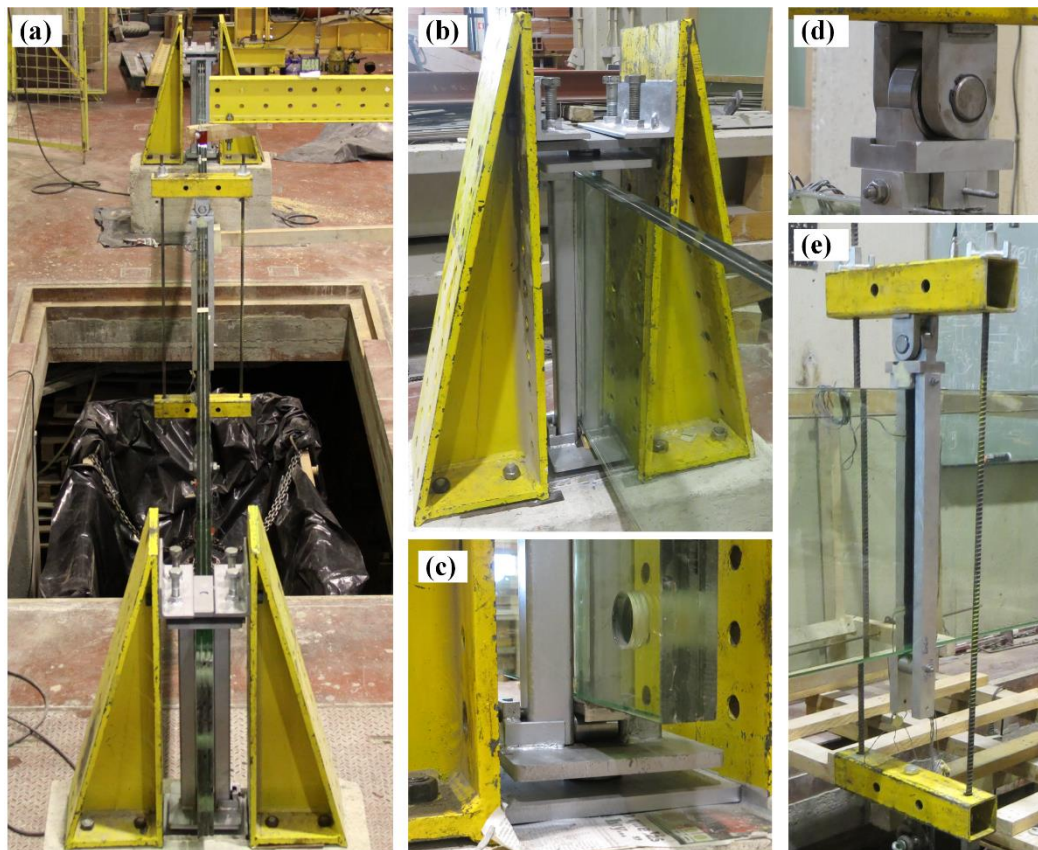


Fig. 3.5 – LTB test setup: (a) overall view, (b) and (c) supports, and (d) and (e) load application system.

The load was applied at the mid-span section by means of a dead weight loading system consisting of a steel container that was filled with water during testing. The container was suspended from the top edge of the beam using metal cables and two steel beams (one above and the other below the glass beam) connected by two *dywidag* bars (Fig. 3.5-e). The entire system, including the load cell, presented an initial weight of 7.4 kN. A high-quality bearing was positioned between the dead weight loading system and the load introduction point on the upper edge of the beam⁴ (Fig. 3.5-d and e). This bearing enabled rotations around the longitudinal axis of the beam, allowing it to freely rotate and laterally displace, due

⁴ Applying the load on the upper edge of the beam decreases its LTB strength (compared to applying the load on the shear center), since the load has a destabilizing effect.

to torsion and out-of-plane bending, without affecting the load direction⁵. The total distance between the upper edge of the beam and the bearing contact point (there was an aluminium frame making the transition between the two points - Fig. 3.5-d) was 89 mm.

Finally, an epoxy adhesive layer and 2 mm thick aluminium films were added to all loaded surfaces (supports and load application region) in order to ensure a uniform load distribution for all the glass panes, as well as to avoid glass-steel contact (Fig. 3.5-c).

3.4.2 Measurement of geometrical imperfections

As for other materials, and regardless of the lamination process, glass may present deviations from the nominal geometric dimensions as well as initial geometric imperfections or initial deflection w.r.t. to its longitudinal axis. These imperfections explain the non-linearity of the LTB behaviour of laminated glass beams. In order to analytically estimate the equilibrium path (as well as its experimental P_{cr}), it is necessary to measure the initial bow, namely the maximum amplitude of the initial bow and the maximum amplitude of the initial rotation imperfection at mid-span. The formulation proposed in Eq. (3.17) assumes that the initial displacement presents a sinusoidal shape, similar to the first lateral buckling mode.

Due to the size of the beam, the initial imperfections were measured using topographic equipment. To this end, the beam was placed over the supports (described in the previous section), the various components of the test setup were adjusted and 19 reflective tape targets (supplied by *Leica*) were bonded at different positions along the length and height of the beam (Fig. 3.6). All the coordinates of those targets were measured using a laser total station (*Leica TCR705*) with precision of 1 mm.

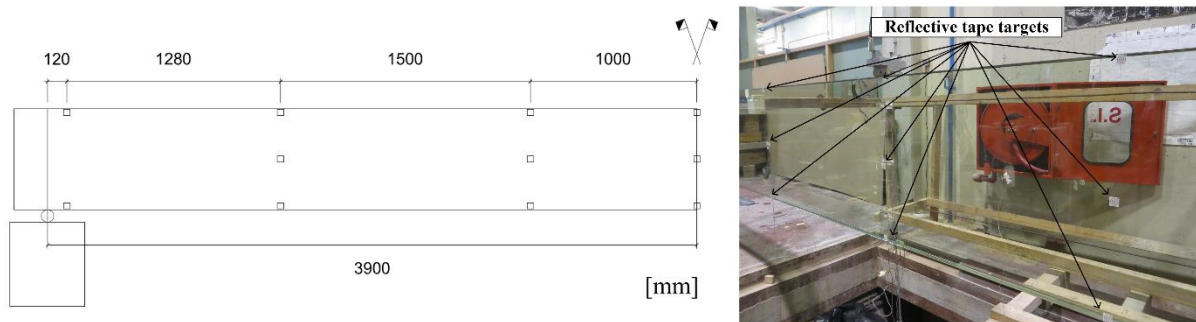


Fig. 3.6 – Reflective tape targets: (left) location and (right) detail at the vicinity of the mid-span section.

3.4.3 Test procedure

The LTB test procedure comprised the following steps: (i) the empty container was smoothly suspended on the beam, which was thus almost instantaneously subjected to an applied load of 7.4 kN; (ii) after the

⁵ In what concerns the load application system, the analytical formulation described in section 3.3 assumes that the applied loads remain vertical during testing and, at the same time, follow the lateral movement of the beam, similarly to gravity loads. This requirement was considered when designing the test setup.

stabilization of the container's movement, which took a few seconds, the water was introduced at a speed rate of 22.5 N/s; (iii) the load introduction was halted at 30 kN. The test was considered to be completed when the out-of-plane displacements reached 50 mm.

The applied load was measured using a *TML* load cell (with capacity of 50 kN and precision of 0.01 kN) placed between the steel container and the beam (Fig. 3.7). The deformation of the beam was monitored at the mid-span section, where the vertical displacement (measured at the aluminium load introduction frame, between the beam and the bearing — close to the top edge of the beam, Fig. 3.7) and the horizontal displacements (at the top and bottom edges of the beam) were measured with *TML* wire displacement transducers (stroke of 500 mm and precision of 0.01 kN, Fig. 3.7). The test was conducted at an average temperature of 23 °C and relative humidity of 55%, and had a duration of about 20 minutes⁶.

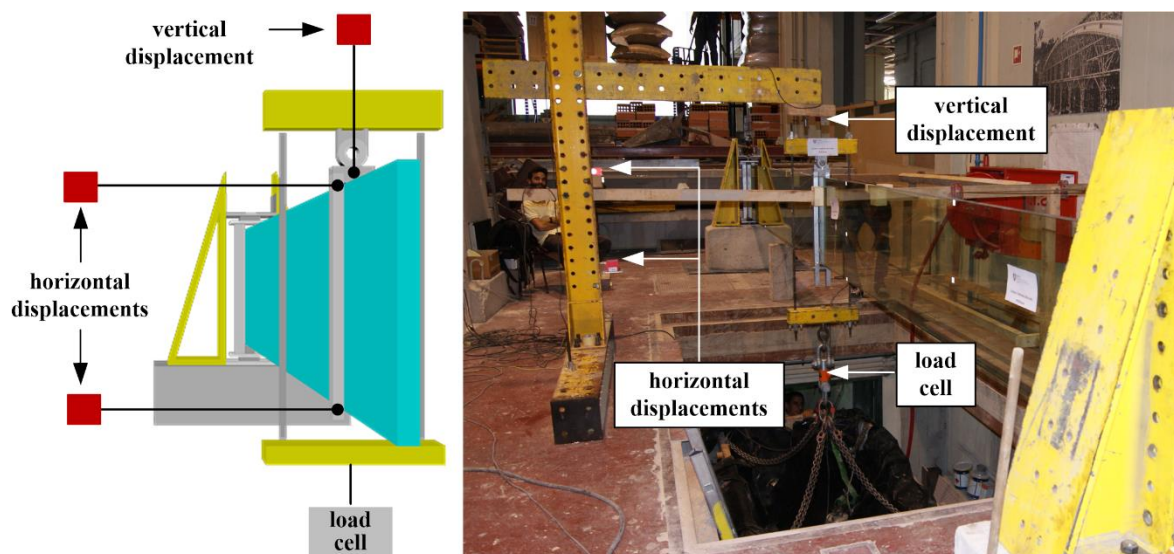


Fig. 3.7 – Measuring equipment, (left) illustration and (right) experimental application (view in perspective).

3.4.4 Test results

3.4.4.1 Initial imperfections

Fig. 3.8 presents the initial bow configuration measured at the centroid height of the beam, along its longitudinal axis. One can observe that the initial bow measured is not symmetrical, it does not present a sinusoidal shape and its maximum value (4.0 mm - about $u_0/L = 0.0005$) is not observed at the mid-span section, but rather at a distance of 80 cm. These results might be due to possible differences in the thickness of the glass panes and not directly due to an out-of-plane deformed shape of the beam itself. Similar shape deviations have been reported in a few specimens of an extensive study conducted by Belis *et al.* [3.33]. In that study, the initial bow of 61 laminated glass beams comprising PVB or Ionoplast SentryGlas (SG) films was measured. The study included beams with lengths ranging from 900 mm to

⁶ The test duration includes an additional period of 4 minutes during which the load was kept constant so that minor adjustments could be introduced in the load application method.

3000 mm, heights ranging from 150 mm to 300 mm and two fully tempered glass layers with thicknesses of 6, 8 and 10 mm. Based on those measurements, the authors determined a mean value of $u_0/L = 0.00105$ mm/mm, which is about two times higher than the experimental measurement. In this study, due to the assumptions made in the analytical study (*cf.* section 3.3), a sinusoidal regression of the experimental data (presenting its maximum at mid-span) was also determined (Fig. 3.8) based on the least squares method. This curve yields a maximum imperfection at mid-span of $u_0 = u_{max} = 2.49$ mm (*vs.* the measurement of 1.00 mm).

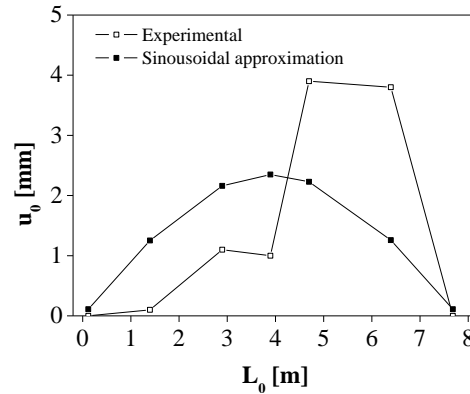


Fig. 3.8 – Experimental and sinusoidal approximation of the initial deformed shape.

Regarding the initial rotation, topographic measurements provided a maximum rotation at the mid-span section of $\theta_0 = 0.0012$ rad. Contrarily to u_0 , there are no experimental studies in the literature reporting average values for θ_0 . However, two studies [3.4, 3.6] have parametrically estimated the possible amplitude of this parameter in beams with lengths up to 3000 mm, by fitting experimental results on the presumed analytical response: Belis *et al.* [3.4] mentioned a value of the same magnitude obtained herein, while Bedon and Amadio [3.6] indicated a value almost 10 times higher.

3.4.4.2 Load-displacement response

Fig. 3.9-a presents the load *vs.* deformation response of the beam in terms of twist rotation, vertical and lateral displacements. The occurrence of lateral-torsional buckling, which was easily observable during the test (Fig. 3.10), can be straightforwardly detected in all deformation curves, which at some point exhibit an almost horizontal plateau.

Fig. 3.9-b compares the analytical load *vs.* out-of-plane displacement u paths obtained with the experimental results. The analytical non-linear post-buckling response of the long-span beam was estimated using Eq. (3.17). The different analytical and numerical (the latter are discussed ahead in section 3.5) curves plotted correspond to the three different glass pane thicknesses considered (the beam total thickness was kept constant): the nominal thickness (15.0 mm) and the upper and lower thickness production limits (respectively, 15.5 mm and 14.5 mm). The time-temperature dependency of the PVB interlayer was considered by assuming its properties for the test loading time and temperature (*cf.* section

3.2.2), together with the initial bow and rotation measured in the tests, respectively, $u_0 = 2.49$ mm and $\theta_0 = 0.0012$ rad.

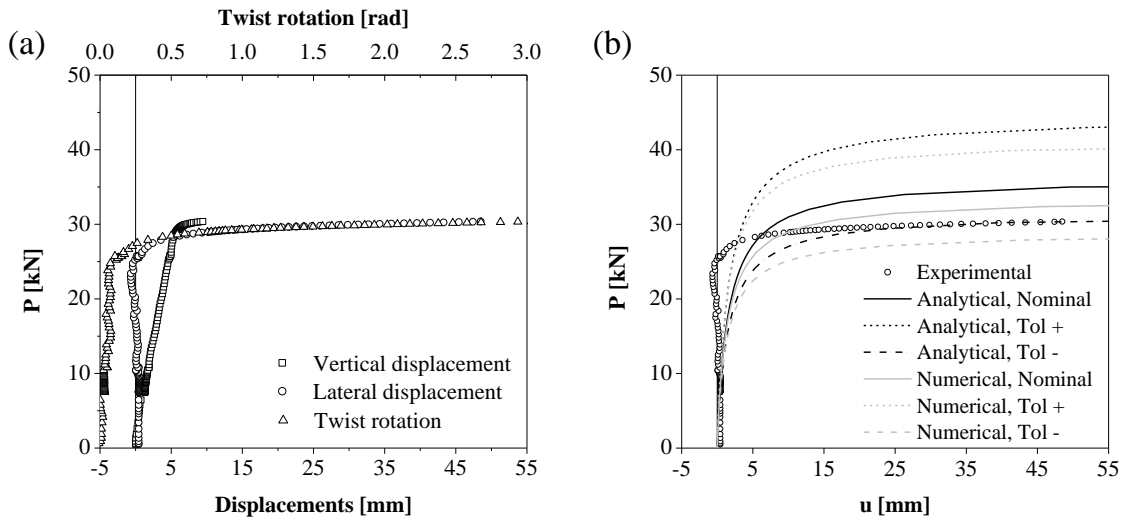


Fig. 3.9 – Experimental load equilibrium path in terms of (a) twist rotation, vertical and lateral displacements; (b) experimental, analytical and numerical load equilibrium path (for different glass panes thicknesses).

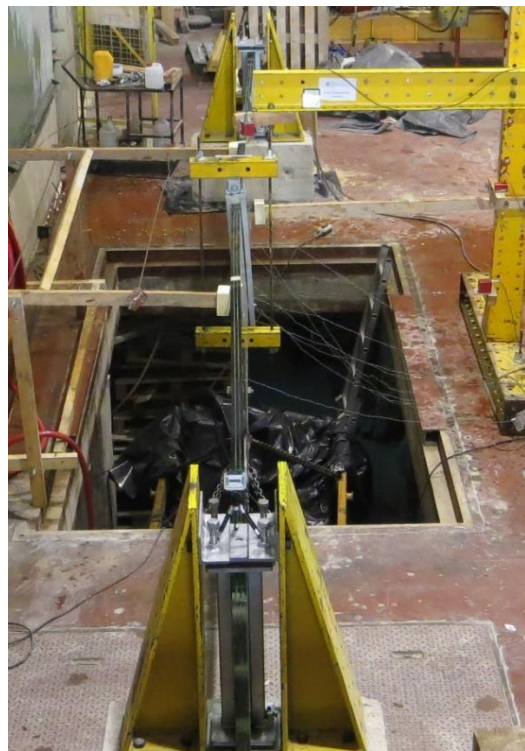


Fig. 3.10 – Deformed shape at the end of the test.

Considering the nominal thickness of the glass panes (15.0 mm), the agreement between experimental and analytical equilibrium paths is poor. In particular, for load values close to the experimental critical load, the analytical model significantly underestimates the lateral displacements, thus providing non-conservative and unsafe predictions of the beam’s performance, given the unstable mechanism that characterizes the lateral-torsional buckling phenomenon. If the estimated glass thickness (14.5 mm) is

considered instead of the nominal one, the analytical equilibrium path becomes much closer to the experimental curve. Similar conclusions were drawn by Belis *et al.* [3.4] for PVB-laminated glass beams with a slenderness ratio from 10 to 25 and a total length of 3000 mm. In that study, the experimental load vs. out-of-plane displacement curves of those beams were bounded by the analytical curves corresponding to the upper and lower limits of glass panes' thickness (assuming the standard thickness tolerances).

3.4.4.3 Elastic buckling load

The elastic buckling load of the beam tested was determined using the Southwell method (*cf.* section 3.3.4). Fig. 3.11 depicts the linear regression of the test data using Eq. (3.18), for which a very high correlation coefficient was observed ($R^2 = 0.9992$). Based on the slope of the regression line, a critical load of $P_{cr,Sth} = 30.0$ kN was estimated.

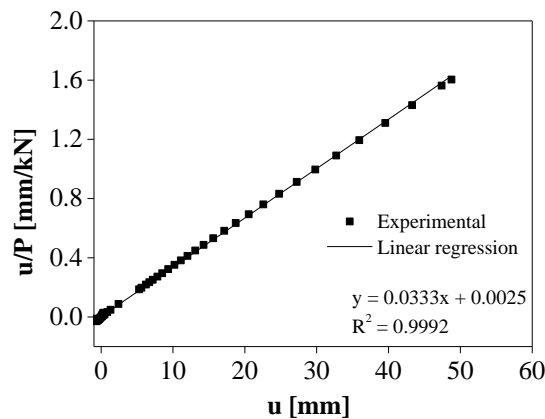


Fig. 3.11 – Southwell plot.

The analytical elastic buckling load was also estimated using Eq. (3.16) taking into account the test conditions, namely the test duration (20 minutes) and temperature (23 °C), which, as discussed earlier, significantly affect the interlayer's shear properties. Accordingly, for a shear modulus of $G_{int} = 0.783$ MPa, and considering the nominal thickness of the glass panes ($t_i = 15$ mm), the analytical critical load is 35.6 kN, which is almost 18% higher than the experimental value. If the estimated thickness ($t_i = 14.5$ mm; *cf.* section 3.2.1) is considered, instead of the nominal one, the analytical critical load becomes 30.3 kN, i.e. only 1.0% higher than that experimentally measured. This result, which is consistent with those obtained for the equilibrium paths (*cf.* Fig. 3.9-b), supports the geometric measurements made in the present experimental campaign. These results are also consistent with previous studies. For example, Belis *et al.* [3.4] reported relative differences of 11% between experimental and analytical critical loads of several beam specimens made of annealed glass, with a ratio L/h of 10. In the same study, lower relative differences were reported for beams made of thermally tempered glass beams.

3.5 NUMERICAL STUDY

This section presents the numerical study developed in order to assess the viability of using conventional FE models in order to simulate the linear, buckling and post-buckling responses of long-span laminated glass beams. The FE model of the beam tested is first described in section 3.5.1. Next, in section 3.5.2, the numerical results are presented and compared with analytical and experimental data; in addition, the model is also used to analyse the stresses in the beam.

3.5.1 Description of the numerical models

A three dimensional (3D) FE model of the 8.20 m long laminated glass beam was implemented using ABAQUS Standard version 6.12 [3.34]. Due to the symmetry of the beam geometry and test setup, only half of the beam's length was modelled – thus, the model was 4.10 m long and 0.60 m high⁷. The thicknesses of the glass layers and interlayer films were defined according to the three different values of glass thickness considered in the analytical study (*cf.* section 3.3.2), with the total nominal thickness of the beam ($t_{total} = 48.04$ mm) being kept constant.

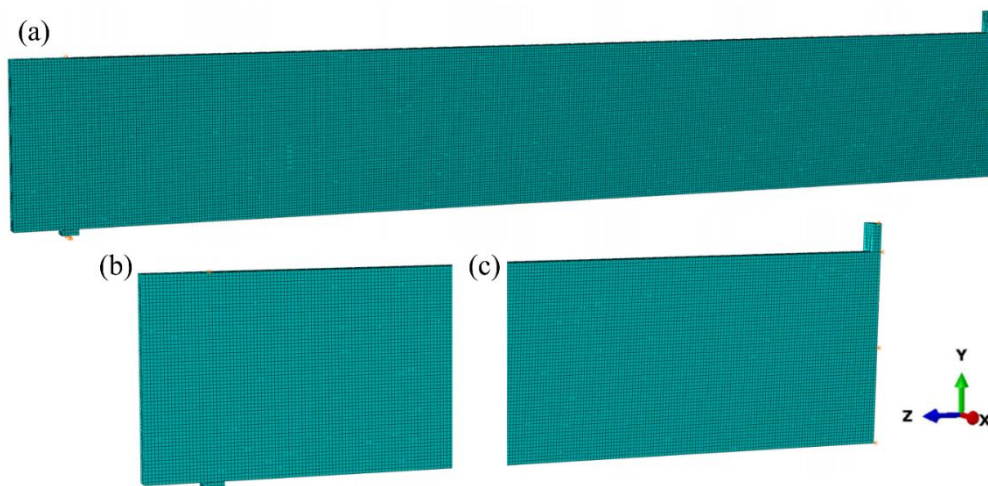


Fig. 3.12 – 3D numerical model: (a) overview, (b) support and (c) point load details.

The glass layers were modelled with 8-node continuum shell elements with reduced integration⁸ (SC8R), whereas the interlayers were modelled with 8-node solid elements with reduced integration (C3D8R).

⁷ Due to its intrinsic symmetry, the numerical model only allows the adoption of symmetric geometrical imperfections, such as the sinusoidal approximation presented before (*cf.* Fig. 3.8). More complex geometrical imperfections (without symmetry) would require the use of a numerical model of the whole beam (without symmetry simplifications) and not only half beam. A more comprehensive analysis, reflecting the asymmetric configuration of the measured imperfection (*cf.* Fig. 3.8), would consider an imperfection of the type $A_1 \sin(\pi x/L_0) + A_2 \sin(2\pi x/L_0)$, combining a first component (symmetric, with one half-wave) with a second component (anti-symmetric, with two half-waves). However, the computation effort would double without significant improvements of the maximum load.

⁸ The reason for adopting continuum shell elements to simulate the glass panes was mostly related with the construction of the FE model, as these finite elements allowed building the layered beam using only 3D elements in just one geometrical part. In fact, conventional shell elements would have required the definition of five different parts; hence, it would have been necessary to provide the kinematic constraints to correctly transfer the moment/rotation at the reference surface of the shell elements to the solid elements.

These latter elements were also used to simulate the steel and aluminium parts used respectively in the supports (Fig. 3.12-b) and in the load application system (*cf.* section 3.4.1 and Fig. 3.12-c). The glass-interlayer interfaces were modeled as rigid connections (merged instances option in ABAQUS⁸). A rigid connection (tie constraint) was considered between the metallic parts (supports and load application system) and the laminated glass beam.

A quadrangular regular mesh was used in both glass (continuum shell) and interlayer (solid) finite elements, with both types of elements presenting $10 \times 10 \text{ mm}^2$ of area along the beam length. Across the thickness, the glass layers were modelled with a single continuum shell element⁹, whereas the interlayer films were discretised using two layers of elements. The model comprised 197,184 finite elements and 678,861 degrees of freedom (Fig. 3.12-a).

Both glass and PVB were simulated as linear elastic isotropic materials, considering the mechanical properties presented in section 3.2.2. The viscoelastic behaviour of PVB was considered by assuming different mechanical properties for two different load durations (3 s and 20 min), both for a temperature of 23 °C (*cf.* section 3.2.2, Table 3.1).

The boundary conditions were defined in order to replicate the test setup: (i) the vertical displacements (*yy* direction) were restrained at the bottom edge of the support's aluminium profile; (ii) the longitudinal displacements (*zz* direction) were prevented along the horizontal axis of symmetry at the mid-span section; and (iii) the lateral displacements (*xx* direction) were restrained at the support along the beam's vertical axis of symmetry.

Linear buckling (eigenvalue) analyses were first performed in order to determine the critical buckling loads and to evaluate the deformed shape of the corresponding buckling modes. Using the results of the linear buckling analysis, initial imperfections with the shape of the first sinusoidal buckling mode were introduced in the FE model, with amplitude of 2.49 mm (corresponds to the maximum mid-span lateral displacement of the sinusoidal approximation curve – *cf.* section 3.4.4.1). Next, a geometrically non-linear static analysis was performed using the static general method of ABAQUS in order to compute the load *vs.* displacement response of the laminated glass beam.

3.5.2 Results and discussion

The numerical load *vs.* vertical displacement curve of the beam is depicted in Fig. 3.13. The numerical major axis flexural stiffness is in very good agreement with its experimental counterpart (relative difference of +3.4%).

⁹ The discretization adopted across the thickness of the constituent element (glass plies and interlayers) was based on a preliminary mesh sensitivity study. The results of the those numerical analyses, with one or two elements across the thickness of the glass layers, were very similar to each other and also to the analytical results. Based on these results, all further analyses were conducted with models comprising one element across the thickness of the glass layers. Unlike the glass layers, it was deemed necessary to consider two finite elements across the thickness of the interlayer, due to its much lower stiffness.

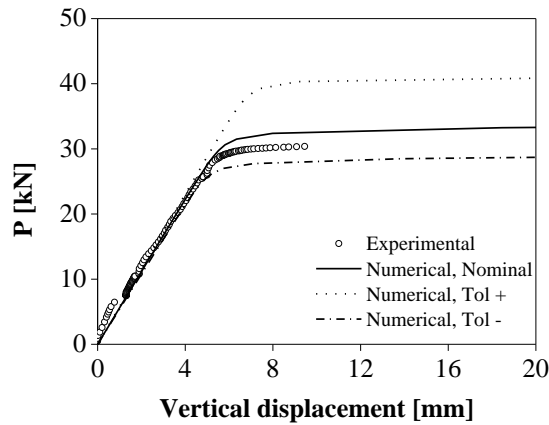


Fig. 3.13 – Experimental and numerical (for different glass panes thicknesses) vertical deflection.

Fig. 3.14-a illustrates the shape of the first buckling mode, corresponding to the lateral-torsional buckling of the laminated glass beam. The numerical critical buckling loads and equilibrium paths are presented respectively in Table 3.2 and Fig. 3.9-b, where they are compared with the corresponding analytical and experimental results. One may see that the numerical results are fairly similar to the analytical ones (maximum relative difference of 6.7%), for the three glass pane thicknesses and two levels of interaction considered (i.e. two different G_{int} that correspond to two different load durations).

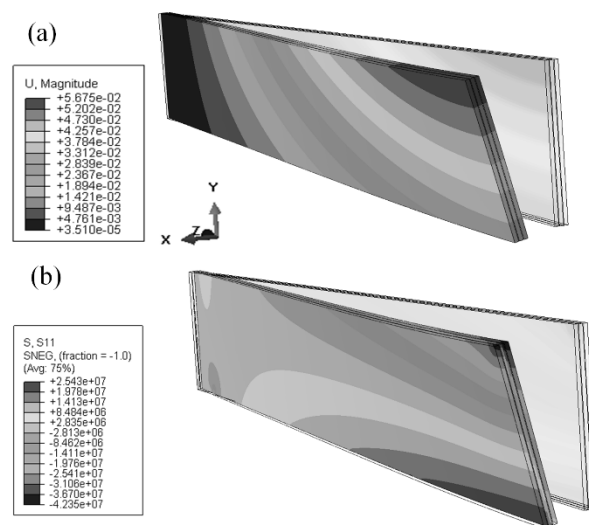


Fig. 3.14 – Numerical buckling shape, (a) displacements (in m, according to colour scale) (b) and principal stresses (in Pa, according to colour scale).

It should be emphasized that the analytical curve tends to the critical load calculated using Eq. (3.16) and this is based on the assumption of fully solid section, i.e. considering the twisting rotation and the lateral displacement as the sole degrees-of-freedom. As shown by Challamel and Girhammar [3.31], the lateral-torsional buckling of bi-layer beams may be influenced by relative (different) vertical displacements between layers. The relevance of this effect (slip between glass layers) strongly depends on the shear stiffness of the interlayer. Despite the fact these relative displacements between glass layers

were not measured in the experiments, these very low slip displacements may influence the post-critical path. In fact, note that the numerical curves in Fig. 3.9-b (grey curves) are below the analytical curves (black curves), meaning that the former reflect less stiffness than the latter due to the consideration of interlayer slip in the finite element model (this is neglected in the analytical formulation of P_{cr}).

Table 3.2 – Analytical, numerical and experimental buckling loads of the beam tested for two different levels of interaction (different G_{int}) and for three different glass thicknesses (within standard tolerances of ± 0.5 mm).

Buckling load [kN]	* $G_{int} = 8.061$ MPa ($t = 3$ s)			# $G_{int} = 0.783$ MPa ($t = 20$ min)		
	$t_i = 14.5$ mm	$t_i = 15.0$ mm	$t_i = 15.5$ mm	$t_i = 14.5$ mm	$t_i = 15$ mm	$t_i = 15.5$ mm
Analytical	58.4	66.9	81.2	30.3 (+1.0%)	34.8 (+16.0%)	42.6 (+42.0%)
Numerical	57.1	65.6	80.4	28.4 (-5.3%)	33.3 (+11.0%)	42.3 (+41.0%)
Experimental	-			30		

G_{int} were obtained considering PVB at a temperature of (*) 20° C and of (#) 23° C, cf. Fig. 3.3).

The best numerical estimates were obtained when the lowest standard thickness of the glass panes (14.5 mm) was considered, together with the interlayer properties corresponding to the test duration and temperature (for PVB material, a loading time of 20 min at 23 °C results in a $G_{int} = 0.783$ MPa). In this case, the relative difference to experimental results in terms of critical buckling load is only -5.3% (vs. +11.0% for the nominal thickness).

Fig. 3.14-b plots the principal stresses in the glass panes corresponding to the maximum lateral deflection attained in the test. For this deformation, one can observe that the maximum principal stress, developing in the bottom part of the mid-span section, is around 25 MPa. This value, which is much lower than the characteristic strength of fully tempered glass, justifies why the beam did not collapse during the test. Fig. 3.15 plots the variation of the maximum principal stresses as a function of the applied load for a laminated glass beam comprising glass panes with 14.5 mm of thickness. One can observe that such strength would be attained for an applied load of 29.9 kN (assuming that the beam could carry loads higher than the numerical LTB critical load), corresponding to a lateral deflection as high as 230 mm.

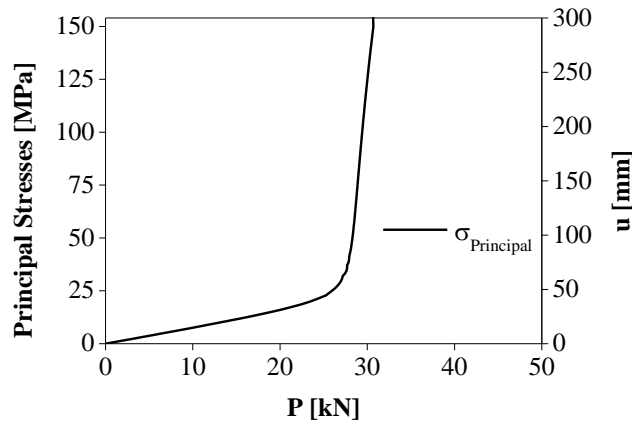


Fig. 3.15 – Evolution of the numerical principal (tensile) stresses evolution during LTB deflection.

3.6 CONCLUDING REMARKS

Chapter 3 presented an analytical, experimental and numerical study on the lateral-torsional buckling behaviour of long-span laminated glass beams. The following main conclusions are drawn:

- 1) The results obtained confirm the susceptibility of laminated glass beams to lateral-torsional buckling and therefore highlight the need to duly take this phenomenon into account during the design stage.
- 2) The analytical study showed that the equations developed by Machado-e-Costa [3.9] aiming to estimate the flexural and torsional stiffness of laminated glass sections used, together with the formulae provided in Eurocode 3 [3.28] and in the recent *Guidance for the European Structural Design of Glass Elements* [3.13] are able to accurately predict the lateral-torsional buckling behaviour of long-span 3-layer laminated glass beams.
- 3) The numerical study showed that conventional numerical FE models are also able to predict with very good accuracy the linear, buckling and post-buckling responses of laminated glass beams.
- 4) This study confirmed the importance of adequately considering at the design stage the influence of both temperature and loading time on the shear behaviour of PVB interlayers, since the elastic buckling load significantly decreases when these parameters increase. For instance, for the conditions tested in this study, when temperature increases from 20 °C to 23 °C the lateral-torsional buckling critical load decreases by 4%; similarly, when the load duration increases from 3 s to 20 min, the lateral-torsional buckling critical load decreases almost 46%.
- 5) This study also highlighted the importance of the glass panes thickness in the lateral-torsional buckling resistance and behaviour of laminated glass beams. It was shown that small reductions in the thickness of the glass panes, even within the standard geometric tolerances, may lead to considerable reductions of the critical load, hence affecting the structural safety of laminated glass members. For the conditions tested in this study, if the thickness of the glass panes decreases from 15.0 mm (nominal value) to 14.5 mm (lower bound of geometric tolerance and estimated value of the beam's real thickness), the analytical and numerical estimates of the lateral-torsional buckling critical load decrease by 13% and 15%, respectively.
- 6) Moreover, a much better agreement between experimental, analytical and numerical results (either in terms of lateral-torsional buckling strength or in terms of post-buckling behaviour) was obtained when the lower bound of the standard thickness tolerances was considered. Similar results had been reported in other studies. Therefore, these potential differences should be duly taken into account by design standards, either through direct assumptions about the members' thickness or through the respective partial safety factors.

One last word to remind that it is not just the polymers' properties that are affected by load duration or temperature. In fact, as discussed in chapter 2, the glass strength, not addressed in the present study, is also highly dependent on those factors [3.35–3.41]. Future studies should address this topic.

3.7 REFERENCES

- [3.1] Luible A. Stabilität von Tragelementen aus Glas. PhD thesis n° 3014, École Polytechnique Fédérale de Lausanne, Switzerland, 2004.
- [3.2] Kasper R, Sedlacek G, Feldmann M. Das Biegedrillknickverhalten von Glasträgern aus Verbundglas. Verlag Für Architekt. Unf. Tech. Wissenschaften GmbH Co KG 2007;76:167–76.
- [3.3] Belis J. Kipsterkte van Monolithische en Gelamineerde Glazen Liggers. PhD thesis, Ghent University, Belgium, 2005.
- [3.4] Belis J, Bedon C, Louter C, Amadio C, van Impe R. Experimental and analytical assessment of lateral torsional buckling of laminated glass beams. *Eng Struct* 2013;51:295–305.
- [3.5] Luible A, Crisinel M. Design of glass beams subjected to lateral torsional buckling. IABSE Symp. Responding to Tomorrow's Challenges *Struct. Eng.*, Budapest: 2006, p. 42–3.
- [3.6] Amadio C, Bedon C. Buckling of laminated glass elements in out-of-plane bending. *Eng Struct* 2010;32:3780–8.
- [3.7] Amadio C, Bedon C. A buckling verification approach for monolithic and laminated glass elements under combined in-plane compression and bending. *Eng Struct* 2013;52:220–9.
- [3.8] Bedon C, Belis J, Luible A. Assessment of existing analytical models for the lateral torsional buckling analysis of PVB and SG laminated glass beams via viscoelastic simulations and experiments. *Eng Struct* 2014;60:52–67.
- [3.9] Machado-e-Costa M. Modelling of The Structural Behavior of Laminated Glass Beams. Study of the Lateral-Torsional Buckling Phenomenon. MSc dissertation, Lisbon University, Portugal, 2015.
- [3.10] Bedon C, Amadio C. Flexural–torsional buckling: Experimental analysis of laminated glass elements. *Eng Struct* 2014;73:85–99.
- [3.11] Galuppi L, Royer-Carfagni GF. Effective thickness of laminated glass beams: New expression via a variational approach. *Eng Struct* 2012;38:53–67.
- [3.12] Foraboschi P. Optimal design of glass plates loaded transversally. *Mater Des* 2014;62:443–58.
- [3.13] Report EUR 26439 EN Guidance for European Structural Design of Glass Components. Institute for the Protection and Security of the Citizen, Joint Research Centre, Luxembourg: 2014.
- [3.14] The Institution of Structural Engineers. *Structural Use of Glass in Buildings* (Second edition). London: The Institution of Structural Engineers (ISE); 2014.
- [3.15] AS 1288 Glass in buildings - Selection and installation. Australia Standards, Sidney: 2006.
- [3.16] CNR-DT 210/2013 Istruzioni per la Progettazione, l'Esecuzione ed il Controllo di Costruzioni con Elementi Strutturali di Vetro. Consiglio Nazionale Delle Ricerche, Roma: 2013.
- [3.17] EN 572-8: 2012 Glass in building - Basic soda lime silicate glass products – Part 8: Supplied and final cut sizes. European Committee for Standardization (CEN), Brussels: 2012.
- [3.18] Callewaert D, Belis J, Depaeppe J. Influence of temperature and load duration on glass/Ionomer laminates torsion and bending stiffness 2. *Int. Symp. Appl. Archit. Glas. ISAAG 2008*, Munich: 2008, p. 51–63.
- [3.19] Callewaert D. *Stiffness of Glass / Ionomer Laminates in Structural Applications*. PhD thesis, Ghent University, Belgium, 2012.
- [3.20] Galuppi L, Royer-Carfagni G. Buckling of three-layered composite beams with viscoelastic interaction. *Compos Struct* 2014;107:512–21.
- [3.21] Duser A van, Jagota A, Bennison SJ. Analysis of glass/polyvinyl butyral laminates subjected to uniform pressure. *J Eng Mech* 1999;125:435–42.

- [3.22] Luible A, Crisinel M. Buckling strength of glass elements in compression. *Struct Eng Int J Int Assoc Bridg Struct Eng* 2004;14:120–5.
- [3.23] Calderone I, Davies PS, Bennison SJ, Xiaokun H, Gang L. Effective laminate thickness for the design of laminated glass. *Glas. Performance Days 2009, Tampere, Finland: 2009*, p. 1–5.
- [3.24] Amadio C, Asce M, Bedon C. Buckling of laminated glass elements in compression. *J Struct Eng* 2011;137, No. 8:803–10.
- [3.25] Kasper R. *Tragverhalten von Glastragen*. PhD thesis, RWTH Aachen University, 2005.
- [3.26] Galuppi L, Royer-Carfagni G. Enhanced effective thickness of multi-layered laminated glass. *Compos Part B Eng* 2014;64:202–13.
- [3.27] Timoshenko SP, Gere JM. *Theory of Elastic Stability*. 2nd Editio. New York: McGraw-Hill; 1961.
- [3.28] ENV 1993-1: Eurocode 3 Design of steel structures - Part 1-1: General rules and rules for buildings. European Committee for Standardization (CEN), Brussels: 1992.
- [3.29] Haldimann M, Luible A, Overend M. *Structural Use of Glass*. Zurich: IABSE-AIPC-IVBH; 2008.
- [3.30] N. Boissonnade, R. Greiner, J.P. Jaspart, J. Lindner. *New Design Rules in EN 1993-1-1 for Member Stability - ECCS publication #119 2006*.
- [3.31] Challamel N, Girhammar UA. Lateral-torsional buckling of vertically layered composite beams with interlayer slip under uniform moment. *Eng Struct* 2012;34:505–13.
- [3.32] Mandal P, Calladine CR. Lateral-torsional buckling of beams and the Southwell plot. *Int J Mech Sci* 2002;44:2557–71.
- [3.33] Belis J, Mocibob D, Luible A, Vandebroek M. On the size and shape of initial out-of-plane curvatures in structural glass components. *Constr Build Mater* 2011;25:2700–12.
- [3.34] Dassault Systèmes. *ABAQUS 6.12 Documentation 2012*.
- [3.35] Haldimann M. *Fracture Strength of Structural Glass Elements - Analytical and Numerical Modelling, Testing and Design*. PhD thesis n° 3671, École Polytechnique Fédérale de Lausanne, Switzerland, 2006.
- [3.36] Rodichev Y, Maslov V, Netychuk A, Bodunov V, Yevplov Y. Bending strength and fracture of glass materials under the different loading conditions 2007:615–8.
- [3.37] Veer F, Louter P, Bos F. The strength of annealed, heat-strengthened and fully tempered float glass. *Fatigue Fract Eng Mater Struct* 2009;32:18–25.
- [3.38] Lindqvist M, Vandebroek M, Louter C, Belis J. Influence of edge flaws on failure strength of glass. *Glas. Perform. Days 2011, Tampere, Finland: 2011*, p. 126–9.
- [3.39] Vandebroek M, Lindqvist M, Belis J, Louter C. Edge strength of cut and polished glass beams. *Glas. Perform. Days 2011, Tampere, Finland: 2011*, p. 476–9.
- [3.40] Veer F a., Rodichev YM. The structural strength of glass: hidden damage. *Strength Mater* 2011;43:302–15.
- [3.41] Wang Y, Wang Q, Shao G, Chen H, Sun J, He L, et al. Experimental study on critical breaking stress of float glass under elevated temperature. *Mater Des* 2014;60:41–9.

FLEXURAL CREEP BEHAVIOUR OF FULL-SCALE LAMINATED GLASS PANELS

ABSTRACT

The structural use of laminated glass elements, comprising either polyvinyl butyral (PVB) or SentryGlas (SG) interlayers, has considerably increased in the last decade. Despite exhibiting significantly different performance, the properties of both interlayers are time and temperature dependent. Therefore, it is relevant to understand their long-term response, namely for glass panels subjected to out-of-plane loads. For now, the viscoelastic models of the interlayers' shear modulus available in the literature are based either on (i) dynamic mechanical analyses (DMA) of small-scale interlayer coupons, or (ii) very short-term creep/relaxation tests of small-scale laminated glass specimens. This chapter presents experimental and analytical investigations on the creep response of full-scale laminated glass panels. The experimental study comprised relatively long-term (350 h) flexural creep tests on full-scale 3-layer PVB and 4-layer SG-laminated glass panels. The experimental data was fit using Findley's power law and the resulting creep predictions were compared with those obtained considering different interlayers' material models available in the literature. The results obtained confirm that laminated glass panels with PVB interlayer present significantly higher creep deformations than those made of SG interlayer: after 350 h of loading, the mid-span deflections of PVB and SG-laminated glass panels increased 120% and 1.6%, respectively. Findley's power law was able to accurately simulate the mid-span deflections of both laminated glass panels during the 350 h of testing. For the PVB panel, deflection predictions for a load duration of 50 years using the DMA-based material models taken from the literature were considerably higher than those predicted using Findley's power law, despite the good initial agreement (up to 4,000 h). For the SG panel, although an overall better agreement was observed between Findley's power law and deflection predictions obtained from material models available in the literature, significant differences were still encountered, namely for the material model based on DMA.

4.1 INTRODUCTION

Laminated glass elements, comprising two or more glass plies bonded with a thin polymeric interlayer, are usually a mandatory requirement for most architectural glass applications, due to their ability to provide safety in case of unforeseen, accidental or malevolent events. Polyvinyl butyral (PVB) is the most used interlayer material since the 1960's¹. However, the relatively poor material properties of PVB, namely its high susceptibility to temperature and long-term actions, prevents glass laminates to be fully exploited in structural applications [4.1–4.3]. In these cases, laminated glass with stiffer interlayers (e.g. stiffer PVBs or ionomer polymers) are now being more frequently used as they allow for substantial gains in terms of pre and post-cracking behaviour [4.4–4.6], being also less prone to the effects of environmental agents, such as humidity and ultraviolet radiation [4.7, 4.8]. Furthermore, for the temperature range of common structural applications (-20 °C to 80 °C) the stiffness of those interlayers is significantly higher and their viscoelasticity is much lower [4.7, 4.9].

Several previous studies have addressed the structural behaviour of laminated glass elements under different temperatures and load durations [4.9–4.13], aiming at fully characterizing their flexural and torsional stiffness and strength for long-term loads under different service conditions. Regardless of the chosen interlayer, both flexural and torsional stiffnesses are highly influenced by the shear modulus of the interlayer (G_{im}) [4.2, 4.14, 4.15], which, on the other hand, presents high time and temperature dependency. Therefore, it is very relevant to carefully investigate and characterize the viscoelastic behaviour of the interlayer's properties and to adequately consider it when designing laminated glass members (e.g. chapter 3).

In previous studies, the long-term response of interlayers or laminated glass members (i.e. their creep and relaxation behaviour) has been evaluated using essentially one of two approaches: (i) dynamic mechanical analyses (DMA) on small-scale interlayer coupons; or (ii) creep/relaxation tests on relatively small-scale laminated glass specimens. The former method is often used by interlayer manufacturers [4.11–4.13] for being easy and fast to perform and relatively inexpensive (described ahead in section 4.2.1). The latter method, used mainly in the form of torsional or flexural tests [4.9, 4.16], has the advantage of allowing to assess the actual performance of (small-scale) laminated glass members, including the potential influence of different factors: the interlayers' properties, size effects, glass-interlayer adhesion effects due to the lamination process, or edge influence. In both approaches, the long-term response of the interlayers/laminates has been predicted (extrapolated) based on the Time-Temperature Superposition Principle² (TTSP) [4.17], which can be applied based on relatively short-

¹ Laminated glass bonded with PVB is commonly referred to as *Laminated Safety Glass*.

² Due to the polymeric nature of interlayers, the effects of temperature and load duration on the structural response of glass laminates can be assessed simultaneously and evaluated using similar methodologies. In fact, TTSP is an empirical principle that makes use of polymers' time-temperature dependency to extrapolate the effects of a long-term load from results of short-term tests conducted at a higher temperature.

term relaxation/creep tests (detailed ahead in section 4.2.1). Despite the advantages of using the TTSP to estimate the long-term behaviour of glass laminates and its successful application for a wide range of polymeric materials, such approach requires validation from long-term experiments in full-scale members. This is especially relevant for many civil engineering structures, which are often designed for service lives spanning various decades [4.18]. According to the best of the author's knowledge³, such validation tests are yet to be performed. Furthermore, all previous studies available in the literature used only the TTSP approach; no other empirical methods or models have been assessed, including those with proved accuracy in the field of composite structures of polymeric nature (e.g. Findley's power law).

This chapter presents experimental and analytical investigations about the creep response of full-scale laminated glass panels. The main objectives of this work are three-fold: (i) to investigate, for a relatively long duration of loading, the creep response of full-scale laminated glass panels comprising two different interlayer materials, PVB and the ionoplast polymer SentryGlas (SG); (ii) to develop a simple predictive creep model, capable of simulating the long-term creep response of the laminated glass panels based on Findley's power law (not using the TTSP), and (iii) to compare the short and long-term predictions obtained from that law with those based on material models of interlayers available in the literature (obtained using the TTSP approach). In addition to the introduction and conclusions section, the chapter is organized in three other sections. In section 4.2 the existing creep models for both PVB and SG interlayers as well as the main assumptions of Findley's power law are briefly presented. Section 4.3 describes the experimental campaign, which comprised flexural creep tests on full-scale PVB and SG-laminated glass panels. Finally, in section 4.4 creep models are proposed based on the experimental data and the corresponding predictions are compared with those obtained from the interlayers' material models reported in the literature.

4.2 REVIEW OF CREEP MODELS

4.2.1 Creep models for polymer interlayers

The creep and relaxation phenomena in laminated glass are essentially related with the viscoelastic nature of polymeric interlayers, whose behaviour can be highly time and temperature dependent. Results obtained in previous studies [4.9, 4.11, 4.12, 4.19] are usually presented in the form of reduction curves of a specific material property valid over a range of loading times and at a given reference temperature, obtained from either DMA tests on interlayer coupons or torsional and flexural tests on (small-scale) laminated glass panels. Frequently, such curves are analytically represented using Prony series⁴, whose multiple parameters are determined through curve fitting of experimental data. The number of Prony series terms depends on the time period of interest and on the experimental data available for curve fitting. In the

³ References published in languages other than English are not mentioned or were not analysed in the present study.

⁴ In such cases, Prony series are used as the mathematical representation of the Maxwell-Weichert viscoelastic model [4.28].

aforementioned works, the shear modulus reduction curves have been represented using 11 to 14 terms, providing a good approximation over a wide range of applications from 10^{-14} to 10^{14} s. Furthermore, using the Williams-Landel-Ferry (WLF) equation [4.17], whose parameters are calculated from the TTSP fitting, it is possible to extrapolate the long-term behaviour for temperatures other than the reference one.

Fig. 4.1 presents the shear modulus reduction curves for PVB reported by van Duser *et al.* [4.11] (also used in the work of Belis [4.19]) and by D’Haene and Savineau [4.12]. These curves refer to PVB products⁵ *Butacite* from DuPont⁶ (hereafter referred to as PVB1999) and *Saflex* from Solutia (hereafter referred to as PVB2007), respectively. Both master curves were obtained from DMA tests and were normalized to a reference temperature of 20 °C. Despite the inherent differences in the chemical composition of the PVB produced by the different manufacturers, the two curves present only minor differences, especially for the range of interest of loading times (from 1 s to 50 years) for structural glass applications in buildings and other common structures [4.18]. Beyond this range, some differences are noticeable, but these are mainly related with the values assumed for the bounds of the PVB properties, which can differ significantly among different authors.

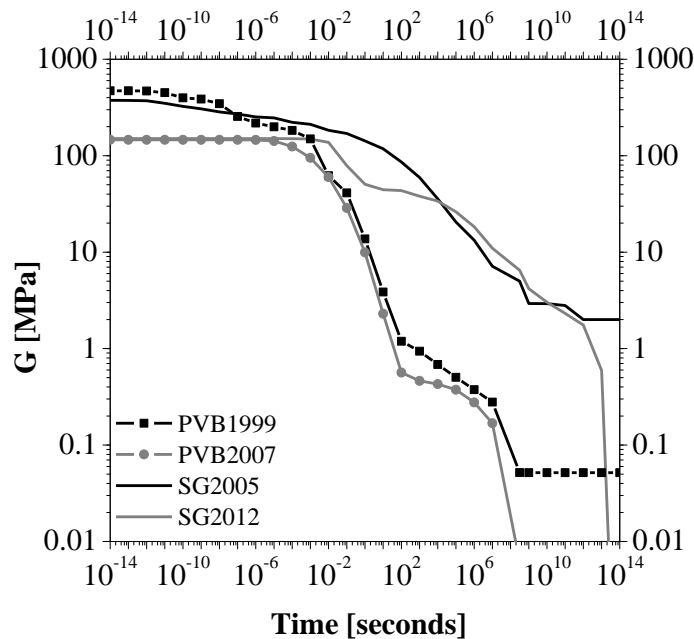


Fig. 4.1 – Shear modulus master curves for the reference temperature of 20 °C of PVB1999 (*Butacite* [4.11]), PVB2007 (*Saflex* [4.12]), SG2005 (DMA tests [4.19]) and SG2012 (tests on glass laminates [4.9]).

For the SG interlayer, two shear modulus reduction curves (G_{SG}) reported in the literature were considered: (i) the DMA results provided by the manufacturer DuPont⁶ (hereafter referred to as SG2005) and presented by Belis [4.19], and (ii) the reduction curve presented by Callewaert [4.9] obtained from

⁵ Each producer has its own formulation (usually classified), thus the interlayer’s properties may change from producer to producer.

⁶ The results were provided prior to the trademark change of Butacite and SentryGlas from DuPont to Kuraray.

experiments on laminated glass panels⁷ (hereafter referred to as SG2012). Fig. 4.1 depicts both master curves normalized to a reference temperature of 20 °C. Despite the fact of being representative of the same material, the estimation of the material properties using these two test setups resulted in some differences. On the one hand, the upper/lower bounds⁸ for G_{SG} assumed/determined by Callewaert were significantly lower than the ones published by the producer using DMA tests (375 MPa vs. 150 MPa, and 2 MPa vs. 0 MPa, respectively). On the other hand, within the typical range of load durations of practical interest (1 s to 50 years), the reduction curves exhibit similar developments intersecting twice. The above-mentioned differences might be related with (i) the different methods (DMA tests on interlayers vs. creep tests on glass laminates) used to assess the interlayer's viscoelastic properties, and/or (ii) differences (even if small) in the chemical composition of SG, which might have changed the material properties. Nevertheless, it is clear that SG presents higher shear modulus than PVB for a large range of temperatures and load durations, which results in improved structural performance (higher shear interaction) for various structural applications.

4.2.2 Findley's power law

Many models have been developed to describe the creep behaviour of polymers [4.20], most of them being empirical, i.e. their analytical expressions do not follow any assumptions concerning the mechanical behaviour of the materials or their physical laws; they are rather entirely based on experimental data. Findley's power law is one of the most commonly used empirical models due to its simplicity and successful application to a wide range of polymers [4.20, 4.21] and fibre reinforced polymer (FRP) materials [4.22–4.26]. Its original form (Eq. (4.1)), developed for tensile properties, states that the total axial strain $\varepsilon(\sigma, t, T)$, which is stress, time and temperature dependent, can be described by the sum of two components: (i) the stress-dependent initial elastic strain, $\varepsilon_0(\sigma, T)$, and (ii) the stress-time-temperature-dependent (viscoelastic) strain, represented by a power law, $m_e \cdot t^{n_e}$, where m_e is the stress-temperature-dependent coefficient, n_e is the stress-independent material constant that may be function of environmental conditions, and t_0 and t are the initial time corresponding to $\varepsilon_0(\sigma)$ and the time period covered, respectively.

$$\varepsilon(\sigma, t, T) = \varepsilon_0(\sigma, T) + m_e \cdot (t/t_0)^{n_e}, \quad t > t_0 \quad (4.1)$$

Eq. (4.1) can be adapted to other loading situations or to other material properties (e.g. compression or shear strains, torsion rotations, total vertical displacement, Young's modulus or shear modulus). Eqs. (4.2-a) and (4.2-b) represent the adaptations for creep shear strain and for creep deflection, respectively,

⁷ Callewaert [4.9] suggested a shear reduction curve based on flexural and torsional tests of 2-layer SG laminates at different temperatures and loading periods. According to the author, the viscoelastic Maxwell-Weichert (fit using Prony series) curve presented should accurately estimate values in a range of temperatures from 5 °C to 65 °C.

⁸ Note that the periods of time corresponding to these bounds (respectively 10^{-14} s and 10^{14} s) are not structurally relevant for civil engineering structural applications.

$$\gamma(\tau, t, T) = \gamma_0(\tau, T) + m_g \cdot t^{n_g} \quad \delta(\sigma, t, T) = \delta_0(\sigma, T) + m_d \cdot t^{n_d} \quad (4.2-a,b)$$

with the equation terms presenting similar meanings as before for the tensile creep, but with the due adaptation for shear strains and deflections.

4.3 EXPERIMENTAL CAMPAIGN

As mentioned, the deformation increase over time of glass laminates subjected to permanent loads occurs mainly due to the viscoelastic nature of polymeric interlayers. Therefore, creep effects will be more significant in applications where the interlayer plays a major role, namely when high shear deformations develop in such layers. This is particularly relevant for structural applications where laminated glass panels are subjected to out-of-plane/transverse loads (e.g. bending about the minor axis). In this chapter, the assessment of the long-term loading effects on long-span glass laminates encompassed flexural tests on two different laminated glass panels: (i) a 3-layer laminated glass panel with PVB interlayer; and (ii) a 4-layer laminated glass panel with SG interlayer. Both laminated glass panels were made of fully tempered glass plies with polished edges.

4.3.1 Specimens geometry

The total length (L), the width (b) of the outer glass plies and the total thickness (t_{total}) of the specimens were measured in several points along their length using a metric ruler with 1 mm of precision for height and length and a calliper rule with 0.05 mm of precision for the total thickness. Table 4.1 summarizes the main nominal and measured dimensions of both panels in terms of L , b and t_{total} , and also the nominal values for the glass layers (t) and interlayer (t_{int}) thickness. Small differences between the nominal and the measured values were found, with all the measured properties being within the production standard (EN 572-8 [4.27]) tolerances⁹.

Table 4.1 - Geometrical properties of panels: nominal and measured (in brackets).

Panel	L [m]	b [mm]	t [mm]	t_{int} [mm]	t_{total} [mm]
3-layer PVB panel	8.20 (8.28)	600 (602)	15	1.52	48.04 (48.26)
4-layer SG panel	9.50 (9.85)	700 (701)	15	1.52	64.56 (63.80)

The laminated glass panels tested were provided by the manufacturer after the lamination process, hence it was not possible to precisely determine the actual thickness of each glass ply. Since the flexural stiffness around the minor axis is highly dependent on the thickness of the constituent elements (it depends on their third power) a more detailed visual inspection was done with the objective of assessing the actual thickness of the glass plies. Despite the difficulty in precisely assessing such, the author was

⁹ EN 572-8 [4.27] accounts for possible production tolerances on glass elements that can go up to ± 0.5 mm for 15 mm thick glass panels.

able to conclude that the glass plies of the PVB panel (similar to that used in the investigations reported in chapter 3) could hardly present the corresponding nominal thickness of 15 mm. Indeed, based on local measurements, it was possible to infer that the geometry of the PVB panel was likely to include 14.50 mm thick glass plies and 2.28 mm thick PVB sheets. Therefore, the PVB panel's analytical study (detailed ahead in section 4.4) was developed assuming such geometry, but considering the total average thickness of the laminate mentioned above. Using a similar procedure, in the SG-laminated glass panel it was concluded that the real thickness of the glass plies matched the nominal one.

4.3.2 Test setup

Both laminated glass panels were horizontally tested in a simply supported 4-point bending configuration, being subjected to gravity loads (self-weight) and additional dead-weights, following a two-stage loading procedure described in detail in section 4.3.3. Due to the expected differences in the behaviour of the two interlayers, the two types of panels were tested in different spans (Fig. 4.2): the PVB panel was tested in a span of 5.000 m, with overhangs of 1.600 m, being loaded at 1.700 m from the supports; the SG panel was tested in a span of 8.000 m, with 0.925 m long overhangs, and was loaded at 2.700 m from the supports.

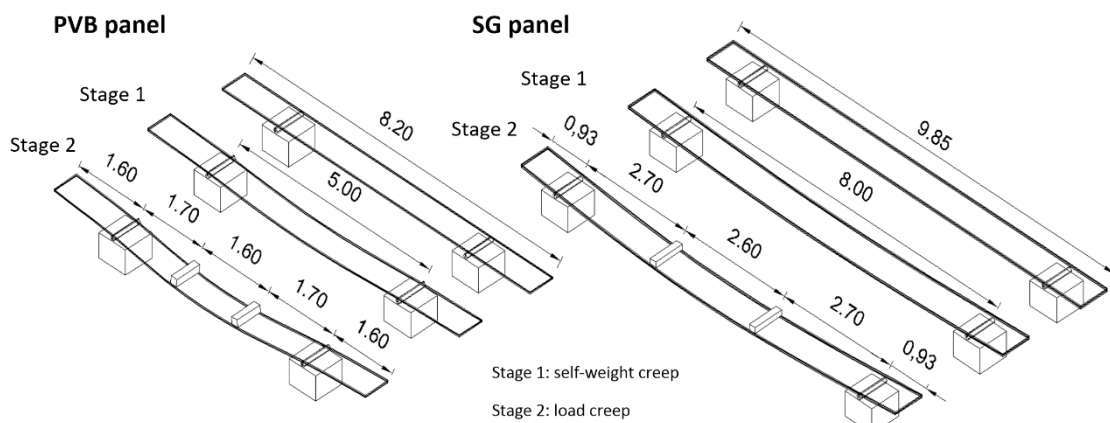


Fig. 4.2 - Creep test setup: illustration of the two stages of the tests.

The panels were supported over linear metal rollers (one allowing for longitudinal sliding), with an aluminium foil in between to avoid glass-metal contact. The PVB panel was loaded using two steel blocks (loading area of $0.10 \times 0.70 \text{ m}^2$), each one weighing 79 kgf (total load of 158 kgf). The SG panel was loaded with two concrete blocks (loading area of $0.15 \times 0.70 \text{ m}^2$), each of them weighing 230 kgf (total load of 460 kgf).

The vertical mid-span deflection was measured by means of two displacement transducers positioned along the mid-span section. The readings were recorded at different rates during the test: in the first 5 minutes, data was acquired at 5 Hz and 10 Hz for the PVB and SG panels, respectively; then, during the

first hour, a reduced rate of 1 Hz was used for both panels; subsequently, until the end of the test, data was acquired twice per day for the PVB panel and was continuously recorded once per hour for the SG panel.

Both creep tests were conducted under laboratory conditions, but without temperature control (due to the full-scale size of the panels), hence small temperature changes occurred over time¹⁰. The average temperature during the test was 19.1 °C for the PVB panel (with maximum and minimum temperatures measured of 22.3 °C and 17.4 °C, respectively) and 17.2 °C for the SG panel (maximum and minimum temperatures of 18.7 °C and 15.3 °C, respectively).

4.3.3 Test procedure

In order to reduce as much as possible the effects of the self-weight on the creep response (due to the extra loads) of the panels, the creep tests were performed in two stages. Stage 1 (Fig. 4.2) comprised the positioning of the panels over the supports and the measurement of the creep deflection due to self-weight. After 500 h, it was concluded that the instrumentation could not detect any further relevant changes in the mid-span deflection, apart from very small changes due to daily temperature fluctuations. Stage 2, which corresponded to the actual creep tests, started once the additional loads were applied to the panels and ended after 350 h of loading time.

The loads were applied simultaneously for both panels, but the loading operation was made using different means. For the PVB panel, the four steel blocks were applied manually (at once), whereas for the SG panel the loading operation was executed using an overhead crane that positioned (also at the same time) the two concrete blocks on the predefined loading points (Fig. 4.3). The first method resulted in smoother initial deflection changes (Fig. 4.4-a), whereas the use of the overhead crane led to much more significant fluctuations during the initial moments of the test, in which non-negligible harmonic variations were measured (Fig. 4.4-b).



Fig. 4.3 – Flexural creep test of the SG panel.

¹⁰ Temperatures during the test were monitored at the same rate of the deflection measurements.

The mid-span deflections measured in the laminated glass panels result from the sum of the two following components: (i) the instantaneous deflection, and (ii) the viscoelastic deflections (*cf.* Eq. (4.2-b)). In order to determine the instantaneous (elastic) deflection resulting from the application of the full load, the derivative of the mid-span deflections was analysed (Fig. 4.4). One can observe that both panels initially presented a high increase of deflection until approximately 2 s of loading time and subsequently the deflection rate rapidly decreased and tended to zero. For the present study, the instantaneous deflection was considered to have finished after 2.5 s of loading for the PVB panel (Fig. 4.4-a) and after 6 s of loading for the SG panel (Fig. 4.4-b). The 6 s instant was considered due to the harmonic loading influence on the deflection.

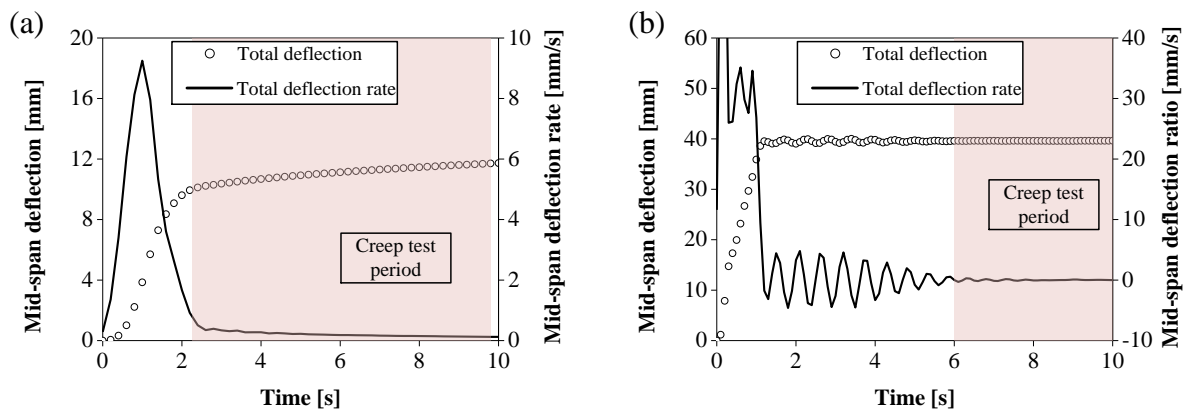


Fig. 4.4 – Initial mid-span deflections and their derivative values measured in the flexural creep test of the (a) PVB and (b) SG laminated glass panels.

4.3.4 Experimental mid-span deflection

Fig. 4.5 illustrates the evolution of the mid-span total deflections during the creep test for both laminated glass panels tested. From a qualitative point of view, one can observe that the magnitude of mid-span deflection increase for both panels was much higher during the initial hours of the creep test. After a relatively short period of time, such increase was attenuated, particularly for the SG panel. From a quantitative point of view, the creepocity exhibited by the two panels was remarkably different: at the end of the creep tests, the mid-span deflection of the PVB panel increased about 123% compared to the initial deflection, whereas in the SG panel the mid-span deflection increased only 1.8% (the mid-span deflection increment of the PVB and SG panels corresponded, respectively, to 55% and 1.7% of the total deflection after 350 h of loading).

4.4 ANALYTICAL STUDY

The main goal of the analytical study was (i) to develop simple predictive models based on Findley's power law to estimate the deflections of both PVB and SG laminated glass panels and the shear modulus of the corresponding interlayers, and (ii) to compare such estimates with those corresponding to material

models available in the literature (presented in section 4.2.1). The analytical study is divided in four parts. Section 4.4.1 presents the methodology used in this study, including the model used to predict the panel's deflection and the shear modulus of the interlayers, together with the formulation (originally presented by Machado-e-Costa [4.15]) to compute the effective flexural stiffness of laminated glass members (with 3 and 4 layers¹¹). In section 4.4.2, based on the work of Findley [4.20], the previously reported creep test results are fit by a one-term power law, and deflection prediction curves are proposed for both PVB and SG laminated glass panels. Next, in section 4.4.3, the predicted deflections from Findley's linear (in a bi-log₁₀ scale) model for a period of up to 50 years are compared with predictions obtained using the creep models of the interlayers available in the literature. In section 4.4.4, the obtained creep model (Findley's power law regression) is used to back-estimate the decay of the interlayers' shear modulus; such estimates are compared with the shear modulus master curves presented in section 4.2.1. Finally, in section 4.4.5 the structural effects of creep on the tested panels are investigated.

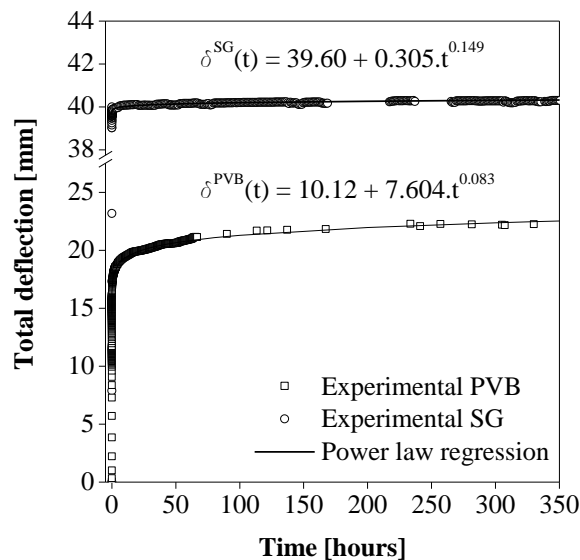


Fig. 4.5 – Mid-span deflection during the creep tests and power law fittings to the experimental data for the PVB and SG laminated glass panels.

4.4.1 Methodology

4.4.1.1 Modelling approach

In this study, the flexural response of the glass laminates was estimated using simplified quasi-static¹² analytical models. Eq. (4.3) yields the vertical deflection $\delta(x)$ at the longitudinal coordinate x of a

¹¹ A similar formulation was presented in chapter 3 regarding 3-layer laminated glass beams subjected to a mid-span pointed load.

¹² The quasi-static models do not account for the continuous effects of polymers' viscoelastic behaviour in structures subjected to changeable temperature and load conditions (the former is a condition of the present study). The assessment of such effects requires relatively complex time-dependent fully viscoelastic analyses. However, in the presence of well-defined temperature and load-time conditions (the case of the present study) and using accurate expressions for the determination of the effective flexural stiffness/thickness it is possible to obtain sufficiently accurate results [4.14, 4.29].

monolithic glass panel¹³ (i.e. without interlayers) with an effective bending stiffness of $EI_{y,eff}$, simply supported over a span length of L_0 and subjected to a total load of P , symmetrically applied in two points, each one situated at a distance L_a from the nearest support ($x < L_a$):

$$\delta(x) = \frac{1}{EI_{y,eff}} \left(-\frac{PL_a}{4} x^2 + \frac{PL_a L_0}{4} x - \frac{PL_a^3}{12} \right) \quad (4.3)$$

The $EI_{y,eff}$ of the laminated glass panels was determined using the formulae derived by Machado-e-Costa [4.15] (based on sandwich theory) that allow determining the $EI_{y,eff}$ of multi-layer laminated glass panels under out-of-plane loads for a variety of load cases (detailed ahead in section 4.4.1.2).

The application of Eq. (4.3) assumes the hypothesis of constant load and temperature. The creep tests were performed under constant load but the measured temperature exhibited some minor changes (*cf.* section 4.3.2.1). The effects of such temperature changes¹⁴ on the structural response of the glass laminates was assessed in a preliminary study, in which the quasi-static deflection estimates obtained assuming the average temperature were compared with those obtained assuming the maximum and the minimum measured temperatures. The latter predictions (maximum and minimum) were determined assuming PVB and SG material models taken from the literature, PVB1999 and SG2005, respectively. The results obtained for the PVB panel showed that the estimates using the maximum or minimum temperatures are 6% higher and 3% lower, respectively, than those considering the average temperature. For the SG panel, the maximum differences in the deflection predictions for those temperature ranges were only 0.4%. Such differences were considered sufficiently low for both panels and hence the analytical study was carried out assuming the average temperatures measured in the tests¹⁵.

The effect of creep due to the panels' self-weight during the second stage of loading was determined by estimating the increase of deflection due to such self-weight at the end of the creep tests. Using the PVB1999 model, a total deflection increment of 0.59 mm during the 350 h of the creep test was estimated. This value represents around 2.65% of the total measured deflection or 5% of the total creep deflection exhibited by that panel, which has been considered sufficiently low to assume that creep deflections due to self-weight had stabilized (namely when compared to those due to the applied loads). In the case of the SG panel, the total deflection due to self-weight was estimated to have increased by 0.013 mm after 350 h using the SG2005 shear modulus decay model. This value represents

¹³ According to Euler-Bernoulli beam theory.

¹⁴ Due to the high reduction magnitude of the interlayers' shear modulus during the first moments of loading (load periods lower than 1 h), even for room temperature, estimates with different temperatures can be significantly different.

¹⁵ In fact, the WLF equation parameters of the PVB2007 model were not available; therefore, such model was not normalized for the corresponding experimental measured average temperature and the corresponding differences were assumed negligible.

approximately 0.03% of the total deflection measured in the test or 1.85% of the total creep deflection, again a sufficiently low value to be considered stabilized (compared to those due to the applied loads).

4.4.1.2 Effective flexural stiffness

According to Machado-e-Costa [4.15], the $EI_{y,eff}$ of laminated glass panels can be determined (Eq. (4.4)) from the sum of (i) the flexural stiffness of the glass plies w.r.t. their own centroidal axes (EI_{gl}), and (ii) the flexural stiffness w.r.t. the neutral axis (EI_s) multiplied by a factor ξ_f (varying from 0 to 1) that reflects the composite action level provided by the interlayer and depends on the following parameters: the interlayer's stiffness, the overhangs' length, the loading and support conditions, and other geometrical parameters. The calculations necessary to evaluate the above-mentioned effects are described from Eqs. (4.5) to (4.11), where L_0 , L_1 , L_a are geometrical parameters (Fig. 4.6), α , β , λ and θ are non-dimensional parameters that account for the influence of the interlayer's stiffness, and ψ and ϕ are non-dimensional parameters relating to the load position and the overhangs' length, respectively. The parameters I_{gl} , I_s and A depend on the number of glass plies of the laminated glass panel, being calculated according to the expressions available in Table 4.2 (restricted to symmetrical cross-sections, Fig. 4.6), where E is the Young's modulus of the glass plies, G_{int} is the interlayer's shear modulus, and b , t_i , t_{int} , a_i and d are geometrical parameters (Fig. 4.6).

$$EI_{y,eff} = EI_{gl} + \xi_f EI_s \quad (4.4)$$

$$\alpha = \frac{I_{gl}}{I_s} \quad (4.5)$$

$$\beta = \frac{1}{AG_{int}} \frac{EI_s}{L_0^2} \quad (4.6)$$

$$\lambda_f = \sqrt{(1 + \alpha)/\alpha\beta} \quad (4.7)$$

$$\theta = \lambda_f/2 \quad (4.8)$$

$$\phi = \lambda_f L_1/L_0 \quad (4.9)$$

$$\psi = \theta L_a/L_0 \quad (4.10)$$

$$\xi_f = \frac{1 + \alpha}{1 + \frac{6}{3\alpha\theta^2 - 4\alpha\psi^2} \left(1 - \sinh(\psi) \frac{2 \cosh(\theta + \psi) + \cosh(\theta + \phi - \psi) - \cosh(\theta - \phi - \psi)}{2\psi \cdot \cosh(\theta + \phi)} \right)} - \alpha, \in [0,1] \quad (4.11)$$

4.4.2 Findley's power law fitting

Fig. 4.7 presents the creep deflections (increase of deformation due to creep - δ_c , in a bi-log₁₀ scale) determined by subtracting the instantaneous deflection to the total deflection value; the former value was 10.12 mm for the PVB panel and 39.6 mm for the SG panel, according to the discussion presented

in section 4.3. In addition, Fig. 4.7 also depicts the experimental creep data (solid area) used to estimate the power law parameters (m_d and n_d) and the corresponding fit curves for each laminated glass panel.

Table 4.2 – Expressions of I_{gl} , I_s and A for cross-sections with 3 and 4 glass plies [4.15].

Parameter	No. of glass plies	
	3	4
I_{gl}	$\sum \frac{bt_i^3}{12}, i = 1,2,3$	$\sum \frac{bt_i^3}{12}, i = 1,2,3,4$
I_s	$\frac{bt_1d^2}{2}$	$\frac{bd^2}{2t_{int}}$
A	$\frac{bd^2}{2t_{int}}$	$\frac{bd}{t_{int}} \cdot \frac{t_1d^2 + t_2a_2^2}{3t_1d + t_2a_2}$

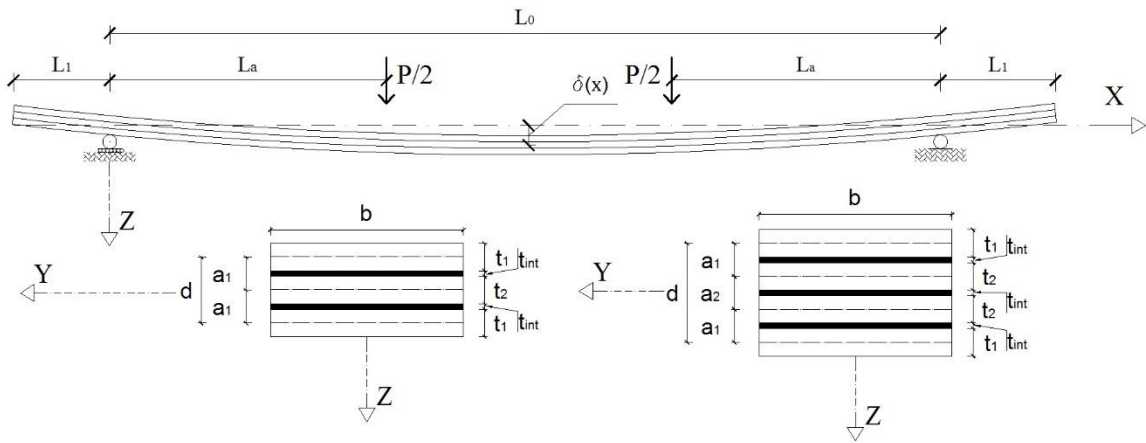


Fig. 4.6 - General laminated glass panel (top) out-of-plane deflection, and (bottom) cross-section geometry of 3 and 4-layer glass panels.

Eq. (4.12) and Eq. (4.13) present the generalized formulae to estimate the total mid-span deflection (in mm) of the 3-layer PVB-laminated glass panel and the 4-layer SG-laminated glass panel, respectively (for the geometry and test conditions used in this study), where t is the time in hours ($t > 0.1$ h). Fig. 4.78 presents their graphical illustration.

$$\delta^{PVB}(t) = \delta_0(t = 2.5 \text{ s}) + \delta_c = 10.12 + 7.604 t^{0.083} \quad (4.12)$$

$$\delta^{SG}(t) = \delta_0(t = 6.0 \text{ s}) + \delta_c = 39.60 + 0.305 t^{0.149} \quad (4.13)$$

Both power law fittings resulted in high correlation coefficients ($R^2 = 0.99$ for the PVB panel and $R^2 = 0.97$ for the SG panel) attesting the accuracy of Findley's power law in simulating the viscoelastic deflections measured from 6 minutes to 350 h. For the PVB panel, the fit power law predicts a total deflection of 22.47 mm after 330 h of loading, which is 0.98% higher than the measured value of 22.25 mm. Regarding the SG panel, the deflection of 40.30 mm measured after 350 h compares very

well with the estimated deflection of 40.32 mm, corresponding to a relative difference to experimental results of +0.05%.

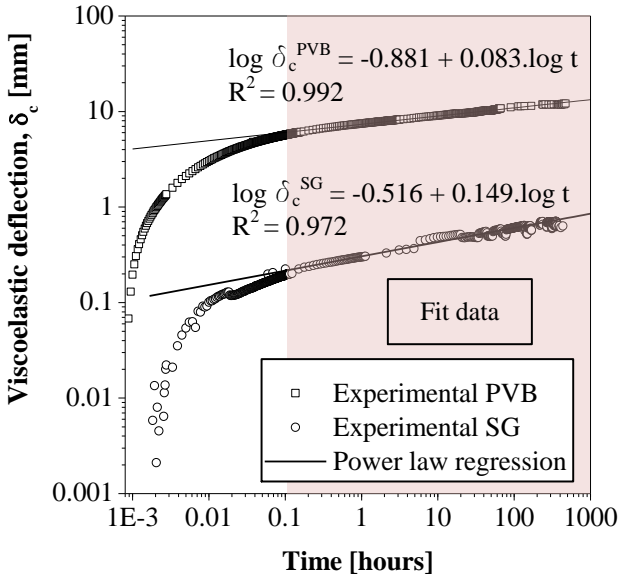


Fig. 4.7 – Viscoelastic mid-span deflection (bi-log₁₀ scale) during the creep tests and fitting of a power law to the experimental data for the PVB and SG panels.

Fig. 4.8 compares the creep deflection evolution during the creep test of the PVB and SG panels with the predictions of Findley’s power law and with the estimates obtained using the PVB and SG material models reported in the literature (*cf.* section 4.2.1). For the PVB panel, predictions obtained from model PVB1999 are in fairly good agreement with Findley’s power law (+2.8%), while the PVB2007 predictions are significantly higher (+13.4%). For the SG panel, the agreement between Findley’s power law and deflections estimated from the SG2005 model is reasonable (+0.2%), whereas deflection predictions obtained from the SG2012 model underestimate the experimental measurements, being much slightly than the predictions obtained from the other models and test data (-1.0%).

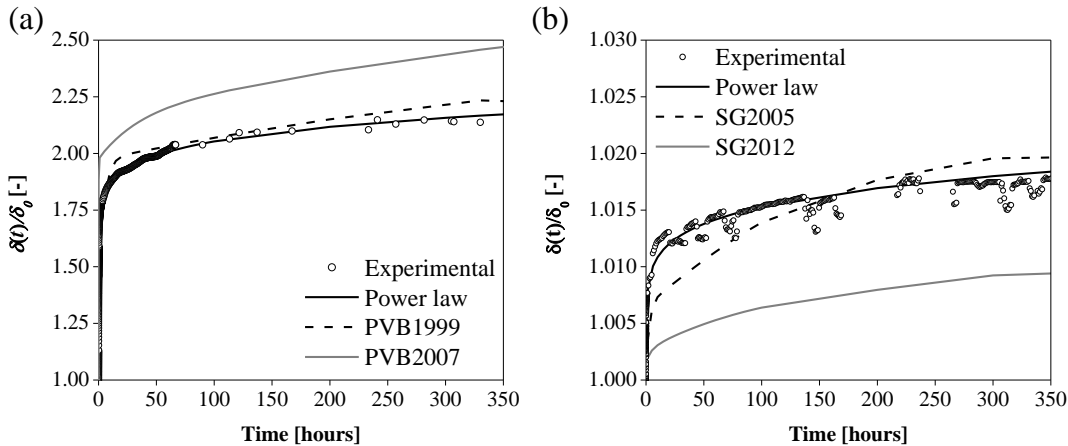


Fig. 4.8 – Comparison between the (a) PVB and (b) SG experimental creep deflection evolution with the corresponding power law fittings and estimates obtained using the PVB and SG material models reported in the literature ([4.9, 4.11, 4.12, 4.19]).

4.4.3 Long-term deflection predictions

4.4.3.1 PVB panel

Fig. 4.9-a depicts the mid-span deflection predictions (reflects the mid-span deflection increase with respect to the instantaneous) over a time period of 50 years using (i) the previously presented power law regression for the PVB panel and (ii) the estimates using the PVB1999 and PVB2007 material models. Although all models present similar predictions during the first 350 h (*cf.* Fig. 4.8-a), the long-term (after 50 years) estimates can be significantly different: 31.8 mm for the power law regression *vs.* 53.9 mm (approximately 1.70 times higher) and 108.7 mm (more than 3 times higher), using the PVB1999 and the PVB2007 models, respectively.

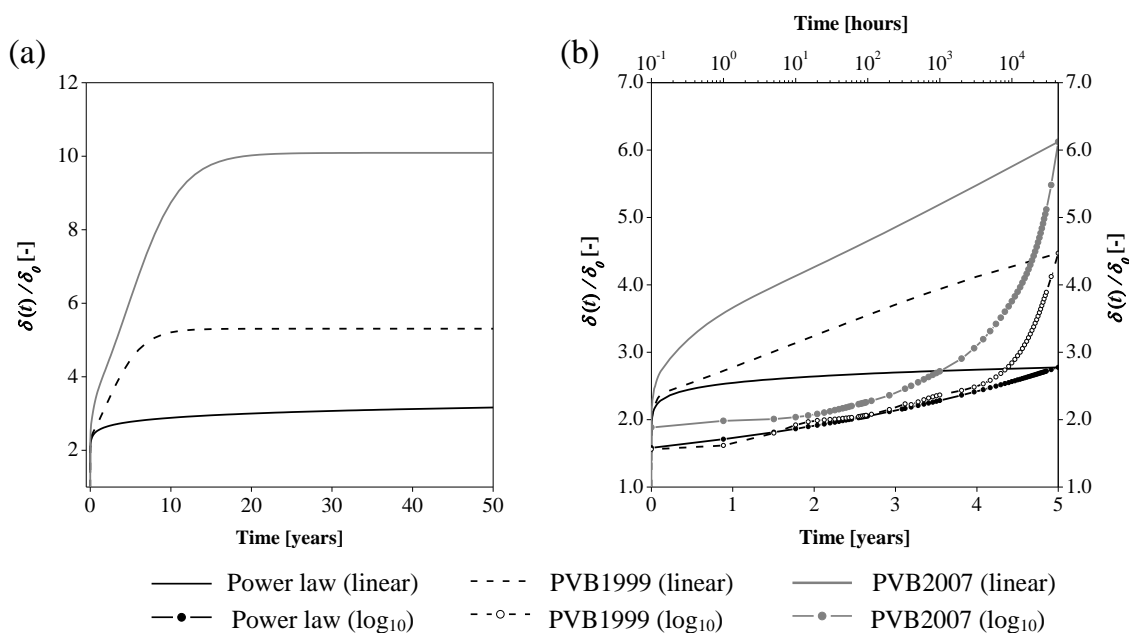


Fig. 4.9 – Mid-span deflection evolution for a creep period of (a) 50 years and (b) 20,000 h (linear and uni- \log_{10} scale), according to the power law regression (black curve), and to models PVB1999 [4.11] (dashed curves) and PVB2007 [4.12] (grey curves).

Fig. 4.9-b shows that the PVB1999 model and the extrapolation of Findley's model provide equivalent predictions during the first 4,000 h of creep (almost 6 months), but from that point onwards the predictions start to diverge: estimates from the power law present a change of slope¹⁶ (bi-linear scale Fig. 4.9-b), with the deflection evolution exhibiting a considerable flattening after 4,000 h, whereas estimates obtained using the PVB1999 model present significant increases even after that point. In other words, the power law presents a steady reduction of deflection rate from the first moments of loading and over the course of the creep period; in opposition, the deflection increment estimated with the PVB1999 model is more irregular (reflecting the different terms of the Prony series) and presents a high increment even after 4,000 h. The PVB2007 model deflection estimates were always significantly higher

¹⁶ The term slope refers directly to the evolution change in the curve in a bilinear scale.

than those retrieved by the other two models, although its deflection evolution was qualitatively similar to that obtained using model PVB1999.

The maximum deflection estimates using the PVB models of the literature are reached after around 15 years of loading, whereas the power law exhibits a steady and slight increase during the entire creep period. The maximum deflections estimated by the PVB1999 and PVB2007 models correspond to the deflections reached by the laminated glass panel when G_{int} equals the lower bounds assumed for those viscoelastic material models. Note that the latter value corresponds to assuming that the interlayer does not provides any level of shear coupling between the glass plies.

4.4.3.2 SG Panel

The Findley’s power law fit for the SG panel (cf. Eq. (4.13)) was also used to predict the long-term behaviour of that panel. Fig. 4.10-a compares the mid-span deflection predictions (reflects the mid-span deflection increase with respect to the instantaneous one) according to Findley’s power law and the predictions using the SG2005 and the SG2012 viscoelastic material models from the literature. As expected, due to the improved SG mechanical properties, the relative differences between the different models assessed for a creep time of 50 years are much lower than those observed for the PVB panel.

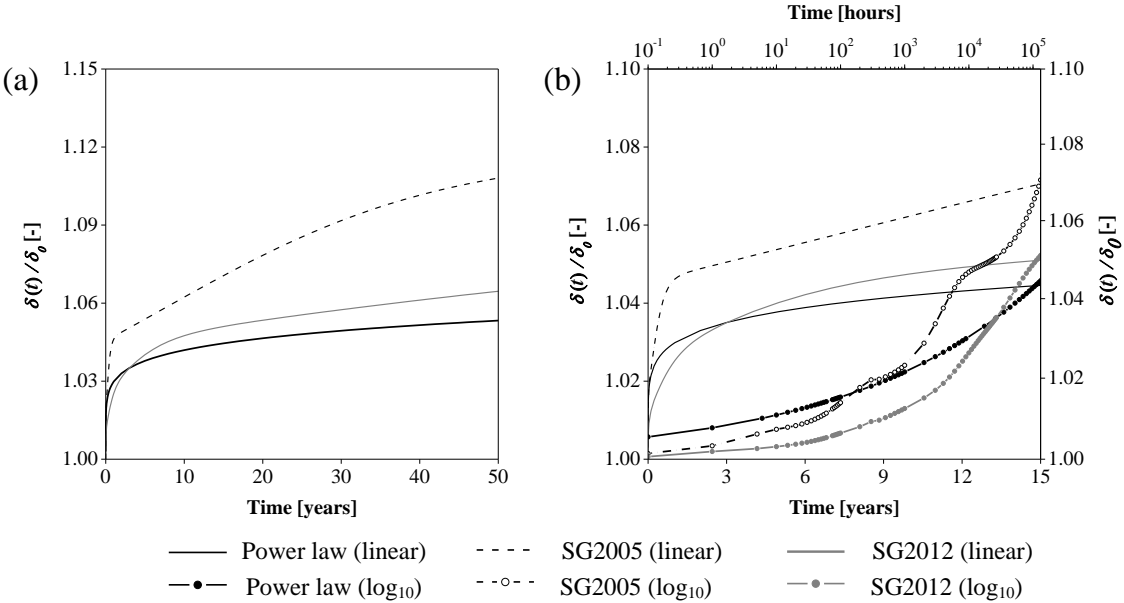


Fig. 4.10 - Mid-span deflection evolution predictions for a creep period of (a) 50 years and (b) 100,000 h (linear and uni-log₁₀ scale), according to the power law regression (black curve), and to models SG2005 [4.19] (dashed curves) and SG2012 [4.9] (grey curves).

Unlike what is observed for the first 350 h of creep (Fig. 4.10-b), the long-term power law regression predictions are closer to the ones obtained using the SG2012 model (0.4% lower) than to the ones provided by the SG2005 model (4% lower). A detailed analysis of the evolution of the deflection rate during the first 100,000 h (bi-linear scale in Fig. 4.10-b – around 15 years) shows that at the first

moments of creep, the predictions obtained from Findley's power law are slightly higher than the ones provided by the other two models. However, while the proposed model exhibits a creep rate according to a negative power law development during the 50 years (which was initially followed by the other two models), the SG2005 and SG2012 models depict several and significant changes of the creep rate after 1 h and 6,000 h (uni- \log_{10} scale in Fig. 4.10-b), respectively, leading to a decrease of the initial differences. The estimates obtained from the SG2005 model (viscoelastic model obtained from DMA tests and superposition principles) present the highest deformation increase, resulting also in the highest deflection estimates after 100,000 h of loading. The deflection estimates using the SG2012 model (obtained from actual short-term small-scale creep tests) are closer to the results of the power law regression during most of the 50-year creep period. This indicates that the proposed power law (obtained from full-scale glass laminates) is in better agreement with the results from small-scale experiments on glass laminates (SG2012) than with those from DMA tests on the interlayer (SG2005).

4.4.4 Estimates of PVB and SG viscoelastic shear modulus

The estimates of the shear modulus variation with time (viscoelastic shear modulus) for PVB and SG ($G_{PVB}(t)$ and $G_{SG}(t)$, respectively) were determined based on the corresponding power law fittings presented in the previous sections and by simply applying an inverse analysis of Eqs. (4.3) to (4.11).

Fig. 4.11 compares the $G_{PVB}(t)$ (in terms of both absolute and normalized values, the latter considering the G_0 of each model) estimated using Findley's power law with material models PVB1999 and PVB2007 reported respectively by van Duser *et al.* [4.11] (extrapolated for a reference temperature of 19.1 °C) and by D'Haene and Savineau [4.12] (20 °C¹⁷). As in the deflection analysis, the $G_{PVB}(t)$ curve predicted by the power law regression follows closely the PVB1999 model for short loading durations, in terms of both initial values and shear modulus evolution with time. However, the latter curve exhibits a change of slope after around 6 months (4,380 h) of creep that is not followed by the predictions obtained from Findley's power law, resulting in significant differences between the two models: after 20 years the G_{PVB} predicted by the power law regression is 0.22 MPa, whereas the PVB1999 model indicates 0.05 MPa (78% lower). The latter value corresponds to the horizontal asymptote considered in the PVB1999 model as a long-term modulus limit; in opposition, the power law regression depicts a continuous decrease (from 20 to 50 years there is a variation of 25%) and does not assume a lower bound for the shear modulus.

The shear modulus predicted by the PVB2007 model is always lower than the other two models, which can be related with the slightly higher reference temperature of that model. The normalized shear modulus variation curve of PVB2007 model is also significantly different from the curves of the other two models. In fact, contrarily to the power law and to the PVB1999 model, which present

¹⁷ As mentioned, such model could not be extrapolated to the experimental average temperature due to absence of the WLF equation; nevertheless, the temperature difference of 1 °C is considered sufficiently low for comparison purposes.

approximately linear development in a bi- \log_{10} plot up to 4,000 h, the PVB2007 model presents a non-linear development throughout its entire range in such a plot.

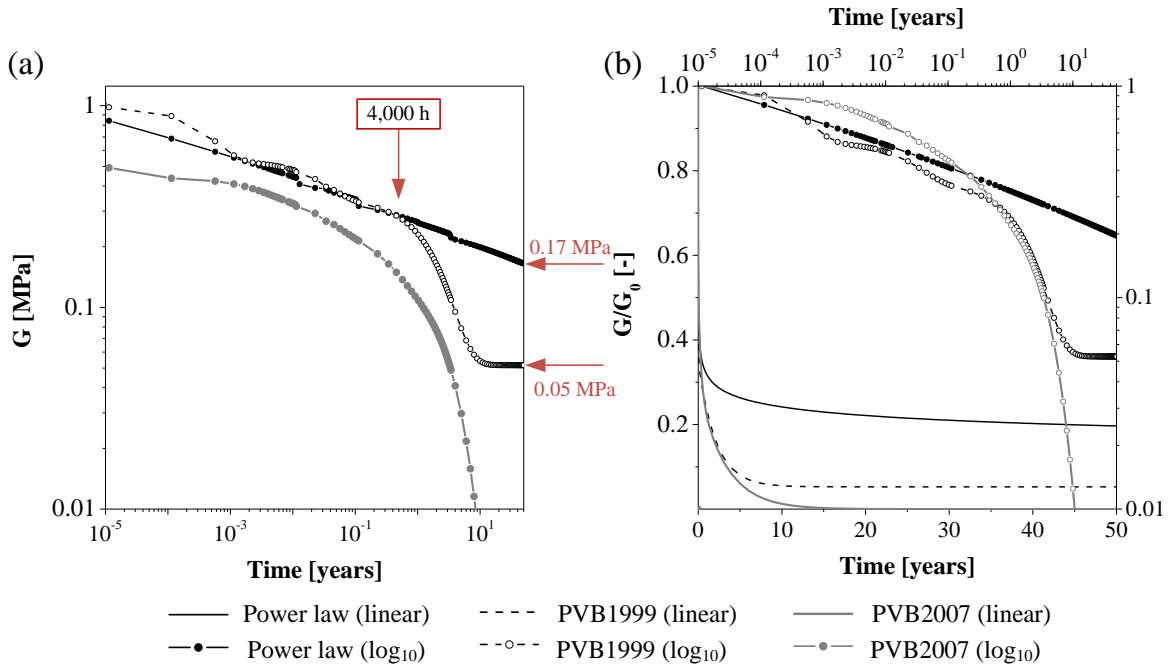


Fig. 4.11 – Comparison of absolute (a) and normalized (b) $G_{PVB}(t)$ curves of power law regression (black) and models PVB1999 (ref. temperature 19.1 °C [4.11], dashed curves), and PVB2007 (ref. temperature 20 °C [4.12], grey curves).

Fig. 4.12 depicts the $G_{SG}(t)$ curve predictions by the proposed power law, together with the extrapolations of both SG moduli master curves presented in section 4.2.1 for a reference temperature of 17.4 °C (as for PVB, it is expressed in terms of both absolute and normalized values, considering the G_0 of each model).

The different predictions are far from being in good agreement, both in terms of absolute values and normalized variations. One can observe that the absolute G_{SG} estimates for load periods of 0.1 h (lower bound of applicability of the proposed viscoelastic model) using the viscoelastic models from the literature are considerably higher than that determined with the proposed model: the predictions using that model are 80% and 58% lower than those of the SG2005 and SG2012 models, respectively. These differences most likely stem from the different methodologies used to extrapolate the G_{SG} , namely those used to set each model G_0 . The aforementioned differences decrease quickly with the load duration (reflecting the significantly higher stiffness decay of both models from the literature, especially SG2005), and after 6 months the SG2005 model is already the one that predicts the lowest values of G_{SG} , whereas the other two models provide similar predictions. After 50 years of loading, the G_{SG} estimated by Findley’s power law is 63% and 7% higher than the SG2005 and SG2012 predictions, respectively.

The modulus decrease rate predicted by the SG2005 model is much higher throughout the 50-year period with respect to the power law (the latter presents a constant decrease rate in a bi- \log_{10} scale), whereas the

SG2012 model presents a relatively constant rate (in a bi-log₁₀ scale) up to 0.01 years (less than 100 h), after which it predicts a significantly higher modulus decrease rate.

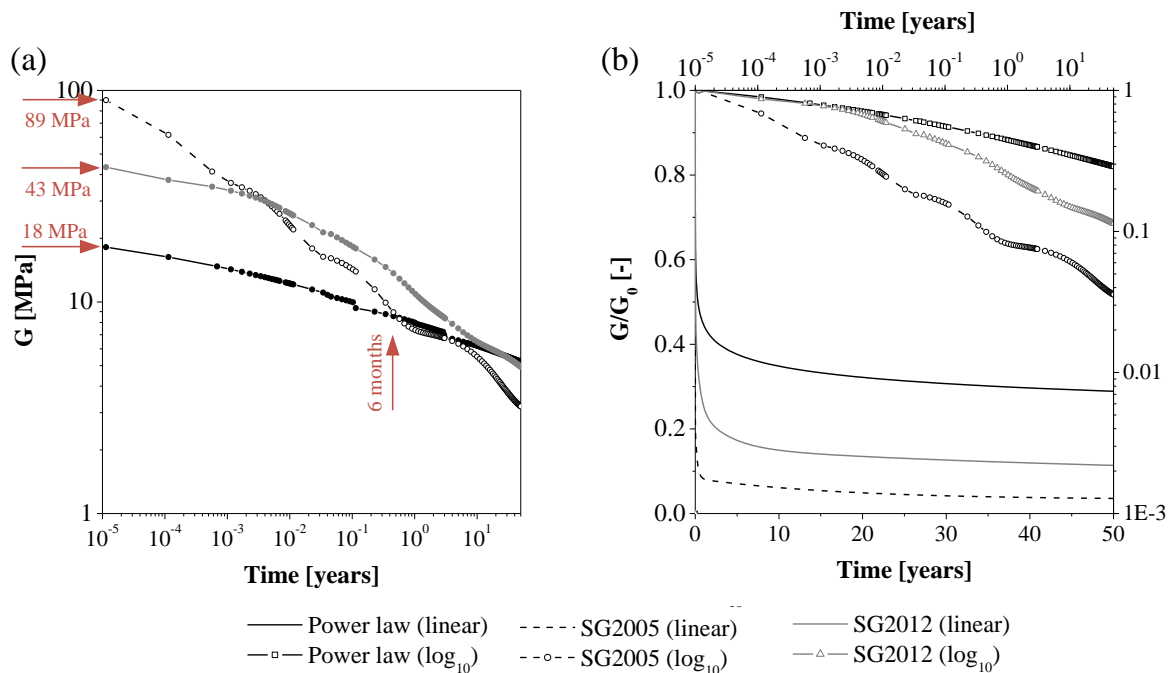


Fig. 4.12 – Comparison of absolute (a) and normalized (b) $G_{SG}(t)$ curves of power law regression (black) and models SG2005 [4.19] (dashed curves), and SG2012 [4.9], (grey curves), ref. temperature 17.4 °C.

4.4.5 Assessment of the long-term shear coupling

Despite the relatively high differences between the estimates of the interlayers' shear moduli obtained from the different models, it is important to quantify their structural effects for a specific load case and geometry of the laminated glass element. In fact, the structural behaviour of laminated glass elements is mainly governed by the level of shear coupling between the interlayer and the glass plies, which is influenced by several factors (Eqs. (4.5) to (4.11)), including the interlayer's shear modulus.

Fig. 4.13-a shows the evolution with time of the shear coupling (expressed by parameter ξ_f , cf. Eq. (4.11)) for the PVB-laminated glass panel studied, according to the power law regression and to both material models from the literature¹⁸ (PVB1999 and PVB2007). According to the G_{PVB} reduction curve proposed here, the shear coupling presents a steady decrease without changes on its evolution rate (in a uni-log₁₀ scale) over the period of analysis. On the other hand, the shear coupling evolution predicted by the PVB1999 material model presents a sudden and significant decrease after around 4,000 h, which is in line with the significant deflection increment predicted by this model around that point (cf. section 4.4.3.1). As a result, for a 50-year loading duration, the shear coupling estimated assuming the DMA literature models is significantly lower than that provided by the proposed model. Likewise, the shear

¹⁸ Again, the reference temperature of the shear modulus reduction curve of D'Haene and Savineau [4.12] is 20 °C instead of 19 °C.

coupling estimated by the PVB2007 model presents several evolution rate changes being always considerably lower compared with the other two models.

Notwithstanding the aforementioned differences, for creep periods longer than 0.1 h, the shear coupling determined using any of the aforementioned models is always lower than 50%, which highlights the low performance of PVB laminates for structural applications.

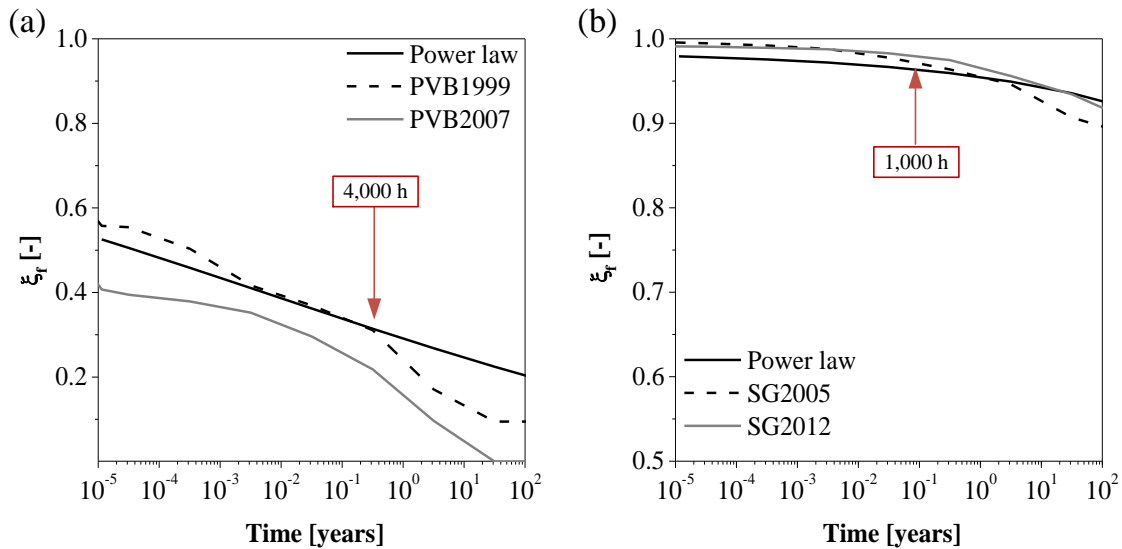


Fig. 4.13 – Shear coupling of the (a) PVB and (b) SG panels.

One of the advantages of SG is its ability to guarantee high levels of coupling for both short and long-term loading. Indeed, as attested by the mid-span deflection development of the SG panel tested, the reduction of the G_{SG} does not significantly affect the deflection magnitude during the creep period of 50 years, i.e. the shear coupling is always higher than 90% during that time regardless of the chosen model (Fig. 4.13-b). Furthermore, from the three viscoelastic models depicted, only the SG2005 model predicts a level of reduction that could result in significant changes of the shear coupling for the time frame analysed (in any case, occurring well beyond 50 years of creep). Finally, it is also interesting to note that the shear coupling evolution determined using the DMA-based shear reduction curve (model SG2005) depicts several changes of evolution within the applicable time period (in line with the analysis of the deflections and G_{SG} reduction curve). In opposition, the shear reduction curves obtained from tests on laminates (the proposed power law regression and model SG2012, by Callewaert [4.9]) estimate a steady and uniform decrease of shear coupling. Therefore, once more it can be concluded that the results extrapolated from DMA tests on interlayers can be significantly different from those estimated from material models derived from small or full-scale tests on glass laminates.

4.5 CONCLUSIONS

This chapter presented experimental and analytical investigations about the long-term flexural response of full-scale laminated glass elements with PVB and SG interlayers. The experimental study comprised flexural creep tests on full-scale laminated glass panels with durations of 350 h. Using Findley's power law, such tests allowed determining analytical expressions to estimate the long-term deflections of the tested elements ($t > 0.1$ h). Such laws were then used to predict (extrapolate) the long-term response of PVB and SG-laminated glass elements and to back calculate the viscoelastic shear moduli of those interlayers. These predictions were compared with those obtained from material models of the PVB and SG interlayers available in the literature. The following main conclusions can be drawn:

1. Both laminated glass panels exhibited viscoelastic behaviour. For the geometry and load conditions used in the creep tests, after 350 h of creep the mid-span deflections of the PVB and SG panels increased 120% and 1.6%, respectively. This confirms the much higher viscoelasticity of PVB compared to SG.
2. Findley's power law regressions were able to accurately describe the creep response of the PVB and SG-laminated glass panels up to 350 h. The corresponding analytical expressions are expected to accurately estimate the long-term behaviour of the laminated glass panels, for the same geometric, load and temperature conditions.
3. For the PVB-laminated glass panel, the mid-span deflection predictions provided by the proposed power law were equivalent to those obtained using the DMA-based PVB1999 material model up to 4,000 h, but were much lower than those given by the DMA-based PVB2007 material model; after 4,000 h, the predictions of the power law and the PVB1999 model started to diverge, since the considerable flattening of the power law regression after that instant was not followed by the deflection predictions estimated using the literature creep models. After 50 years of loading, the deflection estimates obtained from the power law are 45% and 70% lower than those obtained with the DMA-based PVB1999 and PVB2007 material models, respectively.
4. For the SG-laminated glass panel, the relative differences between the deflection predictions obtained from Findley's power law and those based on the viscoelastic models taken from the literature – SG2005 (DMA based) and SG2012 (based on short-term small-scale creep tests) – were much lower (compared to PVB), especially for the SG2012 model. This is attributed to the inherent much lower creeposity of SG. However, as for the PVB panel, the evolution of deflections predicted by the power law was not in full agreement with those given by the material models taken from the literature, namely the one based on DMA tests. After 50 years of loading, the relative differences between the deflection predictions obtained using SG2005 and SG2012 models were respectively 4% and 0.4% lower than those provided by the power law.
5. The structural effects (in terms of shear coupling) of the aforementioned differences in the interlayer models depend on the geometry and load conditions of the laminated glass elements.

Considering the test conditions used in this study, for the PVB models the differences in structural effects start to be relevant after 4,000 h of loading, with shear coupling (ξ_p) at 50 years ranging from 0 (PVB2007) to 0.22 (power law); for the SG models, differences in structural effects are not relevant within the loading period studied, since all models indicate very high shear coupling degrees, ranging from 0.89 (SG2005) to 0.93 (power law).

In the overall, the results obtained for both panels show that deflection predictions based on viscoelastic material models derived from DMA tests can be significantly different from those based on Findley's power law obtained from full-scale tests. In order to further assess and compare the relative accuracy of these two approaches, much longer creep experiments need to be performed in full-scale laminated glass elements. This should be addressed in future investigations.

4.6 REFERENCES

- [4.1] Haldimann M, Luible A, Overend M. *Structural Use of Glass*. Zurich: IABSE-AIPC-IVBH; 2008.
- [4.2] Report EUR 26439 EN Guidance for European Structural Design of Glass Components. Institute for the Protection and Security of the Citizen, Joint Research Centre, Luxembourg; 2014.
- [4.3] The Institution of Structural Engineers. *Structural Use of Glass in Buildings (Second edition)*. London: The Institution of Structural Engineers (ISE); 2014.
- [4.4] Bennison SJ, Smith CA, Duser A van, Jagota A. *Structural Performance of Laminated Glass with a “Stiff” Interlayer*. Glas. Build. ASTM STP 1434. V. Block, West Conshohocken, PA: ASTM International; 2002.
- [4.5] Belis J, Depauw J, Callewaert D, Delincé D, Van Impe R. Failure mechanisms and residual capacity of annealed glass/SGP laminated beams at room temperature. *Eng Fail Anal* 2009;16:1866–75.
- [4.6] Callewaert D, Belis J, Delincé D, van Impe R. Experimental stiffness characterisation of glass/ionomer laminates for structural applications. *Constr Build Mater* 2012;37:685–92.
- [4.7] Bennison SJ, Qin MH, Davies PS. High-performance laminated glass for structurally efficient glazing. *Innov. Light. Struct. Sustain. Facades*, Hong Kong: 2008, p. 1–12.
- [4.8] Serafinavicius T, Lebet J-P, Louter C, Kuranovas A, Lenkimas T. The effects of environmental impacts on durability of laminated glass plates with interlayers (SG, EVA, PVB). In: Louter, Bos, Belis, Lebet, editor. *Challenging Glas. 4 COST Action TU0905 Final Conf.*, Lausanne: CRC Press Taylor & Francis Group; 2014, p. 455–62.
- [4.9] Callewaert D. *Stiffness of Glass / Ionomer Laminates in Structural Applications*. PhD thesis, Ghent University, Belgium, 2012.
- [4.10] Behr RA, Minor JE, Linden MP. Load duration and interlayer thickness effects on laminated glass. *J Struct Eng* 1986;112:1441–53.
- [4.11] Duser A van, Jagota A, Bennison SJ. Analysis of glass/polyvinyl butyral laminates subjected to uniform pressure. *J Eng Mech* 1999;125:435–42.
- [4.12] D’Haene P, Savineau G. Mechanical properties of laminated safety glass - FEM Study. *Glas. Perform. Days 2007*, Tampere: 2007, p. 594–8.
- [4.13] Bennison SJ, Stelzer I, Davies PS, Sloan JG. Calculation methods for the structural behavior of laminated glass. *Glas. Performance Days 2009*, Tampere: 2009, p. 433–4.
- [4.14] Galuppi L, Royer-Carfagni G. Laminated beams with viscoelastic interlayer. *Int J Solids Struct* 2012;49:2637–45.
- [4.15] Machado-e-Costa M. *Modelling of The Structural Behavior of Laminated Glass Beams. Study of the Lateral-Torsional Buckling Phenomenon*. MSc dissertation, Lisbon University, Portugal, 2015.
- [4.16] Kasper R, Sedlacek G, Feldmann M. *Das Biegedrillknickverhalten von Glasträgern aus Verbundglas*. Verlag Für Archit Unf Tech Wissenschaften GmbH Co KG 2007;76:167–76.
- [4.17] Ferry JD. *Viscoelastic Properties of Polymers*. Third Edition. New York: John Wiley & Sons, Inc; 1980.
- [4.18] EN 1990: Eurocode 0 Basis of structural design. European Committee for Standardization (CEN), Brussels: 2002.
- [4.19] Belis J. *Kipsterkte van Monolithische en Gelamineerde Glazen Liggers*. PhD thesis, Ghent University, Belgium, 2005.
- [4.20] Findley WN, Lai JS, Onaran K. *Creep and Relaxation of Nonlinear Viscoelastic Materials: With an Introduction to Linear Viscoelasticity*. New York: Dover Publications, Inc.; 1976.
- [4.21] Findley WN. 26-Year creep and recovery of poly(vinyl chloride) and polyethylene. *Polym Eng*

- Sci 1987;27:582–5.
- [4.22] Scott DW, Lai JS, Zureick A-H. Creep behavior of fiber-reinforced polymeric composites: a review of technical literature. *J Reinf Plast Compos* 1995;14:588–617.
- [4.23] Bank LC. *Composites for Construction: Structural Design with FRP Materials*. New York: John Wiley & Sons, Inc; 2006.
- [4.24] Sá MF, Gomes AM, Correia JR, Silvestre N. Flexural creep response of pultruded GFRP deck panels: Proposal for obtaining full-section viscoelastic moduli and creep coefficients. *Compos Part B Eng* 2016;98:213–24.
- [4.25] Gonilha JA, Correia JR, Branco FA. Creep response of GFRP–concrete hybrid structures: Application to a footbridge prototype. *Compos Part B Eng* 2013;53:193–206.
- [4.26] Garrido M, Correia JR, Branco FA, Keller T. Creep behaviour of sandwich panels with rigid polyurethane foam core and glass-fibre reinforced polymer faces: Experimental tests and analytical modelling. *J Compos Mater* 2014;45:2237–49.
- [4.27] EN 572-8: 2012 Glass in building - Basic soda lime silicate glass products – Part 8: Supplied and final cut sizes. European Committee for Standardization (CEN), Brussels: 2012.
- [4.28] Wiechert E. Gesetze der elastischen nachwirkung für constante temperatur. *Ann Phys* 1893;286:546–70.
- [4.29] Bedon C, Belis J, Luible A. Assessment of existing analytical models for the lateral torsional buckling analysis of PVB and SG laminated glass beams via viscoelastic simulations and experiments. *Eng Struct* 2014;60:52–67.

PART III
STUDY OF THE STRUCTURAL
BEHAVIOUR OF COMPOSITE
GLASS BEAMS

STRUCTURAL BEHAVIOUR OF LARGE-SCALE LAMINATED GLASS-STAINLESS STEEL HYBRID BEAMS

ABSTRACT

The post-cracking flexural behaviour of hybrid glass systems comprising glass and stainless steel profiles has been extensively reported in the literature. Most of the studies conducted to assess the advantages of such systems in terms of post-cracking residual strength and ductility, have relied on small-scale structural elements. The simplified methodology employed in those studies for structural analysis is valid for hybrid glass beams using annealed glass and assumes that cracked glass panes do not provide any residual contribution to the beams structural performance; thus, their post-cracking robustness is mainly assured by the (compressive) uncracked glass areas and the reinforcing steel profiles. On the other hand, the adhesively bonded joints of the hybrid systems were only briefly addressed in those studies; simplified/empirical methodologies were used to design the joints, providing the bonding perimeter necessary to avoid premature joint failure of such small-scale hybrid glass members. In this chapter an exploratory experimental, analytical and numerical study is carried out on long-span PVB and SG-laminated glass-stainless steel hybrid beams. The main objectives of the study were three-fold: (i) to assess the applicability of this hybrid beam concept to full-scale structures; (ii) to quantify the contribution to the post-cracking flexural robustness of fully tempered cracked glass panes, and (iii) to estimate the bond strength of adhesively bonded joints between laminated glass and stainless steel. The experimental campaign comprised flexural tests on two long-span PVB and SG-laminated glass beams reinforced with stainless steel profiles in the top and bottom edges. In the analytical study, a simplified analytical model that accounts for the influence of the fully tempered glass plies on the flexural stiffness of PVB-laminated hybrid glass beams is presented. Finally, the stress state at the adhesively bonded joints of the hybrid beams was numerically investigated. The results obtained show that the fully tempered cracked glass plies of a PVB-laminated hybrid beam provide considerable residual flexural robustness/stiffness; the equivalent elastic modulus of the cracked glass plies was estimated to be 50 GPa in compression and to range from 50 to 25 GPa in tension as a function of the applied load. Results also highlight the high susceptibility to premature debonding of adhesively bonded joints between laminated glass and stainless steel, indicating the need to duly consider shear stresses at the design stage of large-scale hybrid glass structures.

5.1 INTRODUCTION

In order to overcome the brittle failure behaviour of structural glass members, several different authors performed extensive investigations on hybrid glass elements that combine glass with other structural materials, such as wood, steel, stainless steel, reinforced concrete and FRPs. A brief review of those studies was presented in chapter 2, section 2.3. Further details can also be found in the studies of Martens *et al.* [5.1, 5.2], who published an extensive state of the art review of the main investigations on the field of hybrid glass beams. In most of those studies, experimental campaigns were performed and the viability of hybrid systems has been assessed under several different material combinations, cross-section configurations, sizes and shapes, glass types, beam spans, interlayer materials, as well as different joint configurations and types (bolted, bonded or both).

One of the most comprehensive investigations was on hybrid systems that combine glass with stainless steel reinforcement [5.3–5.5]. The feasibility of a beam prototype, consisting of SentryGlas (SG) laminated glass beams reinforced with a stainless steel profile in the bottom edge, was tested with different glass types, reinforcement percentages and beam sizes [5.5]. In that study, by testing several beam configurations, it was proved that (i) the post-cracking performance of *SG-laminated reinforced glass beams* is function of the glass type (hybrid glass beams made with fully tempered glass (FTG) presented the worse post-cracking performance), (ii) the reinforcement area affects both the cracking load and the post-cracking residual strength (the post-cracking ductility is not affected – *cf.* Fig. 2.20), and (iii) the overall performance of *SG-laminated reinforced glass beams* is not affected by the beam's size (for the range of geometries tested).

In the same study, as well as in the studies of Kreher [5.6] and Kreher *et al.* [5.7] on glass-timber hybrid beams, it was shown that hybrid glass beams made with heat-treated glass (heat strengthened glass (HSG) or FTG) achieve higher initial failure loads compared to hybrid beams with annealed glass (ANG)¹. However, the post-cracking performance of the former beams is considerably worse compared to their counterparts with ANG. In fact, hybrid glass beams made with ANG present localized cracks confined to the tensile area that break the glass panes into large-size fragments. As a result, the breakage pattern of ANG provides higher capacity to bridge the shear stresses between the compressive area and the (tensile) reinforcement profile. Furthermore, in ANG cracks are confined to the tensile area, which allows the compressive area to keep its integrity up to large deformation levels, thus enhancing the post-cracking strength together with the post-cracking ductility of the residual load-bearing mechanism². Unlike ANG, once thermal treated glass achieves the maximum tensile strength, the glass panes instantly break into small-size fragments and along all their extension, including the compressive area. The full

¹ The cracking load is mainly affected by the glass maximum strength.

² The residual strength depends on the following two mechanisms: (i) ability of the cracked glass area to transfer shear stresses between the reinforcement profile and the glass compressive area, and (ii) integrity of the glass compressive area.

fragmentation of fully tempered glass panes results in a reduction of not only the capacity to bridge shear stresses in between the small glass pieces and the interlayer, but also of the ability of their compressive area to keep its integrity and stability under higher loads or deflections. In the study of Louter *et al.* [5.5], the residual post-cracking strength and ductility of hybrid glass beams with ANG were, respectively, 13% and (about) 400% higher than those obtained using FTG. In the same study, the authors also refer to an “*additional load-carrying mechanism present in the ANG and in HSG beams but absent in the FTG beams*”.

The results achieved by Kreher [5.6], Kreher *et al.* [5.7] and Louter *et al.* [5.5] confirmed the differences between the post-cracking performance of hybrid glass beams using ANG, HSG and FTG. Nonetheless, and in spite of the observed differences, none of the authors presented any analytical interpretation for the effects of using FTG on the post-cracking strength, ductility or flexural robustness/stiffness. In fact, only few authors have extended the existing studies on the post-cracking performance of laminated glass beams to laminated hybrid glass beams [5.11]³; thereby, the contribution of the different types of glass in the post-cracking performance of hybrid glass beams is yet to be duly assessed and experimentally quantified.

The hybrid glass beams concept has been tested with countless sizes and spans (span-to-height ratio). However, experimental data regarding the behaviour of large-scale structural members is limited. The data collected by Martens *et al.* [5.1, 5.2] shows that most of the concepts developed were tested on beams with spans lower than 3000 mm. In spite of the results presented by Louter *et al.* [5.5], that indicated few differences between small-scale and full-scale glass-stainless steel beams, others have shown that the application of the hybrid glass beams concept to large-scale structures can be challenging, since other design details, such as adhesively bonded joint strength prediction, the susceptibility to LTB phenomenon and the influence of the structural adhesive and interlayer, must be accounted for [5.13]. In that regard, the topic of interfacial stresses at adhesively bonded joints of hybrid beams has been assessed by several authors, especially in studies concerned with the flexural performance of reinforced concrete members strengthened with FRP systems or steel profiles, for which the adhesively bonded connection plays a major role [5.14–5.19]. However, despite the application of similar principles, only few authors have studied the behaviour of adhesively bonded joints in the field of hybrid glass systems [5.20, 5.21].

In this chapter an exploratory experimental, analytical and numerical study is carried out on long-span laminated glass-stainless steel hybrid beams. The main objectives of the study were three-fold: (i) to assess the applicability of the glass-stainless steel hybrid beams concept to large-scale structures, (ii) to quantify the influence on the global post-cracking flexural robustness of fully tempered cracked glass panes of a PVB-laminated hybrid glass beam, and (iii) to estimate the debonding strength of adhesively bonded joints between glass and stainless steel. The experimental campaign comprised flexural tests on

³ Different authors have carried out analytical, experimental and numerical investigations about the post-cracking performance of laminated glass panes and beams with different damage stages [5.8–5.12].

two long-span PVB and SG-laminated glass beams reinforced with stainless steel profiles in the top and bottom edges. In the analytical study, a simplified analytical model that accounts for the influence of the fully tempered cracked glass plies on the flexural stiffness of the PVB-laminated hybrid glass beams is presented. Finally, the stress state at the adhesively bonded joints of the SG-laminated hybrid glass beam was numerically investigated.

5.2 EXPERIMENTAL PROGRAMME

5.2.1 Structural design

Two long-span laminated glass beams were reinforced with stainless steel profiles at both their top and bottom edges. The cross-section of both hybrid beams is depicted in Fig. 5.1. Laminated glass beam S1 was 8200 mm long, 600 mm high, and comprised 3 glass plies with a thickness of 14.5 mm, coupled by means of two PVB sheets. The two outer glass plies were deliberately cracked prior to the application of the reinforcement. Laminated glass beam S2 was 9500 mm long, 700 mm high, and comprised 4 glass plies (uncracked) with a thickness of 15.0 mm, coupled by means of three SentryGlas sheets. The PVB sheets were 2.28 mm thick, while the SG sheets were 1.52 mm thick. All glass plies of both beams were made of FTG with polished edges. The cross-section of the stainless steel reinforcement profiles was $20 \times 40 \text{ mm}^2$ and $20 \times 60 \text{ mm}^2$, respectively in beams S1 and S2.

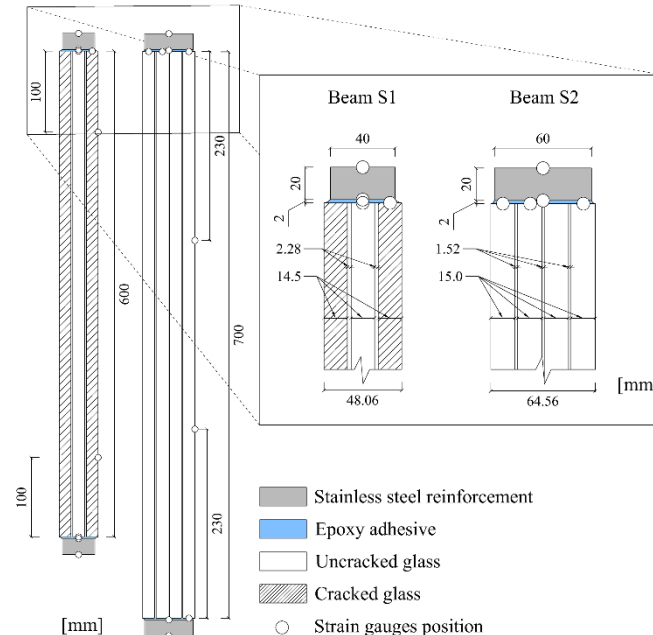


Fig. 5.1 - Cross-section of the glass-stainless steel hybrid beams.

The underlying concept of hybrid glass structures was already explained in chapter 2, section 2.3. In this study, the hybrid glass beams were designed based on the following assumptions and principles: (i) the reinforcement area in the bottom edge was designed to withstand 80% of the maximum tensile load of

the glass plies in their linear stage, assuming that glass presents a maximum tensile strength of 120 MPa; (ii) the reinforcement area in the top edge was set equal to the bottom one in order to withstand part of the compressive stresses developed by the internal load-bearing mechanism and to provide additional stability at the compressive zone, namely in the post-cracking stage; (iii) the adhesive used at the bonded interfaces (detailed ahead in section 5.1.2) was selected based on the experience acquired from previous studies on hybrid glass structures performed at IST.

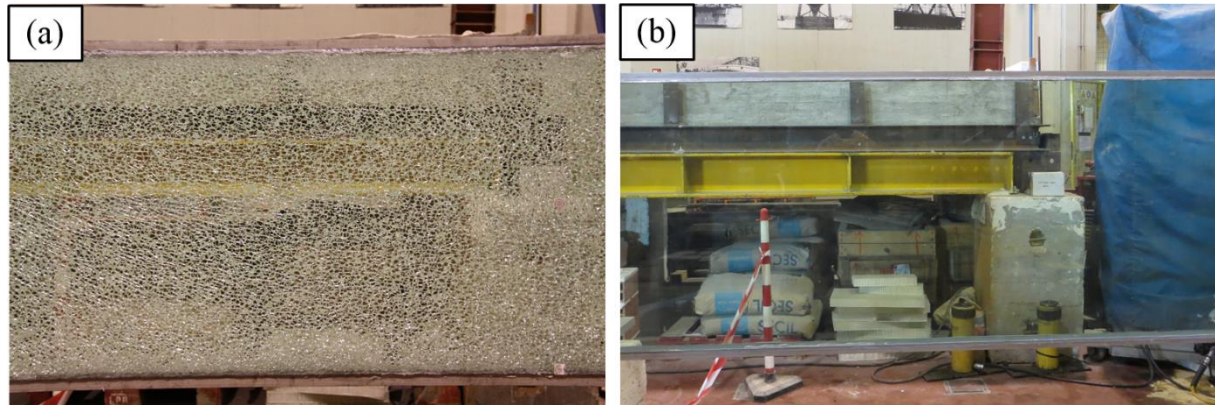


Fig. 5.2 – Longitudinal view of (a) PVB and (b) SG-laminated glass-stainless steel hybrid beams tested (note that the outer glass plies in the former beam are cracked).

5.2.2 Materials

Five different materials were used in this study: (i) fully tempered glass; two different interlayers, (ii) PVB and (iii) SG; (iv) stainless steel; and (v) epoxy resin (*Sikadur 330*). None of the materials was subjected to specific characterization tests, as most of them had been either object of previous tests at IST (adhesive) or duly characterized in the literature [5.22–5.29] (glass, stainless steel and interlayers); concerning glass, its characterization would have required an extensive experimental campaign, not possible to carry out since the glass elements tested were provided already laminated. The average physical and mechanical properties of each material are listed in Table 5.1, namely their elastic modulus (E_i), ultimate tensile strength ($f_{i,t}$) and Poisson's ratio (ν_i). Due to the dimensions required for the reinforcement profiles, two different types of stainless steel were used, with very similar mechanical properties.

Table 5.1 - Average physical and mechanical properties of the materials used on hybrid beams.

Property	Glass ¹	Stainless steel ^{2,7}		Interlayer	Adhesive	
Designation	Fully tempered	1.4301	1.4401	SentryGlas	Polyvinyl butyral	Sikadur 330
E_i [MPa]	70 000	200 000		125 ³	8.1 ³	5132 ⁵
$f_{i,t}$ [MPa]	120	500 - 700	510 - 710	34.5 ⁴	> 20.0 ⁴	23.6 ⁵
ν_i [-]	0.23	0.30		N.I.	N.I.	0.30 ⁶

N.I. - No information

¹ According to [5.25]; ² According to [5.26]; ³ According to [5.27]; ⁴ According to [5.22] for a temperature of 20 °C and a loading time of 3 sec; ⁵ As reported by [5.23]; ⁶ As reported by [5.28], and cited by [5.29].

⁷ Stainless steel 1.4301 applied on beam S1 and 1.4401 applied on beam S2.

5.2.3 Manufacturing of the beams

The manufacturing process of the hybrid glass beams comprised mainly the preparation of the bonding surfaces, both on glass and stainless steel reinforcement elements, and the bonding of the reinforcement elements to the laminated glass panels.

In the case of beam S1 the manufacturing process (Fig. 5.3) comprised the following steps:

1. Cleaning and degreasing of the adherend surfaces of the laminated glass beam using acetone;
2. Mechanical abrading, cleaning and degreasing (using acetone) of the adherend surfaces of the stainless steel reinforcement profiles;
3. Breakage of the outer glass plies of the laminated glass beam⁴;
4. Positioning of the laminated glass beam (Fig. 5.3-a);
5. Positioning of PVC spacers in the inner glass layer of the laminated glass beam in order to guarantee a 2 mm joint thickness (Fig. 5.3-b);
6. Preparation and application of the 2-component epoxy adhesive on the top edge of the laminated glass beam (Fig. 5.3-c);
7. Positioning of the reinforcement profile (Fig. 5.3-d);
8. Finishing of the adhesive joint (Fig. 5.3-e);
9. Curing of the adhesive for 24 hours under light weights (Fig. 5.3-e);
10. Repositioning and readjustment of the beam position in order to receive the bottom reinforcement profile;
11. Repetition of steps 4 to 9 applied to the bottom edge of the hybrid glass beam.

The manufacturing process of beam S2 was equivalent to the one applied to produce beam S1, with the exception of step 3, as beam S2 was tested undamaged.

5.2.4 Test setup and procedure

The reinforced glass beams were subjected to flexural tests in a symmetrical 4-point bending simply supported configuration. The values of the total length (L), flexural span (L_0), distance from the support to the load application points (L_a) and overhangs (L_l) of the two beams tested are detailed in Table 5.2. The lateral displacements were restrained by three pairs of metal frames, one at each support and one at mid-span (Fig. 5.4-a). The configuration of the flexural tests is schematized in Fig. 5.5 and illustrated in Fig. 5.6.

Table 5.2 – Test setup of the flexural tests on glass-stainless steel hybrid glass beams.

Hybrid beam	L [m]	L_0 [m]	L_a [m]	L_l [m]
S1 (3-layer PVB)	8000	7800	2600	200
S2 (4-layer SG)	9500	8000	2660	750

⁴ The outer glass plies were damaged using a hardened tool with an impact tip.

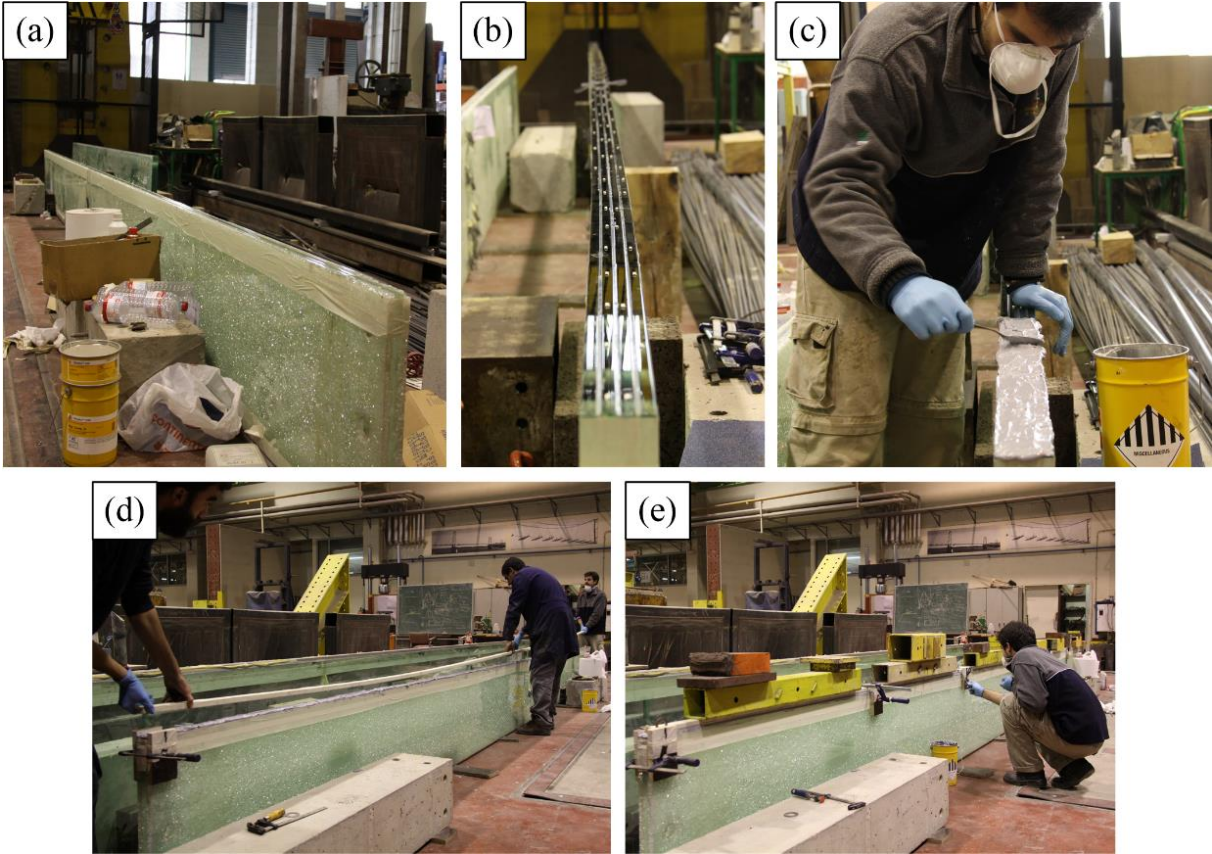


Fig. 5.3 – Manufacturing process of laminated glass-stainless steel hybrid beams: (a) positioning of the laminated glass element, (b) positioning of the PVC spacers, (c) application of the structural adhesive, (d) positioning of the reinforcement profile and (e) finishing of the joint (picture (b) refers to beam S2, all the others to beam S1).

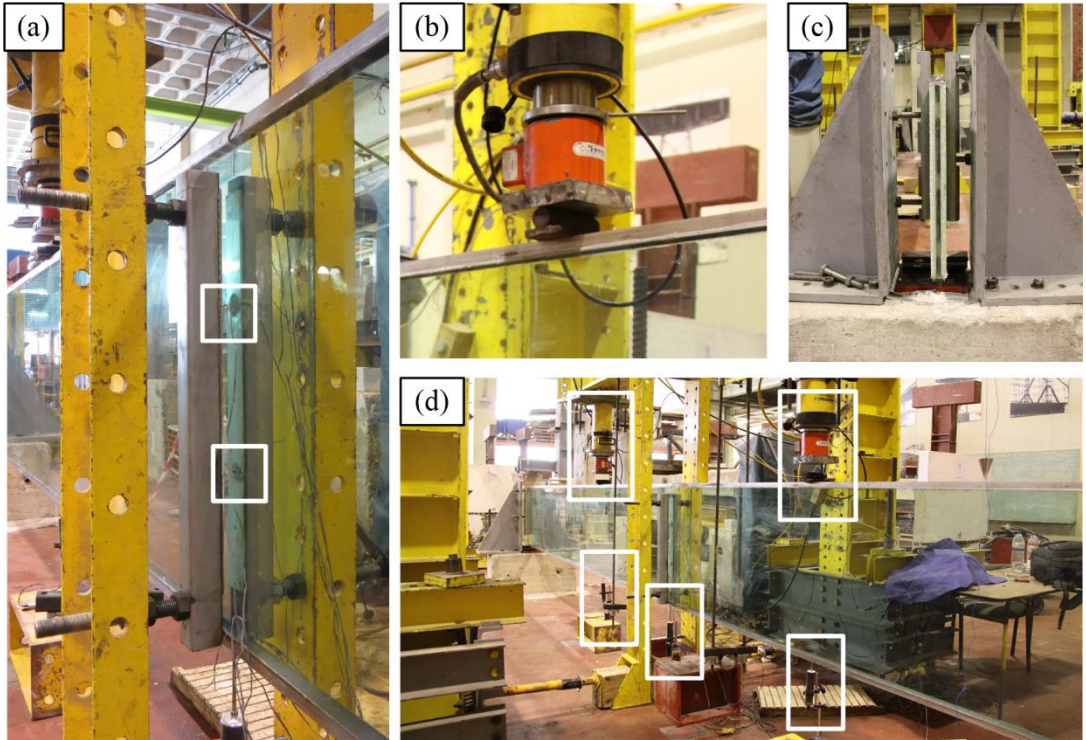


Fig. 5.4 – Glass-stainless steel hybrid beams test setup: (a) mid-span metal frames; (b) load application point; (c) supports; (d) load (top) and deflection (bottom) measurement devices.

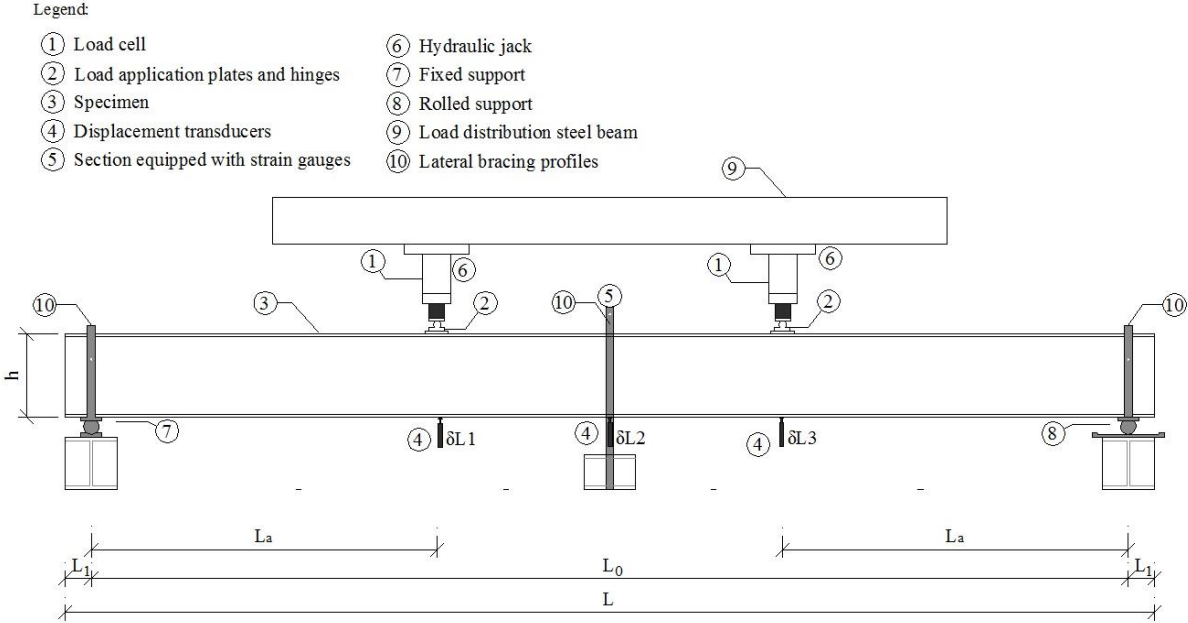


Fig. 5.5 – Illustration of the flexural test setup and its features.

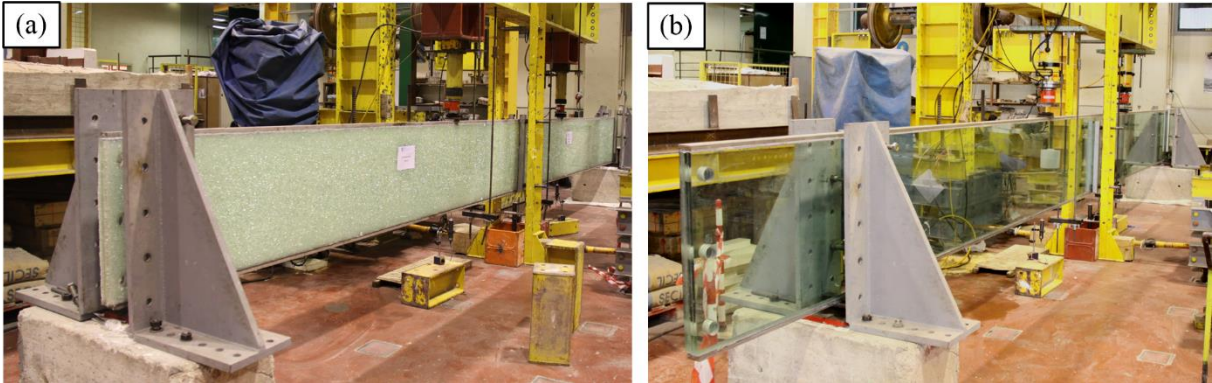


Fig. 5.6 – Test setup of the glass-stainless steel hybrid glass beams (a) S1 and (b) S2.

Both beams were monotonically loaded using two hydraulic jacks reacting against a steel (HEB 300) loading beam, which was connected to a steel resisting frame. Cylindrical metal hinges were positioned between the hydraulic jacks and the top surface of the tested beams (Fig. 5.4-b). The supports consisted of cylindrical rollers, placed in-between metal plates, positioned on top of concrete blocks with a plaster layer in-between that was applied to correct possible altimetry differences (Fig. 5.4-c). The major-axis-flexural rotations were free at both end supports and one of them allowed also for longitudinal sliding.

The load was applied by a *Walter+Bai* hydraulic system that allows controlling the pressure transmitted to the jack and indirectly control the displacement speed. The displacement speed was adjusted and kept constant for both beams at a speed of about 3.00 mm/min. The total duration of the flexural tests was 475 s and 730 s, respectively for beams S1 and S2.

The vertical displacements of the beams were measured at the loaded and at mid-span sections with displacement transducers (strokes of 50 and 100 mm, precision of 0.01 mm). The load applied by each

hydraulic jack was measured with load cells (capacity of 300 kN; precision of 0.01 kN) placed in between the jacks and the top surface of each beam (Fig. 5.4-d). The interaction level at the glass/stainless steel interfaces provided by the adhesively bonded joint, as well as the load distribution among the several glass plies, was assessed by measuring the longitudinal strains at different positions throughout the height of the mid-span section (9 in beam S1 and 10 in beam S2), using electrical strain-gauges (*cf.* Fig. 5.1). The applied loads, vertical displacements and most strain-gauges were measured at an average speed of 10 Hz. The 3 strain-gauges positioned at the top glass-stainless steel interface were measured at 100 Hz.

Both beam tests were carried out in laboratory environment. In the test of beam S1, the average temperature and relative humidity were respectively 11.7 °C and 70%, whereas during the test of beam S2 those figures were 12.1 °C and 55%, respectively.

5.3 EXPERIMENTAL RESULTS

5.3.1 Load-deflection behaviour and strength

Fig. 5.7 presents the load *vs.* mid-span deflection response of both glass-stainless steel hybrid beams. Beam S1, despite presenting two fully cracked glass plies (prior to loading), exhibited a considerable post-cracking residual stiffness (discussed ahead in section 5.4.3) and load bearing capacity, but did not present any residual strength after the breakage of the remaining (inner) uncracked glass ply. Regarding beam S2, unlike what was expected, it collapsed immediately after the breakage of the glass plies - they all broke unpredictably and at the same instant (discussed ahead in section 5.3.2); this means that the stainless steel reinforcement was not able to carry the load released by the broken plies, and hence the beam did not present any post-cracking load bearing capacity. In summary, the breakage of all glass layers resulted in the total loss of integrity of both hybrid glass beams and, after that moment, no residual post-cracking resistance was observed.

Fig. 5.8 depicts the evolution of the secant flexural stiffness (EI_{comp}^{sec}) as a function of the applied load, estimated using Euler-Bernoulli beam's theory⁵. Both beams exhibited a slightly non-linear behaviour, indicating a progressive reduction of flexural stiffness with the load level. In fact, the maximum flexural stiffness of each beam (horizontal dashed line in Fig. 5.8), determined as the maximum derivative of the corresponding load *vs.* mid-span deflection response, was kept only during an initial stage of the tests (approximately up to 20 kN and 50 kN, respectively for beams S1 and S2). Subsequently, a roughly linear reduction of flexural stiffness was observed up to failure. The ultimate (secant) flexural stiffness of beams S1 and S2 was respectively 68.2 kN.m² and 152.6 kN.m², which corresponds to total reductions of 9.1% and 12.6%, respectively. Regarding beam S1, the decreasing trend of the flexural

⁵ The expression used for the estimation of the secant flexural stiffness is equal to Eq. (4.3) presented in chapter 4, section 4.1.1.

stiffness should be related with the detachment of glass fragments and the consequent loss of integrity of the glass plies: it is very likely that such detachment reduced the axial and shear stiffness of the cracked glass plies. In the case of beam S2, where much higher loads were attained, the flexural stiffness reduction might have stemmed from the non-linear behaviour of the adhesive in shear, which affects the coupling (interaction) between glass and stainless steel, thus affecting the global flexural stiffness of the hybrid beam.

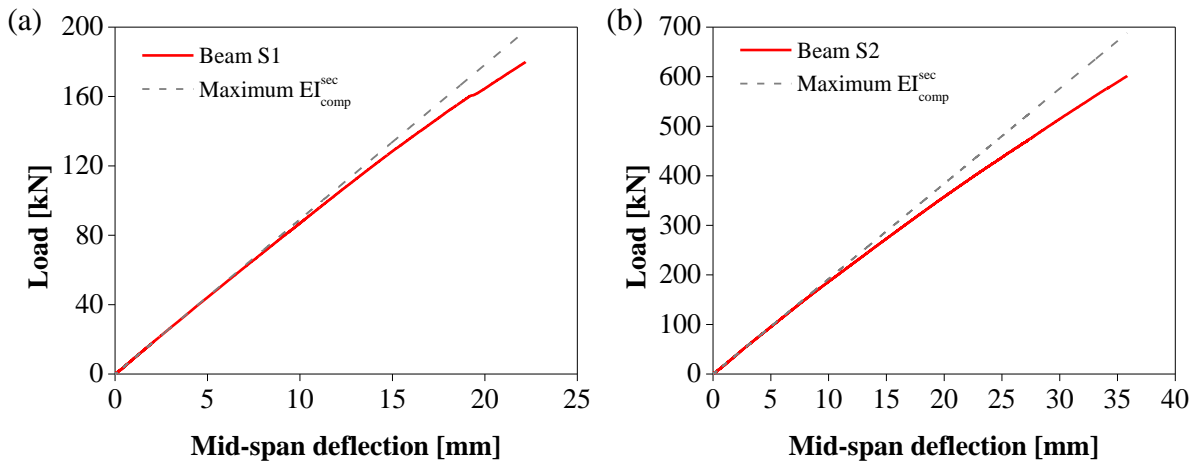


Fig. 5.7 – Load vs. mid-span deflection curves of (a) beam S1 and (b) beam S2.

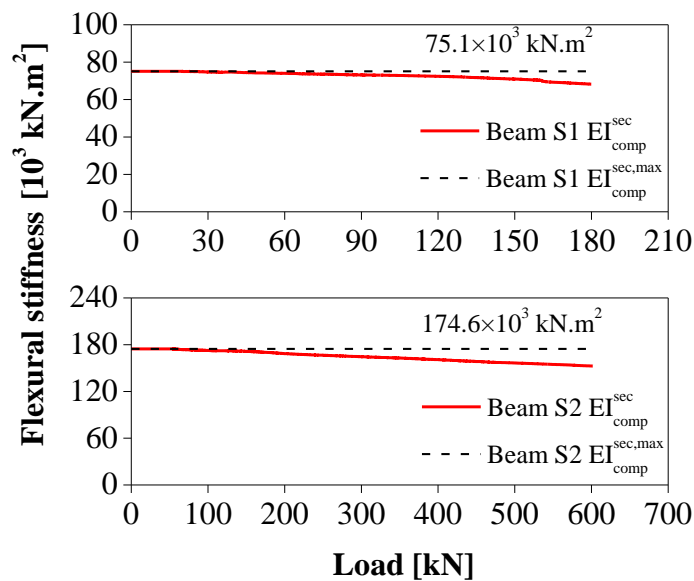


Fig. 5.8 – Flexural stiffness evolution of (top) beam S1 and (bottom) beam S2.

Table 5.3 summarizes the main results of the flexural tests in terms of maximum total load (P_{max}), maximum flexural stiffness ($EI_{comp}^{sec,max}$) and secant flexural stiffness at the moment of failure ($EI_{comp}^{sec,u}$), and mid-span deflection at failure (δ_u).

Table 5.3 – Results of tests of glass-stainless steel hybrid beams.

Beams	P_{max} [kN]	$EI_{comp}^{sec,max}$ [10^3 kN.m ²]	$EI_{comp}^{sec,u}$ [10^3 kN.m ²]	δ_u [mm]
Beam S1	179.9	75.1	68.2 (- 9.1%) ¹	22.5
Beam S2	601.6	174.6	152.6 (-12.6%) ¹	35.9

¹Relative difference to $EI_{comp}^{sec,max}$ in brackets.

5.3.2 Failure behaviour

As mentioned, both beams were monotonically loaded up to failure, which occurred after the breakage of the inner glass ply (the remaining one, in beam S1) or all glass plies (beam S2). After that point, the hybrid glass beams were unable to present (extra) residual strength. At the moment of collapse, the following two mechanisms, which visually seemed to occur almost simultaneously, could be identified: (i) breakage of the (uncracked) glass plies, and (ii) debonding of the reinforcement stainless steel profiles. Using photo and video recordings and readings from the strain-gauges, it was possible to draw further conclusions about the sequence of events at the moment of failure, which are described next.

5.3.2.1 Beam S1

Fig. 5.9 illustrates a sequence of photos taken immediately before and after the ultimate failure of beam S1. The photo and video recordings made during the test of beam S1 indicate that the debonding of the bottom reinforcing profile occurred first (i.e. prior to the breakage of the inner glass ply) and it was this event that triggered the breakage of the inner glass ply. Indeed, in Fig. 5.9-b one may observe that there is a location in this beam, close to one of the supports, where a small explosive fragmentation of the glass ply is visible. This breakage of the glass ply seems to have arisen from that debonding event, since the surrounding area presents a different colour contrast, suggesting a denser breakage pattern⁶. On its turn, the noticeable explosion and the subsequent glass breakage occurred due to the local debonding of the bottom reinforcement bar, which became perfectly clear few instants later (Fig. 5.9-c). Once the debonding occurred, the transfer of tensile stresses between glass and the reinforcement was compromised and the reinforcing profiles could not be activated, thus no residual strength was mobilized. This is supported by the data retrieved from strain-gauges (presented ahead in section 5.3.3), which show a noticeable slippage increase immediately before failure, and maximum tensile stresses (at that moment) in the inner glass ply of around 79.5 MPa, i.e. much lower than its characteristic bending strength⁷ (cf. Table 5.1).

⁶ In laminated glass members, any damage leading to the breakage of a fully tempered glass ply generally results in an instantaneous propagation of the cracks through the remaining glass plies.

⁷ Notwithstanding, the measured tensile stress is within the range of variation of glass tensile strength [5.24].

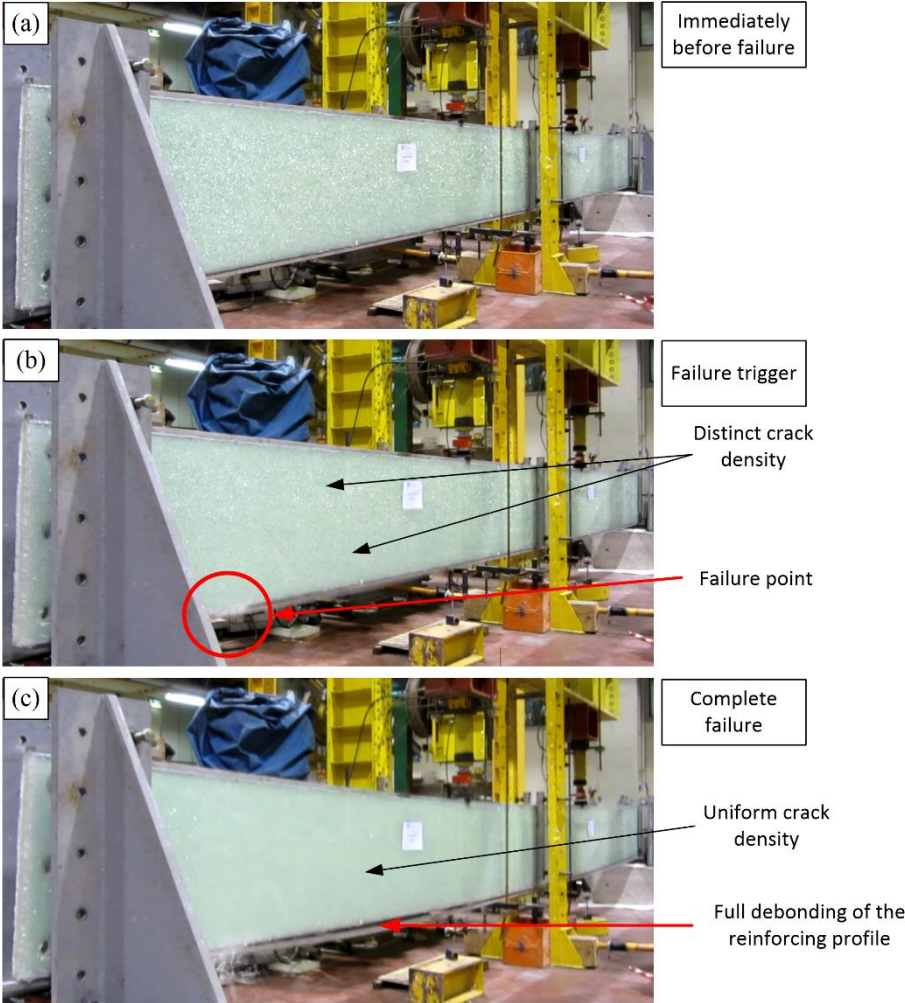


Fig. 5.9 – Failure behaviour of beam S1.

5.3.2.2 Beam S2

The ultimate failure of beam S2 occurred due to the debonding of the reinforcing profile at the bottom adhesive-stainless steel interface, which prevented the hybrid beam to make use of the full potential of the internal load-bearing mechanism. However, neither the video recordings nor the strain-gauges data (through the high speed strain-gauges readings) allowed to conclude if such debonding was the triggering event or the result of the failure of the inner glass plies⁸. In true, both events, the explosive failure close to one of the supports (which suggests the local debonding of the reinforcement - Fig. 5.10-b) and the failure of the inner glass plies, were separated by a time gap of less than 42 ms (time gap between video frames), which makes it very difficult/impossible to draw a definitive conclusion about the actual sequence of events. Furthermore, the strain-gauge measurements (presented ahead in section 5.3.3) indicate that the maximum tensile stress on the glass plies in the brink of collapse was about 124.8 MPa, which is actually (slightly) higher than the characteristic bending strength of fully tempered

⁸ The high-speed strain-gauges readings only allowed to determine that breakage initially occurred in the inner glass plies.

glass (cf. Table 5.1). Therefore, in this case it is not possible to conclude if the debonding of the reinforcing profile and the consequent collapse of the beam was triggered by the failure of the adhesively bonded joint or by the energy release caused by the breakage of the inner glass plies. In either case, once the debonding occurred, all glass plies cracked and the final failure of the beam occurred after an explosive disintegration of the area below the load application point (Fig. 5.10-c). Section 5.4.2 presents a numerical study, where further analysis of these mechanisms is presented.

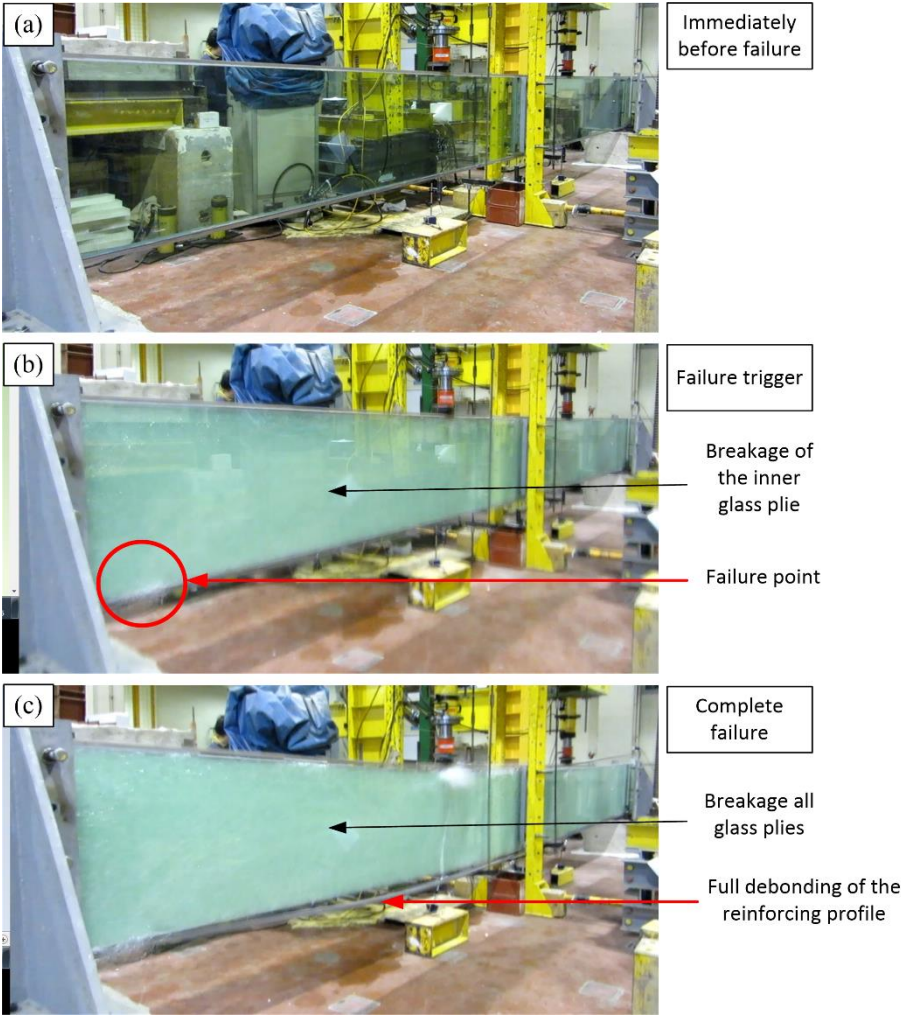


Fig. 5.10 – Failure behaviour of beam S2.

5.3.3 Composite action and position of the neutral axis

The strain-gauge readings provided information about the strain/stress distribution along the height of the mid-span section of the beams, crossing the different components/materials that constitute the cross-section. This allowed assessing the degree of coupling (shear interaction) at the adhesively bonded interfaces of the glass-stainless steel hybrid beams.

Fig. 5.11 illustrates the development of axial strains during the flexural test of beam S1, obtained from the strain-gauges applied either in the inner (uncracked) glass ply (Fig. 5.11-a) or in the outer (cracked)

glass plies (Fig. 5.11-b). The dashed lines in Fig. 5.11-b correspond to measurements obtained from the inner glass ply, thus not considering the readings at the bottom interface between the outer glass plies and the reinforcing profile. One may observe that, although the outer glass plies were cracked, the readings at those elements were not affected and were actually in line with the readings retrieved exclusively from the inner glass ply. Indeed, the cross-section curvature calculated from the readings of the outer strain-gauges match the ones retrieved from the inner strain-gauges. Therefore, one may conclude that the PVB interlayer played an important role in keeping the glass pieces of the cracked/broken glass plies together, making the beam bend as a homogeneous layer.

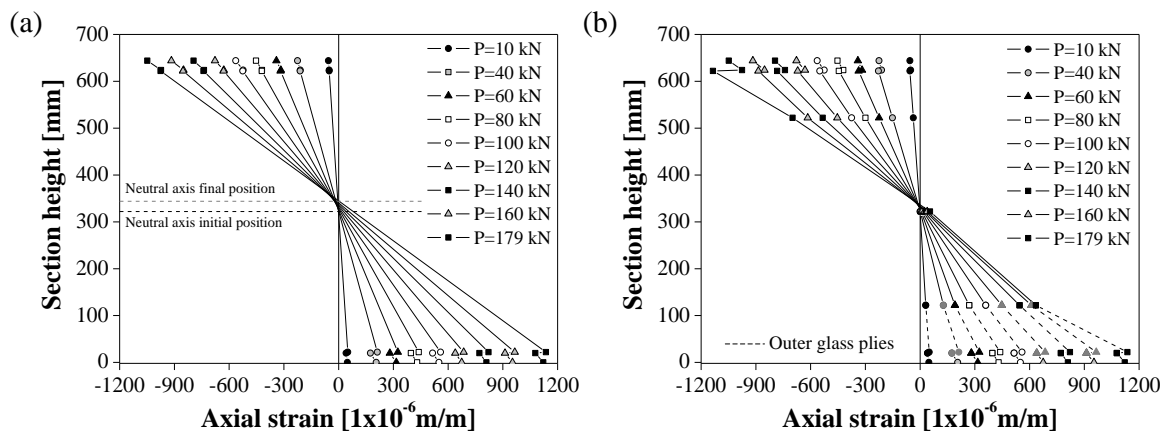


Fig. 5.11 – Axial strains vs. section height in beam S1 for different load levels (in kN) measured at (a) the inner glass ply and (b) the outer glass plies.

In what concerns the degree of coupling of beam S1, one may observe that no slippage occurred between the stainless steel reinforcement and the inner glass ply at the top interface. However, at the bottom interface of the inner glass ply and at the top and bottom interfaces of the outer (damaged) glass ply, a slight difference between the strains in the glass and in the stainless steel reinforcement was measured. This result is consistent with the sudden decrease of flexural stiffness of the beam in the brink of failure, as well as with the observed debonding of the reinforcement profile in that interface (*cf.* Fig. 5.9).

Finally, another interesting result is the slight change of position of the neutral axis during the test of beam S1: initially, the axial strain readings indicated a completely symmetrical distribution of strains throughout the height of the cross-section; however, at a load of 60 kN the position of the neutral axis started to rise up and, at the end of the test, the neutral axis had risen up more than 22 mm (Fig. 5.11-a), indicating an increase of the cross-sectional area subjected to tensile stresses. This should be related with the loss of integrity of the damaged glass plies, which resulted in an uneven stiffness distribution along the cross-section height.

Fig. 5.12 depicts the axial strain readings obtained from the mid-span cross-section of beam S2 during the bending test. The strain-gauges used to measure the axial strains in the top edge of the three glass

plies yielded equivalent readings during all the test, confirming the good coupling performance of the SG interlayer in this configuration (load applied in the beam plane). The epoxy adhesive used to bond the stainless steel reinforcement to glass was unable to guarantee the maximum degree of interaction between both materials and some slippage was observed for all load stages at both interfaces. Such slippage increased with the load level, which is consistent with the loss of flexural stiffness during the beam's bending test.

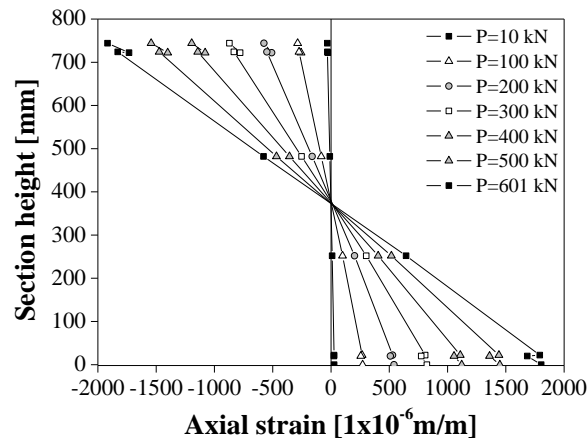


Fig. 5.12 - Axial strains vs. section height for different load levels (in kN) for the beam S2.

5.4 ANALYTICAL AND NUMERICAL STUDY

5.4.1 Preliminary remarks

The experimental results presented in the previous section showed a significant variation of the flexural stiffness of large-scale (cracked and uncracked) laminated hybrid glass-stainless steel beams with the load level (in the case of beam S1 it refers to broken flexural stiffness). On the other hand, the data retrieved from the flexural tests was insufficient to clarify the triggering event that led to the failure of beam S2. In the following sections, complementary analytical (beam S1 and S2) and numerical studies (beam S2) are presented to analyse the observed variation of the flexural stiffness and to assess in further depth the failure mode of the hybrid glass beams.

Section 5.4.2 describes the main scenarios and parameters assumed in the analytical studies that follow. Section 5.4.3 presents the analytical study developed to determine the contribution of the broken glass plies to the global flexural stiffness of hybrid glass beam S1. Such contribution was assumed as an equivalent elastic modulus, which, together with that of the remaining unbroken glass ply, corresponds to the evolution of flexural stiffness measured in the test. Finally, section 5.4.4 describes the numerical study developed to clarify the premature failure of hybrid glass beam S2. Those studies focused on the interaction provided by the adhesive joint and its evolution during the flexural test.

5.4.2 Analytical estimate of the flexural performance of the hybrid glass beams

This section presents the analytical estimate of the flexural performance of the hybrid glass beams. Three different situations or scenarios were considered: (i) non-reinforced laminated glass beams; (ii) reinforced laminated glass beams with the outer plies cracked (the test scenario of beam S1), and (iii) reinforced laminated glass beams with uncracked glass plies (the test scenario of beam S2). For this analytical study, the following parameters concerned with the flexural performance of the hybrid glass beams were determined:

- EI is the bending stiffness of the laminated glass beams without reinforcement;
- EI_{comp} and EI_{comp}^{cr} correspond to the bending stiffness respectively of the uncracked and cracked hybrid glass beams (for the cracked state, one assumes that the outer glass plies are fully cracked);
- P_{cr} is the total load (4-point bending load in a configuration similar to that used in the experiments) that causes a maximum tensile stress of 120 MPa in the glass layers of the laminated beams without reinforcement (assuming uniform stress distribution throughout the glass layers);
- $P_{cr,comp}$ and $P_{cr,comp}^{cr}$ correspond to the loads (applied in the same configuration) that cause a maximum tensile stress of 120 MPa in glass, but now respectively for the uncracked and cracked (outer plies) hybrid glass beams.

The next paragraphs describe the underlying assumptions and formulae used for the determination of the above-mentioned parameters.

The parameters EI and P_{cr} were determined neglecting the physical existence of the interlayer sheets, but assuming that both PVB and SG interlayers provide full interaction to the cross-section of the laminated glass beams⁹.

The composite bending stiffness, EI_{comp} (Eq. 5.1), can be regarded as the sum of (i) the flexural stiffness of all materials w.r.t. their own centroidal axes (EI_{gl}), and (ii) the flexural stiffness of all materials w.r.t. the neutral axis (EI_s) multiplied by a factor ξ_f that reflects the composite action level provided by the joint: $\xi_f = 0$ if the composite level is null and $\xi_f = 1$ for full interaction¹⁰. The parameters EI_{gl} and EI_s are function of the configuration and materials of the hybrid beam and should be calculated according to (Eq. 5.2) and (Eq. 5.3), respectively.

⁹ The influence of the thin interlayer sheets can be disregarded on the determination of the global flexural performance of laminated glass beams, i.e. glass members subjected to loads on their plane and bending around their major flexural axis [5.10].

¹⁰ Different analytical approaches are available in the literature (e.g. [5.20]) to estimate ξ_f . In the present study, the experimental data obtained is used to estimate the variation of ξ_f as a function of the load level (presented ahead in section 5.4.4.1).

$$EI_{comp} = EI_{gl} + \xi_f EI_s = E \sum_i I_i \frac{E_i}{E} + \xi_f \left(E \sum_i d_i^2 A_i \frac{E_i}{E} \right) \quad (5.1)$$

$$EI_{gl} = E \sum_i I_i \frac{E_i}{E} \quad (5.2)$$

$$EI_s = E \sum_i d_i^2 A_i \frac{E_i}{E} \quad (5.3)$$

In the formulae above, i stands for the i^{th} constituent material of the cross-section, E and E_i are the Young's moduli of glass and of the material i , d_i is the distance between the centroid of the material i section and the neutral axis of the beam section, A_i is the cross-sectional area of the material i and I_i is the moment of inertia around the major flexural axis of material i .

The parameters EI_{comp} , EI_{comp}^{cr} , $P_{cr,comp}$ and $P_{cr,comp}^{cr}$ were determined assuming linear elastic response of all materials, full interaction (i.e. $\xi_f = 1$) between all glass layers and between these and the stainless steel reinforcement (note that $P_{cr,comp}$ and $P_{cr,comp}^{cr}$ are only valid for the geometry and load configuration used in the flexural tests of both beams used in this study).

Finally, the parameters EI_{comp}^{cr} and $P_{cr,comp}^{cr}$ were determined assuming that the outer glass layers are fully damaged and, in those conditions, the cracked material (small glass pieces bonded to the interlayer) has no contribution to the flexural performance of the hybrid glass beams (i.e. its elastic modulus is null), but is able to transfer shear stresses between the top and bottom reinforcing sections.

Table 5.4 summarizes the results of the analytical study in terms of the parameters that describe the flexural performance of the hybrid beams S1 and S2. Next, these parameters are compared with experimental data obtained in the tests of beams S1 and S2 (section 5.3.1 presents further insights about the flexural behaviour of those beams).

Table 5.4 – Analytical estimates of the flexural performance of beams S1 and S2, with and without reinforcement and considering the cracking of the outer glass plies (beam S1).

Beam	EI [10^3 kN.m ²]	EI_{comp} [10^3 kN.m ²]	EI_{comp}^{cr} [10^3 kN.m ²]	P_{cr} [kN]	$P_{cr,comp}$ [kN]	$P_{cr,comp}^{cr}$ [kN]
Beam S1	56.7	85.9 (+ 52%) [#]	48.1*	249.2	377.6	211.5*
Beam S2	120.0	179.2 (+49%) [#]	N.A.	441.0	658.1	N.A.

* Assuming that the outer glass plies are fully cracked.

Relative difference to EI (in brackets).

N.A. - not applicable

5.4.3 Beam S1

5.4.3.1 Comparison of analytical and experimental values of flexural stiffness

Table 5.5 compares the experimental flexural stiffness values (*cf.* section 5.3.1) obtained at both the initial ($EI_{comp}^{sec,i}$) and final ($EI_{comp}^{sec,u}$) stages of the test of beam S1, with the corresponding analytical estimates computed in the previous section (*cf.* section 5.4.2).

Table 5.5 – Comparison between experimental and analytical flexural stiffness values of beam S1.

Source	Description	Stiffness [10^3 kNm ²]
Analytical	Uncracked (EI_{comp})	85.9
	Cracked (EI_{comp}^{cr})	48.1 (-44.0%) ¹
Experimental	Initial stage ($EI_{comp}^{sec,i}$)	75.1 (-12.6%) ¹
	Final stage ($EI_{comp}^{sec,u}$)	68.2 (-20.3%) ¹

¹ Relative difference to EI_{comp} (in brackets).

One may observe that the experimental values of the flexural stiffness of beam S1 range between the values estimated analytically (i) considering uncracked glass plies (EI_{comp} , upper bound) and (ii) neglecting the contribution of the cracked glass plies (EI_{comp}^{cr} , lower bound). However, unlike what would be expected *a priori*, the experimental flexural stiffness value, namely in the initial stages of the test ($EI_{comp}^{sec,i}$), was much closer to EI_{comp} (three uncracked glass plies) than to EI_{comp}^{cr} (stiffness of the two outer cracked glass plies completely neglected). In fact, even prior to failure, for which the lowest value of bending stiffness was measured in the tests, the experimental flexural stiffness ($EI_{comp}^{sec,u}$) was only 20.3% lower than EI_{comp} . This analysis shows that neglecting the contribution of the cracked glass plies to the overall flexural stiffness of hybrid beams is a too conservative assumption: the experimental results indicate that the flexural stiffness can be up to 56.1% higher. Such inaccuracy (or over-conservatism) points out the need to account for (and duly quantify) the contribution of the broken glass plies to the flexural response of the hybrid glass beam in a cracked stage.

5.4.3.2 Determination of the equivalent elastic modulus of the cracked glass plies

This section presents a simplified estimate of the contribution of the cracked glass plies to the global flexural behaviour of the hybrid beam. Such contribution was taken into account by assuming an equivalent elastic modulus, E_{equiv} , which reflects the bending stiffness increase observed in the experiments compared to the analytical bending stiffness estimate obtained considering only the uncracked glass ply EI_{comp}^{cr} (i.e. neglecting the contribution of the two outer cracked glass plies).

In this study, the E_{equiv} was estimated considering two different approaches: (i) the cracked glass plies were first assumed homogenous, with the elastic modulus in tension ($E_{equiv,t}$) and compression ($E_{equiv,c}$)

being equal ($E_{equiv,t} = E_{equiv,c} = E_{equiv}$); and (ii) the cracked glass plies were then considered heterogeneous with different behaviour in tension and compression ($E_{equiv,t} \neq E_{equiv,c} \neq E_{equiv}$). In the following paragraphs the main underlying assumptions of each approach are briefly described.

For the first approach, assuming that the cracked glass plies have a similar response in tension and in compression, the strain distribution in the cross-section will be symmetrical w.r.t. to the cross-section centroid. This assumption is consistent with the experimental observations for loads up to 20 kN: indeed, until that load level the neutral axis position was coincident with the cross-section centroid (*cf.* Fig. 5.11). In those conditions, provided that the geometry of the cracked glass plies remains unchanged, the flexural stiffness increase (29,977 kN.m²) w.r.t. to the analytical estimate of EI_{comp}^{cr} is obtained assuming that $E_{equiv,t} = E_{equiv,c} = 50.0$ GPa, which corresponds to a 40% reduction compared to the Young's modulus of uncracked glass (70 GPa).

The underlying principle of second approach is that it is not likely that a cracked glass ply behaves similarly in compression and tension and regardless of the applied load. The response of a cracked glass ply results from the contribution and interaction of three different effects: (i) adhesion (to the interlayer), (ii) interlocking and (iii) friction between the glass fragments. While the adhesion and friction may not be affected by the stress state, the interlocking effect is likely to be different when the (cracked) material is subjected to compression and tension. The experimental data obtained in the test of beam S1 shows that for loads above 20 kN (i) the neutral axis started to move upwards, indicating an increasing cross-section area under tensile stresses, and (ii) the flexural stiffness started to decrease. This scenario suggests a more significant loss of integrity in the bottom part of the cracked glass planes, i.e. the part that was under tensile stresses. Thus, one may conclude that the equivalent moduli in tension and compression are different from each other and should vary with the load/stress level. As mentioned, the movement of the neutral axis shows that $E_{equiv,c} > E_{equiv,t}$; this is logical, as the interlocking effect should be better mobilized in compression than in tension.

Based on the above-mentioned discussion, the values of $E_{equiv,c}$ and $E_{equiv,t}$ as a function of the applied load were defined based on a simplified cross-section analysis¹¹, which considered: (i) the experimental bending stiffness of the cracked composite system (which progressively decreased from $EI_{comp}^{sec,i} = 75,102 \times 10^3$ kNm² to $EI_{comp}^{sec,u} = 68,240 \times 10^3$ kNm²), and (ii) the static equilibrium of internal compressive (F_c) and tensile (F_t) forces developed in the cross-section (Eq. (5.4)).

$$F_c = F_t \quad (5.4)$$

¹¹ It assumes (i) full interaction between the reinforcing profile and all glass plies, and (ii) that compressive and tensile strains in the uncracked and cracked glass plies are equal (fulfilling Bernoulli's hypothesis).

The cross-sectional internal forces during the cracked stage can be calculated assuming a linear strain distribution over the cross-section (Fig. 5.13) as follows:

$$F_c = E_{re} \cdot A_{re} \cdot \varepsilon_{re,c} + \frac{1}{2} \cdot (2E_{equiv,c} + E) \cdot \left(d - x - \frac{t_{re}}{2}\right) \cdot t_i \cdot \varepsilon_c \quad (5.5)$$

$$F_t = E_{re} \cdot A_{re} \cdot \varepsilon_{re,t} + \frac{1}{2} \cdot (2E_{equiv,c} + E) \cdot \left(x - \frac{t_{re}}{2}\right) \cdot t_i \cdot \varepsilon_t \quad (5.6)$$

where ε_c and ε_t are, respectively the compressive and tensile strains in glass, $\varepsilon_{re,c}$ and $\varepsilon_{re,t}$ are, respectively the compressive and tensile strains in stainless steel, A_{re} is the stainless steel profile cross-section area, E_{re} is the Young's modulus of stainless steel, E is the Young's modulus of uncracked glass, $E_{equiv,c}$ and $E_{equiv,t}$ are, respectively, the equivalent Young's moduli in compression and tension of cracked glass, t_{re} is the thickness of the stainless steel profile, t_i is the thickness of the glass plies, d is the distance between the centroid of both stainless steel profiles and x is the geometrical position of the neutral axis according to Fig. 5.13.

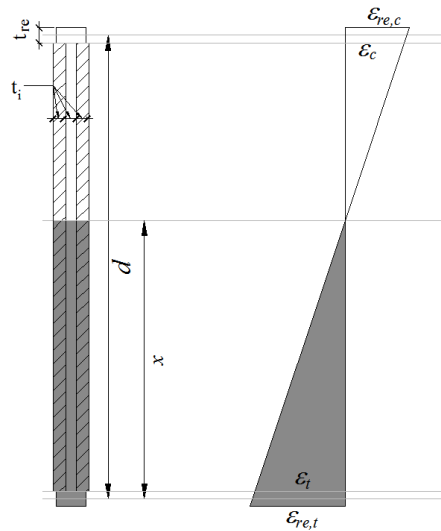


Fig. 5.13 – Schematic representation of the strain distribution in the hybrid glass beams.

The strains in the glass and in the reinforcement can be calculated using geometrical relationships, as per Eqs. (5.7-a) to (5.7-c):

$$\frac{\varepsilon_t}{\varepsilon_{re,t}} = \frac{(x - t_{re}/2)}{x} \quad \frac{\varepsilon_c}{\varepsilon_{re,t}} = \frac{(d - x - t_{re}/2)}{x} \quad \frac{\varepsilon_{re,c}}{\varepsilon_{re,t}} = \frac{(d - x)}{x} \quad (5.7-a, b \text{ and } c)$$

Combining Eqs. (5.7-a) to (5.7-c) into Eq. (5.5) and (5.6) results in a system of equations that are function of the elastic moduli in compression and tension of the cracked glass and the corresponding neutral axis position (Eq. (5.8) and (5.9)).

$$F_c = E_{re} \cdot A_{re} \cdot (d - x) + \frac{1}{2} \cdot (2E_{equiv,c} + E) \cdot \left(d - x - \frac{t_{re}}{2}\right)^2 \cdot t_i \quad (5.8)$$

$$F_t = E_{re} \cdot A_{re} \cdot x + \frac{1}{2} \cdot (2E_{equiv,c} + E) \cdot \left(x - \frac{t_{re}}{2}\right)^2 \cdot t_i \quad (5.9)$$

Fig. 5.14 illustrates the results obtained, namely the evolution of both equivalent moduli of cracked glass as a function of the total applied load, assuming the experimentally observed evolution of the neutral axis position and flexural stiffness. These results prompt the following observations: (i) the elastic modulus in compression suffers little changes with the applied load (the results obtained actually indicate a slight increase, which should be due to the simplifications of the analytical approach and the experimental uncertainty of the measurements) and (ii) the elastic modulus in tension progressively decreases from 50 GPa to about 25 GPa (i.e. approximately half of the initial value).

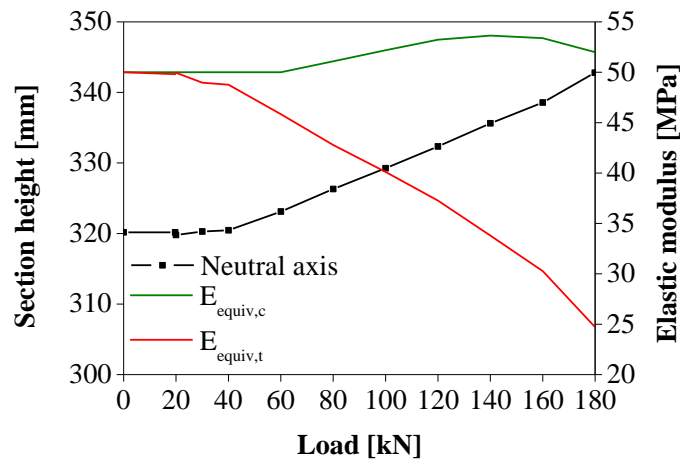


Fig. 5.14 – Experimental height of the neutral axis and analytical evolution of the compressive ($E_{equiv,c}$) and tensile ($E_{equiv,t}$) elastic modulus of cracked glass plies of beam S1.

5.4.4 Beam S2

5.4.4.1 Comparison of analytical and experimental values of flexural stiffness

Table 5.6 compares the experimental flexural stiffness values (*cf.* section 5.3.1) obtained at the initial ($EI_{comp}^{sec,i}$) and final ($EI_{comp}^{sec,u}$) stages of the test of beam S2, with the corresponding analytical estimates computed in the section 5.4.2.

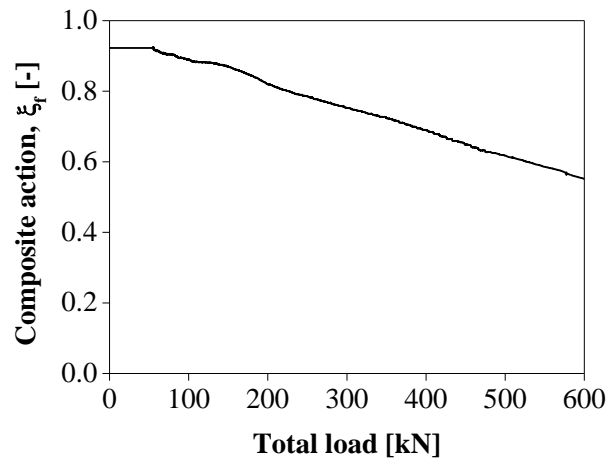
One may see that the initial flexural stiffness measured in the test was only 2.6% lower than the analytical value assuming perfect bond between glass and stainless steel. This means that at the initial stages of the test, the epoxy resin was able to provide an almost full coupling degree (or shear interaction) between the glass plies and the stainless steel reinforcing profiles. This result is in agreement with the experimental data obtained from the strain-gauges at the adhesively bonded joints, which indicated the occurrence of negligible slippage between the materials (*cf.* Fig. 5.12).

Table 5.6 – Comparison between experimental and analytical flexural stiffness values of beam S2.

Source	Description	Stiffness [10^3 kN.m^2]
Analytical	Uncracked (EI_{comp})	179.2
Experimental	Initial stage ($EI_{comp}^{sec,i}$)	174.6 (-2.6%) ¹
	Final stage ($EI_{comp}^{sec,u}$)	152.6 (-14.8%) ¹

¹ Relative difference to EI_{comp} (in brackets).

According to Eq. (5.1), the composite level provided by the adhesive can be described by factor ξ_f . In the present study, this factor was determined using the experimental data, namely the flexural stiffness data (derived from the load vs. deflection curves – cf. Fig. 5.8). Fig. 5.15 depicts the variation of the factor ξ_f as a function of the total applied load on beam S2. One may observe that the maximum composite level provided by the adhesively bonded joint was 0.92 (i.e. almost full interaction) and this degree of coupling was kept roughly constant up to a load of about 50 kN. From that point, a linear reduction of the composite level occurred until failure (in line with the linear reduction of the composite flexural stiffness), for which a value of $\xi_f = 0.55$ was reached.


 Fig. 5.15 – Composite action degree (ξ_f) of beam S2 in function of the total applied load.

5.4.4.2 Numerical study of the interfacial stresses at the bonded joints

Fig. 5.16 depicts a scheme with the stress distribution at the interfaces of an infinitesimal element of length dx of a glass-stainless steel hybrid beam, reinforced with a profile of thickness t_{re} , and subjected to a transverse point load along the span. In Fig. 5.16 the stress distribution was divided into normal (σ_{yy}) and shear (τ_{xy}) stresses and the applied mid-span load into a transverse load V and a moment M (with a variation of dM along dx). Assuming that the flexural stiffness of the adhesive layer is sufficiently low to be neglected, both V and M are distributed among the aforementioned materials according to their flexural stiffness.

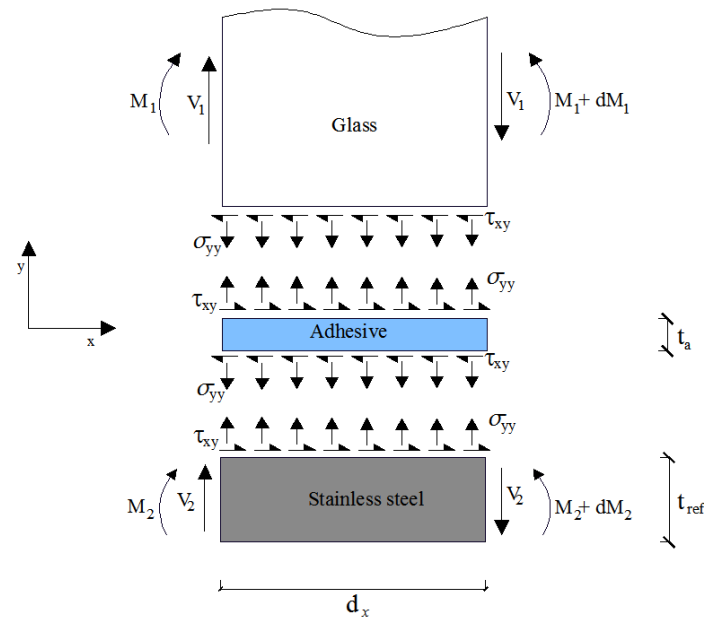


Fig. 5.16 – Equilibrium of forces at the interfaces of an infinitesimal glass-stainless steel hybrid beam.

In order to understand better the stress state at the bonded interface between the adhesive and the stainless steel profile and to obtain further insights about the failure mechanism of hybrid beam S2, a simplified finite element (FE) model was developed. The main goal was to estimate the magnitude of the shear and peeling stresses that apparently caused the debonding failure mechanism in the vicinity of the support sections.

Taking into consideration the symmetry of the flexural test setup and of the beam itself, a simplified two dimensional (2D) FE model of half of the beam's length was developed using ABAQUS (version 6.13-1 [5.30]). All the materials of the beam (laminated glass, adhesive and reinforcing profile) were modelled with 8-node shell elements with reduced integration (S8R), which were also used to model the geometry of the supports. Symmetry and simply supported boundary conditions were applied respectively at the mid-span and support cross-sections. A rigid connection was considered between the support and the hybrid glass beam. Across the height, both the reinforcing profiles and the adhesive were modelled with four layers of finite elements, while the glass was modelled with 45 layers of finite elements. In the longitudinal direction of the model, the approximate size of the finite elements was 15 mm, with exception of the area in the vicinity of the support (contact area between the beam and the support and in a 250 mm length for both sides of the support), where the mesh was refined (Fig. 5.17). In that area, the maximum length of the finite elements was set to 5 mm in order to obtain more accurate and less mesh dependent results (stress peaks).

For all materials, linear-elastic isotropic behaviour was assumed considering the material properties listed in Table 5.1 (*cf.* section 5.2.2). A geometrically linear elastic analysis was performed and a maximum load of 600 kN (the failure load in the experiments) was applied. Fig. 5.18 plots the development of shear and normal stresses at the bottom interface between the adhesive and the

reinforcing profile as a function of the longitudinal position (the origin corresponds to the center of the support). The stresses are plotted from the extremity of the beam up to the section located 500 mm inside the flexural span (total load of 600 kN).

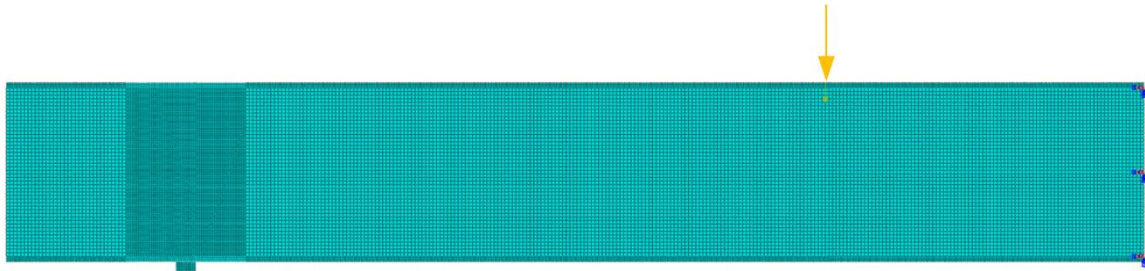


Fig. 5.17- Mesh representation of the numerical model of the hybrid glass beam S2.

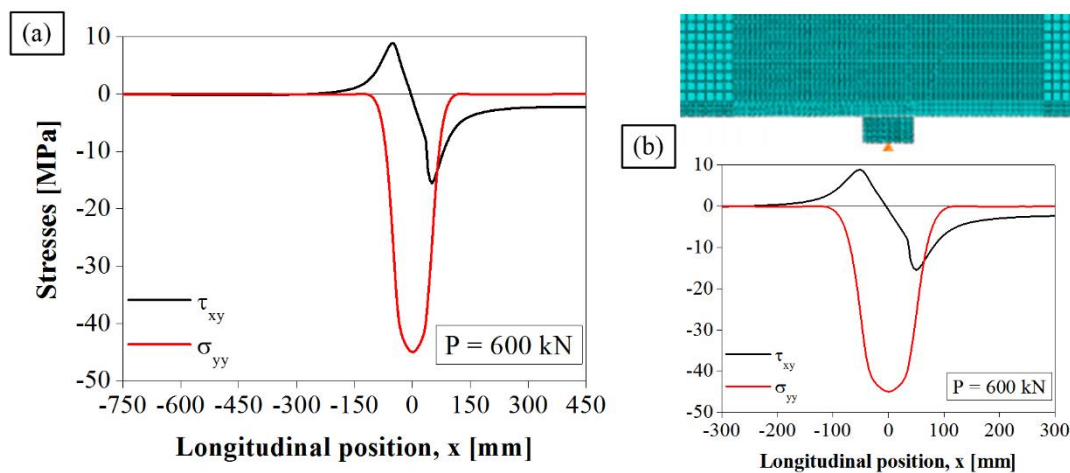


Fig. 5.18 – Longitudinal distribution of shear (τ_{xy}) and normal stresses (σ_{yy}) at the adhesively bonded interface adhesive-stainless steel of beam S2, for a total load of 600 kN: (a) development at the overhang and in the shear span and (b) development at the vicinity of the support.

One can see that the shear stresses are approximately constant and equal to 2.25 MPa up to the section located at a distance of 300 mm from the support. After that section, the shear stresses start to increase smoothly towards the inner limit of the support profile, where they present a maximum value of 15.5 MPa. Over the support area, the shear stress distribution is symmetrical around the center of the metallic frame. Along the overhang, the shear stresses decrease smoothly until they reach a null value.

Regarding the normal stresses, Fig. 5.18 shows that these stresses are negligible along most of the plotted length (Fig. 5.18-a). However, at the vicinity of the support these stresses increase, attaining a relevant magnitude over the support area, reflecting the compressive load. The peeling (tensile) stresses, which are known to contribute also to the debonding of reinforcing elements, are negligible.

According to the best of the author's knowledge, no shear tests were reported for hybrid glass systems using the present combination (glass-epoxy-stainless steel¹²). For comparison purposes, two studies can

¹² Adhesive Sikadur 330.

be considered. In the pull-out tests performed by Louter [5.4] on specimens made of annealed glass bonded to stainless steel profiles by means of SentryGlas interlayer, an average maximum shear stress of 21.8 MPa was attained (assuming a uniform distribution over an area of 500 mm²) with negligible debonding at the interface, i.e. the joint was able to transfer shear stresses up to glass failure. In the study of Correia *et al.* [5.23], double-lap tensile tests were carried out on specimens made of glass and GFRP adherends bonded using *Sikadur 330* epoxy adhesive (the one used in the present study). In that study an average maximum shear stress of 4 MPa was mobilized without any debonding.

Taking into account the results of the FE model and the mentioned studies (as a reference), one may conclude that both the shear stresses and the normal stresses present a low or negligible value along the overhang and along the flexural span. The normal stresses in the vicinity of the support are relatively high but are of compressive nature, thus they should not contribute to the debonding of the reinforcing element. However, over the supports, the shear stress presents a relevant magnitude. Although reference strength values for the specific interface used in these experiments are not available, the shear stresses retrieved by the numerical model seem to be sufficiently high to explain the occurrence of debonding at the stainless steel-glass bottom interface. Further shear tests should be performed in order to confirm the strength of the present joint.

5.5 CONCLUDING REMARKS

This chapter presents results of an exploratory experimental, analytical and numerical study addressing the applicability of the glass-stainless steel hybrid beams concept to large-scale structures. For that purpose, two long-span PVB and SG-laminated glass beams were reinforced with stainless steel profiles and were subjected to flexural tests up to failure. The outer glass plies of the PVB-laminated hybrid glass beam were cracked prior to testing, while the SG-laminated hybrid glass beam was tested uncracked. A simplified analytical model was developed in order to estimate the contribution of cracked fully tempered glass plies to the post-cracking flexural stiffness of the PVB-laminated hybrid glass beams. Finally, the flexural behaviour of the SG-laminated hybrid glass beam was numerically simulated in order to assess the stress distribution and magnitude at the glass-stainless steel adhesively bonded joint.

The cracked PVB-laminated hybrid glass beam exhibited considerable residual post-cracking stiffness and strength, but failed to present residual resistance after the breakage of the remaining uncracked glass ply. The initial residual post-cracking stiffness of the beam was 13% lower than the analytical estimates obtained considering the uncracked glass plies. This result showed that, despite the well-known poor post-cracking performance of fully tempered glass, the small glass fragments combined with the PVB interlayer and stainless steel profiles, are able to provide a significant contribution to the global post-cracking flexural stiffness of hybrid glass beams. Due to the progressive loss of integrity of the glass fragments, the post-cracking residual flexural stiffness measured in the tests exhibited a steady reduction during the test of about 9.1%. In the analytical model proposed, the contribution of the cracked glass

plies together with the observed loss of stiffness were used to estimate an equivalent elastic modulus for the cracked plies, function of the applied load. The compressive and tensile elastic moduli of the cracked glass plies were estimated to present a constant value of 50 GPa up to loads of 20 kN. For higher loads, the tensile elastic modulus was estimated to present a steady reduction up to 25 GPa, while the value of the compressive elastic modulus remained roughly constant. The collapse of the PVB-laminated hybrid glass beam occurred due to the premature debonding of the bottom reinforcing profile at the adhesive-stainless steel interface. It is likely that the strength of such bonded interface was affected by the cracked state of the outer glass plies, which increased the shear stress transfer at the interface of the undamaged glass ply, causing the premature debonding.

The flexural response of the uncracked SG-laminated hybrid glass beam was also slightly non-linear, with a steady reduction of flexural stiffness with increasing load. Such reduction might have stemmed from the non-linear behaviour in shear of the epoxy resin that bonded the stainless steel profiles to the laminated glass, which affected the joint stiffness and, consequently, the global flexural performance of the beam. Unlike what was expected, the SG-laminated hybrid glass beam did not present any post-cracking residual strength and collapsed immediately after the breakage of one of the glass plies. The sudden and unpredictable ultimate failure involved (i) the debonding of the reinforcing system at the bottom adhesive-stainless steel interface and (ii) failure of glass plies. The video recordings and the strain-gauges data did not allow concluding if such failure was triggered by the breakage of the inner glass plies (whose maximum tensile stresses had already exceeded the characteristic tensile strength of tempered glass) or if it was caused by exceedance of the ultimate strength of the bonded joint. Indeed, the simplified numerical models used to estimate the magnitude of the shear and normal stresses at the adhesive-to-stainless steel bonded interface showed that considerable shear stresses developed in the vicinity of the support sections. Those stresses, together with an amplification effect at the moment of the breakage of the glass plies, can also explain a debonding failure mechanism.

Regardless of the beam type and the failure sequence, the results obtained from testing both beams indicated that the application of the concept of glass-stainless steel hybrid glass beams to large-scale structures requires in-depth knowledge on the structural behaviour of adhesively bonded joints between glass and stainless steel. In particular, the resistance of the adhesively bonded joints used in large-scale hybrid glass beams showed to be susceptible to premature debonding, which seems to have occurred due to a poor performance of the joint between the cracked glass plies and the reinforcing element (beam S1) and/or due to the energy release from the failure of fully tempered glass plies (beam S2). Therefore, further investigations should be performed addressing the debonding phenomenon on large-scale hybrid glass systems, and providing practical design methodologies and recommendations. More effective and tailored anchoring systems may need to be developed.

5.5 REFERENCES

- [5.1] Martens K, Caspeele R, Belis J. Development of composite glass beams – A review. *Eng Struct* 2015;101:1–15.
- [5.2] Martens K, Caspeele R, Belis J. Development of reinforced & post-tensioned glass beams - review. *J Struct Eng* 2015:1–23.
- [5.3] Louter PC. Adhesively bonded reinforced glass beams. *Heron* 2007;52:31–57.
- [5.4] Louter C. Fragile yet Ductile - Structural Aspects of Reinforced Glass Beams. PhD thesis, Delft University of Technology, Netherlands, 2011.
- [5.5] Louter C, Belis J, Veer F, Lebet J-P. Structural response of SG-laminated reinforced glass beams; experimental investigations on the effects of glass type, reinforcement percentage and beam size. *Eng Struct* 2012;36:292–301.
- [5.6] Kreher K. Tragverhalten und Bemessung von Holz-Glas-Verbundträgern Unter Berücksichtigung der Eigenspannungen im Glas. PhD Thesis, École Polytechnique Fédérale de Lausanne, Switzerland, 2004.
- [5.7] Kreher K, Natterer J, Natterer J. Timber-glass-composite girders for a hotel in Switzerland. *Struct Eng Int J Int Assoc Bridg Struct Eng* 2004;14:149–51.
- [5.8] Belis J, Delincé D, Callewaert D, Van Impe R. Plastic deformation of polymer interlayers during post- breakage behavior of laminated glass - partim 1: analytical approach. *Int J Mod Phys B* 2008;22:5509–14.
- [5.9] Delincé D, Callewaert D, Vanlaere W, Belis J. Plastic deformation of polymer interlayers during post- breakage behavior of laminated glass - partim 2: experimental validation. *Int J Mod Phys B* 2008;22:5447–52.
- [5.10] Belis J, Depauw J, Callewaert D, Delincé D, Van Impe R. Failure mechanisms and residual capacity of annealed glass/SGP laminated beams at room temperature. *Eng Fail Anal* 2009;16:1866–75.
- [5.11] Bos FP. Safety Concepts in Structural Glass Engineering Towards an Integrated Approach. PhD thesis, Delft University of Technology, Netherlands, 2009.
- [5.12] Bernard F, Krour B, Benyoucef S, Fahsi B. Analysis of the debonding risks and the failure of laminated glass thanks to a coupled analytical-numerical investigation. In: Belis, Louter M, editor. COST Action TU0905 Mid-term Conf. Struct. Glas., Porec: 2013, p. 391–403.
- [5.13] Snijder A, Veer F, Nijssse R, Baardolf G, Romein T. Designing and testing an eight meter span glass portal frame. In: Weller, Schneider, editors. International Conf. Glas., Darmstadt: 2014.
- [14] Vilnay O. The analysis of reinforced concrete beams strengthened by epoxy bonded steel plates. *Int J Cem Compos Light Concr* 1988;10:73–8.
- [5.15] Roberts TM. Approximate analysis of shear and normal stress concentrations in the adhesive of plated RC beams. *Struct Eng* 1989;67:229–33.
- [5.16] Taljsten B. Strengthening of beams by plate bonding. *J Mater Civ Eng* 1997;9:206–12.
- [5.17] Malek AM, Saadatmanesh H, Ehsani MR. Prediction of failure load of R/C beams strengthened with FRP plate due to stress concentration at the plate end. *ACI Struct J* 1998;95:142–52.
- [5.18] Smith ST, Teng JG. Interfacial stresses in plated beams. *Eng Struct* 2001;23:857–71.
- [5.19] Yuan H, Chen JF, Teng JG, Lu XZ. Interfacial stress analysis of a thin plate bonded to a rigid substrate and subjected to inclined loading. *Int J Solids Struct* 2007;44:5247–71.
- [5.20] Report EUR 25316 EN Development of innovative steel-glass structures in respect to structural and architectural design (Innoglast). Unit G.5 - Research Fund for Coal and Steel, Research and

- Innovation, Luxembourg: European Union; 2013.
- [5.21] Firmo F, Jordão S, Costa Neves L, Bedon C. The effect of adhesive joints on the performance of hybrid steel-glass beams - An analytical and experimental study. In: Belis B& L, editor. *Challenging Glas. 5 - Conf. Archit. Struct. Appl. Glas.*, Ghent: 2016, p. 171–85.
- [5.22] Callewaert D. *Stiffness of Glass / Ionomer Laminates in Structural Applications*. PhD thesis, Ghent University, Belgium, 2012.
- [5.23] Correia JR, Valarinho L, Branco FA. Post-cracking strength and ductility of glass-GFRP composite beams. *Compos Struct* 2011;93:2299–309.
- [5.24] Veer F, Louter P, Bos F. The strength of annealed, heat-strengthened and fully tempered float glass. *Fatigue Fract Eng Mater Struct* 2009;32:18–25.
- [5.25] Report EUR 26439 EN Guidance for European Structural Design of Glass Components. Institute for the Protection and Security of the Citizen, Joint Research Centre, Luxembourg: 2014.
- [5.26] EN 10088 Stainless steels - Part 4: Technical delivery conditions for sheet/plate and strip of corrosion resisting steels for construction purposes. European Committee for Standardization (CEN), Brussels: 2009.
- [5.27] Belis J. *Kipsterkte van Monolithische en Gelamineerde Glazen Liggers*. PhD thesis, Ghent University, Belgium, 2005.
- [5.28] Schmid M. *New Adhesive*. EMPA Scientific Report No. 200171 e02/2. Dept. Strength and Technology, EMPA Duebendorf, Zurich, Switzerland: 2002.
- [5.29] De Castro J. *Experiments on Epoxy, Polyurthane and ADP Adhesives*. Technical Report n° CCLab2000.1b/1. École Polytechnique Fédérale de Lausanne, Lausanne, Switzerland: 2005.
- [5.30] Systèmes D. *ABAQUS 6.13 Documentation* 2013.

EXPERIMENTAL STUDY ON THE FLEXURAL BEHAVIOUR OF MULTI-SPAN GLASS–GFRP COMPOSITE BEAMS

ABSTRACT

Glass presents several limitations, including relatively low tensile strength and brittle behaviour, which contrasts with current design philosophies associated with more conventional materials, such as steel and reinforced concrete. One of the possibilities of overcoming these disadvantages is joining reinforcing materials to glass. The main goal of those transparent composite structural solutions is to increase the post-cracking residual strength and ductility of glass beams. This chapter presents results of an experimental study about the flexural behaviour of multi-span composite beams combining annealed glass beams and GFRP pultruded laminates. The main goal of this study was to evaluate the post-cracking behaviour of such beams, namely the influence of the (i) section (reinforcement) geometry, (ii) properties of the adhesive used to couple both materials, and (iii) structural and cross-section redundancy. The experimental campaign comprised (i) tensile tests to characterize the materials, (ii) tensile tests on double-lap joints between glass and GFRP pultruded laminates, bonded with different structural adhesives, and (iii) full-scale flexural tests on simply supported and multi-span glass-GFRP composite beams, with interfaces bonded also with different adhesives. Results showed that multi-span glass-GFRP composite beams are able to exhibit significant post-cracking residual strength and ductility, stemming not only from their cross-sectional redundancy, but also from their capacity to redistribute internal forces among spans. It was confirmed that the post-cracking strength and ductility of single-span glass-GFRP composite beams is highly influenced by the reinforcement geometry and applied adhesive. In particular, the reinforcement area increased the reliability and safety of the hybrid system, by providing an enhanced post-cracking behaviour. On the other hand, and regarding the adhesives properties, composite glass beams bonded with the softest adhesive (polyurethane silicone) exhibited the highest values of ultimate deflection and post-cracking ductility while the composite beams in which the stiffest adhesive (epoxy resin) was applied presented the highest values of ultimate load and post-cracking strength.

6.1 INTRODUCTION

In the previous chapter, an exploratory study on the structural behaviour of glass-stainless steel hybrid beams was presented. The study was based on the work of Louter [6.1] and Louter *et al.* [6.2] who proved the feasibility of such system throughout the development of comprehensive experiments on glass-stainless steel reinforced beams. Several other systems, comprising different structural materials, have been studied along the last decade and they are briefly described in chapter 2 (*cf.* section 2.3) of this thesis or in the state of the art reviews of Martens *et al.* [6.3, 6.4]. In general, most of the studies proved that combining glass with other structural materials enhances the corresponding structural behaviour by yielding post-cracking residual strength and ductility.

The post-cracking ductility can be classified in two groups. It is either achieved through (i) the use of an inherently ductile reinforcement material, or (ii) by cross-sectional structural redundancy. The former approach can be achieved by combining glass, a brittle material, with materials that present ductile (plasticity) failure modes¹, such as steel or stainless steel. The latter approach, usually named pseudo-ductility, is developed at the system level by taking advantage of structural redundancy, cross-sectional redundancy, systems with alternative load paths, back-up systems or multi-component cross-sections.

The potential ductility of structural systems combining brittle components was discussed earlier by Keller and de Castro [6.5]. Such systems are able to exhibit non-linear inelastic load-deformation behaviour, characterized by a progressive stiffness decrease (usually stemming from the sequential failure of brittle components or connections at the system level) and, at the same time, by progressive increase of the ultimate strength capacity. In the glass field, *pseudo-ductile* systems have been assessed by combining glass with CFRP [6.6], GFRP rods and rebars [6.1, 6.7], and with GFRP laminates [6.8–6.10] (*cf.* chapter 2, section 2.3).

In the studies of Valarinho [6.8] and Correia *et al.* [6.9] a preliminary experimental campaign (a brief description can be found in chapter 1, section 1.1.1) on the flexural behaviour of glass-GFRP composite beams was presented. In such studies, it was demonstrated that the combination of GFRP laminates and glass in simply supported beams provides considerable post-cracking residual strength (referred to as post-cracking strength in the remainder of the chapter) and ductility. It was also demonstrated that the characteristics of the (structural) adhesive used to bond GFRP to glass influences the post-cracking performance. In particular, it was shown that post-cracking ductility and strength of hybrid systems comprising glass and GFRP pultruded laminates can be enhanced by exploiting the adhesives non-linear viscoelastic behaviour.

¹ Reinforced concrete can also be included in this category, even though being, on its own, a composite system, whose ductility is yielded by steel rebars.

All studies on hybrid glass systems involving glass have relied on simply supported beams with different spans, with ductility being achieved by the combination of ductile and brittle materials or simply by cross-sectional redundancy. In hyperstatic structures, in addition to lower deformability in service conditions when compared to isostatic systems, the structural redundancy combined with the cross-sectional redundancy may increase the pseudo-ductility at failure, as reported in [6.11, 6.12]. Hyperstatic systems made of reinforced concrete or steel allow designers to perform cross-section plastic analysis, taking into account the force redistribution capacity granted by sections with plastic properties.

In this context, based on the above-mentioned earlier studies [6.8, 6.9], in which the author analysed the feasibility of simply supported glass-GFRP beams bonded with different adhesives, this chapter presents an experimental study on the flexural behaviour of glass-GFRP composite multi-span beams. The goal of the study was two-fold: (i) to develop an experimental campaign complementary to the preliminary studies [6.8, 6.9] in order to assess the statistical variability of the flexural behaviour of the composite system in simply supported beams, and (ii) to evaluate the post-cracking ductility and the post-cracking strength that hyperstatic systems can bring to glass-GFRP composite multi-span beams bonded with different types of adhesives.

The experimental programme included (i) material characterisation tests of all composite beam components, (ii) tests on double-lap joints between glass and pultruded GFRP laminates bonded with different adhesives, and (iii) full-scale flexural tests on simply supported and multi-span glass-GFRP composite beams, bonded with different adhesives. The serviceability behaviour (stiffness, cracking loads, shear interaction at bonded interfaces) and the failure behaviour (cracking pattern, failure loads, failure modes, force redistribution and overall ductility) of the beams is analysed and compared, allowing the evaluation of the potential advantages of using the proposed glass-GFRP composite structural system in hyperstatic structures.

6.2 STRUCTURAL CONCEPT AND MATERIALS

6.2.1 Structural concept

The composite beams comprised GFRP pultruded profiles adhesively bonded to single glass panes of annealed glass. Two different beam geometries of beams were studied (Fig. 6.1): (i) a rectangular glass beam (cross-section of $100 \times 12 \text{ mm}^2$), reinforced at the bottom edge with a rectangular GFRP pultruded profile (cross-section of $8 \times 12 \text{ mm}^2$); and (ii) an I-section beam comprising a glass web ($100 \text{ mm} \times 12 \text{ mm}$), GFRP flanges ($50 \text{ mm} \times 8 \text{ mm}$) and an angle profile ($17 \text{ mm} \times 17 \text{ mm} \times 4.8 \text{ mm}$) used for production purposes. In any case, the two materials (glass panes and GFRP pultruded profiles) were joined by means of three different adhesives: (i) *Sikaflex 265*, (ii) *Sikaforce 7710-L100*, and (iii) *Sikadur 31-cf*. The thickness of the adhesive layers ranged from 1 to 2 mm.

The structural concept of this composite system is based on the following underlying principles: (i) when the tensile strength of glass is attained, there is a considerable increase of stress transfer to the GFRP laminate, which confers tensile reinforcement to the cross-section; (ii) such stress transfer, associated with the high tensile strength and low elastic modulus of the GFRP, together with the deformability of the adhesive, provides post-cracking strength and deformation capacity to the cross-section.

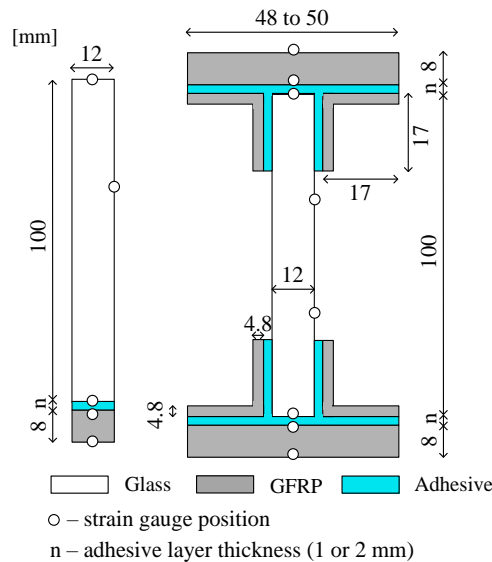


Fig. 6.1 - Cross-section of the glass-GFRP composite beams and strain-gauges position.

The composite glass beams tested in this study were based on the composite beams investigated earlier by the author [6.8, 6.9]. Compared to those beams, the cross-sections investigated now were just slightly amended in order to obtain a more efficient design (enhancement of the beams height/width ratio). The reinforcement cross-section of the rectangular glass-GFRP composite beams was designed in order to withstand the total tensile load upon the glass breakage, which was established to occur when the glass stress reaches 45 MPa^2 . The I-section beams were designed in order (i) to significantly increase the reinforcement area percentage, (ii) to provide further stability to the beam, namely to the glass compression zone, (iii) to have a higher bonded perimeter for stress transfer from glass to the GFRP reinforcement, and (iv) to provide some confinement to the glass compressive area. These design options aimed at achieving an ultimate failure load higher than that provided by the rectangular reinforcement.

6.2.2 Materials

Annealed glass panes with thickness of 12 mm and polished edges were used in the experiments. The comprehensive material and mechanical characterization of glass usually requires extensive experimental

² Assuming a small decrease of the neutral axis height, the total tensile load upon glass breakage was estimated to be 13 kN; for a reinforcement cross-section of $12 \times 8 \text{ mm}^2$ (defined according to the GFRP producer availability), the corresponding maximum tensile stress at the GFRP is 128 MPa, much lower than its maximum tensile strength (around 350 MPa, detailed ahead in section 6.2.2).

tests, which were beyond the scope of this thesis. Therefore, the main mechanical properties of glass available in the literature were considered [6.13, 6.14]. The use of laminated and/or tempered glass was not considered to be adequate for this study. On the one hand, laminated glass was discarded in order to analyse (separately) the effects of the GFRP reinforcement on the post-cracking behaviour of the composite beams³. On the other hand, the higher tensile strength of tempered glass would originate, simultaneously, a decrease in the residual integrity after the initial cracking ([6.2, 6.15]).

The GFRP pultruded profiles used to reinforce the glass beams were made of an isophthalic polyester matrix reinforced with alternating layers of E-glass rovings and mats. The reinforcing GFRP profiles were subjected to tensile characterization tests, performed according to ISO 527-1, 4 [6.16, 6.17]. As expected, all specimens presented linear behaviour and, despite having been extracted from different cross-sections, they presented similar elastic modulus (32 GPa) and ultimate strength (350 MPa).

The following three types of adhesives were used to assemble the GFRP pultruded profiles and the glass panes: (i) an elastic gap-filling polyurethane adhesive, *Sikaflex 265*; (ii) a 2-component (polyol with isocyanate derivatives) structural adhesive, *Sikaforce 7710-L100*; and (iii) a structural epoxy adhesive, *Sikadur 31-cf*, with negligible density of fillers. The adhesives, hereafter referred to as *SFlex*, *SForce* and *SDur*, respectively, were chosen in order to cover a wide range of Young's modulus values. Tensile characterization tests were performed in each adhesive⁴. Due to the distinct mechanical behaviour of the adhesives, different dumbbell geometries were produced in accordance with the corresponding standard (Fig. 6.2-a): ISO 37 [6.18] for *SFlex* and *SForce* (for the determination of the Young's modulus), and ISO 527-1, 2 [6.16, 6.19] for *SForce* (for the determination of the tensile strength) and *SDur*. Different load speeds were applied according to the adhesive and aim of the test: both Young's modulus and ultimate strength of *SFlex* adhesive were determined at a speed of 500 mm/min; the Young's modulus of the *SForce* and *SDur* adhesives was determined at a speed of 0.35 mm/min, while the ultimate strength was determined at speeds of 10 mm/min and 5 mm/min respectively for the *SForce* and *SDur* adhesives. All specimens were cured at room temperature (approximately 20 °C) for about one month prior to testing.

The *SFlex* adhesive exhibited an almost linear behaviour (Fig. 6.3-a), typical of elastomers when tested at this speed, presenting low elastic modulus together with relatively high apparent ultimate stress and high ultimate tensile elongation. The *SForce* adhesive presented non-linear behaviour (Fig. 6.3-b) with an initial stiffness considerably higher than that of the *SFlex* adhesive (about 60 times higher), even though exhibiting an equivalent (apparent) ultimate strength and relatively high elongation at failure. Finally, the *SDur* adhesive exhibited slightly non-linear behaviour and, among the adhesives tested, the highest values of elastic modulus and ultimate stress (Fig. 6.3-c), together with the lowest ultimate tensile strain. The Poisson's ratios were determined using a digital image correlation system, with the

³ The use of interlayers would result in additional residual post-cracking strength and ductility [6.26].

⁴ The study of the long-term behaviour or of the performance under specific exposures were beyond the scope of this study.

SFlex and *SForce* adhesives presenting the highest values ($\nu_{SFlex} = 0.44$ and $\nu_{SForce} = 0.46$, respectively) whereas the *SDur* adhesive exhibited the lowest value ($\nu_{SDur} = 0.25$).

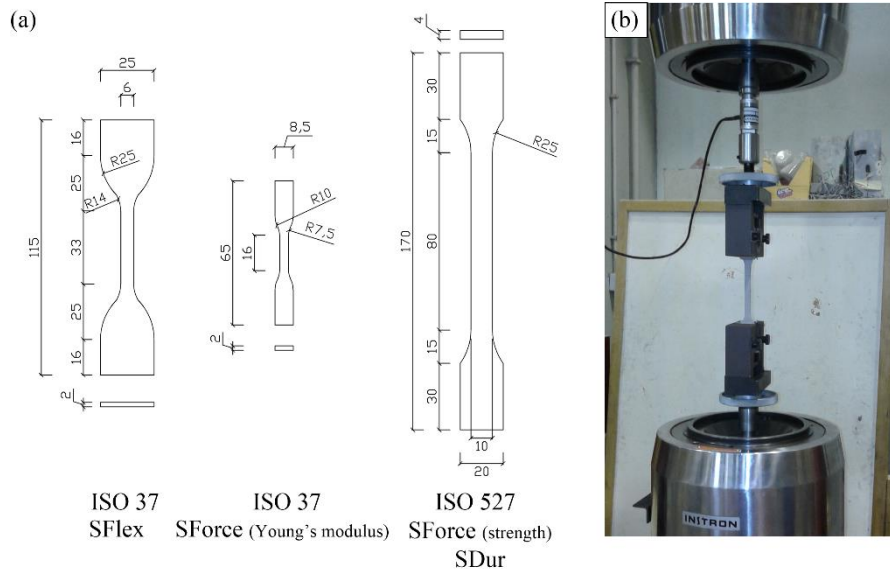


Fig. 6.2 - Adhesives tensile tests: (a) dumbbell specimens' geometry (left to right) of *SFlex*, *SForce* (Young's modulus), *SForce* (tensile strength) and *SDur* and (b) experimental setup.

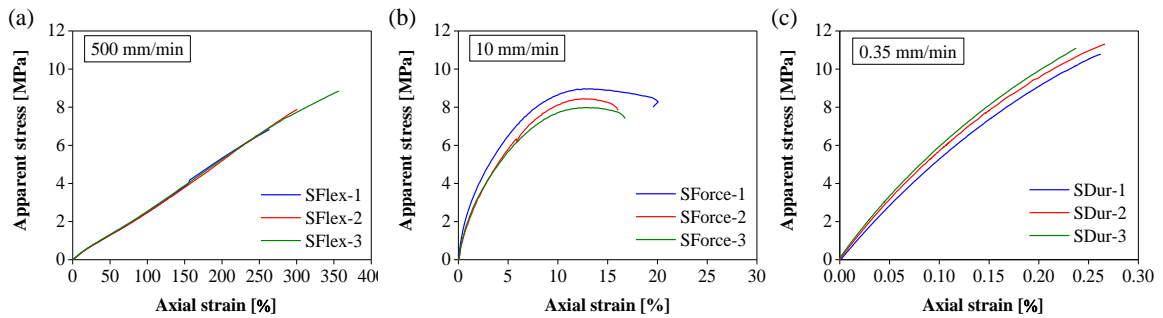


Fig. 6.3 – Apparent stress vs. axial strain curves of a representative set of specimens (specimens used for the determination of the Young's modulus) from (a) *SFlex* (b) *SForce* and (c) *SDur* adhesives.

The Young's modulus (E_i), ultimate strength ($f_{i,t}$), tensile elongation ($\epsilon_{i,b}$) and Poisson's ratio (ν_i) of glass, GFRP and the three different adhesives used in the experiments are listed in Table 6.1.

Table 6.1 - Mechanical properties in tension of the materials used in the glass-GFRP composite beams.

Material	Tensile tests			
	E_i [MPa]	$f_{i,t}$ [MPa]	$\epsilon_{i,b}$ [%]	ν_i [-]
Annealed glass*	70000	30-80	N.A.	0.22-0.24
GFRP profiles	32000	350	N.A.	N.A.
Sikaflex 265	$3.08 \pm 7\%$	$8.13 \pm 12\%$	$317 \pm 15\%$	$0.44 \pm 15\%$
Sikaforce 7710-L100	$183 \pm 20\%$	$8.44 \pm 4\%$	$16.6 \pm 24\%$	$0.46 \pm 11\%$
Sikadur 31-cf	$4257 \pm 16\%$	$11.7 \pm 22\%$	$0.21 \pm 42\%$	$0.25 \pm 13\%$

* According to [6.13, 6.14]

N.A. - not applicable

6.2.3 Manufacturing of the beams

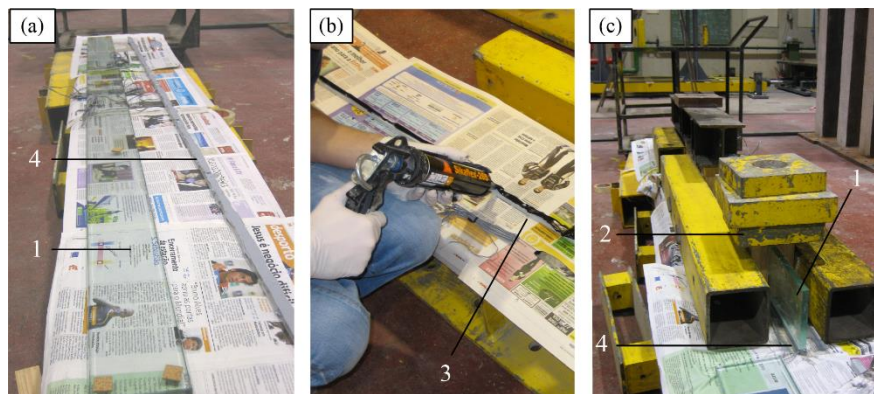
The glass–GFRP composite beams were manufactured with the cross-sections illustrated in Fig. 6.1. The GFRP profiles were adhesively bonded to the glass panes using the three different adhesives mentioned earlier: *SFlex*, *SForce* and *SDur*. The adhesively bonded interfaces were produced with thicknesses of 2 mm (*SFlex* and *SDur* series) or 1 mm (*SForce* series). Again, for the latter series, a lower thickness had to be adopted given the lower viscosity of the adhesive.

The manufacturing process of the beams comprised mainly the bonding of the different elements of the glass–GFRP composite beams. The R-section beams were made of two independent elements, the glass beam and the GFRP reinforcing profile, whereas the I-section beams were made of seven independent elements: the glass beam, four angle profiles and two GFRP reinforcing profiles. The bonding surfaces of each element had to be duly prepared before adding the adhesive.

The manufacturing process of the R-section beams (Fig. 6.4) comprised the following steps:

1. Cleaning and degreasing of the adherend surfaces of the single pane glass beam using acetone;
2. Mechanical abrading, cleaning and degreasing of the adherend surfaces of the GFRP reinforcement profiles;
3. Positioning of aluminium/PVC spacers in the GFRP profile in order to guarantee a 1/2 mm joint thickness (depending on the adhesive used);
4. Preparation and application of the different adhesives (following the corresponding method of application) on the GFRP profile;
5. Positioning of the glass beam;
6. Finishing of the adhesive joint;
7. Curing of the adhesive for 24 hours under light weights;

The curing of the adhesively bonded joint took place for more than 60 days.

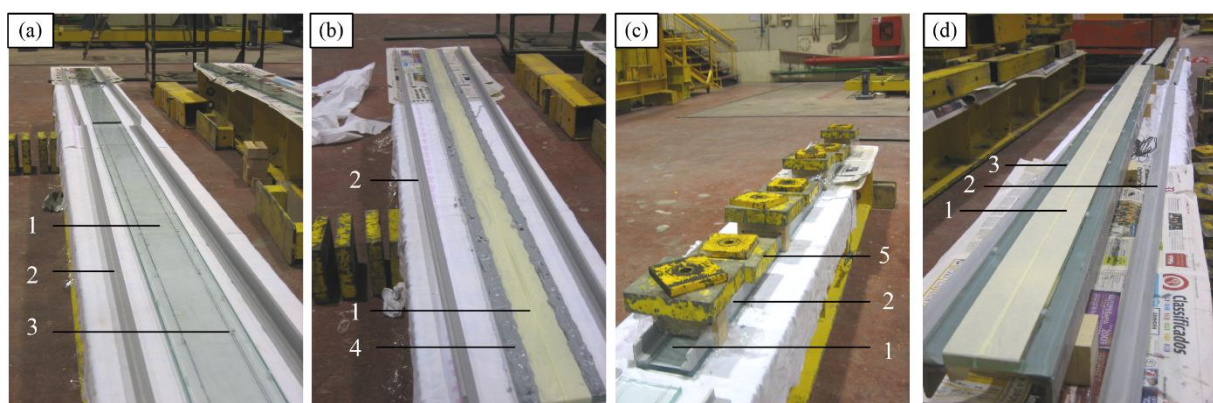


1 – Single glass beam 3 – GFRP reinforcing profile with *SFlex* adhesive
 2 – Light weights 4 – GFRP reinforcing profile with *SDur* adhesive

Fig. 6.4 – Manufacturing process of the R-section composite glass beams: (a) glass beam and GFRP reinforcing profile (with epoxy (*SDur*) adhesive); (b) application of polyurethane (*SFlex*) adhesive in the GFRP reinforcement; (c) beam curing using light weights.

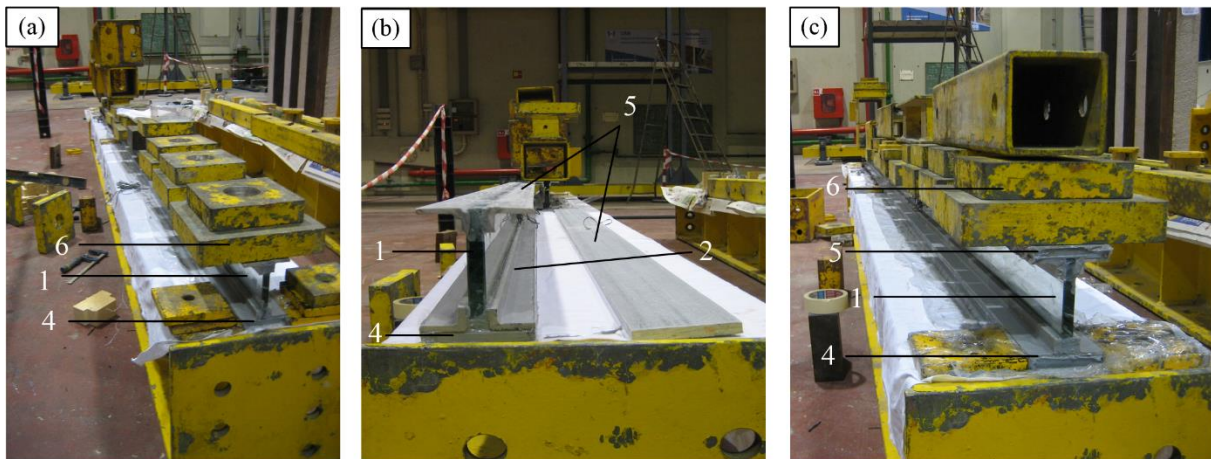
Regarding the I-section beams, the manufacturing process (Fig. 6.5 and Fig. 6.6) encompassed the following steps:

1. Cleaning and degreasing of the adherend surfaces of the single pane glass beam using acetone;
2. Mechanical abrading, cleaning and degreasing of the adherend surfaces of the GFRP reinforcement profiles;
3. Positioning of aluminium/PVC spacers on the glass beam, placed in a horizontal position, in order to receive the GFRP angle profiles;
4. Preparation and application of the different adhesives (following the corresponding method of application) on the glass beam;
5. Positioning of the first two GFRP angle profiles;
6. Finishing of the adhesive joints;
7. Curing of the adhesive for 24 hours under light weights;
8. Repetition of steps 3 to 7 for the other two GFRP angle profiles;
9. Repositioning of the (composite) glass beam in a vertical position, in order to receive the GFRP flanges profiles;
10. Preparation, cleaning and degreasing of the bottom and top edges of the (composite) glass beam;
11. Positioning of aluminium/PVC spacers on the bottom edge of the glass beam;
12. Preparation and application of the different adhesives (following the corresponding method of application) on the glass beam;
13. Positioning of the bottom GFRP flange profile;
14. Finishing of the adhesive joint;
15. Curing of the adhesive for 24 hours under light weights;
16. Repetition of steps 11 to 15 applied to the top edge of the composite glass beam.



- | | | |
|------------------------|--------------------------|---------------------------|
| 1 – Single glass beam | 3 – PVC spacer | 6 – <i>SFlex</i> adhesive |
| 2 – GFRP angle profile | 4 – <i>SDur</i> adhesive | 5 – Light weights |

Fig. 6.5 – Manufacturing process of the I-section composite glass beams – positioning of the GFRP angle profiles: (a) positioning of the PVC spacers on glass; (b) application of the (epoxy) adhesive; (c) curing of the adhesive applied in the angle profiles using light weights; (d) repositioning of the composite beam for the positioning of the two other GFRP angle profiles.



1 – Single glass beam 3 – PVC spacer 5 – Top GFRP flange
 2 – GFRP angle profile 4 – Bottom GFRP flange 6 – Light weights

Fig. 6.6 – Manufacturing process of the I-section composite glass beams – positioning of the GFRP flanges: (a) curing process of the adhesive applied at the bottom GFRP flange; (b) repositioning of the beam for the positioning of the top GFRP flange; (c) curing process of the adhesive applied at the top GFRP flange.

The R-section beams were manufactured in lengths of 1.5 m (*SS-R* series), whereas the I-section beams were 1.5 m or 3.0 m long. The shorter I-section beams were tested in a simply supported configuration (*SS-I* series), whereas the longer ones were tested in a continuously supported scheme (*CS-I* series). A total of 27 beams were produced, 3 of each section geometry, bending configuration and type of adhesive. The following nomenclature was used: *i-j-k-#*, in which *i* stands for the type of bending setup (*SS* or *CS*), *j* labels the section geometry (*R* or *I*), *k* identifies the type of adhesive (*SFlex*, *SForce* or *SDur*) and # is the order number within a test series (1 to 3).

6.3 EXPERIMENTAL PROGRAMME

Besides the material characterization tests (previous section) performed for the GFRP pultruded profiles and adhesives, the main experimental programme comprised: (i) tensile tests on adhesively bonded double-lap joints between glass and GFRP adherends, and (ii) flexural tests on (ii.1) simply supported rectangular and I-section composite glass beams, and on (ii.2) continuous two-span I-section composite glass beams.

The tensile tests on the double-lap joints allowed comparing the performance of the three types of adhesives, namely their ease of application, and assessing the mechanical behaviour of the glass-GFRP adhesively bonded joints, in terms of (i) shear stiffness, (ii) strength, and (iii) axial strain distribution in one of the adhesive-GFRP interfaces.

The flexural tests on glass-GFRP composite beams were performed on two different cross-sections: rectangular (hereafter referred to as R-section) and I-section beams. The R-section beams were tested in a typical 4-point bending system, while the I-section beams were tested in two different structural

systems: simply supported 4-point bending system and continuously supported two-span (5-point) bending configuration. For both cross-sections and systems, the serviceability and ultimate responses of the glass-GFRP composite beams, bonded with the different adhesives, were analysed and compared. Table 6.2 summarizes the experimental bending tests performed.

Table 6.2 - Summary of the flexural tests on glass-GFRP composite beams.

Type of tests	Beams section	Test setup	Adhesives	No. of specimens
Flexural tests on composite beams	R-Section	4-point	SFlex, SForce, SDur	9 (3 per type of adhesive)
	I-Section	4-point		9 (3 per type of adhesive)
		5-point		9 (3 per type of adhesive)

6.4 TESTS ON DOUBLE-LAP JOINTS

The experimental study that follows was based on the works of Keller and Vallée [6.20, 6.21], Vallée *et al.* [6.22, 6.23], and de Castro and Keller [6.24, 6.25], who carry out comprehensive experimental campaigns on adhesively bonded single-lap and double-lap joints between GFRP pultruded profiles. They investigated the influence on the bond-slip behaviour of aspects such as thickness of the adhesive layer and adherends, overlap length and type of adhesive.

6.4.1 Specimen geometry and test setup

Experiments were carried out on double-lap joints, comprising two inner GFRP laminates (10 × 50 mm²) and two outer glass panes (12 × 50 mm²) bonded with the three different adhesives. All adherends presented length of 350 mm and width of 50 mm and the overlap length was set as 100 mm (Fig. 6.7). The thickness of all adhesive layers (ensured by means of small PVC spacers, occupying no more than 1% of the bonding area) was set as 2 mm, with the exception of the *SForce* joints, in which a 1 mm thickness was adopted due to its lower viscosity.

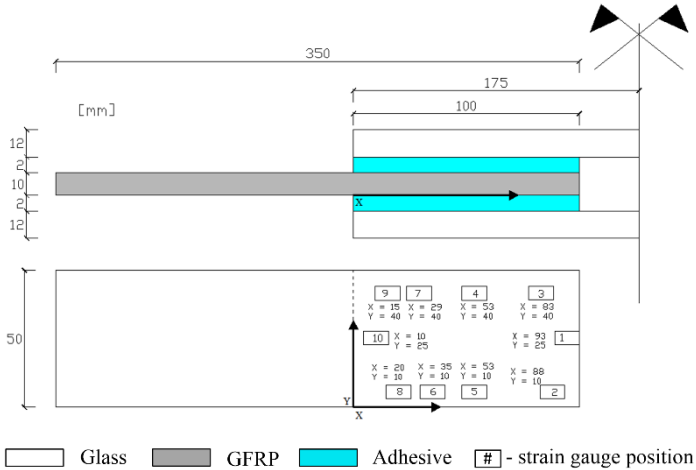


Fig. 6.7 - Geometry of the double-lap joints and location of the strain-gauges along the GFRP bonded interface.

Prior to bonding, the surfaces of the adherends were cleaned and degreased using acetone, the surface veil of the GFRP laminates was mechanically abraded with a fine sander until the first mat fibres became visible and the surfaces were subsequently re-cleaned and re-degreased using acetone.

A total of 15 specimens were tested, distributed by 3 series with the following nomenclature: *DL-SFlex-#*, *DL-SForce-#* and *DL-SDur-#* (with # standing for the n^{th} specimen within a series), corresponding to joints using the *SFlex*, *SForce*, and *SDur* adhesives, respectively. The strain development along one of the bonded GFRP surfaces was measured using 10 strain-gauges (Fig. 6.7).

Specimens were loaded in tension using an *Instron* universal testing machine under displacement control at a speed of 0.017 mm/s (displacement between grips). The applied load and the relative displacement between bonded extremities of both overlap zones were measured during the tests. For this purpose, two *APEK* displacement transducers with a stroke of 10 mm were placed in both sides of the test specimens. The tests were conducted at an average temperature of 19 °C and relative humidity of 59%. Prior to testing, specimens were wrapped with cellophane film, in order to prevent the dispersion of glass fragments after the failure.

6.4.2 Results and discussion

6.4.2.1 Load vs. relative displacement response

Fig. 6.8 depicts the load vs. relative displacement curves of specimens made of the three different adhesives (*SFlex*, *SForce* and *SDur* series, respectively).

As reported in previous tests [6.8, 6.9], the behaviour of *DL-SFlex* joints was not fully consistent. On the one hand, specimens *DL-SFlex-1,4* presented an initial linear behaviour, with loss of stiffness only at the brink of collapse (Fig. 6.8-a – orange and blue curves). On the other hand, specimens *DL-SFlex-2,3,5* exhibited a shorter linear branch and an earlier loss of stiffness that led to premature failure (Fig. 6.8-a). Accordingly, the ultimate loads exhibited relatively high scatter. The stiffness loss was due to the debonding in one of the glass-adhesive interfaces, which ultimately caused the failure of the joints (Fig. 6.9-a). The scatter of results may have been caused by the high viscosity of the adhesive, which affected the manual process used to manufacture the specimens.

Joints *DL-SForce* exhibited slightly non-linear behaviour (Fig. 6.8-b), with constant and marginal loss of stiffness. Excluding results from specimen *DL-SForce-1*, which presented a premature failure due to debonding at one of the glass-adhesive interfaces (eventually due to adhesion problems stemming from a less effective surface preparation in such particular specimen), the other four specimens presented very similar behaviour with a noticeable loss of stiffness for a load of about 25 kN and an ultimate load over 35 kN. All specimens presented failure modes due to the breakage of the glass panes (Fig. 6.9-b). The non-linear behaviour observed in the adhesive (tensile) characterization tests was not reflected in the

joints due to the *premature* failure of glass, which did not allow achieving higher shear stresses in the adhesive joint.

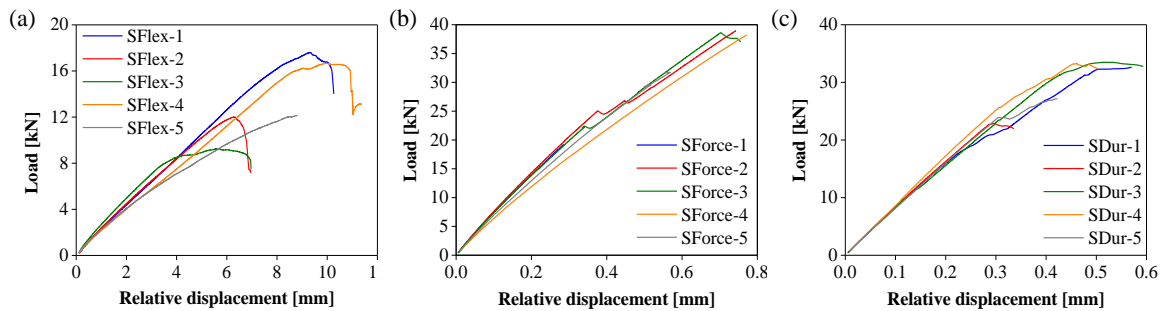


Fig. 6.8 - Load vs. relative displacement curves of specimens from (a) *SFlex*, (b) *SForce* and (c) *SDur* series.

DL-SDur specimens exhibited practically linear behaviour up to failure, without significant stiffness changes during loading (Fig. 6.8-c). The slight loss of stiffness prior to failure was coincident with the appearance of the first cracks on glass at the overlap region. After this point, all specimens were still able to carry additional load up to their ultimate failure, which occurred due to the breakage of one of the glass panes (Fig. 6.9-c). Specimen *DL-SDur-2*, 5 seemed to present a premature failure (most likely due to a premature adhesive failure in all interfaces) attaining a significantly lower ultimate load when compared to the other three specimens of the same series.

Table 6.3 presents a comparison of the results obtained for the different series, concerning elastic stiffness (K), maximum load (P_{max}), corresponding maximum relative displacement (d_{max}) and failure mode. The magnitude of K and d_{max} values were in line with the corresponding adhesive mechanical properties. Among the three series, the joints made with *SFlex* adhesive presented the lowest values of stiffness and strength, with high values of relative displacement, due to the very high deformability of the adhesive and, in addition, to the slippage observed at the adhesive-adherend interfaces (discussed ahead in section 6.4.2.2). The other two adhesives provided similar values of joint stiffness and ultimate strength, much higher than those presented by the *SFlex* adhesive.

Table 6.3 - Summary of results (average plus coefficient of variation) from double-lap joint tests (K , P_{max} , d_{max} and failure mode).

Adhesive Type	K [kN/mm]	P_{max} [kN]	d_{max} [mm]	Failure mode
Sikaflex 265	$2.16 \pm 11\%$	$13.5 \pm 26\%$	$8.37 \pm 23\%$	adhesive
Sikaforce 7710-L100	$73.0 \pm 7\%$	$32.4 \pm 23\%$	$0.63 \pm 30\%$	stock –break (glass)
Sikadur 31-cf	$85.3 \pm 3\%$	$30.3 \pm 14\%$	$0.46 \pm 12\%$	stock –break (glass)

6.4.2.2 Failure modes

Fig. 6.9 illustrates the typical failure modes for each type of adhesive.

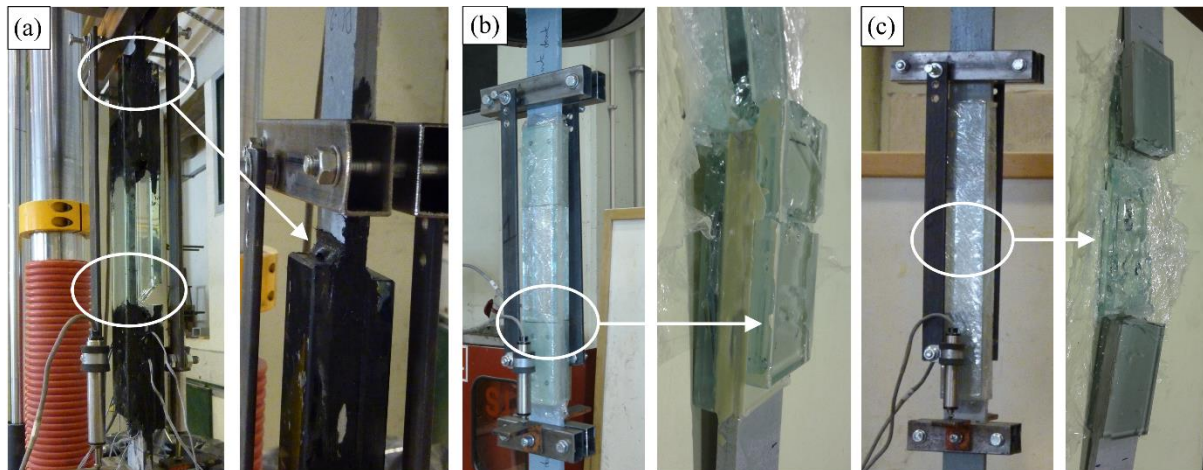


Fig. 6.9 - Failure modes of double-lap joints made of (a) *SFlex*, (b) *SForce* and (c) *SDur* adhesives.

The *DL-SForce* and *DL-SDur* specimens failed due to breakage of both glass adherends (Fig. 6.9-b and c), indicating that those adhesives were able to efficiently transfer shear stresses from the glass to the GFRP adherends without achieving their maximum stress transfer capacity. It is worth mentioning that specimen *DL-SForce-1* presented a progressive damage in the bonded interfaces, noticeable by the consecutive noises audible during the tests (which may have been caused by the degradation of the adhesion for higher loads and/or effects of shear stress concentrations). The *DL-SFlex* specimens also exhibited glass failure but only in one of the inner panes. In these specimens, failure was triggered by the debonding at one of the interfaces (a progressive slippage between adherends developed and it was clearly visible at the glass-adhesive interface prior to failure - Fig. 6.9-a). Due to this slippage, load started to be transferred non-symmetrically, i.e. one of the glass panes progressively carried out an increasing fraction of the axial load. This is attested by the load *vs.* relative displacement behaviour and by the much lower failure load of these specimens (about half of the other series).

6.4.2.3 Axial strains

Fig. 6.10 shows the distribution of axial strains along the length of the GFRP-adhesive interface at loads of 5.0 kN for the *SFlex* adhesive and 20.0 kN for the *SForce* and *SDur* adhesives. The experimental results obtained in terms of axial strains were consistent with the load *vs.* relative displacement curves, as well as with the material characterization tests. In other words, the differences in axial stiffness between the three adhesives were also noticed on the distribution of axial strains: for the *SDur* adhesive, the stiffest one, a higher shear stress transfer develops in the initial length of the bonded interface, with a higher concentration of stresses developing in that region. For decreasing adhesive stiffness, in spite of the typical scatter associated with this type of strain measurements, it was possible to observe a linearization tendency of the shear stress transfer along the interface, with the *SFlex* adhesive, the most flexible one, presenting a roughly linear distribution.

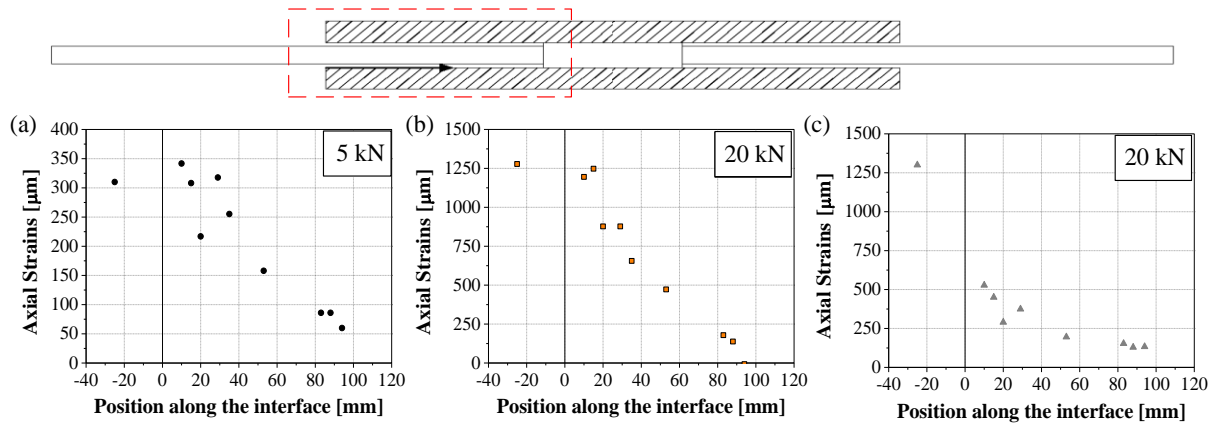


Fig. 6.10 - Measured axial strains for (a) *SFlex*, (b) *SForce*, and (c) *SDur*.

6.5 FLEXURAL TESTS: TEST SETUP AND PROCEDURE

6.5.1 Test setup and procedure

The simply supported beams, with a span of 1.40 m, were tested in a symmetrical 4-point bending configuration with a load span of 0.465 m, as illustrated in Fig. 6.11-a (*SS-R* series) and Fig. 6.11-b (*SS-I* series). The rectangular beams were transversally restrained with two pairs of metal guides symmetrically positioned throughout the span to avoid lateral torsional buckling.

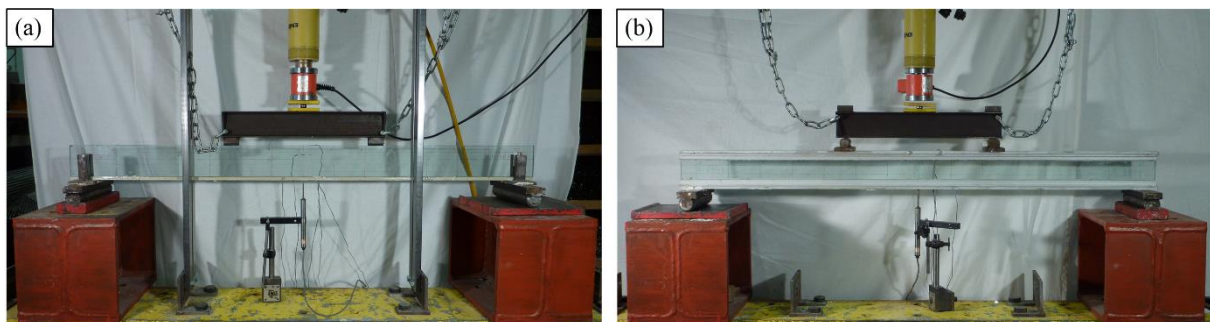


Fig. 6.11 - Experimental setup of the flexural tests on (a) R-section and (b) I-section simply supported beams.

The continuously supported beams, with two spans of 1.40 m, were tested in a symmetrical 5-point bending configuration (Fig. 6.12). The two point loads were applied at a distance of 0.56 m from the central support ($0.4 L_0$), ensuring that the maximum moment developed at the central support section (maximum negative bending moment) would be 1.53 times higher than the maximum moment developed at the span (maximum positive bending moment).

In both configurations, the load was applied by means of a hydraulic jack reacting against a steel loading frame, together with a metallic distribution beam and steel rollers. For the I-section beams, a metal sphere was positioned between the hydraulic jack and the load distribution beam; in addition, metal plates and spheres were placed between the distribution beam and the top surface of the tested beams to

avoid any transverse loading and ensure a symmetrical load distribution (in the linear stage of the *CS-I* series). The supports consisted of cylindrical rollers, placed in-between metal plates. In the *SS* series, the major axis flexural rotations were free at both end supports and one of the supports allowed also for longitudinal sliding. In the *CS* series, the central support was fully fixed, while both lateral supports allowed for longitudinal sliding. In order to correct possible altimetry differences between supports, a thin layer of plaster was applied underneath the supports wherever needed.

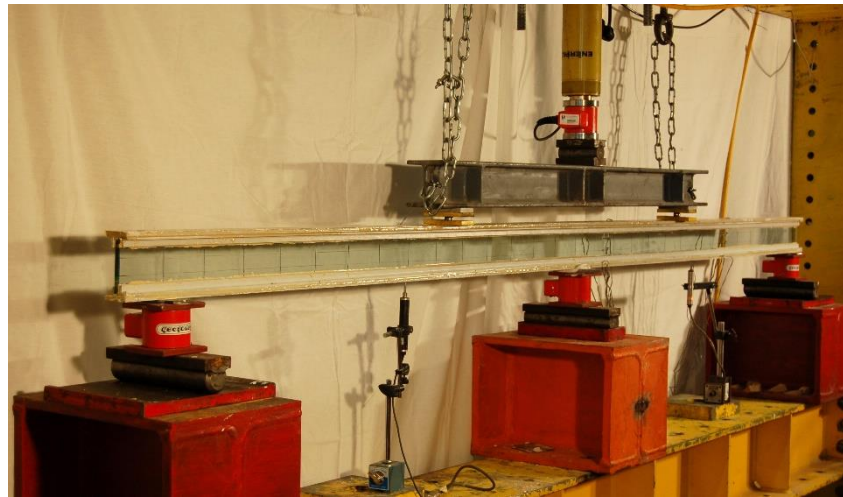


Fig. 6.12 -Experimental setup of the flexural tests on continuously supported beams (*CS-SDur*).

The load was applied using a *Walter+Bai* hydraulic system that allows controlling the pressure transmitted to the jack, capturing possible load drops and recoveries if the beams experience quasi-static damage. The displacement speed was indirectly controlled, being function of the pressure applied on the jack and the response (flexural stiffness) of the beam (Table 6.4).

Table 6.4 – Average displacement speed of the bending tests on composite beams.

Type of beam	Flexural behaviour stage	Displacement speed [mm/min]
SS-R	prior to cracking	0.95 to 1.52
	after cracking	1.70 to 3.21
SS-I	prior to cracking	0.97 to 1.72
	after cracking	1.87 to 4.24
CS-I	prior to cracking	0.51 to 0.96
	after cracking	0.91 to 1.21

Displacements at mid-span (*SS* series) or at the centre of each span (*CS* series) were measured with displacement transducers (strokes of 25, 50 and 100 mm; precision of 0.01 mm). The support reactions and the total applied load were measured with load cells placed below the supports (capacity of 50 kN in the outer supports and 100 kN in the central one; precision of 0.01 kN) and between the hydraulic jack and the distribution beam (capacity of 100 kN; precision of 0.01 kN).

The glass/GFRP interaction level provided by the adhesives was assessed by measuring the longitudinal strains with *TML* electrical strain-gauges (Fig. 6.1). In *SS* series only the mid-span section was instrumented, while in *CS* series two cross-sections were monitored: one under negative bending and the other under positive bending, respectively located at distances of 0.15 m and 0.90 m from the central support. The applied load and vertical displacements were measured at average speeds of 5 Hz.

All beam tests were conducted in laboratory environment. In the tests of the *SS-R* and *SS-I* series the average temperature and relative humidity were 22 °C and 58%, whereas during the tests of the *CS-I* series those figures were 16 °C and 60%, respectively.

6.6 FLEXURAL TESTS: RESULTS AND DISCUSSION

6.6.1 Simply supported R-section beams

6.6.1.1 Load-deflection behaviour and strength

Fig. 6.13 presents the load vs. mid-span deflection curves of the composite beams bonded with the *SFlex*, *SForce* and *SDur* adhesives.

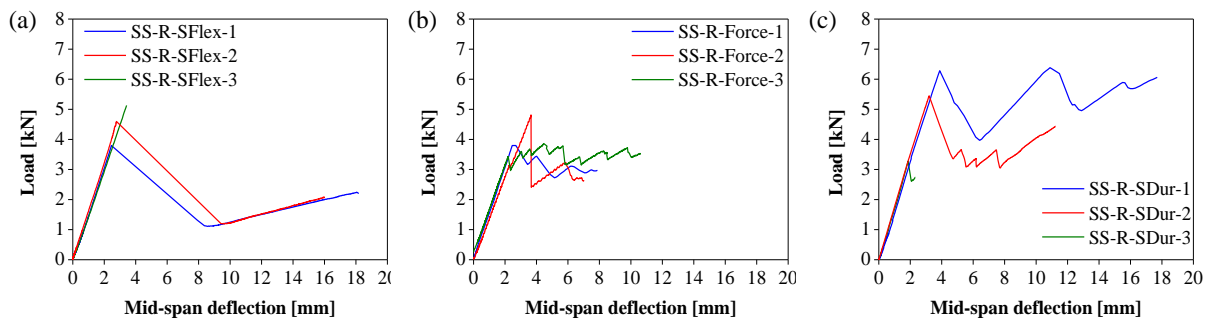


Fig. 6.13 - Load vs. mid-span deflection curves of (a) *SS-R-SFlex*, (b) *SS-R-SForce* and (c) *SS-R-SDur* series.

One may see that the use of GFRP pultruded profiles to reinforce glass beams allowed avoiding the fragile behaviour typical of annealed glass beams [6.26] in the majority of the tests. With the exception of one specimen of the *SS-R-SFlex* and *SS-R-SDur* series, all the R-section glass-GFRP composite beams presented a *pseudo-ductile* response that can be divided in two stages: the first stage was characterized by a linear elastic behaviour until the appearance of the first crack in glass; in the second stage, a progressive loss of stiffness was visible, either due to the development of a single crack in glass (*SS-R-SFlex* series, Fig. 6.14-a), or due to the increase of the number of cracks developing towards the supports (*SS-R-SForce* and *SDur* series, Fig. 6.14-b). The post-cracking residual strength was achieved due to the transfer of stresses from the tensile part of the cracked glass to the GFRP profile which, together with the compressive stresses at the top of the beam, mobilized an internal moment that resisted the applied loads. The ultimate failure of each beam occurred when the extensive crack pattern reached the

compressive zone of the glass web, precluding the mobilization of the binary between the GFRP reinforcement and the glass compression zone.

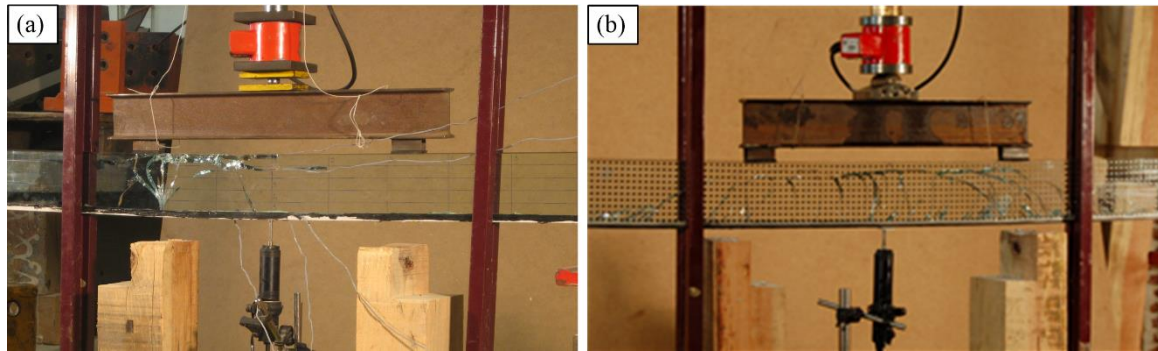


Fig. 6.14 – Illustration of the experimental crack pattern of (a) *SS-R-SFlex* and (b) *SS-R-SDur* series.

Table 6.5 summarizes the main results obtained from the flexural tests on the *SS-R* series in terms of initial stiffness (uncracked stage), cracking load and maximum load (only *R-SDur* beams attained loads equal to the cracking load after the breakage of glass), average post-cracking strength (ratio between the maximum load at the cracked stage and the cracking load), allowing the quantification of the residual strength after the initiation of visible cracking, and the average post-cracking ductility (defined as the ratio between the maximum mid-span deflection attained and the mid-span deflection at the moment of cracking), thereby reflecting the capacity of the beams to deform after the appearance of the first crack.

Table 6.5 - Summary of the results (average plus coefficient of variation) of the 4-point bending tests on *SS-R* glass-GFRP composite beams.

Geometry - Adhesive	<i>SS-R-SFlex</i>	<i>SS-R-SForce</i>	<i>SS-R-SDur</i>
Initial stiffness [kN/mm]	1.41 ± 4%	1.47 ± 6%	1.71 ± 5%
Cracking load [kN]	3.97 ± 15%	4.06 ± 16%	5.00 ± 31%
Maximum load [kN]	3.97 ± 15%	4.16 ± 14%	5.04 ± 32%
Post-cracking strength ¹ [%]	52 ± 19%	88 ± 23%	92.5 ± 15%
Ductility index ¹ [%]	659 ± 18%	284 ± 25%	404 ± 19%

¹ Beams of series *SFlex* and *SDur* that failed prematurely after the crack initiation were not considered (*cf.* Fig. 6.10).

From Table 6.5 one may conclude that, besides the crack pattern, the three adhesives provided different flexural performances, both before and after glass breakage. The *SS-R-SFlex* series presented the lowest initial stiffness and cracking load, whereas the highest values for those parameters were achieved by beams bonded with the *SDur* adhesive. The use of the *SForce* adhesive resulted in intermediate values. Therefore, it is reasonable to conclude that the linear behaviour of the beams was influenced by the adhesive stiffness, which affected the level of interaction between glass and GFRP (detailed ahead in section 6.6.1.2).

The influence of the adhesives' stiffness was also observed in the post-cracking stage. Indeed, the relatively low Young's modulus and high deformation capacity of adhesive *SFlex*, allowed *SS-R-SFlex*

series to present significant post-cracking ductility levels (in average), although such capacity occurred for residual post-cracking resistance (the beams from *SS-R-SFlex* series were unable to recover the initial strength). On the other hand, the higher stiffness of the *SForce* and *SDur* adhesives allowed the corresponding *SS-R* series beams to present higher cracking loads as well as higher levels of post-cracking strength (in average, 87% and 107%, respectively). However, beams from both *SS-R-SForce* and *SDur* series were unable to exhibit ductility indexes as high as those of the *SS-R-SFlex* series. Nevertheless, unlike what would be expected, the lowest ductility index was exhibited by beams from the *SS-R-SForce* series and not by their *SS-R-SDur* counterparts.

The intrinsic scatter of glass strength was attested by the different cracking loads attained in the tests of each series (the average coefficient of variation of cracking load among all beams was around 20%); however, such scatter had only slight influence on the overall post-cracking flexural behaviour of the composite beams. Yet, this scatter seems to have been responsible for the premature failure of the *SS-R-SDur-3* beam, whose glass pane presented an abnormally low tensile strength, which significantly reduced the cracking load of such beam and prevented it to present residual strength. Finally, the poor behaviour and unexpected loss of integrity of the *SS-R-SFlex-3* beam were attributed to a potential critical defect caused during its manufacturing (although no visible signs could be identified) and to the lower bond performance provided by the *SFlex* adhesive (which had already been responsible for a less reliable performance in the double-lap joint experiments, *cf.* section 6.4.2).

6.6.1.2 Composite action

The strain-gauge measurements allowed evaluating the degree of shear interaction at the interfaces (coupling between GFRP and glass) provided by the different adhesives, and therefore the distribution of strains/stresses between the glass panes and the GFRP reinforcing laminates prior to glass cracking, as well as during the glass cracking development.

Fig. 6.15 illustrates the strain development during the flexural tests of the *SS-R* series.

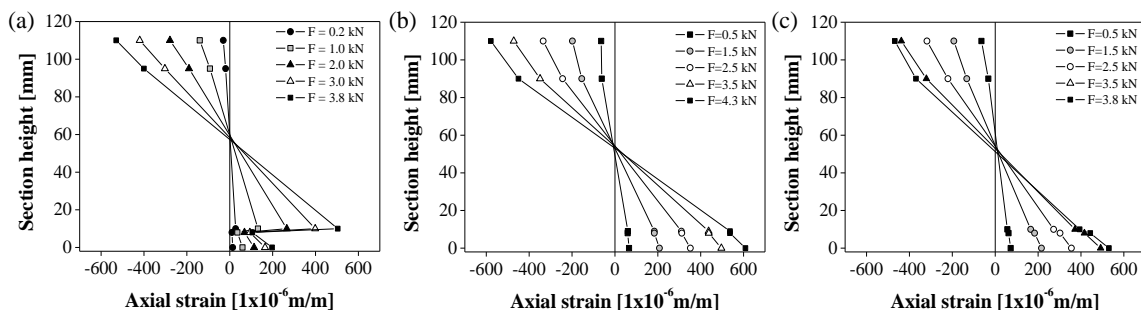


Fig. 6.15 - Axial strains vs. section height for different load levels (in kN) for the (a) *SS-R-SFlex*, (b) *SS-R-SForce* and (c) *SS-R-SDur* series.

Due to the low Young's modulus of the *SFlex* adhesive, beams from the *SS-R-SFlex* series (Fig. 6.15-a) were unable to achieve the full level of interaction between glass and GFRP, which clearly affected the

beams' performance in the linear stage (e.g. the cracking loads were the lowest). The higher values of Young's modulus of the other two adhesives allowed for a higher level of interaction, which improved the performance of the corresponding beams, not just in terms of initial stiffness and cracking load, but also in terms of post-cracking strength.

6.6.2 Simply supported I-section beams

6.6.2.1 Load-deflection behaviour and strength

Fig. 6.16 shows the load vs. mid-span deflection curves for the simply supported beams produced with the three different types of adhesives. Table 6.6 summarizes the main results obtained from those curves and provides an insight about the post-cracking performance. In particular, the post-cracking ductility was evaluated assuming (i) the deflection at failure, and (ii) when a reduction of the post-cracking residual strength was observed, the deflection at 80% of the maximum load.

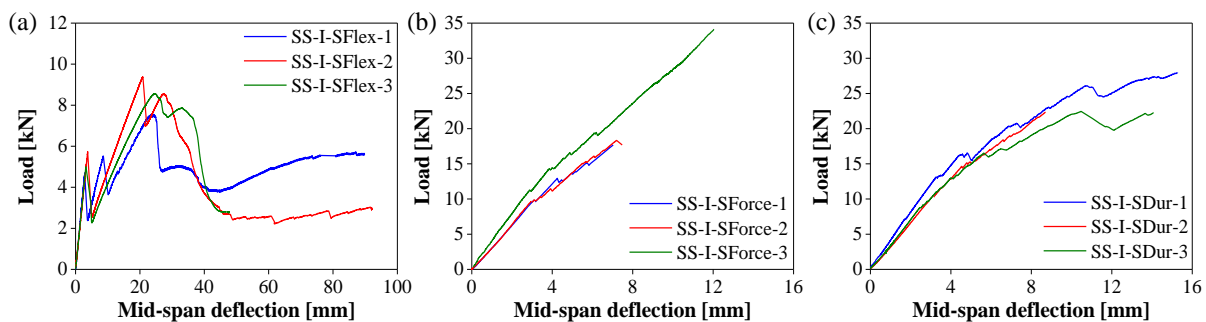


Fig. 6.16 - Load vs. mid-span deflection curves of SS-I- (a) *SFlex*, (b) *SForce* and (c) *SDur* series.

The load vs. mid-span deflection curves presented in Fig. 6.16 show that the overall flexural behaviour of the *SS-I* series was qualitatively similar to the one observed in the *SS-R* counterparts, even though the former presented improved performance due to the increase of GFRP reinforcement and change of geometry. The flexural behaviour presented two distinct stages, separated by the appearance of the first crack. Contrarily to the *SS-R* beams, when the first crack appeared on the glass pane of the *SS-I* series, all glass-GFRP composite beams were able to maintain their integrity, being capable of transferring the stresses from the cracked glass to the GFRP reinforcement.

As in the *SS-R* series, the initial stiffness of the beams increased with the stiffness of the adhesive used in the bonded interfaces: minimum values were obtained in *SS-I-SFlex* series (gap-filling polyurethane adhesive), while maximum values were obtained in *SS-I-SDur* and *SS-I-SForce* series (epoxy and 2-component structural adhesives, respectively), which presented similar results. As discussed for the *SS-R* series, such difference stem from the degree of composite action at the bonded interfaces, which was almost full for the two last adhesives and was very limited for the first (discussed ahead in section 6.6.2.2). Also as a consequence of such different composite action, the cracking load for beams *SS-I-SFlex* was almost half of that obtained in series *SS-I-SForce* and *SS-I-SDur*.

The highest maximum load measured (24.3 kN) and the average post-cracking strength (282%) were obtained in *SS-I-SDur* series, while the lowest ones (8.5 kN and 165%, respectively) were attained by *SS-I-SFlex* series. Regarding the beams from *SS-I-SForce* series, although they presented a similar performance to the beams of the *SS-I-SDur* series in the linear stage, two of those beams presented a worse performance during the second behavioural stage, exhibiting much lower maximum load and post-cracking strength (around 18 kN and 184%, respectively). Such worse performance seems to have stemmed from the lower capacity to transfer load between the glass pane and the GFRP reinforcement during the cracking progression, associated with limited adhesion at the bonded interface. The third beam from this series somehow exhibited a much better performance than the other two, presenting a similar behaviour to that of *SS-I-SDur* series.

Table 6.6 - Summary of the results (average plus coefficient of variation) from flexural tests on *SS-I* series.

Setup – Beam	<i>SS-I-SFlex</i>	<i>SS-I-SForce</i>	<i>SS-I-SDur</i>
Initial stiffness [kN/mm]	1.7 ± 4%	3.5 ± 15%	3.7 ± 8%
Cracking load [kN]	5.2 ± 8%	10.3 ± 13%	8.9 ± 15%
Maximum load [kN]	8.5 ± 9%	23.4 ± 39%	24.3 ± 11%
Post-cracking strength [%]	165% ± 3%	224% ± 25%	282% ± 27%
Deflection at first visible crack [mm]	3.1 ± 6%	3.0 ± 3%	2.5 ± 23%
Deflection at failure (or before unloading) [mm]	75.5 ± 28%	8.8 ± 26%	12.7 ± 23%
Deflection at 80% of the maximum load [mm]	32.1 ± 16%	N.A.	N.A.
Ductility index at failure [-]	2456% ± 32%	297% ± 29%	569% ± 44%
Ductility index at 80% of maximum load [-]	813% ± 4%	N.A.	N.A.
Deflection/span at first visible crack [-]	428	471	564
Deflection/span at failure [-]	25	160	110

N.A. - not applicable

In what concerns ductility, the typical fragile behaviour of annealed glass beams was avoided, i.e. all composite beams exhibited a *pseudo-ductile* behaviour after initial cracking, which, similarly to strength, varied with the type of adhesive. As expected, beams with *SFlex* adhesive presented much higher ductility than the other beams, exhibiting an almost horizontal branch in the load-deflection curves, albeit such plateau occurred for a load level slightly lower than the maximum load (for these beams, the ductility index was calculated in this plateau based on the deflection corresponding to 80% of the maximum load). The higher ductility of the former beams stemmed not only from the distribution of stresses between the two materials (also observed in the latter beams) but, essentially, from the higher deformability and lower stiffness of the gap-filling (non-structural) polyurethane adhesive, which caused significant slippage between the two materials. It should be mentioned, however, that the achievement of higher ductility levels led to a worse performance in terms of initial stiffness, cracking load, ultimate load and post-cracking strength capacity.

The different types of adhesives led also to different cracking patterns: beams from *SS-I-SFlex* series (gap-filling polyurethane) had a cracking pattern characterized by few cracks, with a considerable spacing between them and more concentrated under or in the vicinity of the load application points (Fig. 6.17-a); in opposition, beams from *SS-I-SDur* series (epoxy) and *SS-I-SForce* series (structural 2-component) had a much more regular crack pattern (roughly similar to that exhibited by reinforced concrete beams), with vertical bending cracks in the central part of the beams and increasingly inclined shear cracks towards the supports along the shear span (Fig. 6.17-b).

The ultimate failure modes of the *SS-I-SForce* and *SS-I-SDur* series were very similar and were caused by the sudden and explosive disintegration of the glass web after a high level of damage was attained with extensive cracking in the glass web. In opposition, the *SS-I-SFlex* series were unloaded without having collapsed, but in any case those beams presented an extensive level of glass damage. In fact, some parts of the glass pane had already fallen down prior to unloading.

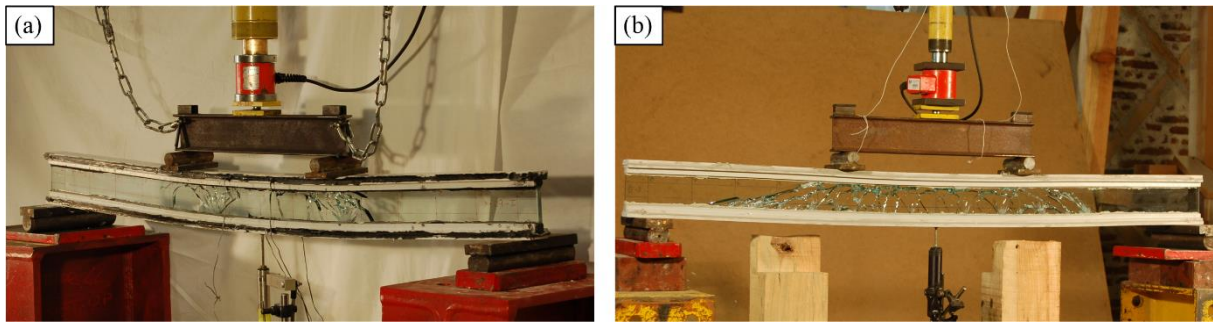


Fig. 6.17 - Crack pattern of (a) *SS-I-SFlex* and (b) *SS-I-SDur* beams.

6.6.2.2 Composite action

Fig. 6.18 shows the axial strains, both prior and after cracking, for different load levels at different depths of one of the beams from *SS-I-SFlex*, *SS-I-SForce* and *SS-I-SDur* series, before and after cracking.

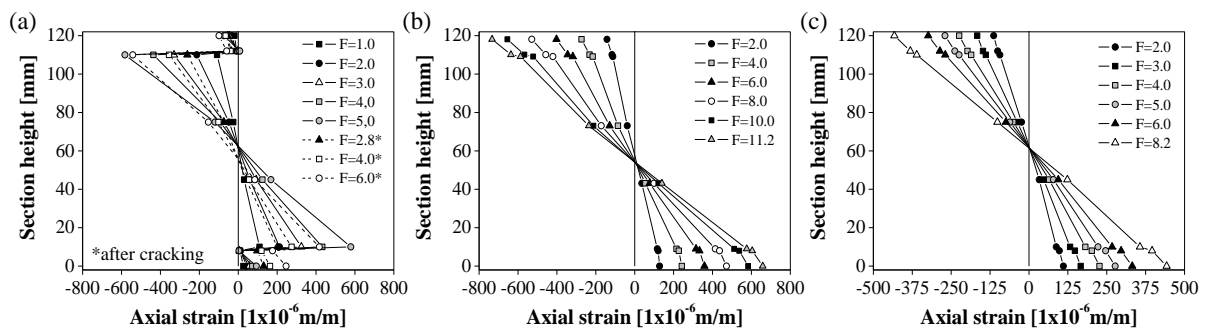


Fig. 6.18 - Axial strains vs. section height for different load levels (in kN) for *SS-I-* (a) *SFlex*, (b) *SForce* and (c) *SDur* series.

One may see that although all adhesives were able to distribute stresses from the glass pane to the reinforcing material, the degree of shear interaction at the bonded interfaces varied for the different

adhesives, in agreement with results reported earlier for the *SS-R* series. While an almost full composite action was observed in series *SS-I-SDur* and *SS-I-SForce* (Fig. 6.18-b and c), a considerable slippage occurred at the interfaces of series *SS-I-SFlex* (Fig. 6.18-a), causing a much lower level of interaction. As a consequence, in these latter beams, the Bernoulli's hypothesis was not verified and therefore both the stiffness and cracking load were considerably reduced.

6.6.3 Continuous beams

6.6.3.1 Load-deflection behaviour and strength

Fig. 6.19 shows the load vs. mid-span deflection curves for both spans (LD and RD) of the continuously supported beams produced with the three different types of adhesives. Table 6.7 summarizes the main average results obtained from those curves.

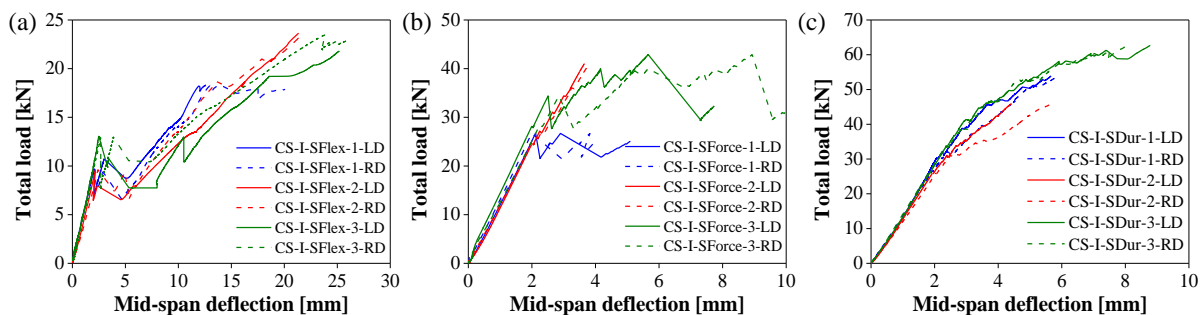


Fig. 6.19 - Load vs. mid-span deflection curves of the (a) *CS-I-SFlex*, (b) *CS-I-SForce* and (c) *CS-I-SDur* series.

Table 6.7 - Summary of average results from flexural tests on *CS-I* series.

Setup - Beam	CS-I-SFlex		CS-I-SForce		CS-I-SDur	
	Left	Right	Left	Right	Left	Right
Span						
Initial stiffness [kN/mm]	4.76	4.69	13.1	12.5	14.3	13.6
Cracking load [kN]	10.8		28.5		30.0	
Maximum load [kN]	21.8		36.9		54.1	
Post-cracking strength [%]	202%		130 %		180 %	
Deflection at first visible crack [mm]	2.24	2.36	2.21	2.27	2.12	2.22
Deflection at failure (or before unloading) [mm]	19.71	22.60	5.46	6.43	7.18	6.59
Deflection/span at first visible crack [-]	625	593	635	617	661	631
Deflection/span at failure [-]	71	62	204	156	195	212
Ductility index [-]	879%	958%	312%	396%	329%	296%

From Fig. 6.19 one may see that the overall load-deflection behaviour of the continuous beams was qualitatively similar to that observed in the simply supported beams. Accordingly, there are two behavioural stages separated by the occurrence of the first visible crack. In the first stage all beams exhibited a linear behaviour with a similar stiffness in both spans. The second stage was characterized by the propagation of cracks and the corresponding progressive loss of stiffness, resulting in a *pseudo-*

ductile behaviour, which was registered in most of the beams, but presenting some differences between spans within the same beam.

As expected, beams bonded with the *SFlex* adhesive exhibited the lowest initial stiffness (4.7 kN/mm), about 2.7 to 3.0 times lower than that of beams bonded with *SForce* (12.8 kN/mm) and *SDur* (14.0 kN/mm) adhesives, respectively. As for the *SS* series, such lower performance of *CS-I-SFlex* series stemmed from the lower degree of shear interaction at the bonded interfaces (discussed ahead in section 6.6.3.2).

With respect to the cracking load, as for the initial stiffness, beams *CS-I-SForce* and *CS-I-SDur* presented the best performance, with cracking loads being more than two times higher than those of series *CS-I-SFlex*. When the first visible crack developed, the mid-span deflection of all beams was about 2.3 mm ($L_0/585$ of the span).

Regarding the maximum load attained, the three types of beams bonded with the different adhesives, presented a clearly distinct behaviour. Again, *CS-I-SDdur* beams presented the best performance, attaining an average maximum load of 54.1 kN. The beams bonded with polyurethane presented much lower strength, especially beams *CS-I-SFlex*, with an average maximum load of 21.8 kN, which is about 2.5 times lower compared to that of the beams bonded with epoxy adhesive. Beams *CS-I-SForce* presented an intermediate strength of 34.8 kN. Despite the marked difference in terms of ultimate load between beams *CS-I-SDur* and *CS-I-SFlex*, both types of beams presented a very similar post-cracking strength (180% for the former and 202% for the latter), indicating that both adhesives result in equivalent post-cracking performance.

Unlike deflections at cracking, deflections at failure were very dissimilar for the different types of adhesives. Before unloading (or failure), beams *CS-I-SFlex* exhibited an average deflection of 19.7 mm at the left mid-span, much higher than that exhibited by beams *CS-I-SForce* and *CS-I-SDur* (5.5 mm and 7.2 mm, respectively). Consequently, the ductility index was much higher in the former beams (almost 900%) than in the latter (around 300%).

The crack pattern development was of two types: beams *CS-I-SFlex* exhibited few cracks that had a continuous development during the test and were particularly concentrated over the central support and on the loaded sections (Fig. 6.20); in the remaining beams, the glass pane displayed a more distributed crack pattern (Fig. 6.21-a). Those distinct behaviours, already identified in the *SS* series, can be attributed to the level of interaction at the bonded interfaces, which, as discussed previously, is low for the *SFlex* adhesive and high for the two other adhesives.

Although in the majority of the beams tested the first cracks developed in the vicinity of the central support, it is worth mentioning that in two beams (*CS-I-SForce-2* and *CS-I-SFlex-2*) the first cracks developed within the spans. This fact must be attributed to the intrinsic variability of glass tensile strength (note that the maximum elastic moment over the support was 1.53 times higher than that of the span).

In beams *CS-I-SForce* and *CS-I-SDur* the ultimate failure modes were very similar and were caused by the sudden and explosive disintegration of the glass web (in most specimens, this only occurred in one of the spans or at the central support – Fig. 6.21-b) after a high level of damage was attained, with extensive cracking in the glass web. One of the beams from *CS-I-SFlex* series (*CS-I-SFlex-1*) was unloaded without having collapsed (i.e. without web disintegration) after a considerable lateral (out of plane) deformation became visible, particularly in one of the loaded sections (Fig. 6.20). In the other two beams of that series (*CS-I-SFlex-2,3*) the lateral displacements were restricted by means of two pairs of vertical steel bars in each span and the test was not interrupted. However, the out of plane deformation was not completely avoided and the beam eventually failed due to a mechanism that involved lateral bending and crushing of the glass web below one of the loaded sections. The above-mentioned lateral deformation (apparently, an instability phenomenon) may have been due to the reduced composite action provided by the *SFlex* adhesive, which caused considerably higher compressive stresses in both the flange and the web.



Fig. 6.20 - Crack pattern of beam *CS-I-SFlex-1* (before unloading).

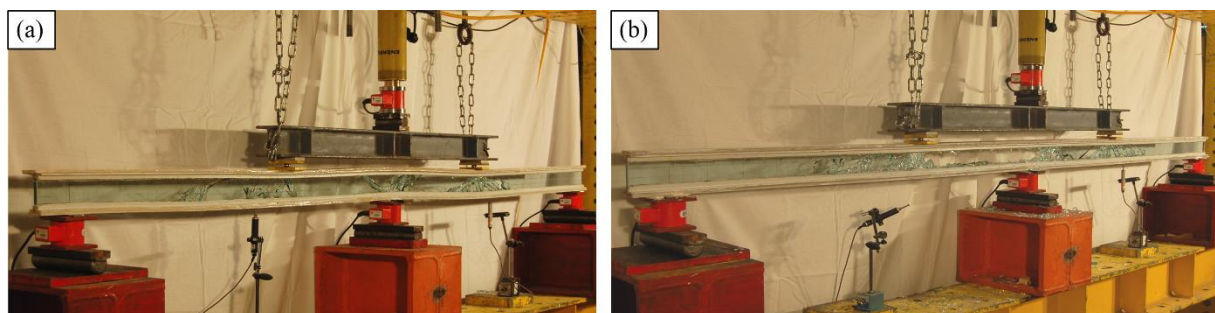


Fig. 6.21 – Crack pattern of beam (a) *CS-I-SForce-1* and (b) *CS-I-SDur-1* (after failure).

6.6.3.2 Composite action

As for the simply supported beams, the analysis of the axial strain measurements allowed assessing the shear interaction level provided by the different adhesives and the distribution of stresses between the glass panes and the GFRP reinforcement, now at two cross-sections under positive and negative bending.

Fig. 6.22 shows the axial strain distributions, prior to cracking, for different load levels for beams *CS-I-SFlex-1*, *CS-I-SForce-1* and *CS-I-SDur-1*, respectively.

Results obtained for the continuous beams are qualitatively very similar to those presented for the *SS* ones: in fact, while *CS-I-SDur* and *CS-I-SForce* beams exhibited full shear interaction (cross-sections remain plane after deformation), beams *CS-I-SFlex* displayed considerable slippage at the bonded interfaces, causing a reduction of stiffness and an increase of the overall deformability.

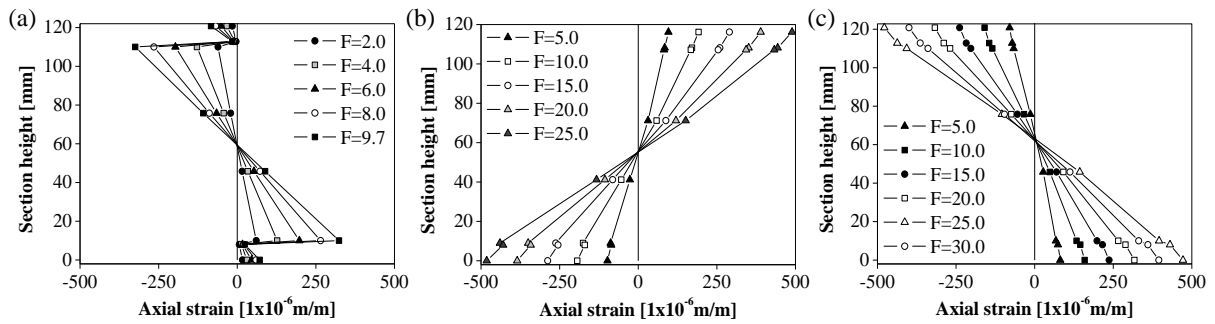


Fig. 6.22 - Axial strains vs. section height for different total loads (in kN) for beams (a) *CS-I-SFlex-1* (M+), (b) *CS-I-SForce-1* (M-) and (c) *CS-I-SDur-1* (M+) (prior to glass cracking).

6.6.3.3 Reactions, internal forces and moment redistribution

The flexural tests on the continuous composite beams also allowed analysing the capacity of force redistribution between the central support and the loaded sections. To this end, the variation of the reactions at the supports as a function of the applied load was analysed. Based on equilibrium considerations, the distribution of internal forces as a function of the applied load was also determined.

As an illustrative example, Fig. 6.23 plots the results obtained for beam *CS-I-SDur-3*, in terms of the distribution and variation of support reactions and bending moments as a function of the total load. In those figures, the theoretical curves corresponding to elastic force analysis are also plotted.

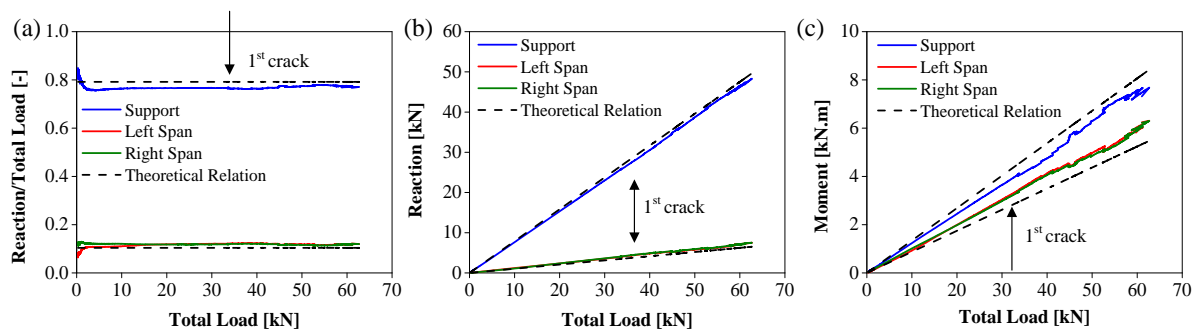


Fig. 6.23 - Beam *CS-I-SDur-3* (a) experimental and theoretical load vs. distribution of reactions, (b) load vs. variation of reactions and (c) load vs. variation of bending moments.

Fig. 6.24 presents the moment redistribution during the test for the three different series (results of a representative beam within each series are plotted). The moment redistribution was calculated based on

the ratio between the experimental values of the bending moment at a given stage of the test and that corresponding to the elastic stage. The complete results obtained from this analysis for all tested beams are summarized in Table 6.8, in terms of maximum bending moments at the support and spans and maximum redistribution of bending moments.

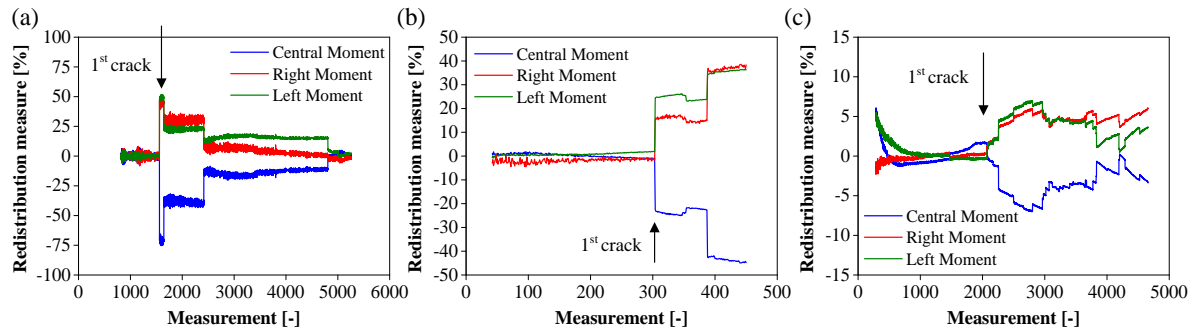


Fig. 6.24 - Redistribution of bending moments during the tests of beams (a) *CS-I-SFlex-3*, (b) *CS-I-SForce-1* and (c) *CS-I-SDur-2*.

Table 6.8 - Analysis of maximum bending moments, ductility index and moment redistribution for the continuously supported beams.

Beam	Ultimate load [kN]	Maximum moment [kN.m]			Ductility index [-]	Maximum redistribution [%]	
		Left	Support	Right		Support	Span
<i>CS-I-SFlex-1</i>	18.3	2.07	2.18	2.34	810%	-59%	15%
<i>CS-I-SFlex-2</i>	23.6	2.50	2.87	2.50	944%	51%	-35%
<i>CS-I-SFlex-3</i>	23.5	2.57	2.49	2.46	988%	-75%	52%
<i>CS-I-SForce-1</i>	26.7	3.05	3.49	3.16	221%	-45%	39%
<i>CS-I-SForce-2</i>	41.0	3.91	5.40	3.92	487%	4%	4%
<i>CS-I-SForce-3</i>	42.9	5.00	4.27	4.91	356%	-27%	28%
<i>CS-I-SDur-1</i>	45.9	4.51	5.00	4.57	255%	-11%	17%
<i>CS-I-SDur-2</i>	53.8	5.46	5.90	5.56	269%	-7%	7%
<i>CS-I-SDur-3</i>	62.7	6.30	7.68	6.31	414%	-5%	9%

^a Average from both spans

One may observe that all beams were able to redistribute internal forces, following the damage propagation in their cross-sections. Yet, such capacity was considerably different amongst the beams tested. Results obtained indicate that beams *CS-I-SFlex* presented by far the highest redistribution capacity in line with their highest ductility index. This result is consistent with the differences in the mechanical properties of the *SFlex* adhesive compared with the two other adhesives (*SForce* and *SDur*), and the influence of such properties on the ultimate strength of the beams (and also on the maximum moment and redistribution capacity). Beams *CS-I-SForce* and *CS-I-SDur*, despite having similar values of ductility index, showed considerably different redistribution capacities, with beams *CS-I-SForce* exhibiting higher capacity than beams *CS-I-SDur*. These differences were related with the differences

exhibited by the two types of the adhesives: the much lower elastic modulus and the non-linear behaviour of the *SForce* adhesive provided a better performance in terms of force redistribution.

As shown in Fig. 6.24-a, beam *CS-I-SFlex-1* achieved the highest value of redistribution after the appearance of the first crack (the central support lost 75% of its elastic moment, while that in the spans increased 50%), and with the crack development the level of redistribution considerably reduced, even approaching 0% in the right span. Beam *CS-I-SDur-2* presented a similar behaviour, with the differences that it was only able to redistribute 10% of the moment at the central support and during crack development the redistribution decay was lower. On the other hand, in beam *CS-I-SForce-1* the moment redistribution increased during the second stage, attaining a maximum level (about 40% in both sections) in the brink of collapse. This different behaviour is most likely related with the limited post-cracking strength exhibited by this particular beam (*cf.* Fig. 6.19-b).

Since the redistribution of moments is a consequence of the loss of stiffness on several sections (due to the damage increase) and, in this case, is not due to the mechanical behaviour of the materials involved (as in steel or reinforced concrete structures), in most of the beams, the maximum moment redistribution from the central support to the spans was only momentarily observed, most of it occurring after the appearance of the first crack. With the development of the crack pattern and with the appearance of cracks in the spans, the beams had the tendency to re-equilibrate the force distribution, approaching the original elastic one (Fig. 6.24). However, several beams (*CS-I-SForce-2,3* and *CS-I-SDur-2,3*) showed progressive and continuous moment redistribution, showing that is possible to guarantee a stable behaviour in terms of redistribution of internal forces.

6.6.4 Summary of results

6.6.4.1 Simply supported series

For the simply supported configuration, composite beams were tested with two different glass-GFRP cross-sections, joined by means of three different adhesives. The results showed that relatively safe failure mechanisms are achievable using the GFRP reinforcement, thus overcoming the fragile failure of traditional glass beams. However, the flexural performance of the glass-GFRP composite beams presented significant differences depending on the cross-sectional area of the GFRP reinforcement and the type of adhesive. Fig. 6.25 illustrates the flexural behaviour of a representative beam from the different types tested.

In the single-span glass-GFRP composite beams the overall flexural performance of the *I*-section beams was better compared to the rectangular counterpart. Regardless of the adhesive, both the initial stiffness and the cracking load were (in average) higher in *SS-I* series than in *SS-R* series. The *SS-I* series also presented more reliable and improved post-cracking performance, with all beams being able to keep their integrity after the appearance of the first crack. Such enhanced performance was achieved due to

the increase of GFRP reinforcement area but, foremost, due to the higher bonding area provided by the GFRP I-section configuration compared to the rectangular one.

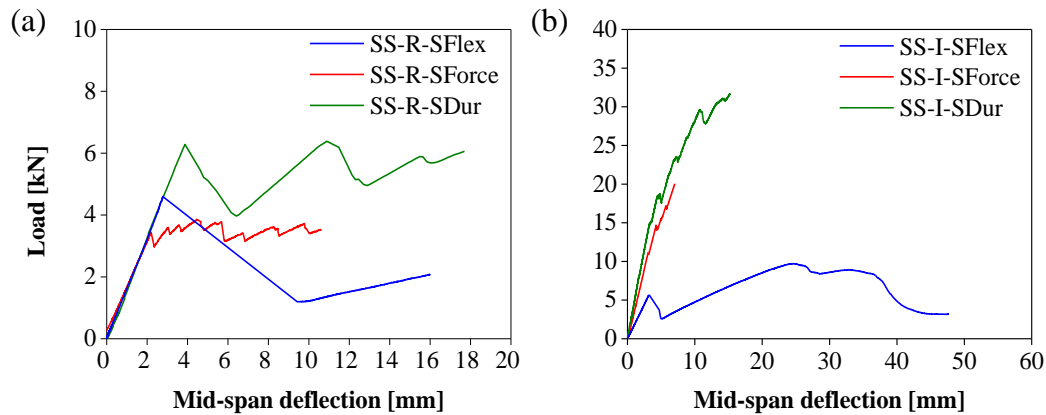


Fig. 6.25 – Example specimen of each series of the simply supported glass-GFRP composite beams.

The increase of GFRP reinforcement also improved the post-cracking residual strength. In fact, for all types of adhesives, the ultimate loads of beams from the *SS-I* series were higher than their cracking loads; this was a significant improvement for beams bonded with the *SFlex* and *SForce* adhesives (note that the corresponding rectangular counterparts failed to recover the initial strength after cracking). The post-cracking strength of the *SS-I* beams increased about 3.2, 2.5 and 2.7 times, respectively for the *SFlex*, *SForce* and *SDur* adhesives, compared to the corresponding *SS-R* beams. In addition, while the *SS-I-SFlex* beams presented much higher deformability capacity compared to their *SS-R-SFlex* counterparts (from 649% to 1039%), the *SS-I-SForce* and *SS-I-SDur* beams presented only a slight increase of their post-cracking ductility with respect to the *SS-R-SForce* and *SS-R-SDur* beams. In summary, the application of higher reinforcement areas together with larger bonding areas resulted in more efficient usage of both glass and GFRP reinforcement components, before and after glass breakage.

The influence of the three different types of adhesives was consistent for both cross-section beam geometries. Indeed, the mechanical properties of the adhesive directly affected the flexural behaviour of the glass-GFRP composite beams. Such influence was set by the level of interaction at the bonded interfaces, which on its turn, was function of the adhesives stiffness. In particular, the *SFlex* adhesive (the softest) was not able to guarantee a high level of coupling between glass and GFRP, which significantly affected the strength of such beams, with both rectangular and I-section geometry. The major negative effects of such low interaction were the low values of initial flexural stiffness and cracking load, which were significantly lower than the theoretical values with full interaction⁵. Nevertheless, the slippage occurring at the interfaces was useful on both *SS-R-SFlex* and *SS-I-SFlex* series as it contributed to a safer failure mechanism, since it allowed such beams to present high values

⁵ Theoretically, the *SS-R* and *SS-I* series would have yielded initial stiffnesses of 1.61 kN/mm and 3.91 kN/mm, respectively.

of ultimate deformation, namely on the *SS-I* series. On the other hand, the beams bonded with the *SForce* and *SDur* adhesives presented a much higher level of interaction, without slippage at the interfaces, which resulted on high flexural stiffness and strength, both before and after the appearance of the first crack. However, the beams using the stiffer adhesives were unable to explore the post-cracking deformability capacity in the same extent as the beams made with the less stiff adhesive *SFlex*.

Applying a wide range of adhesives Young's modulus, from about 3 MPa to approximately 4000 MPa, successfully resulted in an increasing level of performance in terms of initial stiffness, cracking load and post-cracking strength. However, the adhesive with intermediate stiffness, *SForce*, did not result in intermediate values of post-cracking ductility. In fact, beams bonded with the *SForce* adhesive consistently presented the lowest values of post-cracking ductility, for both *SS-R* and *SS-I* series. Furthermore, the glass-GFRP composite beams failed to take advantage of the non-linear behaviour (in tension, cf. Fig. 6.3-b) of the *SForce* adhesive. Different aspects may have been at the origin of such result. At first, glass-GFRP composite beams bonded with the *SForce* adhesive were manufactured with a lower adhesive thickness (1 mm vs. 2 mm). Secondly, the adhesive is subjected mainly to shear rather than tension. Therefore, in order to guarantee that composite glass beams take advantage of the non-linear behaviour of the applied adhesive, further mechanical characterization tests of the adhesives are required, namely to evaluate its response under shear stresses.

6.6.4.2 Continuously supported series

Table 6.9 presents a comparative summary of the performance of both structural systems tested, namely the simply supported single-span and the continuously supported two-span, in terms of cracking load, ultimate load, post-cracking strength and post-cracking ductility.

Results obtained for both structural systems were compared taking into account the level of the maximum elastic moment expected: for the simply supported beams the maximum moment is equal to $M_{max,ss} = 0.166 \times P \times L_0$, being P the total load and L_0 the length of the flexural span; for the continuously supported beams the maximum moment over the central support is equal to $M_{max,cs} = 0.095 \times P \times L_0$ (i.e. for an identical total applied load the *CS* beams have a maximum moment 0.57 times lower than that of the *SS* beams; in other words, for a linear elastic analysis the *CS* beams should sustain a total load 1.73 times higher than that of the *SS* beams; in fact, in some beams this ratio should be slightly higher since the maximum moment measured at the central support was lower than the theoretical one. However, one should note that after the appearance of the first crack the elastic force distribution is no longer verified and thereby the comparison of the two structural systems is less relevant.

Results listed in Table 6.9 show that beams from *CS* series presented in average an increase of the cracking load of about 2.74 compared to the corresponding beams from the *SS* series, which is about 58% higher than what would be expected from linear elastic analysis (1.73). This result may be related with the differences in the test setups of both series, the brittle nature of glass and the consequent size

effect on strength: indeed, the maximum bending moment develops in 1/3 of the span of *SS* beams, while in *CS* beams it only occurs on the central support section. It is also worth mentioning that the increase of cracking load from the *SS* to the *CS* series increased with the stiffness of the adhesive, being minimum for the *SFlex* and maximum for the *SDur*.

Table 6.9 - Comparison between simply supported (*SS-I*) and continuously supported (*CS-I*) series.

Adhesive	<i>SFlex</i>		<i>SForce</i>		<i>SDur</i>	
	<i>SS</i>	<i>CS</i>	<i>SS</i>	<i>CS</i>	<i>SS</i>	<i>CS</i>
Cracking load [kN]	5.2	10.8	10.3	28.5	8.9	30.0
Ratio (<i>CS/SS</i>) [-]	2.08		2.77		3.37	
Ultimate Load [kN]	8.5	21.8	23.4	36.9	24.3	54.1
Ratio (<i>CS/SS</i>) [-]	2.56		1.58		2.23	
Post-cracking strength [kN]	165%	202%	224%	130%	282%	180%
Variation (<i>CS-SS</i>) [%]	+37%		-94%		-102%	
Post-cracking ductility [-]	1825%	919%	297%	354%	569%	313%
Variation (<i>CS-SS</i>) [%]	-906%		+57%		-256%	

Regarding the ultimate load, and although the elastic relationship is a less significant criterion to compare both systems, one can state that *CS-I-SFlex* and *CS-I-SDur* beams achieved an ultimate load that is more than 2 times higher than the one registered in the corresponding simply supported beams, while the improvement in the *CS-I-SForce* beams was only 1.48. In spite of those variations in terms of ultimate load values, the post-cracking strength only increased with the *SFlex* adhesive (in average, from 165% to 202%). For the other two types of beams there was a significant reduction of post-cracking strength (almost 100% in both cases), showing that these continuous beams bonded with stiffer adhesives had more difficulty in achieving higher loads after the appearance of the first crack.

In what concerns deformability, one expected that the use of a hyperstatic system would cause a considerable reduction of deflections, something that was verified in all beams at the elastic stage (deflection at the moment of the appearance of the first crack) and more significantly at the non-linear stage (deflection at failure). Consequently, the ductility index of the *CS* beams presented an appreciable reduction, namely in the *CS-I-SFlex* beams (from 1039% to 825%). For these beams, the use of a hyperstatic system caused the appearance of a new failure mode (apparently triggered by an instability phenomenon), which prevented these beams from achieving higher displacements at failure. For the other two types of beams, the reduction may be related with the extensive damage in the web that did not allow those beams to achieve better post-cracking performances.

6.7 CONCLUDING REMARKS

This chapter presents results of experimental investigations on single and two-span composite structural beams made of annealed glass panes and GFRP pultruded profiles, bonded with different types of adhesives.

The experimental tests proved the advantages and the technical viability of using glass–GFRP composite beams in hyperstatic systems. In particular, it has been shown that in continuously supported beams it is possible to reproduce the post-cracking behaviour observed in simply supported beams, making use not only of the cross-sectional redundancy, but also of the hyperstaticity and force redistribution (structural redundancy). It has also been shown that the post-cracking performance, particularly the ultimate strength and post-cracking ductility, is affected by the area of GFRP reinforcement and the type of adhesive.

As expected, the increase of GFRP reinforcement as well as the bonded area improved the beams performance, both before and after glass cracking. Regardless of the type of the adhesive, the I-section beams consistently presented higher initial and post-cracking stiffness, cracking load, ultimate load, post-cracking strength and ductility than their corresponding R-section counterpart. The post-cracking flexural performance of the *SS-I* beams was also more reliable compared to their rectangular counterparts, with all beams of the *SS-I* series presenting post-cracking residual strength, contrarily to some beams of the *SS-R* series that failed prematurely after the appearance of the first crack. Moreover, the beams bonded with the *SFlex* and *SForce* adhesives were able to achieve ultimate loads higher than their cracking loads, increasing the average post-cracking strength from 57% and 87% to 165% and 224%, respectively. The *SS-I-SDur* beams also exhibited a substantial gain of resistance, of about 2.8 times, compared to the *SS-R-SDur* beams. The increase of post-cracking ductility was also noteworthy, namely on the *SS-I-SFlex* beams, whose ultimate deformation was more than 2 times higher (1.6 times higher for a residual strength not lower than 80% of the maximum attained load) than in their rectangular counterparts. The increase of post-cracking ductility obtained with the *SS-I-SForce* and *SS-I-SDur* beams (compared to the corresponding rectangular beams) was less pronounced.

The use of a hyperstatic structural system affected the strength (cracking load and ultimate load) and bending stiffness of the composite beams. Beams with two spans were able to achieve higher cracking and ultimate loads than expected from linear elastic analysis. This result may be related with the differences in the test setups of both series, the brittle nature of glass and the consequent size effect on glass strength. In spite of those variations, the post-cracking strength only increased from *SS* to *CS* series with the *SFlex* adhesive

In terms of deflections, as expected, the use of a hyperstatic system caused the reduction of the deformability in all beams, both for the linear and non-linear stages. As a consequence of such flexural stiffness increase, the post-cracking ductility was reduced compared to that of simply supported beams.

All two-span beams presented force redistribution capacity, with the highest one being provided by the *SFlex* adhesive, the one with the lowest stiffness. However, since the redistribution of moments stemmed from the loss of stiffness on several sections, the maximum moment redistribution from the central support to the spans was only momentarily observed.

The experimental tests also showed that the mechanical properties of the adhesives considerably influence the performance of the composite beams, in terms of cracking load and ultimate strength. The beams bonded with the adhesive with the lowest stiffness and strength (*SFlex*) presented the lowest cracking and ultimate loads in both structural systems. This behaviour was related with the low level of interaction granted by this adhesive, which did not allow for an efficient use of the GFRP reinforcing material, even in the linear stage. The beams bonded with the other two adhesives (*SForce* and *SDur*) exhibited full interaction and, consequently, presented similar cracking loads in both structural systems. However, in terms of ultimate strength, those adhesives provided different performances, with the beams bonded with the stiffer *SDur* adhesive providing higher strengths. For the simply supported beams the *SFlex* beams presented the lowest values of post-cracking strength, but for the continuously supported beams such adhesive provided the highest post-cracking strength, taking advantage of its distribution capacity.

Regarding deformability, the *SFlex* adhesive provided the lowest values of initial stiffness and, consequently, the highest deflections when the first crack appeared. At the second (non-linear) stage, the high deformation capacity and the low stiffness of this adhesive allowed for higher levels of deformation, providing higher values of post-cracking ductility in both structural systems. However, these beams presented a considerable lower performance in terms of cracking load, ultimate strength and post-cracking strength. Beams bonded with *SForce* adhesive achieved the lowest values of ductility index, which may be related with the adhesion problems identified in the double-lap joint tests.

6.8 REFERENCES

- [6.1] Louter C. Fragile yet Ductile - Structural Aspects of Reinforced Glass Beams. PhD thesis, Delf University of Technology, Netherlands, 2011.
- [6.2] Louter C, Belis J, Veer F, Lebet J-P. Structural response of SG-laminated reinforced glass beams; experimental investigations on the effects of glass type, reinforcement percentage and beam size. *Eng Struct* 2012;36:292–301.
- [6.3] Martens K, Caspeele R, Belis J. Development of reinforced & post-tensioned glass beams - review. *J Struct Eng* 2015:1–23.
- [6.4] Martens K, Caspeele R, Belis J. Development of composite glass beams – A review. *Eng Struct* 2015;101:1–15.
- [6.5] Keller T, de Castro J. System ductility and redundancy of FRP beam structures with ductile adhesive joints. *Compos Part B Eng* 2005;36:586–96.
- [6.6] Palumbo D, Palumbo M, Mazzuchelli M, Schiavon A, Rebeschini A. A new roof for the XIII th Century “Loggia de Vicari” (Arquà Petrarca -PD – Italy) based on structural glass trusses : A case study. *Glas. Process. Days* 2005, Tampere: 2005.
- [6.7] Louter C, Leung C, Kolstein H, Vamborský J. Structural glass beams with embedded glass fibre reinforcement. In: Bos, Louter V, editor. *Challenging Glas. 2 - Conf. Archit. Struct. Appl. Glas.*, Delf: 2010, p. 439–48.
- [6.8] Valarinho L. Construção em vidro estrutural: Comportamento estrutural de vigas mistas vidro-GFRP. MSc dissertation (in Portuguese), Technical University of Lisbon, Portugal, 2010.
- [6.9] Correia JR, Valarinho L, Branco FA. Post-cracking strength and ductility of glass-GFRP composite beams. *Compos Struct* 2011;93:2299–309.
- [6.10] Speranzini E, Neri P. Structural behaviour of GFRP “reinforced glass beams.” *Glas. Perform. Days* 2011, Tampere: 2011, p. 604–9.
- [6.11] Correia JR, Branco FA, Ferreira J. GFRP-concrete hybrid cross-sections for floors of buildings. *Eng Struct* 2009;31:1331–43.
- [6.12] Correia JR, Branco FA, Ferreira J. Flexural behaviour of multi-span GFRP-concrete hybrid beams. *Eng Struct* 2009;31:1369–81.
- [6.13] Haldimann M, Luible A, Overend M. *Structural Use of Glass*. Zurich: IABSE-AIPC-IVBH; 2008.
- [6.14] Report EUR 26439 EN Guidance for European Structural Design of Glass Components. Institute for the Protection and Security of the Citizen, Joint Research Centre, Luxembourg: 2014.
- [6.15] Kreher K, Natterer J, Natterer J. Timber-glass-composite girders for a hotel in Switzerland. *Struct Eng Int J Int Assoc Bridg Struct Eng* 2004;14:149–51.
- [6.16] ISO 527 Plastics - Determination of the tensile properties - Part 1: General principles. International Organization for Standardization, Genève: 1993.
- [6.17] ISO 527 Plastics - Determination of the tensile properties - Part 4: Test conditions for isotropic and orthotropic fibre-reinforced plastic composites. International Organization for Standardization, Genève: 1997.
- [6.18] ISO 37 Rubber, vulcanized or thermoplastic - Determination of tensile stress-strain properties. International Organization for Standardization, Genève: 2011.
- [6.19] ISO 527 Plastics - Determination of the tensile properties - Part 2: Test conditions for moulding and extrusion plastics. International Organization for Standardization, Genève: 1993.
- [6.20] Keller T, Vallée T. Adhesively bonded lap joints from pultruded GFRP profiles. Part I: stress–strain analysis and failure modes. *Compos Part B Eng* 2005;36:331–40.

- [6.21] Keller T, Vallée T. Adhesively bonded lap joints from pultruded GFRP profiles. Part II: joint strength prediction. *Compos Part B Eng* 2005;36:341–50.
- [6.22] Vallée T, Correia JR, Keller T. Probabilistic strength prediction for double lap joints composed of pultruded GFRP profiles part I: Experimental and numerical investigations. *Compos Sci Technol* 2006;66:1903–14.
- [6.23] Vallée T, Correia JR, Keller T. Probabilistic strength prediction for double lap joints composed of pultruded GFRP profiles - Part II: Strength prediction. *Compos Sci Technol* 2006;66:1915–30.
- [6.24] De Castro J, Keller T. Ductile double-lap joints from brittle GFRP laminates and ductile adhesives, Part I: Experimental investigation. *Compos Part B Eng* 2008;39:271.
- [6.25] De Castro J, Keller T. Ductile double-lap joints from brittle GFRP laminates and ductile adhesives, Part II: Numerical investigation and joint strength prediction. *Compos Part B Eng* 2008;39:282–91.
- [6.26] Bos FP. Safety Concepts in Structural Glass Engineering Towards an Integrated Approach. PhD thesis, Delft University of Technology, Netherlands, 2009.

NUMERICAL SIMULATION OF THE FLEXURAL BEHAVIOUR OF GLASS-GFRP COMPOSITE BEAMS USING SMEARED CRACK MODELS

ABSTRACT

This chapter presents a numerical study about the flexural behaviour of rectangular glass-GFRP composite beams, comprising annealed glass and GFRP pultruded profiles bonded with two different adhesives: (soft) polyurethane and (stiff) epoxy. The main objectives of this study were two-fold: (i) to fully characterize the non-linear behaviour of glass using the smeared crack approach; and (ii) to assess the applicability of different options to simulate adhesively bonded glass-GFRP joints. An extensive parametric study was developed to evaluate the influence of five parameters on the glass post-cracking non-linear behaviour: (i) glass fracture energy, G_f , (ii) crack band width, h , (iii) glass tensile strength, $f_{g,t}$, (iv) shape of the tension-softening diagram, and (v) shear retention factor, β . The wide range of the joints' shear stiffness was simulated by either (i) assuming a perfect bond between glass and GFRP (i.e. neglecting the presence of the adhesive), or (ii) explicitly considering the adhesive, by means of using (ii.1) plane stress elements, or (ii.2) interface elements. For the beams analysed in this thesis, the following material model for glass provided a good agreement with experimental results: G_f in the range of 3 to 300 N/m, h equal to the square root of the finite element area, $f_{g,t} = 50$ MPa, linear softening diagram and β according to a quadratic power law. It was also shown that the hypothesis of perfect bond at the GFRP-glass interfaces allows for an accurate simulation of joints with high levels of interaction (epoxy), while calibrated interface elements are needed for joints with low level of interaction (polyurethane).

7.1 INTRODUCTION

In chapter 2 the concept of hybrid glass systems reinforced with different materials was introduced (*cf.* section 2.3) and in chapter 5 a short experimental campaign was carried out to assess the flexural behaviour of a hybrid glass-stainless steel beam. In chapter 6 a comprehensive experimental campaign on glass-GFRP composite glass beams was reported. In the late campaign, it was shown that the use of hybrid systems comprising glass and GFRP pultruded profiles provides significant improvements in terms of post-cracking resistance and ductility, leading to less brittle failure mechanisms compared to all-glass beams.

In spite of such achievements, hybrid glass systems are not yet being used on a regular basis in industrial applications. Among other reasons, this is due to the lack of reliable analysis and design tools¹. Because the geometrical shapes of composite beams and the material (glass) responses can vary considerably and be rather complex, finite element (FE) models are useful tools to assist the structural design of composite glass members. In this respect, the main challenge relies on the ability to accurately simulate (i) the fracture behaviour of glass, a brittle material, often causing numerical instabilities, and (ii) the interaction between glass and the reinforcing materials.

This chapter presents a numerical study about the flexural behaviour of composite beams made of annealed glass panes and GFRP pultruded laminates. Two-dimensional (2D) FE models were developed using the FEMIX software [7.1] which makes use of a multi-fixed smeared crack model to simulate the linear and non-linear behaviour of brittle materials. The models were parametrically developed using the results of the extensive experimental campaign presented in chapter 6. The objectives of the study were two-fold: (i) to define the parameters that describe the non-linear material response of glass, and (ii) to evaluate different options to simulate adhesively bonded interfaces.

In addition to the introduction and concluding remarks, this chapter is organized in three sections. Section 7.2 comprises a short literature review about the numerical modelling of reinforced/composite glass beams, presenting the main strategies that have been followed to simulate glass fracture. Section 7.3 describes the numerical models developed to simulate, firstly, the shear behaviour of the glass-GFRP adhesively bonded joints, and secondly, the flexural behaviour of the composite glass-GFRP beams. Finally, Section 7.4 compares the numerical results with the experimental data presented in chapter 6.

¹ The recent Italian guidelines [7.22] and the recent British [7.23] and European [7.19] guidance for structural glass do not provide information about the analysis and design of reinforced or composite glass beams.

7.2 LITERATURE REVIEW

For now, only a few studies addressed the numerical simulation of hybrid glass systems. The existing ones can be divided according to the approach adopted to simulate the (quasi) brittle glass material: (i) the *kill element* approach (KEA); (ii) the smeared crack approach (SCA), and (iii) the discrete crack approach (DCA).

The KEA approach was applied by Ølgaard *et al.* [7.2] and Louter and Nielsen [7.3] using a commercial FE-package (with the addition of user-subroutines) and tested on two dimensional (2D) and three dimensional (3D) FE models of reinforced glass-stainless steel beams with SentryGlas² [7.4, 7.5]. The different models were tested with several mesh densities, with constant and random glass tensile strengths and with different interlayer shear stiffness values. The models were able to correctly reproduce the overall load *vs.* deflection behaviour of the reinforced glass beams. In addition, the 2D models accurately reproduced the crack pattern. However, the 3D models were not able to simulate precisely the three-dimensional process of cracking, as cracks were predicted to occur uniformly across the whole cross-section thickness instead of being randomly distributed along its thickness. Despite the good results and the simplicity of its principles, this approach does not exist in the most popular commercial FE packages and hence it needs to be developed and added by users.

The SCA has been used for decades to numerically reproduce the cracked stage of reinforced concrete and other quasi-brittle materials. According to Bazant and Oh [7.6], two main assumptions are made in this numerical approach: (i) the damaged area is distributed along a specific crack band width (h), and (ii) the constitutive law of the material in the damage area is characterized by a tension-softening diagram, which, together with the fracture energy (G_f), are considered material properties and important input data³. Regarding the G_f of glass, experimentally determined in [7.7–7.9], an average value of 3 N/m is commonly accepted [7.4, 7.10, 7.11]. This is an extremely low value when compared with other quasi-brittle⁴ materials (e.g. it is around 20 to 30 times lower than that of normal concrete [7.12, 7.13]) to which the SCA has been applied. The SCA approach also requires several other parameters, including the type of tension-softening diagram, the shear retention factor (β) and the number of possible cracks that can arise in each single integration point [7.14].

Louter [7.4] and Bedon and Louter [7.11] used the SCA to numerically simulate the behaviour of reinforced glass-stainless steel beams. Using 2D and 3D models, the authors performed parametric studies

² SentryGlas was used both as interlayer and as structural adhesive [7.4].

³ The fracture energy criterion and the existence of a softening branch are also assumed in the DCA.

⁴ Applying the SCA to glass requires the assumption that the stable fracture of glass [7.7–7.9] is equivalent to the quasi-brittle behaviour of concrete. In true, glass is known to be a homogeneous brittle material that only presents stable fractures (or softening, in analogy to concrete) under very specific situations [7.7]. Moreover, it should be noted that the stable fracture of glass falls in the linear elastic fracture mechanics field, whereas concrete softening of lab-size specimens falls mostly (it depends on the relationship between the crack size and the size of the adjacent fractured zone) on the non-linear fracture mechanics field [7.24]. Other terms have been used to describe the stable fracture of glass (e.g. Haldiman *et al.* [7.10] framed it in the “*quasi-brittle linear elastic fracture mechanics*”).

to assess the effects of G_f , mesh size, mesh geometry, β , shear stiffness of the SentryGlas and reinforcement ratio in the overall flexural behaviour of the reinforced beams and in their crack pattern propagation [7.4, 7.11]. It was shown that G_f (ranging from 3 N/m to 8 N/m), mesh size (square finite elements with 5 and 10 mm of size for a total span of 1500 and 3200 mm, respectively), β (with constant values or power laws) or the shear stiffness of the interlayer (varying from 240 MPa to 20 GPa) have minor influence on the overall flexural behaviour of the aforementioned beams (only crack pattern differences were noticeable). In opposition, the mesh geometry (and the reinforcement ratio) proved to have significant influence on the global behaviour of the beams and on their crack pattern. Notwithstanding the good match between numerical and experimental results, on the one hand, Louter [7.3] used a numerical strategy to overcome glass brittleness (*saw-tooth* reduction diagrams) that is far from being universally accepted; on the other hand, Bedon and Louter's [7.11] models were computationally highly demanding.

The DCA was successfully applied by Neto *et al.* [7.15] to model the flexural behaviour of glass-GFRP composite beams. A parametric study was developed to assess the ability of the DCA to represent glass cracking, taking into account the influence of the mesh size and glass tensile strength ($f_{g,t}$). It was proved that when using DCA both mesh size and $f_{g,t}$ have minor influence on the global behaviour of the numerical models of the composite beams. The major disadvantage of the DCA is its low popularity compared to the SCA and the fact that it is not available in most commercial FE packages.

The extreme brittleness of glass, i.e. the very low value of its G_f , causes numerical problems like snap-back instabilities or convergence difficulties. Typically, these problems are overcome by either (i) applying numerical tools or strategies that help models to converge (e.g. the above-mentioned *saw-tooth* reduction diagrams), (ii) non-iterative methods [7.15], (iii) or by developing heavy computational models in terms of mesh density [7.11]. In spite of the above-mentioned limitations, none of the numerical studies reviewed above in which the SCA or the DCA were used has assessed the possibility or the effects of adopting fracture energies higher than the reference value for glass in reinforced or composite glass beams (the maximum G_f used in those numerical models was 8 N/m [7.4, 7.11]).

Furthermore, in the aforementioned studies only two types of hybrid systems were simulated: (i) glass-stainless steel (bonded with SentryGlas), and (ii) glass-GFRP composite beams (bonded with epoxy adhesives). With the single exception of the work of Neto *et al.* [7.15], none of the works have applied smeared crack models in combination with interface laws to numerically simulate the behaviour of the bonded interfaces in which a wide range of adhesives (with different mechanical properties) can be used. Note that the two types of adhesives that have been studied in [7.15] were considered stiff enough to neglect the potential slippage at the interfaces. The effect of using softer adhesives, although object of experimental studies [7.16, 7.17], was never numerically investigated.

7.3 DESCRIPTION OF THE NUMERICAL MODELS

7.3.1 Initial considerations

The numerical models aimed at simulating the flexural responses of the rectangular glass-GFRP composite beams described in chapter 6, namely the pre and post-cracking behaviour of the beams made with the *Sikaflex 265* and *Sikadur 31-cf* adhesive (hereafter referred to as *SFlex* and *SDur* adhesives, respectively).

The first step of the simulations required the correct definition of the glass non-linear material characteristics according to the SCA. To describe the non-linear tensile softening behaviour of glass an extensive parametric study was developed in order to assess the influence of the following parameters (Table 7.1): (i) tensile strength of glass, $f_{g,t}$, (ii) mode-I fracture energy, G_f , (iii) crack band width, h , (iv) shape of the tension-softening diagram, and (v) type of shear retention factor law, β . For simplicity, at this stage the parametric studies on glass-GFRP composite beams were performed on models assuming perfect bond at the interfaces.

Table 7.1 - Numerical options tested for the definition of the glass non-linear behaviour.

Parameter studied	Tested range
Glass strength, $f_{g,t}$ [MPa]	30; 45; 50*; 55; 80
Mode I fracture energy, G_f [N/m]	3; 30; 188*#; 300; 3000
Crack band width, h [mm]	$\sqrt{A_{element}}$ *; 1.0; 0.1
Shape of tension-softening diagram	Linear*; Bilinear; Exponential
Shear retention factor, β	1×10^{-5} ; 1×10^{-1} ; 0.99; $p = 1$; $p = 2^*$; $p = 3$

*Default value considered when evaluating the effects of the other parameters (*SNLMMG*, detailed ahead section 7.3.3.1).

This value is 5% higher than the threshold defined by the software (to avoid snap-back instabilities).

The second step of the simulation focused on the numerical modelling of the adhesively bonded joints of the composite beams. For that, three different models of the beams' joints were tested: (i) the Perfect Bond (PB) model, where perfect bond between glass and GFRP was assumed, neglecting the physical existence of the adhesive; (ii) the Plane Stress Elements (PSE) model, in which the adhesives were explicitly simulated using plane stress elements together with the hypothesis of perfect bond at the glass/adhesive and adhesive/GFRP interfaces⁵; and (iii) the Interface Elements (IE) model, where interface elements were used to simulate the effects of both the adhesive and the interfaces (glass/adhesive and adhesive/GFRP). In the last two models the parameters that define the mechanical properties of the joints were obtained using two different approaches. On one hand, the joints of the PSE models were simulated using the information retrieved from the adhesives' tensile characterization tests. On the other hand, the parameters that define the linear and non-linear constitutive laws of the bonded

⁵ The *DL-SFlex* specimens failure mode reported in the double-lap joint tests (*cf.* chapter 6, section 6.4.2) was neglected, thus the model does not account for adhesive failure modes.

interfaces, namely the ones that define the shear behaviour of the interface elements for the two different adhesives, were parametrized through inverse FE analysis of the double-lap joints tests (detailed ahead in section 7.3.2.1). Table 7.2 summarizes all the models developed, as well as their assumptions and applicability.

Table 7.2 - Summary of the FE models developed for the composite beams adhesively bonded joints.

Beam model	Assumptions*	Applicability
Perfect bond (PB)	No elements used to simulate the adhesive joint Perfect bond between glass and GFRP	<i>R-SDur</i>
Plane stress elements (PSE)	Joint simulated by plane stress adhesive elements Perfect bond at all interfaces	<i>R-SDur, R-SFlex</i>
Interface elements (IE)	Joint simulated using interface elements Coupled adhesive and interfaces simulation	<i>R-SFlex, R-SDur</i>

*Glass was always simulated as a non-linear material following the *SNLMMG* model (detailed ahead in section 7.3.3.1).

7.3.2 Geometry, boundary conditions and type of elements

7.3.2.1 Double-lap joints

The double-lap joints were modelled as a plane stress problem. Due to their double symmetry, only 1/4 of the double lap joint specimens was simulated. The geometry, mesh, boundary conditions and load configuration are shown in Fig. 7.1. Both glass and GFRP materials were simulated using 8-node Serendipity plane stress elements with 2 x 2 Gauss-Legendre integration scheme. The adhesive layer that connects the GFRP and glass was simulated by 6-node zero thickness interface elements with 3-points Gauss-Lobatto integration rule. The thickness of the adhesive layer was reproduced by positioning both adherends at a distance of 2 mm with the interface elements in between.

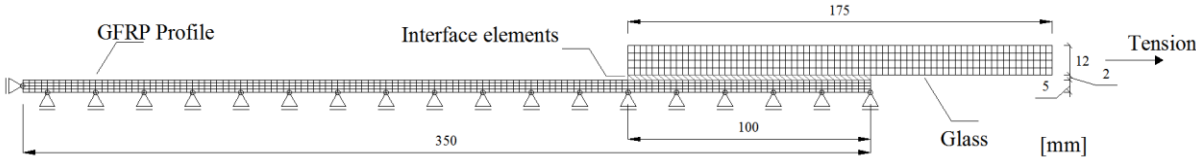


Fig. 7.1 - Mesh and boundary conditions of the double-lap joints numerical models.

7.3.2.2 Composite beams

The rectangular composite beams were numerically simulated taking into account symmetry considerations and considering their real geometry. Therefore, only half of the span of the composite beams was modelled. Both the single glass pane and the GFRP reinforcement were modelled by means of 8-node Serendipity plane stress elements with 2 x 2 Gauss-Legendre integration scheme (plane stress analysis).

For the adhesive joints the three different approaches mentioned above were studied. Fig. 7.2 depicts the geometrical differences of each approach, as well as the overall geometry of the numerical models

of the composite beams, their boundary conditions, load configuration and mesh size adopted⁶. The depth of the adhesive joints of all models, simulated either with plane stress elements or with interface elements (6-node zero thickness interface elements⁷ with 3 points Gauss-Lobatto integration rule), was equal to the glass web thickness. The maximum number of elements was 975 on the PB models, 1200 on the PSE models and 1050 on the IE models; in all cases, the mesh density was much lower than the ones adopted in [7.11, 7.18] for beams with comparable geometry and length.

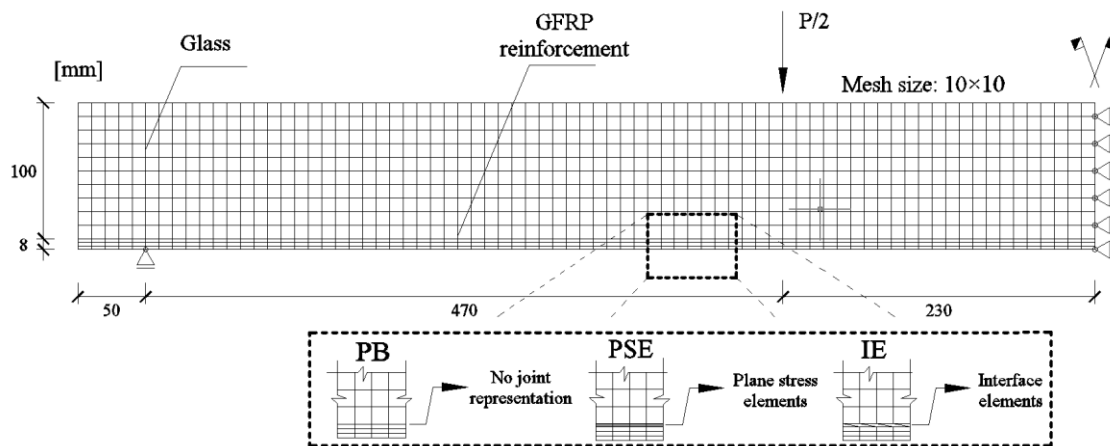


Fig. 7.2 - Mesh, boundary conditions and joint properties of the beams numerical models.

7.3.3 Constitutive models of materials and interfaces

The hybrid glass system comprises three different materials. In chapter 6, section 6.2.2, the main material and mechanical properties experimentally determined for the adhesives and GFRP were presented. This section presents detailed information on how each material was numerically simulated, namely the constitutive models used to represent the fracture of glass, as well as all the joint properties and constitutive laws adopted to simulate the mechanical behaviour of beams bonded with different adhesives.

7.3.3.1 Glass

For simulating the linear elastic behaviour of glass, the recommendations of the *Guideline for European Structural Design of Glass Components* [7.19] were followed, for which annealed glass has a Young's modulus (E) of approximately 70 GPa, a Poisson's ratio of 0.23 and a tensile strength ($f_{g,t}$) ranging from 30 to 80 MPa⁸.

In the models of the double-lap joints (*cf.* section 7.3.2.1), glass was simulated as linear elastic, for both compression and tension, using the aforementioned properties. No failure criterion was considered. For

⁶ A mesh sensitivity analysis was performed in preliminary studies developed with linear elastic materials; those studies showed that 8-node Serendipity elements with a mesh of $10 \times 10 \text{ mm}^2$ give sufficiently accurate simulations.

⁷ Constitutive laws presented in section 7.3.3.3.

⁸ $f_{g,t}$ is a mechanical property of glass known to be dependent on a variety of factors, such as size of existing micro cracks, surface side, panel size, stress distribution or load duration. Depending on these factors and under a relatively low stress rate, crack growth develops on small existing flaws, increasing their size and ultimately causing the collapse of glass elements. Some studies indicate that strength may vary from 30 MPa to 80 MPa due to those factors [7.25, 7.26].

the glass-GFRP composite beam models glass was simulated as linear elastic in compression and in tension prior to cracking; after cracking, non-linear behaviour was considered with cracking being simulated according to the SCA (non-linear fracture mechanics). For glass in compression, no failure criterion was considered. It is worth noting that the constitutive models of glass investigated in this study consider only monolithic glass (not applicable to laminated glass).

An extensive numerical assessment, summarized in Table 7.1, was performed in order to calibrate five important parameters required for the definition of the non-linear material model of glass. In the next paragraphs a detailed description of the assumptions made for each parameter is provided. The following nomenclature (5 labels) was considered to name each model: “ $G_f - h - f_{g,t} - \text{shape of tension-softening diagram} - \beta$ ”. A single parameter was changed at a time (all the others remained with their default value), with the exception of models with G_f lower than 188 N/m⁹, where h was also changed, in order to achieve low G_f values (detailed ahead in this section). The default properties of the glass non-linear material (hereafter referred to as *Standard Non-linear Material Model for Glass* or *SNLMMG*) are highlighted in Table 7.1. The calibrated non-linear model of glass was then used in the PSE and IE models.

As a result of the two main assumptions made in the SCA (mentioned in section 7.2), the crack normal stress (σ_n^{cr}) is determined by a tension-strain constitutive law (usually named tension-softening diagram) defined by the $f_{g,t}$, G_f and h . The first two parameters (as well as the shape of the tension-softening diagram) are considered material properties and the last one is inherent to the SCA. Traditionally, for computational reasons, two additional assumptions are made in the SCA: (i) computational instabilities and convergence issues (e.g. snap-back instabilities) should be avoided, and (ii) mesh objectivity should be preferably assured. The snap-back instability is avoided by ensuring a maximum value of h (Eq. (7.1-a)), which is dependent on the maximum unidimensional slope (b) of the softening branch in the tension-softening diagram, G_f , $f_{g,t}$ and E [7.6, 7.14]. The mesh objectivity is ensured by simply assuming a relationship between h and mesh size (e.g. h equal to the square root of the finite elements’ area [7.6]). In summary, the classical numerical approach to guarantee stability and convergence in smeared crack models involves controlling the h (and not any of the other parameters, which are assumed to be constant material properties), which is mesh-dependent. Therefore, according to Eq. (7.1-a), there is a maximum value of h that can be used in order to simulate a specific material or, in other words, the FE mesh size is directly dependent on the simulated material and its properties. In brittle materials like glass, which presents very low G_f , that assumption requires the use of highly discretised models, with all the disadvantages involved.

$$h \leq \frac{G_f \cdot E}{f_{g,t}^2 \cdot b} \qquad G_{f,min} \geq \frac{f_{g,t}^2 \cdot h \cdot b}{E} \qquad (7.1-a,b)$$

⁹ Corresponding to the minimum G_f to avoid snap-back instabilities, as discussed in this section.

The above-mentioned numerical approach was originally developed for concrete in softening. Since its applicability to glass fracture was not yet comprehensively assessed, in this study the influence of all parameters in Eq. (7.1) (with the exception of E) was investigated considering the following two criteria: (i) the mesh size was kept as $10 \times 10 \text{ mm}^2$, and (ii) the snap-back instability was avoided by assuming a G_f value higher than the minimum required by Eq. (7.1-b), which results from a direct manipulation of Eq. (7.1-a). The main objective was to assess the effects of using models with less discretized meshes and, consequently, higher G_f values, which, although not fully accurately representing the fracture properties of glass, would be much less time consuming and would face much less convergence issues.

The influence of G_f on the PB model was assessed by testing a wide range of G_f values from 3 N/m (the reference value reported in the literature) to 3000 N/m (Table 7.1). The tested values were lower, higher and equal to the minimum energy required when assuming a $10 \times 10 \text{ mm}^2$ mesh size and h equal to the square root of the FEs' area¹⁰.

The complete range of tested G_f was defined by assuming two different hypotheses for h : (i) for $G_f > G_{f,min}$, mesh objectivity was kept, thus $h = \sqrt{A_{element}} = 10 \text{ mm}$; (ii) for $G_f < G_{f,min}$, the mesh objectivity was neglected and h was equal to 1.0 mm and 0.1 mm, resulting in G_f values of 30 N/m and 3 N/m, respectively. The analysis of the effects of h on the numerical response of the composite beams is included in the discussion about the influence of fracture energy (discussed ahead in section 7.5.1.1), since the main goal of changing h was to achieve the glass fracture energy mentioned in the literature.

In this study, the following five different $f_{g,t}$ values were considered: 30 MPa, 45 MPa, 50 MPa, 55 MPa and 80 MPa. The three intermediate values cover the range of values observed in the beam bending tests, whereas the minimum and maximum values correspond to the lower and upper bounds referred in the literature [7.19]. The main objective was to assess the possible influence of the cracking load (as experimentally observed) on the behaviour of the numerical models. Since the $G_{f,min}$ of the numerical models is dependent on the material's tensile strength (Eq. (7.1-b)), two approaches were adopted: (i) G_f was assumed equal to the minimum required for each $f_{g,t}$ considered (changing from model to model), or (ii) G_f was considered constant and equal to the minimum required by the model with $f_{g,t} = 55 \text{ MPa}$ (model " $G_{f,min} - \sqrt{A_{element}} - 55 - \text{Linear} - 2$ "). Therefore, the latter approach was only simulated on models with $f_{g,t}$ ranging from 45 to 55 MPa due to objectivity purposes.

The non-linear material behaviour of glass was analysed using three different tension-softening diagrams (Fig. 7.3): (i) the *Linear* diagram that corresponds to a linear softening branch, which minimizes G_f ($b = 0.5$); (ii) the *Bilinear* diagram that aims at representing a higher energy loss in the

¹⁰ In true, the value of G_f considered was 5% higher than the value yielded by Eq. (7.1-b) due to convergence issues. Models with a mesh of $10 \times 10 \text{ mm}^2$ and different parameter combinations have repeatedly shown convergence issues after the appearance of the first crack or in a premature crack stage. Therefore, the $G_{f,min}$ was slightly increased from 178.57 N/m (the minimum value yielded by Eq. (7.1-b)) to 188.04 N/m.

beginning of the softening branch, which is a possible feature of brittle materials with a semi-stable fracture [7.7] ($b = 0.9$); and (iii) the *Cornelissen* diagram [7.20], a negative exponential softening law that presents a smooth energy degradation, providing advantages in terms of convergence ($b \approx 1.37$). The last two diagrams have the disadvantage of presenting a higher maximum slope, which also affects the $G_{f,min}$ value needed for the simulations (Eq. (7.1-b)). Therefore, the models that required higher G_f values, more precisely, the models with the *Bilinear* and *Cornelissen* diagram were simulated with fracture energy values of 321 N/m and 487 N/m, respectively.

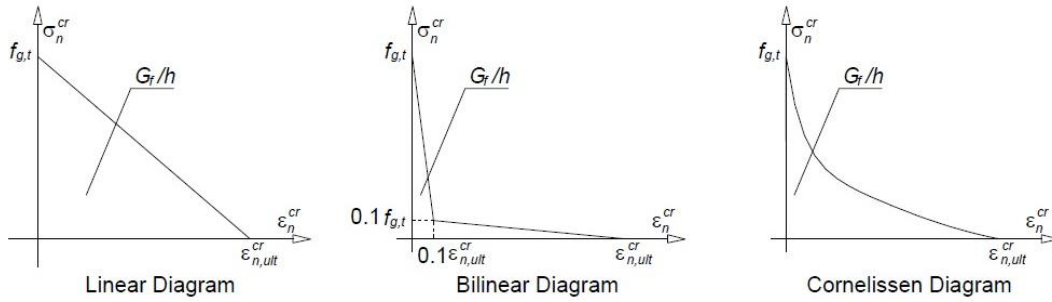


Fig. 7.3 – Tension-softening diagrams simulated for glass non-linear material.

The non-linear material model used allows the evaluation of the shear retention factor in two distinct ways [7.21]: (i) a constant value, and (ii) a non-constant value defined by Eq. (7.2),

$$\beta = \left(1 - \frac{\epsilon_n^{cr}}{\epsilon_{n,ult}^{cr}} \right)^p \quad (7.2)$$

where p is a parameter that can assume the values of 1, 2 or 3, and ϵ_n^{cr} and $\epsilon_{n,ult}^{cr}$ are the crack normal strain and the ultimate crack normal strain, respectively. The PB models of the beams were tested for constant values of $\beta = 0.00001$, $\beta = 0.01$, $\beta = 0.1$, $\beta = 0.99$ and all the possible power laws available ($p = 1, 2, 3$).

In what concerns crack triggering and initiation, in the multi-fixed smeared crack model used, a new crack is initiated when the maximum principal stress in a specific integration point exceeds the uniaxial tensile strength and the angle between the direction of the existing cracks and the direction of the maximum principal stress exceeds the value of a predefined threshold angle [7.14]. In this study, the threshold angle was assumed constant and equal to 30° and a maximum of 2 cracks per integration point was allowed to arise.

7.3.3.2 GFRP

In the models of the double-lap joints and the glass-GFRP composite beams, GFRP was modelled as linear elastic, for both tension and compression, according to the mechanical properties experimentally determined and presented in chapter 6, section 6.2.2.

7.3.3.3 Adhesives and interfaces

PB models, i.e. models that assume perfect bond at the interfaces, are only valid for connections that present high levels of interaction. In this study, it was assumed that this hypothesis was a good approximation for joints bonded with the *SDur* adhesive (*cf.* chapter 6, section 6.6.1.2). For beams that presented low levels of interaction (*R-SFlex* beams) this approximation could not be accounted for and different models were tested: the PSE models and the IE.

In the PSE models the adhesives were modelled as linear elastic. The Young's modulus and Poisson's ratio of each adhesive were defined based on experiments (*cf.* chapter 6, section 6.2.2). Due to their high simplicity, these models did not account for any slippage at the interfaces nor for any potential influence of the adhesives' viscoelasticity. Hence, they were not able to accurately represent the interface behaviour reported, for example, on the *DL-SFlex* experiments, where debonding at the interfaces took place. On the other hand, in the IE models both the mechanical properties of the adhesive and the adhesion characteristics at the interfaces were considered. The interface elements in these models were defined using two different constitutive laws in accordance with the adhesive simulated and the corresponding initial experimental stiffness observed in the double-lap joints. For the *IE-SDur* models (developed to simulate the *R-SDur* beams) a linear elastic law characterized by the normal and tangential stiffnesses (K_n and K_t , respectively) was adopted. In the *IE-SFlex* models (for the *SFlex* adhesive), a non-linear bond stress-slip relation was assumed, defined by the linear elastic normal stiffness K_n and by Eq. (7.3), where τ_m and s_m are, respectively, the maximum shear stress and the corresponding maximum slip, and α and α' are the parameters that define the shape of the pre and post-peak curves, respectively [7.14]:

$$\tau(s) = \begin{cases} \tau_m \left(\frac{s}{s_m} \right)^\alpha & \text{if } s \leq s_m \\ \tau_m \left(\frac{s}{s_m} \right)^{-\alpha'} & \text{if } s > s_m \end{cases} \quad (7.3)$$

K_n could not be calibrated, neither with the data retrieved from the shear tests nor with the data from the beams' flexural tests. Therefore, based on Sena-Cruz [7.14], K_n was taken as 10^6 kN/m³ to avoid any influence on the shear behaviour of the interface elements. Table 7.3 presents the properties of the interface elements used to model each type of adhesively bonded specimens.

Table 7.3 - Properties of the interface elements considered for the two adhesives.

Adhesive	K_n [N/m ³]	K_t [N/m ³]	s_m [mm]	τ_m [MPa]	α [-]	α' [-]
Sikaflex 265	10^6	N.A.	4.20	1.70	0.90	N.A.
Sikadur 31-cf	10^6	200	N.A.	N.A.	N.A.	N.A.

*N.A. = not applicable

7.3.4 Type of analysis

In the models of the double-lap joints, load was applied under displacement control at the end of the glass adherend. Two different failure criteria were set to control the numerical simulations: (i) for the *SFlex* adhesive the simulation was stopped when the maximum experimental displacement was attained¹¹, whereas (ii) for the *SDur* adhesives simulations were performed until the stress in the glass adherends reached 30 MPa in pure tension (the maximum axial stress that was estimated to have occurred in the experiments).

In the beam tests, load was applied at one single point at the top edge of the glass pane, according to the experimental setup, and the numerical analysis was also undertaken under displacement control. The analysis was stopped when the maximum experimental displacement was attained (*R-SFlex* models) or when the initial strength was recovered (PB and *R-SDur* models).

7.4 DOUBLE-LAP JOINTS: RESULTS AND DISCUSSION

The load vs. relative displacement curves obtained from the numerical models are plotted and compared with the experimental data in Fig. 7.4. One may see that even for the *DL-SFlex* specimens, whose behaviour was slightly non-linear, the constitutive models adopted reproduced accurately the initial slope of the experiments.

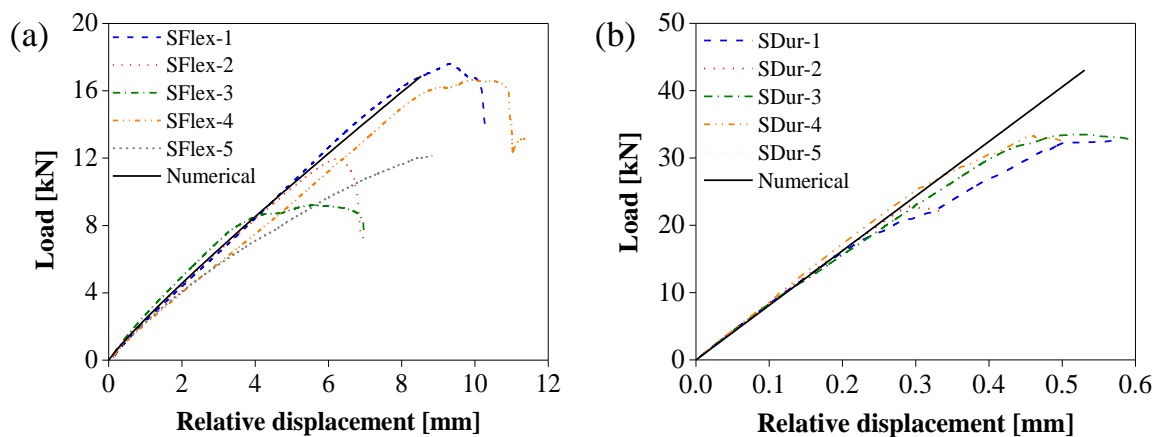


Fig. 7.4 – Double-lap joints: experimental and numerical comparison of the load vs. relative displacement for specimens (a) *DL-SFlex* and (b) *DL-SDur*.

Fig. 7.5 shows the numerical results in terms of axial strains along the overlap length of the specimens and the respective comparison with the experimental results. As for the load vs. relative displacement curves, in spite of the relatively high scatter of experimental data, a general good agreement was

¹¹ Despite the visual reports of an adhesive failure of the *DL-SFlex* joints, the debonding was only observed on a slight branch of the joints' load vs. relative displacement curves (*cf.* chapter 6, section 6.4). The (double) redundancy of the specimens as well as the test setup and test measurement equipment did not allow to fully record the debonding phase. Therefore, debonding was not included in the numerical models of the double-lap joints.

obtained between measured strains and numerical results, providing further validation to the FE models and, in particular, to the parameters used to simulate the constitutive relations of the bonded interfaces. Using interface elements with higher tangential stiffness led to a steeper initial distribution of axial strains (Fig. 7.5-b). In opposition, a lower tangential stiffness caused a more linear distribution of axial strains along the overlap length (Fig. 7.5-a).

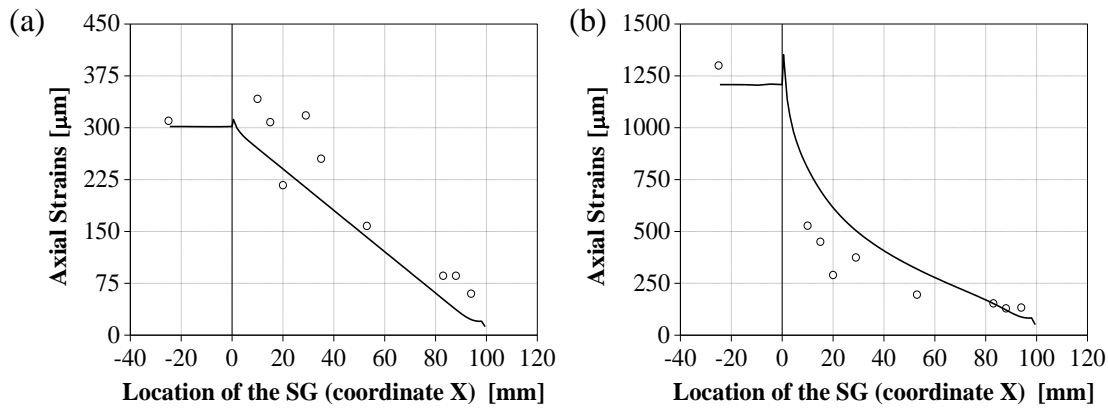


Fig. 7.5 – Double-lap joints: experimental (dots) and numerical (lines) axial strains (a) at 5.0 kN for *DL-SFlex-2* and (b) at 20 kN for *DL-SDur-4*.

7.5 COMPOSITE BEAMS: RESULTS AND DISCUSSION

7.5.1 Effect of glass material options

7.5.1.1 Fracture energy

Fig. 7.6 compares the experimental load vs. mid-span deflection responses (*cf.* chapter 6, section 6.6.1.1, Fig. 6.13) to numerical curves obtained considering different G_f values. The results show that all models properly reproduced the overall experimental behaviour of the glass composite beams, with the exception of the model with $G_f = 3000$ N/m. The overall numerical behaviour was similar to the experimental observations, presenting an initial linear response (initial flexural stiffness of 1.57 kN/mm) followed by a post-cracking stage with progressive loss of stiffness.

With the exception of model “3000 – $\sqrt{A_{element}} - 50 - \text{Linear} - 2$ ”, all the numerical models accurately predicted the crack initiation load (equal to 5.0 kN). After this point, as in the experiments, a sudden load decay was observed. However, a large difference can be observed between the numerical and experimental deflections at this specific point. That difference is attributed to the fact that the data acquisition speed (5 Hz) was not fast enough to capture such sudden load drop in the experiments. The post-cracking stage was very similar between models and minor differences were found. In true, if the displacement path would be kept, all models (with the exception of model with $G_f = 3000$ N/m) would yield the same post-cracking response. This result seems to indicate that adding GFRP reinforcement to glass beams allows using a

relatively wide range of G_f values (3 to 300 N/m), considerably higher than the reference value reported in the literature, with no significant loss of precision.

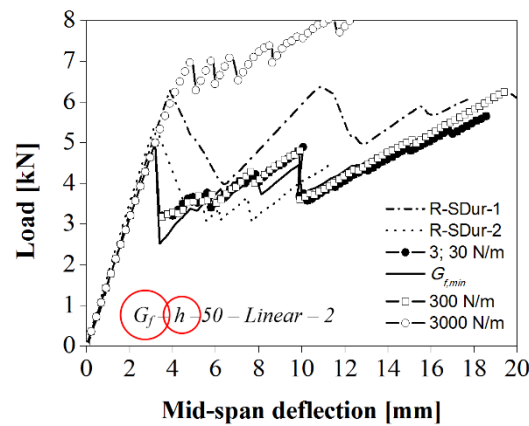


Fig. 7.6 - Effect of G_f on the load vs. mid-span deflection curves of *R-SDur* beams.

Fig. 7.7 presents the effect of G_f on the crack pattern of the beams obtained for two different deflection values¹². As for the flexural behaviour, all models showed an equivalent behaviour, with an overall good agreement with the corresponding experimental observations (*cf.* chapter 6, Fig. 6.13). In addition, in all models the oblique cracks developing at the GFRP vicinity along the shear span could be perfectly traced in the experimental prototype. During the post-cracking stage, the existing cracks are always *fully opened* (cracks in purple), i.e. mode-I fracture energy is fully exhausted in those cracks.

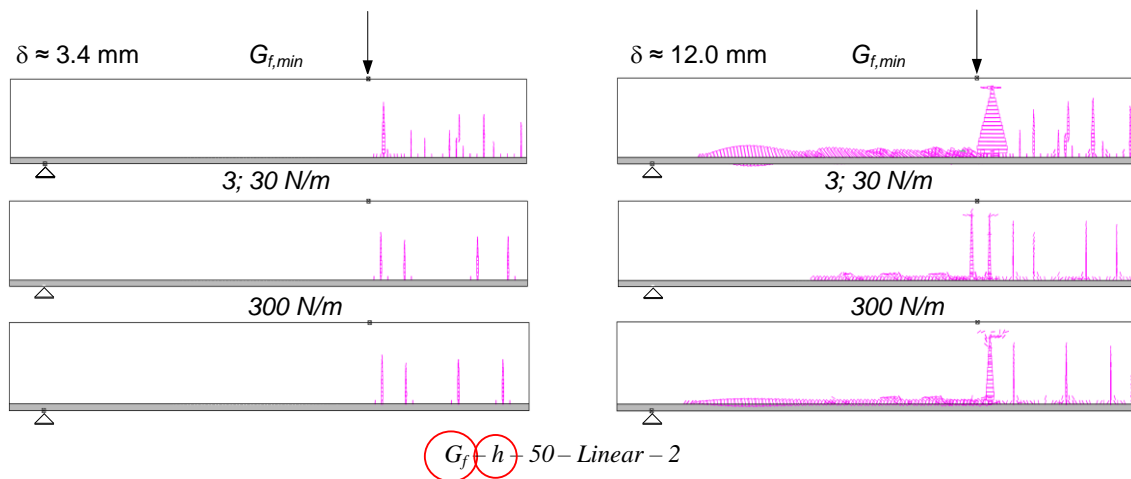


Fig. 7.7 - Effect of G_f on the composite beam's crack pattern. Crack legend: fully-open (purple).

Finally, all models were able to recapture the initial strength, which was set as the stopping criterion in the models. At this point, no substantial differences were detected between the different numerical models in terms of deformed shapes, stress distributions and crack patterns (Fig. 7.8). This result, once

¹² The behaviour of the model with $G_f = 3000$ N/m was not considered in this comparison due to the poor compliance with the experimental load vs. deflection results.

more, sustains that during the post-cracking stage the GFRP reinforcement was the main component governing the beam’s behaviour, and hence a fully accurate definition of G_f was not a critical factor.

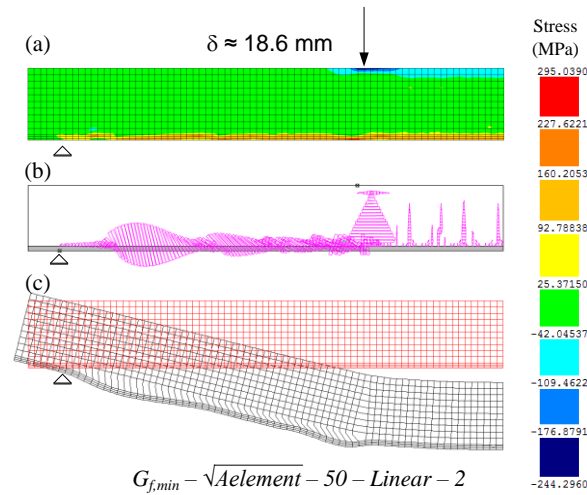


Fig. 7.8 - Numerical results of model “ $G_{f,min} - \sqrt{A_{element}} - 50 - Linear - 2$ ” in terms of (a) stress distribution, (b) crack pattern and (c) deformed shape. Crack legend: closed (green), and fully-open (purple).

7.5.1.2 Tensile strength

Fig. 7.9 presents a comparison between the experimental and numerical load vs. mid-span deflection curves of *R-SDur* beams, by considering $f_{g,t}$ of 30, 45, 50, 55 and 80 MPa. One can see that changing the $f_{g,t}$ did not affect the overall qualitative behaviour of the beams for both modelling approaches considered¹³. Aside from the expected differences on the cracking loads and initial load drop, all models were able to keep their integrity and restore the beams’ initial strength. The post-cracking process, the progressive loss of stiffness and the residual strength were similar among the different beams.

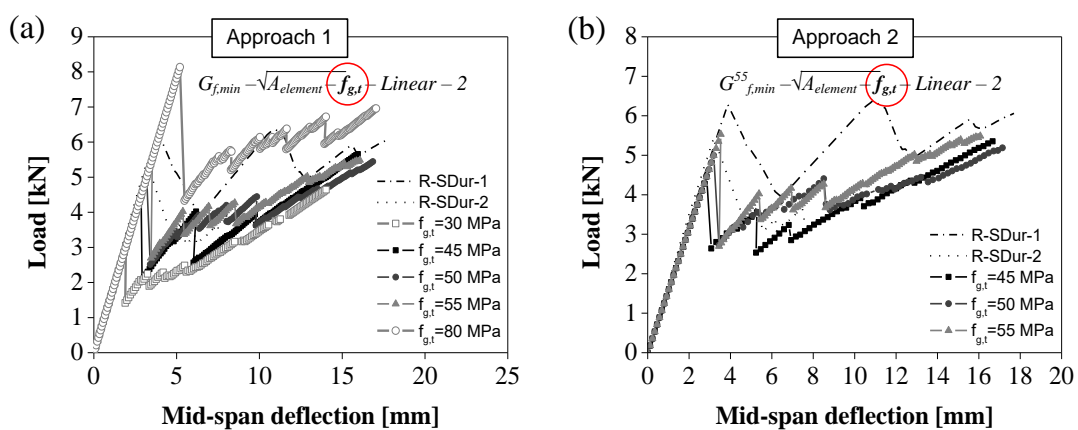


Fig. 7.9 – Effect of $f_{g,t}$ on the load vs. mid-span deflection curves, considering (a) approach 1, and (b) approach 2.

¹³ Approach 1 assumes $G_f = G_{f,min}$ of each model; Approach 2 assumes a unique G_f in models with $f_{g,t} = 45, 50$ and 55 , equivalent to the $G_{f,min}$ of model with $f_{g,t} = 55$ MPa.

In what concerns crack pattern, minor differences were found between the models with $f_{g,t} = 30$ MPa, 45 MPa and 50 MPa (Fig. 7.10). However, the models with higher $f_{g,t}$ (55 and 80 MPa) were unable to simulate multiple cracks with high vertical development and, for a high value of displacement, a significant reduction of the number of shear cracks was visible. This is in line with the general behaviour that would be expected from a material with a higher tensile strength.

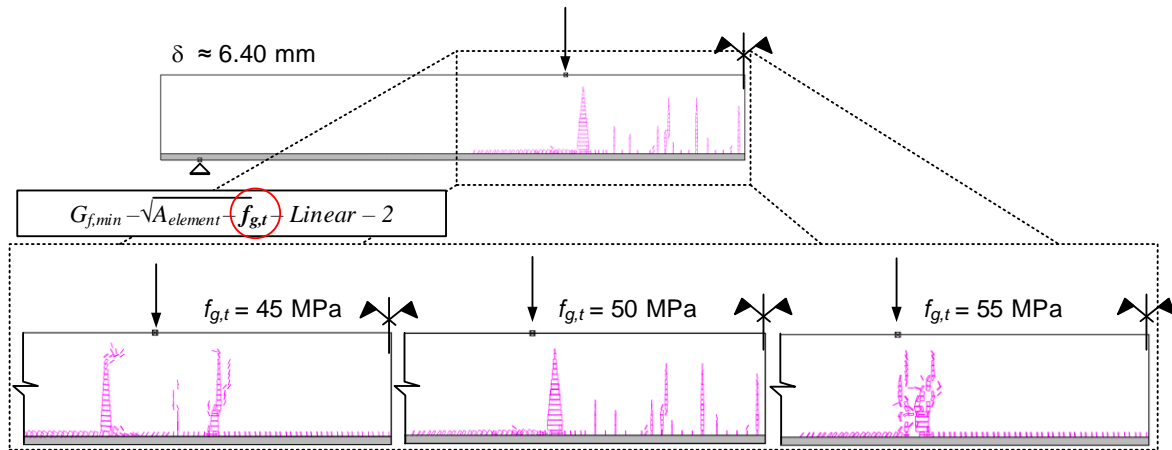


Fig. 7.10 - Effect of $f_{g,t}$ on the crack pattern for (left to right) $f_{g,t} = 45$ MPa, 50 MPa and 55 MPa (approach 1). Crack legend: fully-open (purple).

7.5.1.3 Tension-softening diagram

Fig. 7.11 shows the comparison between the experimental flexural behaviour of the *R-SDur* beams and the numerical behaviour obtained for the three different tension-softening diagrams simulated. One may observe that the *linear* shape is the one that best simulates the observed experimental behaviour. The other two constitutive laws clearly overestimated the post-cracking flexural performance and did not exhibit a progressive loss of stiffness after the initial load drop: for a displacement of 10 mm, the residual strength in those models was higher than the initial strength and around 42% higher than the experimental residual strength measured in *R-SDur-2* beam specimen. These differences can also be observed in the crack pattern. Indeed, apart from the *Linear* diagram, none of the other two models tested was able to replicate shear cracks towards the supports in an early stage¹⁴, thus being unable to present a steeper progressive loss of stiffness (cf. Fig. 7.10 with $f_{g,t} = 50$ MPa and Fig. 7.12). Although higher fracture energies had to be used with *Bilinear* and *Cornelissien* diagrams (respectively 1.7 and 2.6 times higher compared to the *Linear* one), the differences highlighted above are attributed essentially to the change of the shape of the different tension-softening diagrams; indeed, for the *Linear* diagram, no significant changes in the numerical results were obtained when the fracture energy was increased up to 2.6 times the default value (the aforementioned results are not presented in this study).

¹⁴ The first shear cracks were visible around a vertical deflection of 6.0 mm and 10.0 mm, respectively in the *Linear* and *Cornelissien* diagrams; models using the *Bilinear* diagram were unable to present any development of shear cracks even in an advanced damage stage.

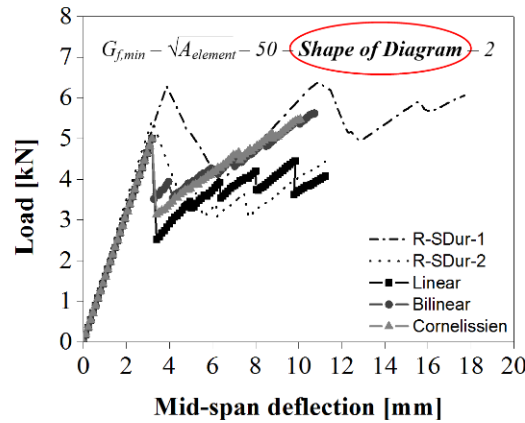


Fig. 7.11 - Effect of the tension-softening diagram shape on the load vs. mid-span deflection curves.

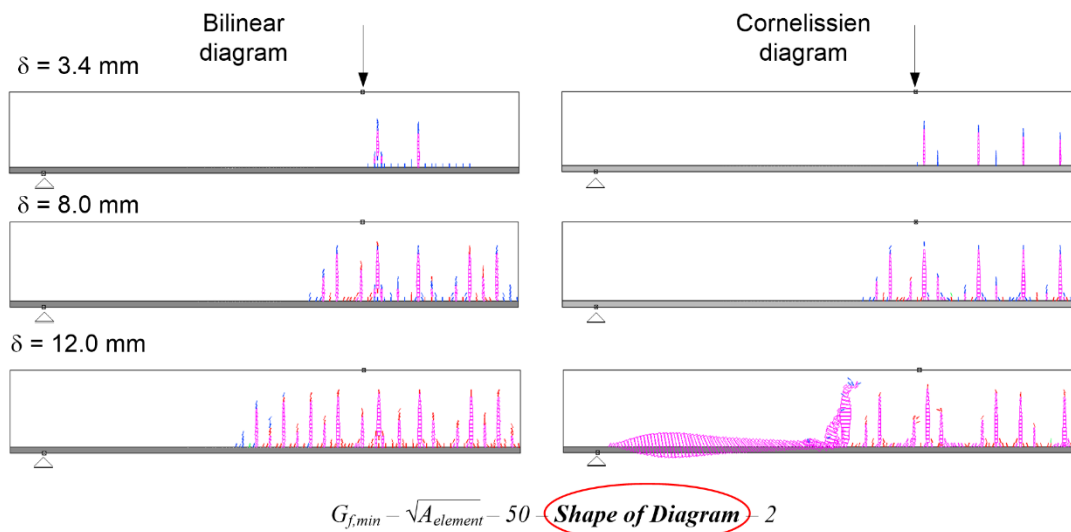


Fig. 7.12 - Effect of the tension-softening diagram shape on the crack pattern.
Crack legend: opening (blue), closed (green), reopening (red) and fully-open (purple).

The reported differences may be related with the expected fracture behaviour of glass, which is closer to the *Linear* (brittle materials with semi-stable fractures) diagram than to the *Bilinear* or *Cornelissien*. The first diagram is the only one capable of rapidly exhausting the total low fracture energy of glass, presenting a low ultimate crack normal strain, which is a central criterion for simulating highly quasi-brittle materials, even if featuring a semi-stable fracture. The other two diagrams seem to have the disadvantage of retaining normal stresses for higher crack normal strains, not accurately representing the physical behaviour of glass.

7.5.1.4 Shear retention factor

Fig. 7.13 shows the influence of the shear retention factor on the numerical flexural response of the glass-GFRP composite beams. For low constant values of β (< 0.00001), the flexural behaviour presented good agreement with the experimental data, whereas for high constant values of β the numerical models overestimated the residual strength. This result, together with the fact that during glass

propagation most of the cracks are *fully-open*, shows that glass cracks are either characterized by low values of β or by high shear stiffness degradation once the $f_{g,t}$ is attained. Therefore, high constant values of β do not correctly simulate the experiments and, conversely, low constant values seem to be a good approximation¹⁵. Models with non-constant β values, i.e. dependent on the current and ultimate crack normal strains, predicted the overall experimental response with fairly good accuracy, since they replicated high initial shear degradation. Minimum differences were found between the model with $\beta = 0.00001$ or power law degradations using $p = 1, 2$ and 3 . These results are in agreement with the study of Bedon and Louter [7.11].

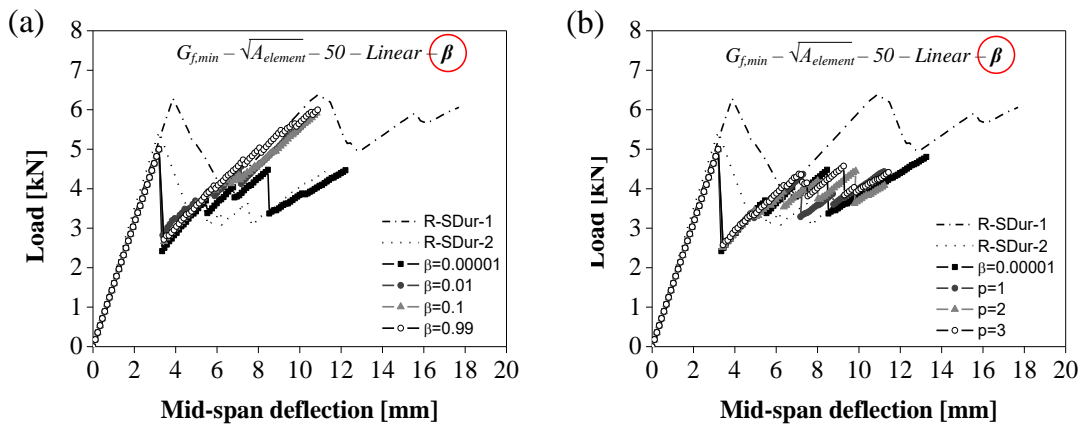


Fig. 7.13 - Effect of (a) constant and (b) variable β on the load vs. mid-span deflection.

Similar conclusions can be drawn when analysing the crack pattern (Fig. 7.14), i.e. low constant values of β yielded crack patterns with shear cracks as well as horizontal cracks on the upper part of the cross-section (tensile area), whereas for higher values of β these two types of cracks were not yielded, despite a noticeable development of vertical cracks towards the supports. The best correlations were obtained using a non-constant value of β , namely by taking $p = 2$ (cf. Fig. 7.10 and $f_{g,t} = 50$ MPa).

7.5.2 Effect of adhesive's properties

The previous sections addressed the implementation of a non-linear model to simulate the fracture behaviour of glass. Several parameters were calibrated in order to guarantee a stable and convergent model, capable of reproducing the fracture process on the glass-GFRP composite beams with perfect bond. After selecting the glass material model¹⁶, the next step was to explicitly adopt a constitutive law for the adhesive joints aiming at the simulation of the composite glass beams bonded with an arbitrary adhesive.

¹⁵ It should be noted that the numerical model considers only monolithic glass panes. For laminated glass the complexity should increase significantly; for instance, with stiff interlayers it is likely that different shear retention factors need to be considered to simulate local shear transfer effects.

¹⁶ *SGNLMM* assumes 10×10 mm², $G_f = G_{f,min}$, $h = \sqrt{A_{element}}$, $f_{g,t} = 50$ MPa, linear tension-softening diagram, and $\beta = (1 - \frac{\epsilon_n^{cr}}{\epsilon_n^{ult}})^2$.

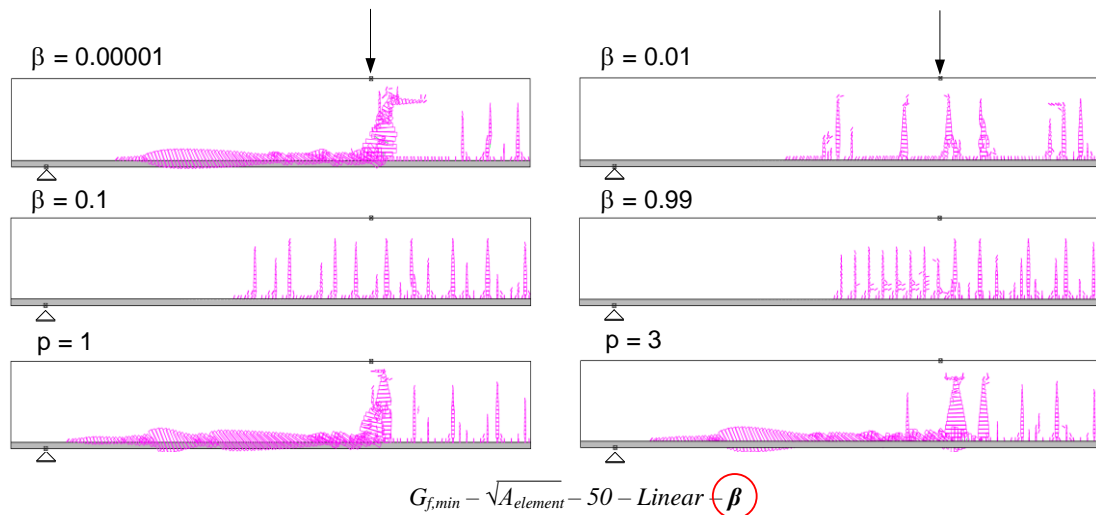


Fig. 7.14 – Effect of β on the composite beam crack pattern ($\delta = 13.75$ mm).
Crack legend: closed (green), and fully-open (purple).

Fig. 7.15 compares the experimental flexural responses with the numerical results obtained from the PB, PSE and IE models. One can conclude that the PB model (*R-SNLMMG-PB*) overestimates the flexural response of rectangular glass-GFRP composite beams bonded with the applied low stiffness adhesive (Fig. 7.15-a). Therefore, such models are inappropriate for simulating the *R-SFlex* beams.

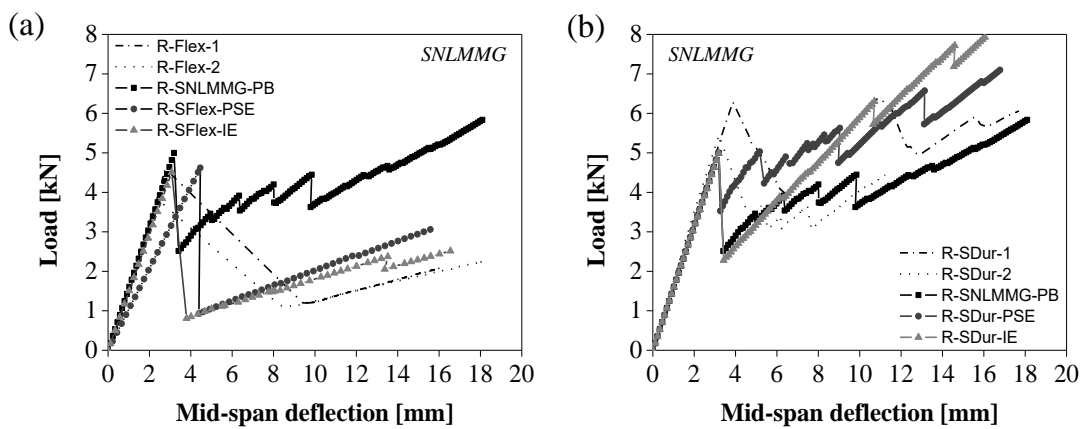


Fig. 7.15 – Experimental and numerical flexural behaviour of (a) *R-SFlex* and (b) *R-SDur* beams assuming: (i) no adhesive layer (PB), (ii) plane stress elements (PSE), or (iii) interface elements (IE) to represent the adhesive layer.

In addition, Fig. 7.15-a shows that the PSE models underestimated the flexural stiffness of the *R-SFlex* beams (26.5% lower than measured). This relative difference may be due to the experimental difficulty in accurately estimating the material properties of this very flexible and viscoelastic adhesive. Indeed, the properties considered in this study were obtained from tensile tests, when in the beam tests the adhesive is subjected mostly to shear. On the other hand, with the interface elements (IE model), the numerical response of the glass composite beams bonded with the *SFlex* adhesive was reproduced with much higher accuracy in terms of (i) initial stiffness (only 3.5% higher than measured) and (ii) load

reduction after the appearance of the first crack. In this regard, as mentioned, the differences to test data shall stem from the experimental measuring system, which was unable to capture with sufficient accuracy the complete path of the load drop.

In terms of crack pattern slight differences were found between the models used to simulate the *R-SFlex* beams response. The numerical introduction of the adhesively bonded interface led to the appearance of a significantly lower number of cracks in both PSE and IE models when compared to the PB model (cf. Fig. 7.8). However, only the PSE model succeeded in accurately simulating the localized crack pattern of the *R-SFlex* beams, which was characterized by the appearance and development of a single crack under the load application section (Fig. 7.16). The development of the crack pattern in the *R-SFlex-IE* model was localized but restricted to three cracks instead of only one.

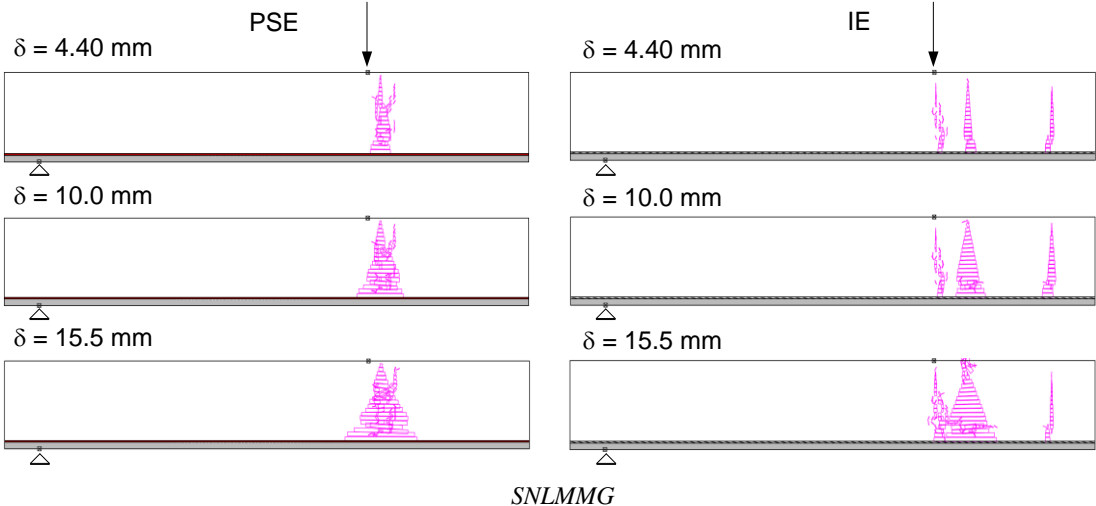


Fig. 7.16 - Crack pattern of *R-SFlex* beams when (left) PSE or (right) IE models were adopted to represent the adhesive layer. Crack legend: closed (green), and fully-open (purple).

Regarding the *R-SDur* beams, Fig. 7.15-b shows that the PSE models accurately estimated the initial stiffness of the composite beams and their cracking load. However, the post-cracking stage was not fully accurately captured; indeed, the models succeeded to simulate a progressive loss of stiffness and successive load drops, but yielded higher residual strength than the beams tested with the same cracking load. The models exhibited a shorter initial load drop, which affected the entire simulation, overestimating residual strength since the appearance of the first crack.

As for the PSE models, it was expected that the introduction of interface elements simulating the adhesive layer would not impair the good accuracy already achieved with the PB and PSE numerical models. However, Fig. 7.15-b shows that the IE models were able to accurately simulate the initial linear elastic stiffness, but were not so successful in capturing the second stage stiffness, as well as its progressive decrease during the crack propagation in the glass pane. Comparing the crack pattern of *R-SDur-PB* model with that of *R-SDur-IE* model, it is noticeable that some precision was lost

(Fig. 7.17): for a displacement of 17.2 mm, the numerical models were unable to present horizontal cracks or oblique shear cracks towards the supports. This may be due to the intrinsic limitations of the double-lap shear tests performed (*DL-SDur* specimens) in retrieving the complete response of the glass/*SDur* adhesive/GFRP bonded interfaces of the composite beams, namely in representing the cracked stage of their flexural response¹⁷.

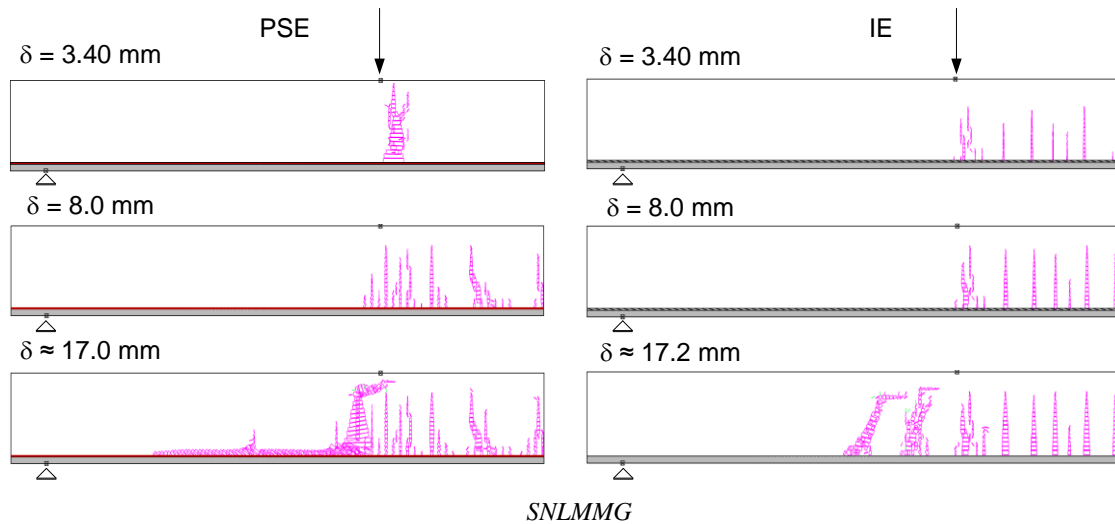


Fig. 7.17 - Crack pattern of *R-SDur* beams with (left) PSE and (right) IE models representing the adhesive layer. Crack legend: closed (green), and fully-open (purple).

7.6 CONCLUDING REMARKS

This chapter presented a numerical study about the development of plane FE models to simulate the flexural behaviour of rectangular glass-GFRP composite beams. The study had two main objectives: (i) to calibrate a standard non-linear material model for glass according to the smeared crack approach (SCA), and (ii) to assess a suitable method to reproduce adhesively bonded joints of glass-GFRP composite beams.

The numerical models developed show that the SCA is able to reproduce glass fracture in composite beams and that the introduction of calibrated interface elements enhances the numerical models with bonded joints comprising soft adhesives.

The correct use of a standard model for glass requires the definition of several parameters. The numerical results that best fit the experimental response were obtained when the following parameters were adopted: (i) tensile strength of 50 MPa; (ii) fracture energy equal to the minimum value necessary to avoid snap-back instability, (iii) available under a linear tension-softening diagram and (iv) combined with a quadratic shear retention factor law; (v) crack band width equal to the square root of the finite

¹⁷ Alternative experiments could involve single lap shear tests (to avoid *structural redundancy*), compressive loads (to prevent premature glass failure) and eventually cracked glass adherends to assess the influence of cracks in the stress transfer at the bonded interfaces.

elements' area (assuring mesh objectivity); (vi) threshold angle of 30° for the development of new cracks; and (vii) maximum number of two cracks per element.

It was shown that it is possible to simulate glass fracture considering a higher G_f than the experimental (reference) value of 3 N/m. Indeed, the overall flexural behaviour of the glass-GFRP composite beams, characterized by a linear elastic pre-cracking stage and a *pseudo-ductile* post-cracking stage, was successfully reproduced using G_f in the range 3 N/m to 300 N/m. Therefore, it seems that it is possible to simulate glass-GFRP composite beams without using highly discretized meshes, thus requiring less computation time and allowing the use of more practical and stable numerical models.

For the geometries, materials and load conditions considered in this study, changing the glass strength did not affect the overall qualitative behaviour of the composite beams, but retrieved different cracking loads, in line with the experimental observations (prone to glass scatter). Regarding the tension-softening diagram, the models showed that a better correlation is found when a linear shape (the one that minimizes G_f) is used. Finally, the study on the shear retention factor proved that non-constant values are suitable for the shear stress transfer after cracking.

Regarding the effect of using different adhesives to bond GFRP to glass, the accuracy of the different numerical approaches depended on the adhesive at stake. The joints bonded with the *SFlex* adhesive presented low levels of interaction (considerable slippage), which resulted in lower flexural stiffness and global strength, but enhanced post-cracking ductility (*cf.* chapter 6). The most accurate numerical predictions of the aforementioned behaviour were obtained by simulating the adhesive joint using interface elements with the following constitutive law: exponential shear law ($\alpha = 0.90$), with peak point at a slippage of $s_m = 4.20$ mm and $\tau_m = 1.70$ MPa and with normal stiffness of $K_n = 10^6$ kN/m³. On the other hand, the composite beams bonded with the *SDur* adhesive presented high levels of interaction with negligible slip at the interfaces. Therefore, for these beams, the most accurate models were those in which the adhesive was not physically represented and perfect bond between glass and GFRP was considered.

It is worth mentioning that the material models developed in this study consider only monolithic glass. Future developments are needed to investigate their applicability to laminated glass, as well as to other structural systems comprising different composite beam concepts and reinforcing materials.

7.7 REFERENCES

- [7.1] Sena-Cruz J, Barros J, Azevedo Á, Ventura-Gouveia A. Numerical simulation of the nonlinear behavior of RC beams strengthened with NSM CFRP strips. C. 2007 - Congr. Numer. Methods Eng. XXVIII CILAMCE - Iber. Lat. Am. Congr. Comput. Methods Eng., 2007, p. 13–5.
- [7.2] Ølgaard AB, Nielsen JH, Olesen JF. Design of mechanically reinforced glass beams : modelling and experiments. *Struct Eng Int* 2009;19:130–6.
- [7.3] Louter C, Nielsen JH. Numerical analyses of the effect of SG-interlayer shear stiffness on the structural performance of reinforced glass beams. In: Belis, Louter, Mocibob, editors. COST Action TU0905, Mid-term Conf. Struct. Glas., vol. 1, Porec: 2013, p. 405–12.
- [7.4] Louter C. Fragile yet Ductile - Structural Aspects of Reinforced Glass Beams. PhD thesis, Delf University of Technology, Netherlands, 2011.
- [7.5] Louter C, Belis J, Veer F, Lebet J-P. Structural response of SG-laminated reinforced glass beams; experimental investigations on the effects of glass type, reinforcement percentage and beam size. *Eng Struct* 2012;36:292–301.
- [7.6] Bazant ZP, Oh BH. Crack band theory for fracture of concrete. *Mater Struct* 1983;16:155–77.
- [7.7] Nakayama J. Direct measurement of fracture energies of brittle heterogeneous materials. *J Am Ceram Soc* 1965;48:583–7.
- [7.8] Outwater JO, Gerry DJ. On the Fracture Energy of Glass. NRL Interim Contract Report. University of Vermont, Burlington, Vt.: 1966.
- [7.9] Wiederhorn SMS. Fracture surface energy of glass. *J Am Ceram Soc* 1969;52:99–105.
- [7.10] Haldimann M, Luible A, Overend M. Structural Use of Glass. Zurich: IABSE-AIPC-IVBH; 2008.
- [7.11] Bedon C, Louter C. Exploratory numerical analysis of SG-laminated reinforced glass beam experiments. *Eng Struct* 2014;75:457–68.
- [7.12] Modéer M. A Fracture Mechanics Approach to Failure Analyses of Concrete Materials. PhD thesis, Lund Technical University, Sweden, 1979.
- [7.13] Petersson P-E. Crack Growth and Development of Fracture Zones in Plain Concrete and Similar Materials. PhD thesis, Lund Technical University, Sweden, 1981.
- [7.14] Sena-Cruz JM. Strengthening of Concrete Structures with Near-Surface Mounted CFRP Laminate Strips. PhD thesis, University of Minho, Portugal, 2004.
- [7.15] Neto P, Alfaiate J, Valarinho L, Correia JR, Branco FA, Vinagre J. Glass beams reinforced with GFRP laminates: Experimental tests and numerical modelling using a discrete strong discontinuity approach. *Eng Struct* 2015;99:253–63.
- [7.16] Correia JR, Valarinho L, Branco FA. Post-cracking strength and ductility of glass-GFRP composite beams. *Compos Struct* 2011;93:2299–309.
- [7.17] Valarinho L, Correia JR, Branco FA. Experimental study on the flexural behaviour of multi-span transparent glass-GFRP composite beams. *Constr Build Mater* 2013;49:1041–53.
- [7.18] Martens K. Numerical investigation of two-sided reinforced laminated glass beams in statically indeterminate systems. *Glas Struct Eng* 2016;1:1–15.
- [7.19] Report EUR 26439 EN Guidance for European Structural Design of Glass Components. Institute for the Protection and Security of the Citizen, Joint Research Centre, Luxembourg: 2014.
- [7.20] Cornelissen HAW, Hordijk DA, Reinhardt HW. Experimental determination of crack softening characteristics of normalweight and lightweight concrete. *Heron* 1986;31:45–56.
- [7.21] Valarinho L, Correia JR, Branco F, Sena-Cruz J. Experimental investigations on continuous

- glass-GFRP Beams. Preliminary non-linear numerical modelling. In: Bos, Louter, Nijse, Veer, editor. *Challenging Glas. 3 Conf. Archit. Struct. Appl. Glas.*, Delft: Amsterdam: IOS Press; 2012, p. 745–58.
- [7.22] CNR-DT 210/2013 Istruzioni per la Progettazione, l'Esecuzione ed il Controllo di Costruzioni con Elementi Strutturali di Vetro. Consiglio Nazionale Delle Ricerche, Roma: 2013.
- [7.23] The Institution of Structural Engineers. *Structural Use of Glass in Buildings (Second edition)*. London: The Institution of Structural Engineers (ISE); 2014.
- [7.24] Bažant Z. Fracture in concrete and reinforced concrete. In: Ltd. JW& S, editor. *Mech. Geomaterials Rocks, Concr. Soils*, 1985, p. 259–303.
- [7.25] Veer F, Louter P, Bos F. The strength of annealed, heat-strengthened and fully tempered float glass. *Fatigue Fract Eng Mater Struct* 2009;32:18–25.
- [7.26] Vandebroek M, Louter C, Caspee R, Ensslen F, Belis J. Size effect model for the edge strength of glass with cut and ground edge finishing. *Eng Struct* 2014;79:96–105.

PART IV
CONCLUSIONS AND
FUTURE DEVELOPMENTS

CHAPTER

8

CONCLUSIONS AND FUTURE DEVELOPMENTS

8.1 CONCLUSIONS

8.1.1 General conclusions

This thesis aimed at improving and develop the understanding about the structural behaviour of glass structures for civil engineering applications, regarding both (i) current laminated glass structures, and (ii) new hybrid structural systems combining glass with other materials.

The study focused on four main topics: (i) the assessment of the lateral-torsional buckling (LTB) behaviour of long-span multi-layer laminated glass beams, (ii) the characterization of the creep behaviour of full-scale multi-layer laminated glass panels, (iii) the assessment of the post-cracking stiffness of glass-stainless steel hybrid beams, and (iv) the development of a new composite structural system made of glass and pultruded GFRP profiles. The objectives set for the thesis were globally accomplished, as new insights were obtained for the different topics, providing in-depth understanding about the behaviour of laminated glass structures and showing the potential of hybrid/reinforced/composite structural systems, including the one developed in this thesis. A detailed description of the main conclusions drawn in each research domain is presented in the following paragraphs.

8.1.2 Structural behaviour of laminated glass members

8.1.2.1 *Flexural behaviour of large-scale multi-layer laminated glass beams*

For the first research domain, experimental, analytical and numerical studies were performed about the lateral-torsional buckling (LTB) behaviour of long-span multi-layer laminated glass beams.

The experimental campaign comprised a flexural test of a long-span 3-layer PVB-laminated glass beam. The test confirmed the susceptibility of this type of structural members to the LTB phenomenon. The analytical study provided important data regarding the accuracy of existing expressions (including those developed at IST in the frame of the present study) for the determination of the LTB resistance and post-buckling behaviour of multi-layer laminated glass beams. The numerical study showed that commercial FE tools are able to predict the linear, buckling and post-buckling responses of laminated glass beams with very good accuracy; nonetheless, the successful numerical modelling of such large-scale beams required considerable computational effort.

This study also confirmed the importance of duly considering, at the design stage, the influence of both temperature and loading time on the shear properties of the PVB interlayer sheets that connect the glass plies of laminated beams. Such effects, which depend on the geometry of the beams and their loading and support conditions, stem from the inherent viscoelastic behaviour of polymer base interlayers. For the experimental conditions used in this study, it was shown that when temperature increases from 20 °C to 23 °C the LTB critical load decreases by 4%; more importantly, it was shown that when the load duration increases from 3 s to 20 min, the LTB critical load decreases by 46%.

8.1.2.2 Creep behaviour of full-scale laminated glass panels

The second topic, the long-term flexural response of laminated glass members, was addressed by performing relative long flexural creep tests (350 h) of full-scale laminated glass panels with PVB and SG interlayers. The results of those tests were then used to develop simple analytical models (based on Findley's power law), able to predict the creep response of the laminated panels and the viscoelastic shear properties of the interlayers. The predictions were compared with those obtained from material models of the interlayers available in the literature, which generally rely on (i) DMA tests of interlayer coupons or (ii) short-duration torsional and flexural tests of small-scale laminated glass specimens (both methods require the application of time-temperature superposition principle (TTSP) techniques).

The results of the creep tests highlighted the viscoelastic behaviour of both laminated glass panels and confirmed the much higher viscoelasticity of PVB compared to SG. For the panel geometries and load conditions used, at the end of the tests, the mid-span deflections of the PVB and SG panels increased 120% and 1.6%, respectively.

The results obtained showed the ability of Findley's power law methodology to accurately describe the flexural behaviour of both PVB and SG-laminated glass panels during the creep test period. The analytical expressions obtained are expected to be also able to accurately estimate the long-term behaviour of the laminated glass panels, for similar geometric, loading and temperature conditions.

This study showed that for both types of laminated panels, the short and long-term predictions provided by Findley's approach (supported up to 350 h by the results of creep tests on full-scale panels) can present considerable differences when compared to predictions based on the viscoelastic material models from the literature. Longer creep experiments in full-scale laminated glass elements are needed to further assess and compare the relative accuracy of these two approaches.

The different prediction models were used to estimate the structural effects of the interlayers' viscoelasticity (in terms of shear coupling) as a function of time. For the conditions used in the tests, after 50 years of sustained loading, the shear coupling degree varied from 0% (model from literature) to 22% (power law) for PVB, whereas for SG it varied from 89% (model from literature) to 93% (power law).

8.1.3 Structural behaviour of large-scale laminated glass-stainless steel hybrid beams

This thesis presented an exploratory study about the structural behaviour of large-scale laminated glass-stainless steel hybrid beams. Two large-scale PVB and SG-laminated glass beams, with fully tempered glass panels, were reinforced with stainless steel profiles on both edges and subjected to bending tests up to failure. The PVB-laminated hybrid glass beam was tested with the outer plies fully cracked to assess its robustness, while the SG-laminated hybrid glass beam was tested with all glass plies uncracked. A simplified analytical model was developed in order to estimate the contribution of fully tempered glass plies to the post-cracking flexural stiffness of the PVB-laminated hybrid glass beams.

The cracked PVB-laminated hybrid glass beam exhibited considerable residual post-cracking stiffness and strength. However, regardless of the damage condition of the laminated glass panels, none of the beams was able to present post-cracking residual strength after the breakage of the glass plies (the inner one, in the case of the PVB-laminated hybrid glass beam). The ultimate failure of both beams involved the debonding of the stainless steel reinforcing element in the vicinity of one of the supports. In the case of the PVB-laminated hybrid glass beam, such debonding was the triggering failure mechanism; it is likely that the strength of the stainless steel-adhesive interface was affected by the cracked state of the outer glass plies, which increased the shear stress transfer at the interface of the undamaged glass ply, thus causing the premature debonding. Regarding the SG-laminated hybrid glass beam, it was not possible to draw definitive conclusions about the triggering failure mechanism. Indeed, the maximum tensile stress attained in the glass plies exceeded the characteristic tensile strength of fully-tempered glass and, consequently, premature debonding may have occurred due to the energy release after the failure of one of the inner glass plies. However, at the same time, the numerical model of this beam showed that considerable shear stresses developed in the vicinity of the support sections. In any case, the results obtained show that large-scale hybrid glass beams are highly susceptible to interfacial debonding and that more effective and tailored anchoring systems may need to be developed. Further investigations should also be carried out to understand the influence on the structural response of the adhesively bonded joints of (i) glass fragmentation and (ii) energy release due to glass failure.

The flexural tests performed on the PVB-laminated hybrid glass beam were also used to improve the understanding of the post-cracking flexural behaviour of hybrid glass beams made with fully cracked glass panels. In particular, a simplified analytical model was developed in order to estimate the contribution of fully tempered cracked glass plies to the post-cracking flexural stiffness of PVB-laminated hybrid glass beams. Based on this model, the compressive elastic modulus of the cracked glass plies was estimated to present a value of 50 GPa, which was kept roughly constant during the test. The tensile elastic modulus was also estimated to be 50 GPa for loads up to 20 kN, while for increasing loads it presented a steady reduction up to 25 GPa (at failure). Despite the well-known poor post-cracking performance of fully tempered glass, the results obtained show that the small glass fragments,

combined with the PVB interlayer and stainless steel profiles, are able to provide a non-negligible contribution to the global post-cracking flexural stiffness of hybrid glass beams.

8.1.4 Structural behaviour of glass-GFRP composite glass beams

8.1.4.1 Experimental study

The structural behaviour of glass-GFRP composite beams was first assessed by means of an extensive experimental campaign aiming at the characterization of the flexural behaviour of full-scale multi-span glass-GFRP composite beams. The effects of the reinforcement geometry, of the structural adhesive stiffness and of the number of spans were investigated. For the reinforcement geometry two different GFRP configurations were tested: rectangular (R-section) and I-section. Three types of adhesives (*Sikaflex 265*, *Sikaforce 7710-L100* and *Sikadur 31-cf*) were used, covering a wide range of Young's modulus values. Finally, the redundancy and robustness of the composite beams were also assessed in simply supported (SS) and continuously supported (CS) configurations. The experimental campaign proved the advantages and technical viability of using glass-GFRP composite beams. It was shown that the brittleness of glass structures can be overcome by combining glass with GFRP pultruded profiles using different structural adhesives.

For the SS configuration, the I-section beams presented higher initial and post-cracking stiffness, cracking load, ultimate load, post-cracking strength and ductility, when compared to beams reinforced with the rectangular GFRP profile. Therefore, the reinforcement increase enhanced the beams performance, both before and after glass fracture. With the exception of most *R-Sikadur* beams (bonded with the stiffest adhesive), the rectangular composite beams were unable to recover the initial cracking strength, mostly due to the debonding at the glass-adhesive interfaces. On the other hand, the I-section beams presented considerable increase of post-cracking strength, ranging from 1.6 to 2.8 times the initial cracking strength. The increase of post-cracking ductility was also noteworthy, namely on the *I-Sikaflex* beams (bonded with the softest adhesive), which exhibited an ultimate deformation more than 2 times higher than the *R-Sikaflex* beams. The increase of post-cracking ductility of *I-Sikaforce* and *I-Sikadur* beams was less relevant compared to their rectangular counterparts.

The experimental campaign proved that the mechanical properties of the adhesives affect both the pre and post-cracking performances. Indeed, the adhesive with lowest apparent Young's modulus did not provide enough shear coupling at the bonded interfaces, which reduced significantly the cracking and post-cracking strength. However, the slippage at the interfaces observed with the *Sikaflex* adhesive for both reinforcement geometries provided a safer failure mechanism, since it allowed the beams to present high values of ultimate deformation, namely with the I-section geometry. In opposition, the beams bonded with the stiffer adhesives were unable to explore such deformation capacity, even those bonded with the adhesive featuring intermediate mechanical properties and non-linear tensile behaviour (*Sikaforce*).

The experimental campaign on CS beams proved that the post-cracking performance of hybrid glass members can be improved not only due to the cross-sectional redundancy, but also due to the force redistribution achieved with such structural configuration. In fact, the use of a hyperstatic structural system positively influenced the strength (cracking load and ultimate load) and bending stiffness of the composite glass beams. Beams with two spans were able to achieve higher cracking and ultimate loads compared to estimates obtained from linear elastic analysis. This result may be related with the differences in the test setups of both series (4-point vs. 5-point testing), the brittle nature of glass and the consequent size effect on strength. In spite of those variations, the post-cracking strength achieved by composite glass beams bonded with the *Sikaflex* adhesive increased from the SS to the CS configuration, as well as the post-cracking ductility of beams bonded with the *Sikaforce* adhesive. Unlike the other two types of beams, composite glass beams bonded with *Sikadur* adhesive presented a considerable reduction of post-cracking performance on the SS configuration.

8.1.4.2 Numerical study

The experimental tests of the rectangular glass-GFRP composite beams were numerically modelled using FEMIX software, which makes use of the smeared crack approach (SCA) to simulate the non-linear behaviour of (quasi) brittle materials. The study aimed at (i) defining/calibrating the parameters that describe the non-linear material response of glass according to the SCA, and (ii) to assess a suitable method to simulate the adhesively bonded interfaces of glass-GFRP composite beams.

The first goal was successfully achieved and a material model for glass was defined based on the evaluation of five parameters (described next) that characterize the non-linear behaviour of glass according to the SCA. Considerable attention was given to the effects of using the intrinsic low fracture energy of glass (G_f) on the stability and convergence of the models. The results obtained indicate that it is possible to simulate the fracture of glass by assuming higher values of G_f than those reported in the literature; this brings important computational advantages, in terms of convergence and mesh density. In fact, no significant differences were found in the results obtained from models of glass-GFRP composite beams using G_f ranging from 3 N/m to 300 N/m.

The numerical results that best fit the experimental response were obtained when the following parameters were adopted: (i) tensile strength of 50 MPa; (ii) G_f equal to the minimum value necessary to avoid snap-back instability, (iii) available under a linear tension-softening diagram and (iv) combined with a quadratic shear retention factor law; (v) crack band width equal to the square root of the finite elements' area (assuring mesh objectivity); (vi) threshold angle of 30° for the development of new cracks; and (vii) maximum number of two cracks per element.

The numerical study of the glass-GFRP composite beams allowed to conclude about the applicability of different approaches to simulate the behaviour of the glass-GFRP joints, depending on the mechanical properties of the adhesives. For joints comprising stiff adhesives, which guarantee perfect bond between

glass and GFRP (e.g. epoxy resin), accurate results were obtained considering perfect bond at the interface, thus without simulating explicitly the adhesive layer. For joints made of low stiffness adhesives, more accurate results were obtained using calibrated interface elements.

8.2 FUTURE DEVELOPMENTS

The experimental, analytical and numerical investigations presented in this thesis provided a better understanding of the structural behaviour of laminated glass members and composite structural systems combining glass with stainless steel or GFRP. The study presented in the research domain of hybrid glass structures, namely of hybrid beams made of glass and GFRP, is relatively new; therefore, there are several aspects that need to be investigated in further depth. This section describes the recommendations for future research in the domains of laminated glass structures and hybrid/reinforced/composite glass structures.

8.2.1 Flexural behaviour of laminated glass structural members

In the domain of laminated glass structural members the major challenge at this moment is the development of design guidelines that can be used in engineering practice. The data from different studies need to be compiled and discussed so it can be used for design purposes. The publication of a standard draft would enable the increase of this type of structural glass applications.

In the particular domain of structural stability, the knowledge about the behaviour of laminated glass beams can be further extended by focusing on the following aspects:

- Development of standardized analytical methodologies to determine the LTB resistance of laminated glass elements taking into account the glass productions tolerances, the viscoelastic mechanical behaviour of interlayers (of any type) and glass strength;
- Assessment of the effects of continuous elastic lateral restraints on the LTB resistance and post-buckling behaviour of laminated glass elements (a topic that has been recently object of several studies, e.g. [8.1–8.4]);
- Assessment of the LTB resistance and post-buckling behaviour of laminated hybrid glass beams, i.e. the assessment of the contribution of the reinforcing material to the stability of the laminated glass members.

Future research about the long-term behaviour of laminated glass members should focus on the following aspects:

- Long-term experimental creep studies on PVB and SG laminates in order to clarify the differences encountered between deformation predictions using the proposed power laws and the material models available in the literature;

- Based on the aforementioned experiments, confirming/updating the analytical formulation proposed herein in order to more reliably and accurately estimate the long-term behaviour of PVB and SG laminates;
- Similar experimental and analytical studies on other types of interlayers and for different environmental conditions (e.g. temperature and relative humidity).

8.2.2 Structural behaviour of hybrid glass systems

Hybrid glass systems is still a relatively recent topic in the structural glass field. Further investigations are needed in order to fully understand their behaviour and to develop reliable solutions with commercial prospect. In the studies performed until now, several different material combinations have been tested but they generally focused on a single or limited number of behavioural aspects; comprehensive experimental campaigns addressing the various relevant aspects of the structural behaviour of composite glass beams are still necessary. In this context, the following general aspects of hybrid glass structures can be further investigated:

- Development of the concept of hybrid glass structures to other types of structural members different than beams, such as wall/slab panels or columns;
- Optimization of production methods, namely those that rely on the application of structural adhesives.

In the specific domain of adhesively bonded joints, there are interesting developments and requests from the glass industry that indicate that such solutions will have a higher demand in the near future, not just for applications involving the connection of glass to other structural materials, but also for glass-to-glass connections. In that regard, the following aspects are worth being further investigated:

- Development of a standardized test setup to determine the mechanical properties in shear, tension and compression, of adhesively bonded joints involving glass adherends;
- Experimental, analytical and numerical studies to fully characterize the bond behaviour between glass and other materials, either using structural adhesives or common interlayers;
- Experimental studies to characterize the long-term behaviour of adhesively bonded joints between glass and other materials, subjected to different load levels and environmental agents;
- Experimental investigations in order to understand in further depth how adhesive connections can take advantage of the adhesives' or interlayers' viscoelastic properties to improve the structural safety of glass structures.

Regarding the structural behaviour of glass-stainless steel composite beams, in spite of the extensive studies available in the literature, there are important questions that still need to be addressed, namely in what concerns the post-cracking capacity and robustness of such systems when tempered glass is used. The following aspects should be object of further investigations:

- Experiments to fully characterize the mechanical behaviour of cracked glass beams reinforced with stainless steel taking into account the effects of (i) different levels of tempering, (ii) different interlayers, and (iii) different loading levels (energy release);
- Experimental tests and analytical/numerical studies addressing the effect of the section geometry and reinforcement percentage on the optimization of the post-cracking behaviour of composite glass beams;
- Experiments and analytical/numerical studies addressing the potential increase of the beam's ultimate load capacity by increasing the reinforcing area;
- Development of analytical and numerical tools able to describe the post-cracking behaviour of composite laminated glass members using different levels of tempering, thus exhibiting different fracture patterns.

In what concerns the flexural behaviour of glass-GFRP composite glass beams, the following aspects deserve further investigations:

- The understanding of the influence of the mechanical properties of the adhesives on the post-fracture behaviour can be further improved by performing tensile/compressive tests on single and double-lap joints between glass and GFRP; within the scope of this work, similar tests can be performed considering a damaged area of glass (laminated or not);
- Experiments on glass-GFRP composite beams made of laminated glass panels produced with different interlayers and comprising a wider range of structural adhesives in order to obtain an optimized post-fracture performance;
- The structural behaviour of glass-GFRP composite glass beams can be further developed by testing different section geometries aiming at improving the aesthetical appearance, together with the post-fracture performance;
- Experimental and analytical/numerical studies about the flexural behaviour at elevated temperature or under fire exposure of glass-GFRP composite glass beams, due to the well-known time and temperature dependency of the adhesives and GFRP;
- Further analytical and numerical tools should be developed in order to improve the understanding about these structures and provide engineers with accurate tools for their design.

The results obtained from the numerical study proved the applicability of the classical smeared crack approach to simulate the behaviour of composite glass-GFRP beams. The results can be further extended in future investigations by:

- Applying the FEMIX software and the proposed non-linear glass material model in 3D models in order to simulate the I-section beams;
- Performing numerical simulations on other composite glass systems, including those made of laminated glass, for which specific non-linear glass material models need to be developed;

- Improving the FEMIX software by developing numerical algorithms that improve the convergence of the models to a wider range of scenarios;
- The non-linear behaviour of glass-GFRP composite beams can be further improved by extending the material models library; this should involve considering the post-cracking performance and viscoelastic properties of the adhesives, which are time and temperature dependent.

8.3 REFERENCES

- [8.1] C. Bedon, J. Belis, C. Amadio, Structural assessment and lateral–torsional buckling design of glass beams restrained by continuous sealant joints, *Eng Struct* 2015;102: 214-229.
- [8.2] A. Luible, D. Schärer, Lateral torsional buckling of glass beams with continuous lateral support, *Glas Struct & Eng* 2016;1:153-171.
- [8.3] Sonck D, Belis J. Elastic lateral-torsional buckling of glass beams with continuous lateral restraints. *Glas Struct Eng* 2016;1:173–94.
- [8.4] C. Bedon, C. Amadio, Analytical and numerical assessment of the strengthening effect of structural sealant joints for the prediction of the LTB critical moment in laterally restrained glass beams, *Mat and Struct* 2016;49: 2471-2492.

